STRONG MICROWAVES: SOURCES AND APPLICATIONS

2009

Volume 1

Institute of Applied Physics
Nizhny Novgorod

RUSSIAN ACADEMY OF SCIENCES
INSTITUTE OF APPLIED PHYSICS

STRONG MICROWAVES: SOURCES AND APPLICATIONS

PROCEEDINGS
OF THE VII INTERNATIONAL WORKSHOP

Nizhny Novgorod, 27 July – 2 August 2008

Edited by
A. G. Litvak

In two volumes
Volume 1

Nizhny Novgorod – 2009

Edited by decision of the Editorial
and Publishing Board of the IAP RAS

ISBN 978-5-8048-0083-4

Editor's Preface

This two-volume publication comprises the materials of the International Workshop "Strong Microwaves: Sources and Applications", which took place on board "Georgiy Zhukov", a river boat cruising the Volga River. It was the seventh workshop in a series of traditional triennial workshops organized by the Institute of Applied Physics of the Russian Academy of Sciences starting in 1990. The main objective of these workshops has been to bring together engineers developing high-power microwave sources and scientists using these sources in fundamental and applied research. Earlier, these workshops were called "Strong Microwaves in Plasmas", since main attention was given to microwave applications in the plasma physics, specifically, microwave experiments on RF plasma heating in magnetic fusion setups. In recent years, the range of microwave applications considered at the workshops has widened greatly and now includes application of microwave sources in radar location and remote diagnostic of natural and laboratory processes, accelerators of charged particles and nuclear physics, and the development of new industrial technologies for material processing. Therefore, the International Programme Committee made the decision about reviewing the general title of the Workshop while retaining the continuity of its general rules including the workshop venue on board a boat cruising the Volga. A week-long stay of the workshop participants in a convenient enclosure of

a comfortable boat allows combining presentations at workshop sessions with practically unlimited discussions in between.

The Workshop hosted 107 scientists from 15 countries. Its scientific programme contained 26 invited plenary lectures, 26 invited topical talks, and 64 original contributions.

A major part of these papers is included in this publication. As usual, the texts of some important papers have not been submitted by their authors, mainly because these papers had been already published. Nevertheless, the presented material gives a sufficiently detailed idea of the state-of-the art and new trends in the field of development of high-power microwave sources and their applications.

Alexander Litvak

HIGH POWER MILLIMETER AND TERAHERTZ WAVE SOURCES

HIGH POWER 170 GHz GYROTRON DEVELOPMENT IN JAEA

K. Sakamoto, K. Kajiwara, A. Kasugai, K. Takahashi, N Kobayashi, Y. Oda

Japan Atomic Energy Institute, Naka, Ibaraki, Japan

Recent activities on the developments of high power 170 GHz gyrotron in JAEA are presented. A basic criterion of ITER gyrotron was satisfied using a $TE_{31,8}$ mode gyrotron The demonstrated typical operation parameters are the output power of 1.0 MW for 800 s with an efficiency of 55 %, and 0 8 MW, 1 hr, 57 %, etc And, the repetitive power output with 0.8 MW of 400 s pulse duration for every 30 min was achieved, which simulates the operation on ITER. The gyrotron is being operated for 3 years, and recorded the total output energy of 200 GJ. As a next step, a new gyrotron was designed and fabricated, which operates at higher order resonator mode to enable the operation at greater than 1 MW output power. In parallel, feasibility studies of power modulation and dual frequency gyrotron were carried out.

1. Introduction

On ITER (International Thermonuclear Experimental Reactor), a 20 MW electron cyclotron heating and current drive (EC H&CD) system is being planned for a plasma initiation, heating, current drive and MHD instability control [1, 2]. As a power source, 1 MW 170 GHZ long pulse gyrotron is required. A development of the 170 GHz gyrotron has been carried out in Russia, Europe and Japan [3, 4] since EDA phase (Engineering Design Activities). In 1990's, important breakthrough technologies for high power long pulse gyrotrons, such as a high efficiency mode converter [5], a depressed collector [6], and a diamond window [7–9], were developed, which gave a route to the realization of 170 GHz 1 MW CW gyrotron. In 2000's, quasi-CW operations were demonstrated by some gyrotrons. On 140 GHz gyrotrons developed for Wenderstein-7X, 30 min operations were demonstrated by EU and US using an advanced built-in mode converter in 2003–2005 [10, 11]. As for ITER gyrotron, a 1 MW oscillation was demonstrated at 170 GHz [12, 13]. In JAEA, a stable 1 MW oscillation was proved at CW-relevant pulse duration (800 s). Here, the efficiency was 55 % with the depressed collector at optimum oscillation parameters in the so-called hard excitation region. The achieved parameters satisfy a basic criterion required for ITER gyrotrons. Using this gyrotron as a power source, R&D works for a transmission line and a launcher are underway for ITER procurement, in addition to the reliability test of the gyrotron. As a next activity, the gyrotron development of higher power generation using a higher resonator mode is planned. A resonator diameter is raised by increase the mode number, which reduces a heat load density on the resonator wall. And, possibilities of a power modulation for application to the MHD instability suppression on ITER plasma and frequency tunability are considered for advanced operation.

In this paper, recent activities and next plan for gyrotron development at JAEA are described. In section 2, experimental results of 170 GHz gyrotron are shown. The R&D works on transmission line and launcher development are introduced in section 3. Next activities for the advanced gyrotron are discussed in section 4. Conclusion is given in section 5.

2. 170 GHz 1 MW Gyrotron for ITER

A picture of JAEA gyrotron is shown in Fig. 1 [14, 15]. An electron gun is a triode-type magnetron injection gun (MIG). In the beam tunnel, conical silicon carbide cylinders are installed to suppress a parasitic oscillation. A resonator is a cylindrical cavity, whose Q-factor is 1530 at $TE_{31,8}$ mode. An inner surface of the built-in mode converter is optimized to generate a Gaussian beam output by using CCR-LOT and Surf3D codes [16]. The RF beam radiated from the converter and is transmitted with 4 mirrors and is outputted through the diamond window of 1.853 mm in thickness. The disk edge is coated by Copper to protect the bonding material (Alminium) between the cuffs and the diamond from the corrosion. A control of the anode voltage of the triode MIG V_{ak} permits the pitch factor optimization of the electron beam at any beam voltage. With a combination of resonator field B_c (magnetic field in the resonator), electron parameters (cyclotron frequency and pitch factor) can be optimized during the oscillation. In Fig. 2 a history of the gyrotron operation is shown. Operation begun at March 2006, and important results, such as 1 hour oscillation, 1 MW / 800 s / 55 % and 0.8 MW / 1 h / 57 %, have been demonstrated as indicated in the figure. The total output energy records ~200 GJ. The output power and deposition power in the tube was measured calorimetrically. Sum of measured powers, output power from the window (1020 kW), collector deposition (742 kW), a stray radiation (24 kW) and ohmic loss (63 kW), agrees

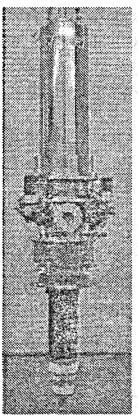

Fig. 1. Picture of JAEA 170 GHz gyrotron

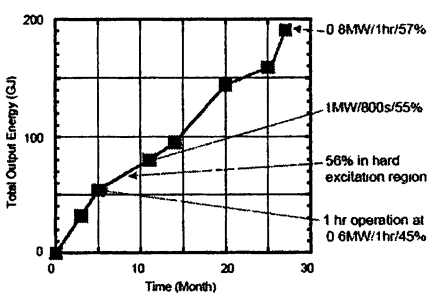

Fig. 2. Time history of output energy from the window of the 170 GHz gyrotron

well with the DC input power by the electron beam, 1854 kW. Owing to the high efficiency, the deposition power into the collector is suppressed significantly. This contribute to the reliability increase, shorter conditioning time and the trouble on the collector could be avoided. In Fig. 3 the beam current dependence of the output power and the efficiency with (h_{total}) and without (h_{os}) the depressed collector are shown. Pulse duration of all data is greater than 5 min. The accelerated beam voltage is ~72 kV. By the active control of V_{ak} and B_c, the operation parameters (electron cyclotron frequency and its pitch factor in the resonator) are optimized for each data in the hard excitation region. The maximum efficiency was ~60 % at 0.6 MW output.

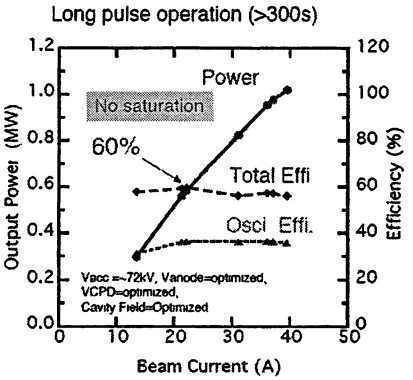

Fig. 3. Beam current dependence of output power and efficiencies with (h_{total}) and without (h_{os}) the depressed collector

Figure 4 shows the depressed collector voltage V_{dp} dependence of the output power and the efficiencies. The beam voltage and the beam current is ~72 kV and ~30 A, respectively. The V_{ak} and B_c are optimized during the oscillation as with the results of Fig. 3. The oscillation efficiency and the power are higher at lower V_{dp} since the higher pitch factor operation is available. Here, η_{os} = 39.1 % was obtained, which corresponds to the 42.5 % of the interaction efficiency at the resonator at V_{dp} = 21 kV. However, the total efficiency decreases due to the shallow depressed collector. The maximum total efficiency of 57 % was obtained at V_{dp} = 27 kV.

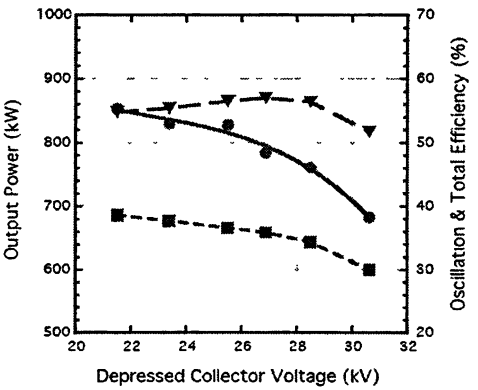

Fig. 4. The depressed collector voltage V_{dp} dependence of the output power and the efficiencies. The beam voltage and the beam current is ~72 kV and ~30 A, respectively. Circles are output power, squres are oscillation efficiency (η_{os}) and triangles are total efficiency with depressed collector

Figure 5 shows a time history of the applied voltages, beam current (~30 A), magnetic field at the resonator, a light signal observed in the tube, RF signal at a directional coupler, vacuum pressure in the tube at the output power of 0.8 MW. The efficiency was 57 %. The oscillation was very stable during the shot. The pressure increased for 40 mın, however, that kept a constant value after 40 min. Commonly, the pressure increase is observed after the end of the very long pulse shot, and soon returns to the original level. This pressure behavior is explained as follows. During the operation, the electron beam ionizes neutral particles in the tube. These positive ions are accelerated by the strong electric field applied for the depressed collector and absorbed by the collector wall. In other words, depressed collector gyrotron act as an ion pump inherently. When the operation ended, such pumping effect disappears. Consequently, the pressure increase is observed because the deposit particles are being released from the collector wall.

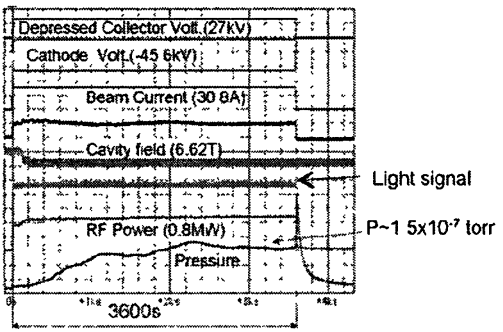

Fig. 5. A time history of the applied voltages, beam current (~30 A), magnetic field at the resonator, a light signal observed in the tube, RF signal at a directional coupler, vacuum pressure in the tube at the output power of 0.8 MW. The total efficiency is 57 %.

As a simulation of gyrotron operation on ITER, a high repetitive RF generation was demonstrated at 0.8 MW. Figure 6 shows the time history of the shots. Ten shots were repeated for every 30 min with the pulse duration of 400 s. The efficiency with the depressed collector was ~56 %. No conditioning shot was required between shots, which gives a prospect of stable operation in ITER [17]. In Fig. 7 a progress of the JAEA 170 GHz gyrotron performance is shown.

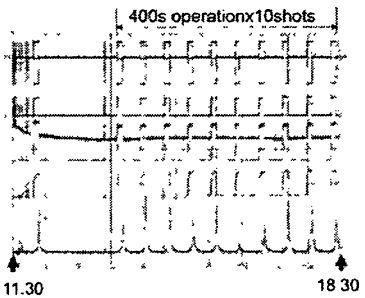

Fig. 6. Time history of the 10 shots in series. The pulse duration of each shot is 400 s, and the total efficiencies are ~56 %.

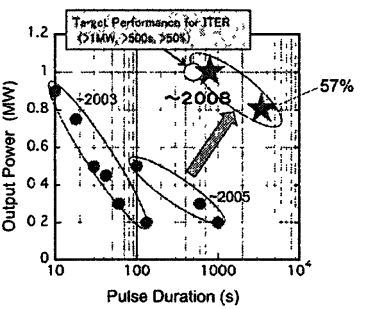

Fig. 7. Progress of the gyrotron performance

3. RF power transmission and launcher for ITER

In ITER, the 20 MW H&CD system is planned using 24 tubes of 1 MW / 170 GHz gyrotron. Here, a transmission efficiency of 83 % is assumed. In the transmission line, many components such as a matching optics unit (MOU) that interfaces the gyrotron output power with the waveguide, 7–9 miter bends, 1–2 isolation valves, a torus window for tritium confinement, and a launcher, are included. The development of the launcher and demonstration of high efficiency high power transmission are important R&D issues for ITER EC H&CD system. On the test stand in JAEA, developments of transmission line and launcher components are underway using the 170 GHz gyrotron as a power source [18].

In Fig. 8 picture of the test transmission line in JAEA test stand is shown. The output power couples with the waveguide of 63.5 mm in diameter via two-phase correlation mirrors in a matching optics unit (MOU), and 92 % of the output power was transmitted to the dummy load via 40 m evacuated transmission line with 7 miter bends. Here a coupling loss in the MOU is ~4.5 %. At the end of the transmission line, some components, such as the torus window for ITER, arc detector, low loss miter bend, polarizer, are connected. High power and long pulse tests of these components are underway as international collaborations.

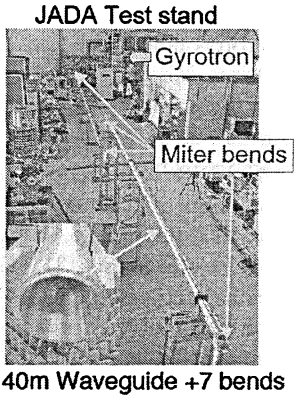

Fig. 8. Picture of transmission line in JAEA RF test stand

In parallel, a preliminary launcher mock-up was manufactured as shown in Fig. 9. The mock-up has one of three quasi-optical RF beam lines of the equatorial launcher. High power mm wave is radiated from one waveguide and reflected by a focusing mirror and radiated from the steering mirror. The surfaces of two mirrors are optimized to minimize the heat load on the mirrors [19, 20]. The angle of the final mirror can be controlled by using an ultrasonic motor. The power is received by a metal dummy load. The configuration of the system includes most of the essential components, which will be a basic model of ITER EC H&CD system, and will provide useful database for the detailed design of the EC system.

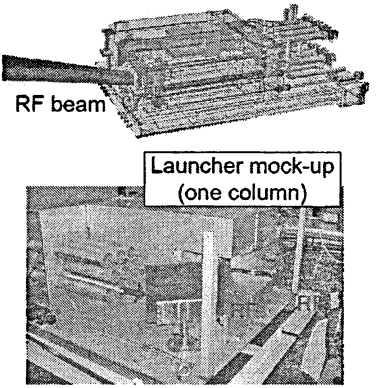

Fig. 9. Conceptual picture of one section of the quatorial launcher for ITER (upper), and picture of the launcher mock-up (lower)

4. Advanced Gyrotron

4.1. 170 GHz gyrotron of higher mode oscillation

The R&D of high power gyrotron using a higher mode oscillation has been started. The oscillation mode is $TE_{31,12}$. By increasing the oscillation mode, the resonator diameter is raised from 17.9 mm to 21.8 mm, and the heat load to the resonator wall significantly decreases. This will contribute to the higher power generation and relax a thermal stress on the resonator. On the other hand, careful setup and operation will be required to establish the stable and high efficiency oscillation. The MIG is the same configuration of the $TE_{31,8}$ gyrotron. As a first step, a short pulse gyrotron was fabricated and tested. The output power of ~1.57 MW was obtained at 170 GHz. Based on the result, a long pulse $TE_{31,12}$ mode gyrotron is fabricated.

4.2. Power modulation

In ITER, high frequency power modulation up to 5 kHz will be required for suppression of the neo-classical tearing mode. For this purpose, a test of high power modulation of JAEA gyrotron is planned by using a voltage modulation of a body power supply [21]. Generally, when the power modulation is applied, the collector heat load increases since the powerful electron beam without power loss by the oscillation impact the collector. In case of the JAEA gyrotron, however, the modulated voltage of the body V_m appears as a decrease in the anode-cathode voltage of the triode MIG since the anode-body voltage is kept constant. As a beam current decreases as the anode-cathode voltage V_{ak} does, the beam current decrease during the modulation must be much larger than that of a diode type MIG. Furthermore, if the anode modulation is added on, V_{ak} could be decreased to 0 V. Consequently, the beam current could be reduced to small level. Then, the averaged collector heat load can be suppressed significantly, which will give a possibility to increase the beam current and oscillation power at the identical gyrotron.

4.3. Dual Frequency gyrotron

In the design of dual frequency gyrotron, a set of $TE_{31,11}$ and $TE_{25,9}$ modes for 170 GHz and ~136 GHz, respectively, are proposed since these show high mode conversion ratio's to the Gaussian beam. The mode corresponds to the transparent frequency of the diamond window of 1.853 mm in thickness. By adjusting the anode voltage the mirror ratio between the resonator and MIG fields, optimized pitch factor can be selected at any beam voltage. Consequently, 1 MW high efficiency oscillation will be obtained at both modes.

4.4. Fast field control of super conducting magnet

For a step tunable frequency control at reasonable beam parameters, a magnetic field control should be accompanied. For a fast control of B_c, He-free super conducting magnet with an additional sweeping coil was developed as shown in Fig. 10. A diameter of a room temperature bore is 240 mm, and the 7 T at the center. Using commercially available DC power supplies, the magnetic field sweeping was demonstrated with a speed of 0.4 T / 10 s at 7 T.

5. Conclusion

A basic requirement of the ITER gyrotron performance is been demonstrated by the JAEA 170 GHz gyrotron. As the next activity, the higher order mode gyrotron is under development for a higher power generation. In parallel, the demonstration of the power modulation is planned for ITER application using a body voltage modulation. And, the design of the dual frequency gyrotron was proposed. The high power gyrotron is used as a power source for the developments of transmission line and ITER launcher.

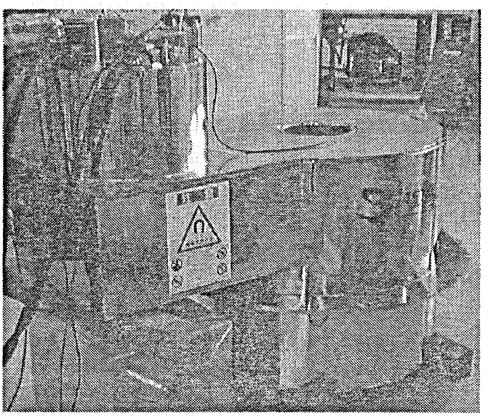

Fig. 10. Pictue of 7 T super conducting magnet solenoid coil for fast B_c sweeping. Liqid He-free, and room temperature bore is 240 mm.

Acknowledgements

Authors would thank to Mr. Y. Ikeda and Mr. S. Komori of JAEA for gyrotron operation, and to Mr. Y. Mitsunaka and Mr. Hayashi of Toshiba Electron Tubes and Devices Co. for contribution to the gyrotron fabrication. The authors thank to the encouragement of Drs. M. Akiba, R. Yoshino, H. Takatsu and T. Tsunematsu.

References

1 *How J (ed)* Project Integration Document PID ITER_D_2234RH Ver3.0, 2007, and https // user.iter org/?uid=2234RH&version=v3.0
2 *Henderson M , Saibene G* Nuclear Fusion, **48**(5) 054017 (2008).
3 *Thumm M* Int J. Infrared and mm waves, **26**, 4, 483 (2005)
4 *Sakamoto K* Fusion Sci. &Tech., **52**, 145 (2007)
5 *Denisov G. G et al* Int. J. Electronics, **72**, 1079 (1992).
6 *Sakamoto K. et al* Phys. Rev. Lett., **73**, 3532 (1994).
7 *Braz O et al.* Inj. J. Infrared and mm waves, **18**, 1945 (1997)
8 *Kasugai A. et al.* Rev. Sci Instrm., **69**, 2160 (1998).
9 *Sakamoto K. et al* Rev. Sci. Instrm., **70**, 208 (1999).
10 *Felch K et al.* J. Phys Conf. Ser , **25**, 13 (2005)
11 *Dammertz G et al.* IEEE Trans Plasma Sci , **34**, 173 (2006)
12. *Sakamoto K. et al* Nat Phys., **3**, 411 (2007)
13. *Denisov G. G. et al.* Nucl. Fusion., **48**, 054007 (2008)
14. *Sakamoto K et.al* Nucl. Fusion. **43**, 729 (2003)
15. *Kasugai A. et al.* Nucl. Fusion, **48**, 5, 054009 (2008).
16. *Neilson J.* IEEE Trans Plasma Science, **34**, 635 (2006).
17. *Kajiwara K et al.* to be published in J. Plasma and Fusion Res. (2009).
18 *Takahashi K et al* to be submitted.
19. *Takahashi K. et al.* Nucl. Fusion, **48**, 5, 054014 (2008).
20 *Kajiwara K.* Fusion Eng Design, **84**, 1, 72 (2009)
21 *Bonicelli T. et al.* Proc. 22nd Symp. Fusion Technology (SOFT02), Helsinki, Finland, September, 2002, p. 543

GYROTRONS FOR FUSION RESEARCH. STATE OF THE ART AND PROGRESS TRENDS

G. G. Denisov[1], A. G. Litvak[1], V. E. Myasnikov[2], E. M. Tai[2], V. I. Ilin[3], E. V. Zapevalov[1]

[1] Institute of Applied Physics, Nizhny Novgorod, Russia
[2] GYCOM Ltd, Nizhny Novgorod, Russia
[3] Kurchatov Institute, Moscow, Russia

Introduction

Gyrotrons are the most powerful sources of millimetre wavelength radiation [1–8]. They are widely used in electro-cyclotron-wave systems of plasma fusion installations (e.g. see [8–15]). For the next generation of fusion installations gyrotrons with unit power at least 1 MW in CW regime are required [16]. The present paper continues in the frames of SMP Conference proceedings [6–8] to monitor general tendencies in MW-power gyrotron development.

First experiments with gyrotrons were done in 1964 [1–3]. In 70-s gyrotrons already were doing very well – we can mention here just two achievements: 28 GHz / 100 kW / CW and 100 GHz / 1 MW / 100 μs. Also the first application of gyrotrons for plasma fusion setups TM-3 and TUMAN-2 took place [9]. In 80-s several scientific and industrial institutions worked on development of gyrotrons. Lots of scientific and technological tasks were solved at that time. Real fruitful collaboration and simultaneously strong competition of the main gyrotron developers began in 90-s with the start of ITER activity and wide use of gyrotrons at plasma installations. The requirement of 1 MW / CW gyrotron operated at very high frequency (above 100 GHz) was issued.

In the earlier review papers of the previous conferences three first periods of "modern gyrotron history" in MW gyrotron development were observed. In the period of 1995–1999 the following principal steps were made:

- efficient gyrotron operation was shown at very high-order modes. This solves the problem of cavity thermal loading;
- depressed collector were introduced in gyrotrons. This gave a great move in solving collector and power supply problems;
- gyrotron windows made of artificial diamond discs were developed. Such a window is still the only option for long-pulse megawatt tubes.

The achievements in the next period 1999–2002 were also very bright:

- demonstration of very long-pulse (hundreds seconds) operation of MW tubes equipped by diamond windows and depressed collectors;
- tests of short-pulse prototypes for multi-frequency and 1.5–2 MW gyrotrons;
- integration of MW gyrotron complexes at major fusion installations.

The period 2002–2005 showed:

- demonstration of CW operation of megawatt power gyrotrons,
- first tests of multi-frequency tubes,
- demonstration of very high gyrotron efficiency.

The present paper discusses the latest events (in 2005–2008 period between last SPM Conferences) in gyrotron development and progress trends of the development. The highlights of the period are:

- Operation of 170 GHz gyrotrons for ITER at 1 MW power with efficiency exceeding 50 %.
- Results on multi-frequency and 1.5–2 MW gyrotron prototypes.
- First experiments on fast directional switching gyrotron wavebeams.

Operation of 170 GHz gyrotrons for ITER at 1 MW power with efficiency exceeding 50 %

Gyrotrons for the electron-cyclotron system of ITER are developed by three groups (EU, Japan, and Russia) and each of them cooperate efforts of several scientific and industrial institutions. In the mentioned period all parties demonstrated very interesting and important results. The main technical requirements for the ITER gyrotron are: long-pulse (400–1000 seconds) operation at power at least 1 MW with efficiency exceeding 50 %, and fast (up to several kHz) gyrotron power power modulation for NTM instabilities control. Two teams – Japan and Russia – have already demonstrated efficient operation of ITER gyrotron prototypes in pulses of hundreds seconds. The most impressive results were obtained by Japan team (see, for example, [17]). In particular 1 MW gyrotron operation was achieved in pulses up to 800 seconds. Figures 1 and 2 illustrate a sophisticated JAEA gyrotron switching-on scenario and a high level performance of all gyrotron sub-systems.

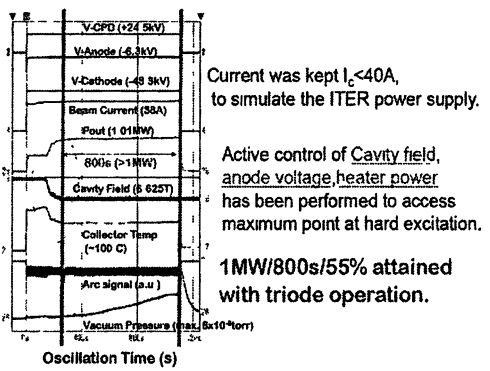

Fig. 1. Time traces of the main JAEA gyrotron parameters

Input Beam Power	1853.7 48 4kVx38 3A
Total measured power	1853.5
Generated RF power at cavity (A + B)	1111 5
Collector heat load	742

RF Loss in the Gyrotron (A)	87.2
relief windows	8 7
Ceramic insulator for CPD	15 2
Mirrors (1st-3rd)	5 9
Launcher	15 3
Beam tunnel	2 6
Gyrotron body & 4th mirror	5
Cavity	34.5

Gyrotron Output (B)	1024.3
Dummy Load	968
Miter Bends	2.7
Waveguide	8
MOU	45.6

(unit : kW)

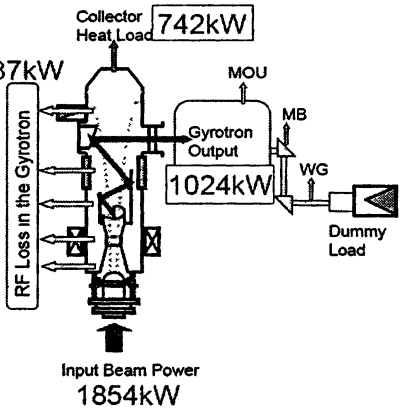

Fig. 2. Power balance for 1 MW JAEA gyrotron operation

In experiments with ITER gyrotron in Russia the output power slightly exceeding 1 MW was shown in pulses of 100–150 seconds [18]. Efficiency calculated as ratio of power in the paraxial part of the output wave beam to power of the main power supply was 52 % (Fig. 3). The gyrotron pulse duration was limited by the test stand capabilities: the pulses were stopped because of air breakdown in atmospheric dummy load or transmission line. Now the stand is equipped by a new fully evacuated transmission line and a load.

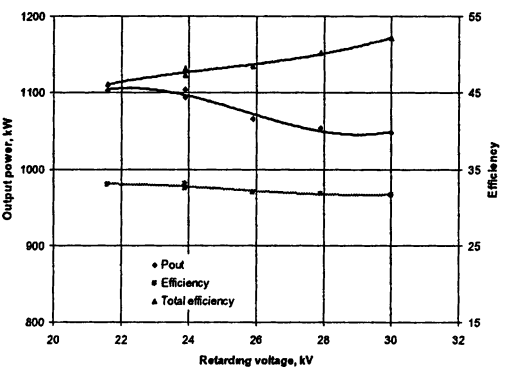

Fig. 3. Output power and efficiency of the 170 GHz IAP/GYCOM gyrotron. The parameters correspond to 46 A electron beam current and 76 kV full accelerating voltage.

The successful development of ITER gyrotrons made it possible to discuss further increase of ECW microwave power for this international tokamak.

Results on multi-frequency and 1.5–2 MW gyrotron prototypes

Multi-frequency gyrotrons

A gyrotron capable to operate at several frequencies is very attractive for plasma experiments. The use of step-tunable gyrotrons can greatly enhance flexibility and performance of ECRH/ECCD systems due to larger accessible radial range, possible replacement of steerable antennas and higher CD efficiency for NTM stabilization. Even two-frequency gyrotrons can bring real improvements of the system. Russian and European teams jointly develop dual- and multi-frequency gyrotrons for 105–140 GHz frequency range [18, 19]. There are some other multi-frequency gyrotron developed by IAP/GYCOM in last three years (see Table 1).

Table 1. Multi-freqency gyrotrons developed and tested in 2005–2007

Frequency, GHz	Power, MW	Pulse, s	Note
105 / 140	0.7–0.9	10	2 tubes delivered to ASDEX-Up
147 / 170	0.7–0.9	0 1	CW design, 50 % eff
100–150	1.2–1.5	10–4	Short-pulse mock-up, 6 frequencies, high-efficiency converter
100–150	0.7–0.8	0.1	Short-pulse mock-up, 11 frequencies, BN Brewster window
105–140	0.7–0.9	0.1 (10)	CW design, 4 frequencies High-efficiency mode converter
71.5 / 74.8 / 78.1	0.8	0.1	3 frequencies, 56 % efficiency, BN Brewster window

The main problems in development of multi-frequency gyrotrons are to provide:

- efficient gyrotron operation at different modes,
- efficient conversion of different modes into a Gaussian beam,
- reliable operation of broadband or tuneable window.

Considering this three key problems one can say that first two of them are solved. Efficient gyrotron operation at several frequencies was demonstrated in many experiments. New synthesis methods [20] allow design of efficient mode converters for multi-frequency gyrotrons. In particular the internal mode converter with a wave pre-shaping consisting of a dimpled-wall waveguide launcher and four mirrors recently developed for the multi-frequency 105–140 GHz gyrotron reduces the power fraction carried away by stray radiation to about 3 % for all operating modes (see also Fig. 4).

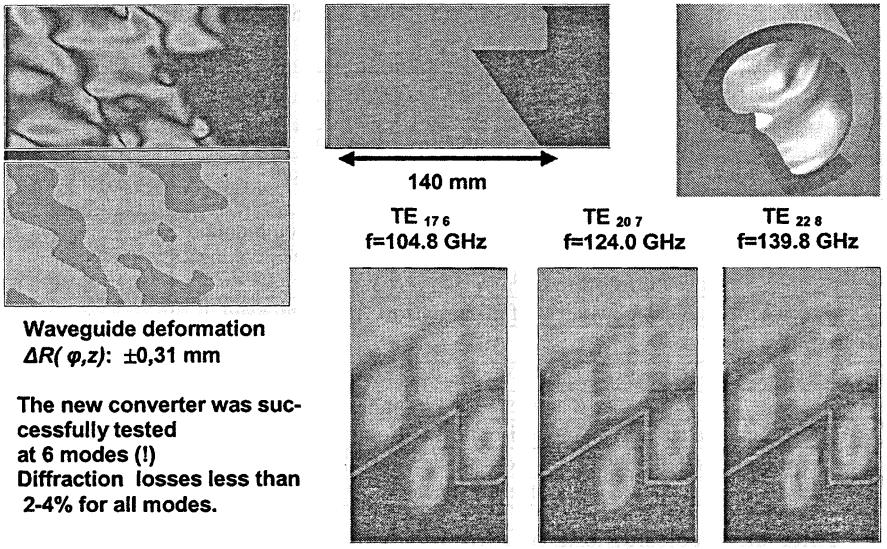

Fig. 4. Synthesized launcher for the quasi-optical mode converter of the 105–140 GHz multi-frequency gyrotron. Upper line pictures show unrolled surface of the launcher with its deviation ($\Delta R(\varphi, z)$) from a cylindrical surface and exaggerated (10 times) deformation in 3-D view. The lower line pictures show field amplitude on the launcher surface.

However realization of a CVD diamond window for a megawatt power level multi-frequency gyrotron met some real difficulties. Two window concepts are now under consideration: Brewster-angle window and double-disc resonant window. Both these versions have advantages and drawbacks. The main of them are indicated in the Table 2 below.

The table shows how challenging is the multi-frequency window elaboration. Having considered these window versions we chose for first experiments a Brewster angle window. The Brewster window is very attractive because of very wide instant frequency band, but the converter design in this case is more complicated.

A Brewster-angle window version based on a circular disc was chosen since the brazing of a circular disc is much simpler than of an elliptical one. A set of mirrors forms a required wave beam size at the disc and provides an oblique incidence of the beam. The window scheme was checked in an experiment with 105–140 GHz gyrotron and BN ceramics disc. In short pulses (0.1 seconds) limited by ceramic window heating the gyrotron showed a reliable operation at 11 modes in the frequency range of interest.

Table 2. Advantages and drawbacks of two CVD diamond window versions

Double-disc window

Two discs required for the window	–
Vacuum pumping between discs required	–
Smaller disc diameter possible (e.g. 75 mm)	+
Without an external disc in the window the gyrotron is capable to operate at two frequencies	+
Strong reflection from the window (up to 80 %) and from combination of two windows (up to 90 %) at some frequencies near the operating ones may disturb the gyrotron operation	–
Precise mechanical adjustment of discs, narrow frequency band	–

Brewster window

One disc required for the window	+
Large disc diameter (e.g. 120 mm)	–
More complicated system of quasi-optical mirrors inside the tube	–
Relatively small wave beam cross-section near the window	–
Wide instant frequency band	+

After the successful tests of gyrotrons with ceramics Brewster-angle windows a CVD diamond window of this type was brazed and mounted to the gyrotron. The main features of such a window are extended radial cuffs and edge disc brazing at rather large diameter 106 mm (Fig. 5). The calculated safety factor for the disc of 1.8 mm thickness – ratio of the internal strength in the brazed disc to its maximum possible value – was found about 2. The factor was considered as quite moderate; however it was decided to begin high-power experiments with the gyrotron. Multiple arcs happened during the gyrotron conditioning because of a relatively small wave beam size near the window. The arcs were normally stopped by the gyrotron protection system, nevertheless one of them broke the window (Fig. 5). The failure demonstrates that additional safety measures are necessary: use of evacuated transmission line, more sensitive arc protection system, use of a thicker disc, etc.

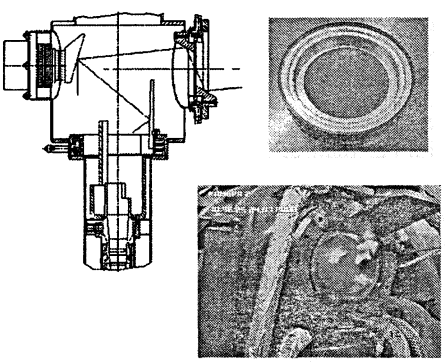

Fig. 5. Sketch of output unit of the multi-frequency gyrotron mock-up with Brewster window and brazed CVD diamond disc for the Brewster window. The right-bottom picture shows the arc which destroyed the diamond disk. Diagnostics showed that during the pulse a disruption of the operating regime to generation of an opposite rotating mode happened. It was one of many shocks due to arcing which finally destroyed the window disc with internal strengths.

Development of 1.5–2 MW power gyrotron prototypes

There are two lines in development of gyrotrons with enhanced power: to advance conventional-type gyrotrons with cylindrical cavities and to develop more complicated gyrotrons with coaxial cavities. The main effort in the development of the coaxial tube is carried out by EU team [21]. Many encouraging results have been obtained in short pulse experiments though there are some open questions as discrepancy in predicted and measured parameters.

IAP/GYCOM and JAEA/Toshiba teams study a possibility to use a higher order mode in a gyrotron conventional cavity. Their designs based on $TE_{28\,12}$ and $TE_{31\,12}$ modes are in consideration.

Table 3. Main design parameters of the GYCOM/IAP 1.5 MW gyrotron

Cylindrical Cavity Mode	TE 28.12
Cavity diameter	41.5 mm
Peak thermal load for ideal copper	< 1.35 kW/cm^2
Beam voltage	100 kV
Beam current	50 A
Pitch-factor	1.2
Efficiency (without DC)	30–33 %

In 2008 an advanced short-pulse (100 μs) gyrotron model (Fig. 6) operating with $TE_{28.12}$ mode was tested at IAP [22]. The model showed very robust operation at relatively high electron energies (up to 100 keV in the cavity) necessary to achieve the high goal power (Figs 7, 8).

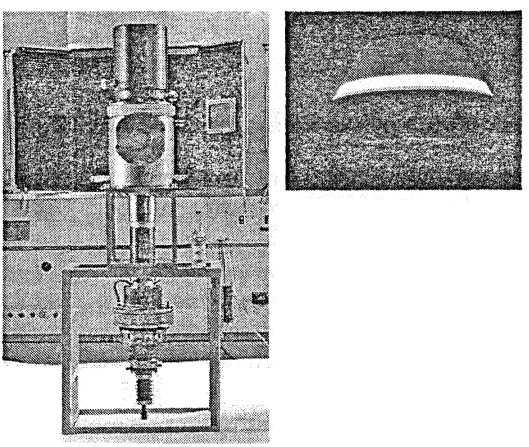

Fig. 6. Photo of 1.5 MW gyrotron model and its cathode

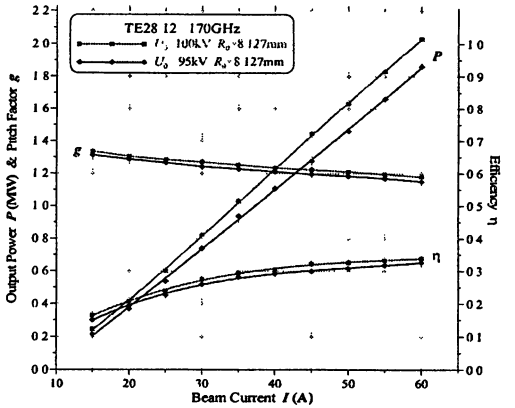

Fig. 7. Power and interaction efficiency of short-pulse high-power gyrotron model for different electron energies

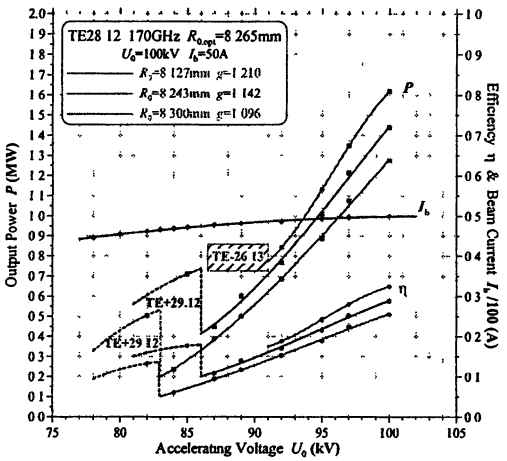

Fig. 8. Mode map versus the electron beam radius and voltage

First experiments on fast directional switching gyrotron wavebeams

An important task of electron cyclotron resonance heating (ECRH) and current drive (ECCD) systems for tokamaks is the control of MHD instabilities by directing narrow EC wave beams to the resonant layer. For ITER, the suppression of neo-classical tearing modes (NTM) is a key purpose of ECCD applied from the upper launchers. As the islands rotate with frequencies of typically 1 to 10 kHz, injection of the launched power synchronous with the rotating islands may be required. Up to now, synchronous current drive is performed by power modulation of the gyrotron, with the disadvantage that half of the installed power is wasted. An alternative for power modulation could be synchronous toggling of the gyrotron power between two launchers directing the beam to poloidal or toroidal planes, which are about 180° apart from each other with respect to the phase of the NTM (Fig. 9).

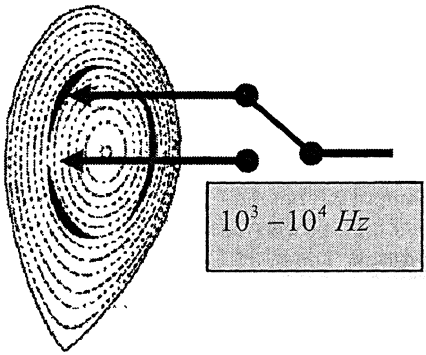

Fig. 9. Simplified scheme of the wave beam switching

The switching is performed with a fast directional switch (FADIS) [23, 24], while the source operates continuously. The FADIS is based on a small frequency-shift keying of the gyrotron between f_1 and f_2 and a narrow-band frequency diplexer, which directs an input beam into one of two output channels. The diplexer was realized on the base of four-mirror ring cavity (Fig. 10).

Low power measurement of the transmission functions for the resonant and nonresonant channel, yielding efficiencies of about 93 % and 98 %, respectively. The round-trip loss in the resonator was measured to be < 1.3 % and is near to the theoretical value of about 1 % determined by the ohmic loss, atmospheric attenuation, and beam truncation by the resonator mirrors. The measured quality factor is 14000; thus, for the FADIS application, a good switching contrast can be reached for $\Delta f_S > 30$ MHz.

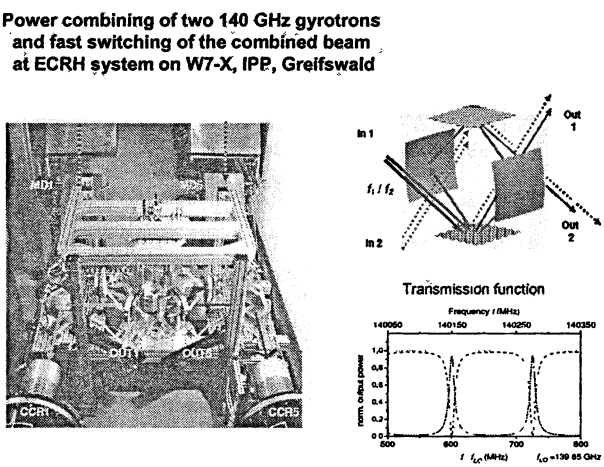

Fig. 10. Four mirror diplexer and its realization at IPP, Greifswald.

A fast frequency control of a free running single-mode gyrotron can be achieved by changing an operation voltage: the change transforms electron beam parameters, including the reactive part of RF conductivity, and finally results in a frequency shift. For the high-power test of the FADIS, the TED prototype gyrotron 'Maquette' with depressed collector was used; the control voltage is applied between the collector and the RF cavity. The frequency variation is, obviously, accompanied by some modulation of the output RF power.

A proof-of-principle experiment with a high-power-fed diplexer has been realized in Greifswald, using a 140 GHz gyrotron. The FADIS was equipped with a motorized drive of the upper resonator mirror which allowed the tuning of the transmission curve with respect to the gyrotron frequency. The device was installed in front of the CW calorimetric loads in the transmission duct of the ECRH system for W7-X. Most of the experiments were carried out in a power range 300–600 kW (Fig. 11). In the experiment the voltage modulation of 4 kV, 5 kHz square wave resulted in a frequency-shift of $\Delta f_s \approx 30$ MHz. The device operated without remarkable problems. Arcing occurred very infrequently, although the maximum power density in the beam close to the grating surface was about 0.5 MW · cm^{-2}.

The first tests of the quasi-optical FADIS show good agreement with theory and confirm the possibility of fast switching of high-power millimetre wave beams.

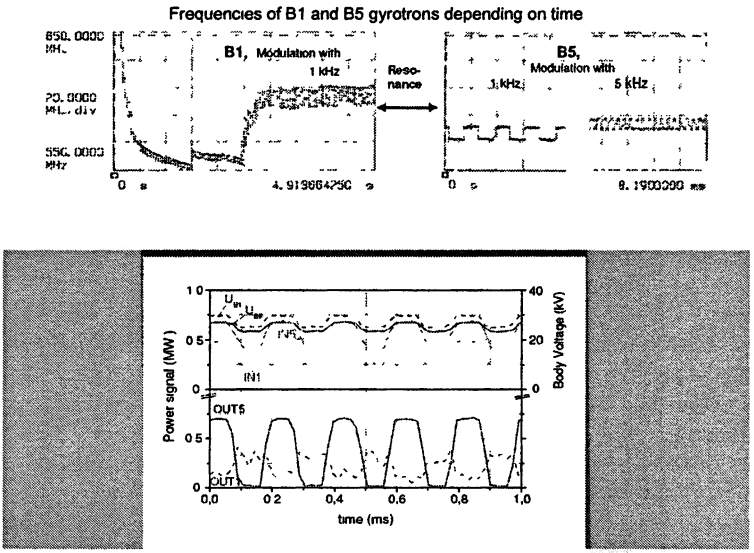

Fig. 11. Fast switching of the combined (about 1 MW) wave beam. Modulation frequency is 5 kHz.

Summary and future tasks

Strong collaboration and competition of gyrotron developers resulted in the great progress in the device performance. Megawatt power level gyrotrons operating in CW regime have been demonstrated. The successful development of ITER gyrotrons made it possible to discuss further increase of ECW microwave power for this international tokamak.

Development studies of multi-frequency gyrotrons and gyrotrons with enhanced power are in progress. Several multi-frequency gyrotrons were tested successfully. However a CW window for such gyrotrons seems to be still an open issue.

Gyrotron efficiency enhancement is probably even more strategic task than the power increase with some drop of efficiency. High-efficiency gyrotron system consumes less power and water for cooling systems, and also more compact. There are no physical limitations for MW gyrotrons to operate with efficiency of 60–70 %.

References

1. *Gaponov A. V. et al.* Induced synchrotron radiation of electrons in cavity resonators. Pis'ma ZhETF, 1965, **15**, 430–435 (JETP Lett., **15**, 2267–269).
2. *Gaponov A. V., Flyagin V. A., Goldenberg A. L., Nusinovich G. S., Tsimring Sh. E., Usov V. G., Vlasov S. N.* Powerful millimeter-wave gyrotrons // Int. J. of Electronics. 1981. V. 51, № 4. P 277–302
3. *Nusonovich G.* Introduction to the Physics of Gyrotrons. The Johns Hopkins Univ. Press, 2004.
4. *Felch K. L , Danly B. G., Jory H R. et al.* Characteristics and Applications of Fast-Wave Gyrodevices // Proceedings of IEEE. 1999. V. 87, № 5. P. 752–781.
5. *Thumm M.* State-of-the-Art of High power Gyro-Devices and Free Electron Masers. Update 2007. Forschungcentrum Karlsruhe, Germany, 2008.
6. *Denisov G. G.* Megawatt gyrotrons for fusion research State of the art and trends of development // Proc. of 4th Int. Workshop "Strong Microwaves in Plasmas". Nizhny Novgorod, 2000. P. 967–986.
7. *Denisov G G.* Development of 1 MW output power level gyrotrons for fusion systems // Proc. of 5th Int. Workshop "Strong Microwaves in Plasmas". Nizhny Novgorod, 2003. P. 29–45.
8. *Denisov G. G., Litvak A. G., Myasnikov V. E., Tai E. M., Il'in V. I., Zapevalov V. E.* Megawatt-power gyrotrons for fusion // Proc. of 6th Int. Workshop "Strong Microwaves in Plasmas". Nizhny Novgorod, 2006. P. 62–75.
9. *Alikaev V. V. et al.* Electron cyclotron heating at the TM-3 tokamak // Pis'ma ZhETF, 1972, **15**, 41–44 (JETP Lett., **2**, 27–29).
10. *Zohm H. et al.* Confinement and stability studies with ECRH in ASDEX upgrade // Proc. of 5th Int. Workshop "Strong Microwaves in Plasmas". Nizhny Novgorod, 2003. P. 281–295
11 *Erckman V. et al.* 20 years of ECRH at W7-A and W7-AS // Proc. of 5th Int. Workshop "Strong Microwaves in Plasmas". Nizhny Novgorod, 2003. P. 281–296.
12. *Igami H. et al.* High power injection and steady state ECRH operation in LHD // Proc. of 6th Int. Workshop "Strong Microwaves in Plasmas" Nizhny Novgorod, 2006. P. 398–408.
13. *Felch K. et al* Operating experience on six 110 GHz, 1 MW gyrotrons for ECRH applications // Nuclear Fusion, 2008, **5**, 054008.
14 *Lenholm M. et al.* Electron cyclotron heating and current drive on Tore Supra 2002–2005 // Proc. of 6th Int. Workshop "Strong Microwaves in Plasmas". Nizhny Novgorod, 2006. P. 448–456
15. *Pochelon et al.* Recent physics results with electron cyclotrion heating in TCV // Proc. of 6th Int. Workshop "Strong Microwaves in Plasmas" Nizhny Novgorod, 2006. P 421–433.

16. *Luce T. C* ECRH physics and technology in ITER // Nuclear Fusion, 2008, **5**, 050201.
17. *Kasugai A., Sakamoto K. et al* Steady-state operation of 170 GHz–1 MW gyrotron for ITER // Nuclear Fusion, 2008, **5**, 054009.
18. *Denisov G G., Litvak A. G et al.* Developnet in Russia of high-power gyrotrons for fusion // Nuclear Fusion, 2008, **5**, 054007.
19. *Wagner D. et al.* Status of the new multi-frequency ECRH system for ASDEX Upgrade // Nuclear Fusion, 2008, **5**, 054006.
20. *Chirkov A. V et al* Huygens principle application for the field analysis and synthesis in oversized waveguides // J. of Radiophysics and Quantum Electronics. 2006. V. 49, № 5.
21. *Piosczyk B. et al* Progress in the development of the 170 GHz coaxial cavity gyrotron for ITER // 6th Int. Workshop "Strong Microwaves in Plasmas". Nizhny Novgorod, 2006. V. 1. P. 91–99.
22 *Popov L. G. et al.* Development in Russia of 170 GHz Gyrotron for ITER // Proceedings of the 33 Int. Conf. on Infrared, Millimeter and Terahertz Waves. Pasadena, USA, 2008.
23. *Kasparek W, Petelin M. I, Erckmann V., Shchegol'kov D Yu., Bruschi A., Cirant S, Thumm M, Plaum B., Grünert M and Malthaner M* Fast switching and power combination of high-power electron cyclotron wave beams: principles, numerical results and experiments // Fusion Sci. Technol. 2007, **52**, 281–290.
24. *Kasparek W., Petelin M. I., Shchegol'kov D Yu., Erckmann V., Plaum B., Bruschi A.* A fast switch, combiner and narrow-band filter for high-power millimetre wave beams // Nucl. Fusion, 2008, **48**, 054010.

HIGH-POWER MICROWAVE DIPLEXERS FOR ADVANCED ECRH SYSTEMS

W. Kasparek[1], M. Petelin[2], D. Shchegolkov[2], V. Erckmann[3], A. Bruschi[4], H. Braune[3], F. Hollmann[3], L. Jonitz[3], G. Michel[3], H. P. Laqua[3], F. Noke[3], F. Purps[3], T. Schulz[3], P. Brand[1], B. Plaum[1], W. Wubie[1], Y. Koshurinov[2], L. Lubyako[2], W. Bin[4], O. D'Arcangelo[4], and ECRH groups at IPP Greifswald[3], FZK Karlsruhe[5], IFP Milano[4], IAP Nizhny Novgorod[2], and IPF Stuttgart[1]

[1]Institut für Plasmaforschung, Universität Stuttgart, D-70569 Stuttgart, Germany
[2]Institute of Applied Physics, RAS, 603950 Nizhny Novgorod, Russia
[3]Max-Planck-Institut für Plasmaphysik (IPP), EURATOM-Ass., D-17491 Greifswald, Germany
[4]Istituto di Fisica del Plasma, EURATOM-ENEA-CNR Ass., via R. Cozzi 53, 20125 Milano, Italy
[5]Forschungszentrum Karlsruhe, Association EURATOM-FZK, IHM, D-76021 Karlsruhe, Germany

Combination of the power of two (or more) gyrotrons is an attractive feature for large ECRH systems, e.g. for ITER Fast switching of the power from continuously operating gyrotrons between two antennas synchronous to the rotation of the magnetic islands in tokamaks maximizes the efficiency for stabilization of neoclassical tearing modes. Both tasks can be fulfilled with a high-power four-port diplexer, utilizing small frequency differences or small frequency-shift keying (some tens of MHz, by modulation of a supply voltage) of the gyrotrons. In the paper, high-power diplexer designs for quasi-optical and corrugated waveguide transmission systems including numerical and experimental results are discussed In more detail, the principle and the design of a quasi-optical resonator diplexer is presented. Low-power measurements at 140 GHz of switching contrast, mode purity and efficiency are shown to agree well with theory. Results from high-power experiments on fast switching and power combination of two gyrotrons using the ECRH system for the stellarator W7-X are presented Near-term plans for high-power experiments at ASDEX Upgrade and FTU are described (Note that there are also plans for in-line ECE on ASDEX Upgrade). Finally, applications of diplexers for the ECRH system on ITER assuming conventional gyrotrons are discussed, and future possibilities offered by phase-controlled gyrotrons like multi-beam combining and switching are highlighted.

1. Introduction

Electron cyclotron resonance heating is of high importance as an effective and flexible heating system for tokamaks and stellarators. Technology for sources, transmission and launchers is highly developed. Further improvements can be obtained by introduction of high-power diplexers [1, 2, 3, 4, 5, 6] which might be used for several applications, leading to an increase of flexibility, performance or to a simplification of the system.

Combining of powers from two (or more) conventional gyrotrons would essentially reduce the number of transmission lines and launchers for ECRH systems of large fusion devices, e.g. ITER. High-power combiners (multiplexers)

can be composed of oversized four-port diplexers, each representing a kind of interferometer or quasi-optical resonator; the gyrotrons being implied to generate slightly different frequencies.

In any gyrotron, modulation of a voltage results in a small, within some tens of MHz, shifting of the radiation frequency. This shift can provide, by using an adequate multiplexer, switching of the combined wave beam between output channels (Fast DIrectional Switch, FADIS). In particular, fast, non-mechanical, electronically controlled switching of the power from continuously operating gyrotrons between two antennas synchronous to the rotation of the magnetic islands in the tokamak plasma would maximize the efficiency for stabilization of neo-classical tearing modes [7]. Additional scenarios for multi-beam combining and controlled switching of the combined beam could be offered by using phase-controlled gyrotrons (if the latter ones were developed at frequencies and powers of interest).

The reciprocity and filter characteristics of diplexers are favourable for sharing the same antenna to combine high-power ECRH launching with reception of a low-power plasma diagnostic signal (e.g. ECE) [8].

In the paper, various diplexer designs for quasi-optical and corrugated waveguide transmission systems including some numerical and experimental results are presented. Results from fast switching of a high-power beam between two output channels using a gyrotron, and recent experiments for power combination of two gyrotrons from the ECRH system for the stellarator W7-X are reported. Plans for application of diplexers for synchronous MHD-mode stabilization at ASDEX Upgrade and FTU are presented. Finally, the possible implementation of power combiners and fast switches in the ECRH system of ITER is discussed.

2. Designs for high-power diplexers

Frequency diplexers can be designed in various forms. Basically, these diplexer are four-port devices consisting of a directional coupler (hybrid) at the input, a delay-line (used in single-path or in multi-path), and a second hybrid at the output.

Well-known designs compatible with high-power millimetre waves are two-beam interferometers (e.g. the Mach-Zehnder type [2, 6]), multi-beam interferometers (Fabry-Perot type, or ring resonator [1, 3]), and combinations thereof.

As high-power compatible hybrids, low-loss dielectric beam splitters [2, 6], metallic phase gratings (magic Y) [4, 10], and square corrugated waveguides [5, 11] have been identified up to now. In principle, any of the solutions found can be integrated into corrugated waveguide as well as in beam waveguide transmission systems by using appropriate interface elements. In Fig. 1 we show three possible designs with the corresponding transmission characteristics, being periodic with $\Delta f_F = c/L$. Details can be found in the references given above.

The Mach-Zehnder type diplexer shown in Fig. 1*a* [6] consists of two dielectric power splitters integrated into HE11 waveguide with a direct connection and a delay line with a length difference L with respect to the direct line. For the angle of incidence of 45° and s-polarization, CVD diamond is an appropriate material for a high-power 3 dB splitter. For strongly oversized systems, e.g. 170 GHz and ∅ 63.5 mm waveguide, the theoretical transmission loss is very low. By choosing the appropriate L, the period of the sinusoidal transmission characteristics can be easily matched to the application envisaged. The device as sketched in Fig. 1*a* is very compact; instead of the (expensive) diamond discs, gratings or Talbot splitters can be used, if space requirements are not so stringent.

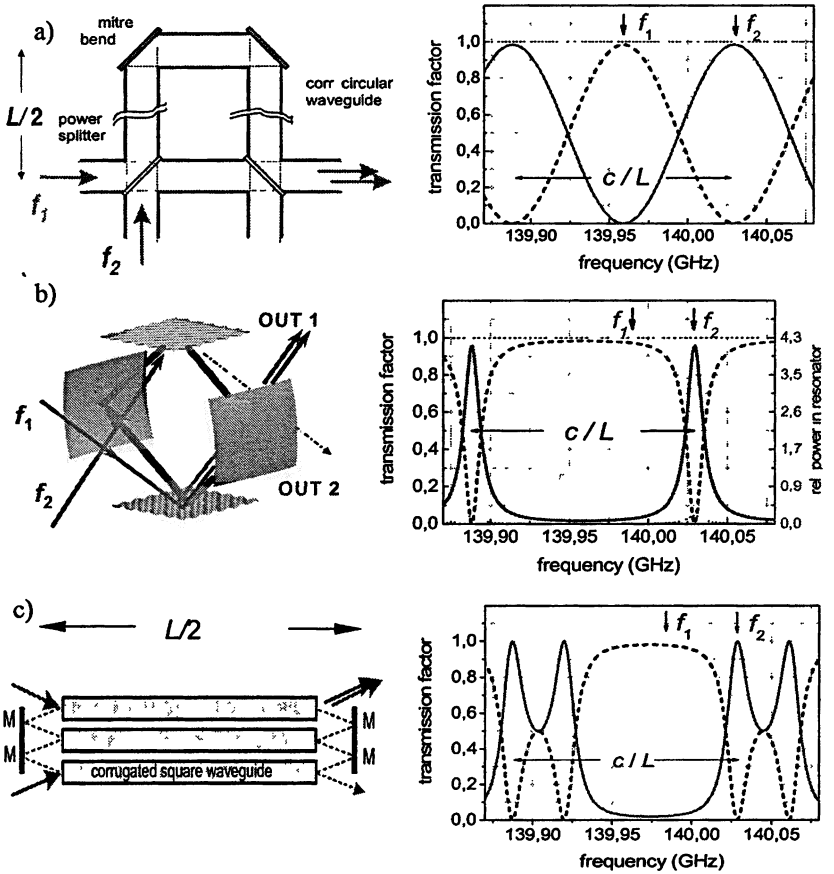

Fig. 1. Possible designs of high-power diplexers and the corresponding transmission functions: *a*) Mach-Zehnder type interferometer with dielectric beam splitters; *b*) ring resonator (round-trip length L) with coupling gratings; *c*) two-loop diplexer using square waveguide splitters.

The resonant diplexer in Fig. 1*b* is a 4-mirror ring resonator [2, 3, 9] consisting of two focussing mirrors and two plane phase gratings for coupling of the incident beams to the resonator via the –1st diffraction order. Additional mirrors provide matching to the input and output beam or waveguide. The transmission characteristics are defined by the grating efficiency and the path length L of one round-trip in the resonator. Special features are the relatively narrow resonant transmission channels separated by broad non-resonant bands. Transmission loss of a few percent [3] affects mainly the resonant channel due to absorption of the mirrors in the resonator.

The two-loop resonant diplexer (Fig. 1*c*) consists of two nested loops [5] formed by square corrugated waveguides with length $2a^2/\lambda$ used as 3 dB hybrids [11], and the reflectors M. Additional mirrors provide matching of the inputs and outputs to the transmission system. The periodicity of the transmission function is determined by the overall length $L/2$ of the system. Special features are the steep slopes and the double-humped structure of the resonant channels. Some insertion loss occurs in the waveguides and due to the coupling between the guides via the mirrors [12].

3. Experimental investigations

For the high-power diplexer concepts discussed before and others [2–6, 9–12], test systems have been built and investigated with low power. Within the experimental possibilities of these mock-ups, a good agreement with theory is obtained for all set ups. Especially the quasi-optical diplexer (Fig. 1*b*) was investigated in great detail. The parameters agree well with calculations. The measurement of transmission functions and the output beam patterns for the two outputs are depicted in Fig. 2 as an example. Note especially the high TEM_{00} mode purity (non-resonant output: 99.0%; resonant output: 99.75 %) of the output beams. Details can be found in the respective references [2, 3].

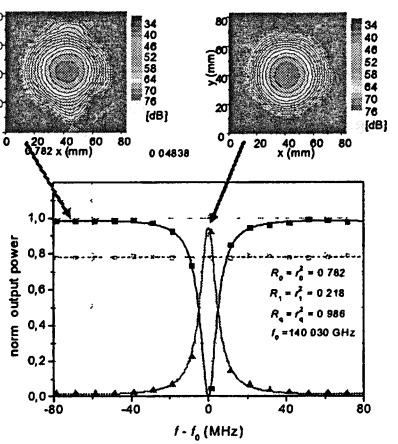

Fig. 2. Calorimetrically measured (symbols) transmission functions of the quasi-optical diplexer compared to theory (solid lines, [3]). On top, beam patterns recorded at a non-resonant and a resonant frequency (see arrows) are shown.

The quasi-optical resonant diplexer was as well exposed to high-power tests, which were performed at the ECRH system for the stellarator W7-X [13]. For this purpose, the diplexer was integrated into the beam duct with the help of matching optics, such that one or two gyrotrons (B1 and B5) could be fed into the inputs, and the outputs were connected to cw calorimetric loads (see Fig. 3). Experiments were performed with power around 500 kW and pulse lengths limited to several seconds by the un-cooled mirrors in the mock-up diplexer.

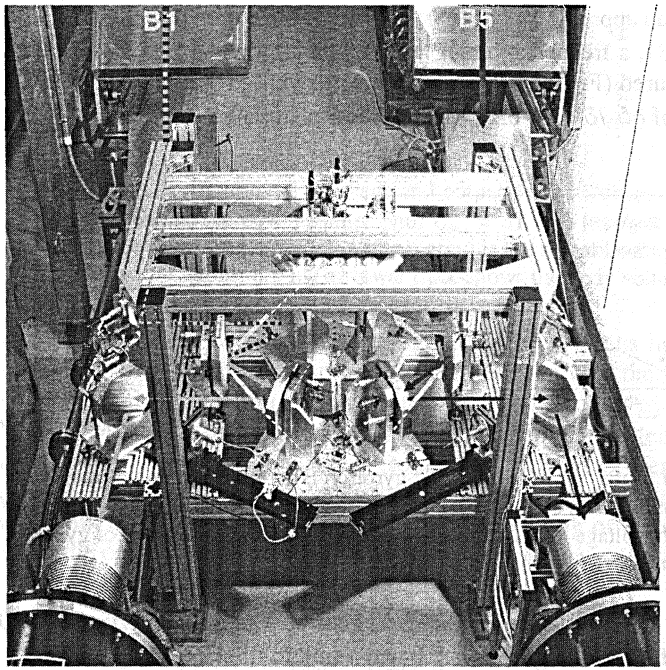

Fig. 3. Photograph of the FADIS installed in the beam duct of the ECRH system on W7-X. The input beams from gyrotrons B1 and B5 are coupled from the rear into the resonator, the output beams are focussed to absorbing loads in the foreground left and right. Output signals OUT1 and OUT 5 are obtained from grating couplers on the last mirrors before the loads.

An essential ingredient is the frequency modulation characteristic of the gyrotrons. The 140 GHz Thales gyrotrons used at W7-X are diode-type gyrotrons with depressed collector. Here, the only possibility to influence the frequency electronically is the modulation of the acceleration ("body") voltage. For this purpose, each gyrotron is equipped with a HV modulator with a rise time of 600 V/μs. For recording of the frequency characteristics of the gyrotrons, a down-converter with a local oscillator (LO) frequency of f_{LO} = 139.65 GHz, fol-

lowed by a Hewlett Packard 5372A frequency analyzer was used. It was connected to simple horn couplers near to the gyrotron output window.

Frequency measurements on the gyrotrons B1 [6, 9] and B5 (similar result like for the series tube No.1 described in [10]) show the following behaviour. For about 0.5 s after switch-on, the gyrotrons exhibit a strong frequency chirp of several hundreds of MHz, which is mainly due to heating and thermal expansion of the gyrotron cavity. The total chirp Δf_G, i.e. the difference of the start frequency $f_{G,\ t=0}$ and the frequency $f_{G,\ t>1s}$ after thermal equilibrium of the cavity has occurred, is an approximately linear function of the output power of the tubes [10]. For gyrotron B1, a frequency tuning via the output power of $\partial f_{B1}/\partial P_{B1} \approx 0.34$ MHz/kW was measured (Fig. 4, left); for B5, a somewhat lower value (due to better cavity cooling) of $\partial f_{B5}/\partial P_{B5} \approx 0.26$ MHz/kW was estimated.

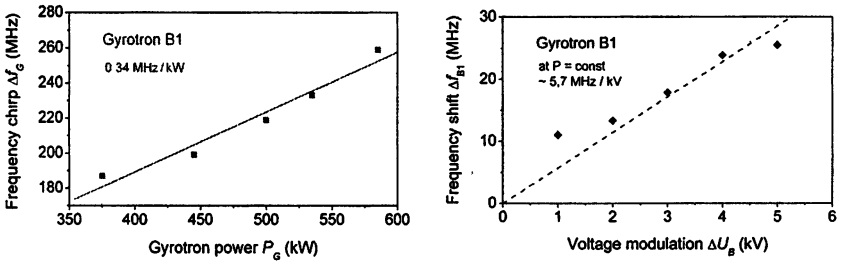

Fig. 4. *Left*: Total frequency chirp of gyrotron B1 from beginning of the pulse (t = 0) until stabilization (t > 1 s) as function of the output power. *Right*: Frequency shift Δf_{B1} as function of body voltage modulation amplitude ΔU_{B1} for the parameters of gyrotron B1 used in the experiment.

After thermalization of the cavity, the frequency is very stable. Over pulse lengths of 10 s, the gyrotron B1 was stable within typically ±4 MHz. Gyrotron B5 showed more frequency jumps yielding a stability of typically ±8 MHz. The instantaneous line-width of the gyrotron is always much less than 1 MHz; the broadening of the frequency seen in the plots is due to a modulation of the LO frequency (±1.8 MHz) caused by 50 Hz noise on the power supply.

Switching experiments have been performed with gyrotron B1 by modulating the body voltage U_B (square wave, 1 kV ≤ ΔU_B ≤ 5 kV, 1 kHz ≤ f_{mod} ≤ 20 kHz). As shown in Fig. 4, right, a frequency-shift keying of the gyrotron B1 with $\Delta f_{gyr} \leq 30$ MHz could be obtained. By adjusting the resonator frequency such that the average gyrotron frequency was on the slope of the resonant curve, the power could be toggled between the two outputs in the rhythm of the frequency shift. A contrast of better than 90 % could be reached, as shown in Fig. 5 for the example for $f_{mod} = 5$ kHz and $\Delta U_B = 4$ kV [3].

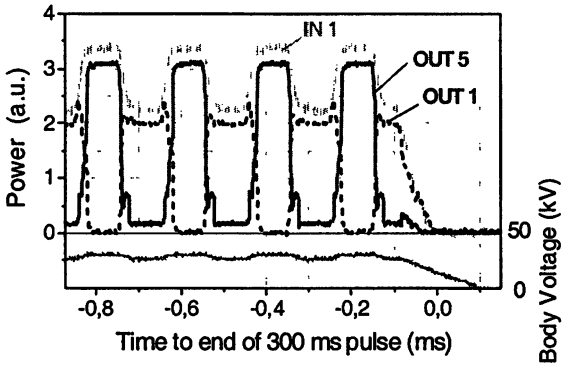

Fig. 5. Power signals from output 1 (dashed) and output 5 (solid) from the diplexer, shown at the end of a 300 ms pulse with U_{acc} = 81.5 kV, ΔU_B = 4 kV, f_{MOD} = 5 kHz square wave. The enveloping trace (grey) is the signal from the gyrotron power monitor of gyrotron B1. The lower trace shows the body voltage.

Power combination was demonstrated by feeding two gyrotrons into the diplexer [14]. It was tuned such that a resonance was coincident with the frequency of gyrotron B1 (after thermalization of the cavity). The frequency of gyrotron B5 was set about 40 MHz below the frequency of B1 using the dependence of the cavity temperature and thus the frequency from the generated power. A 10 s pulse (Fig. 6) showed a power combination with an efficiency of better than 90 %.

By modulating the frequency of the two gyrotrons, toggling of the combined power between the outputs in the kHz range could be demonstrated [14].

4. Applications of high-power diplexers

4.1. Frequency tracking

When comparing the frequency of gyrotron B1 and the combined output (OUT5) in Fig. 6, it is obvious, that the degree of combination depends on the match of the gyrotron frequencies to the resonant frequency of the diplexer. The frequency jumps/drifts of B1 clearly correlate with jumps and drifts in OUT5/OUT1. In this experiment, the gyrotron was free running, and the diplexer was at a fixed tuning. In principle, the dependence of the gyrotron frequency on the voltage could be used to synchronize the gyrotron frequency with the diplexer. However, to minimize power loss due to voltage variation, a mechanical tuning of the diplexer is preferable. Only fast frequency shift keying should be done via gyrotron voltage modulation.

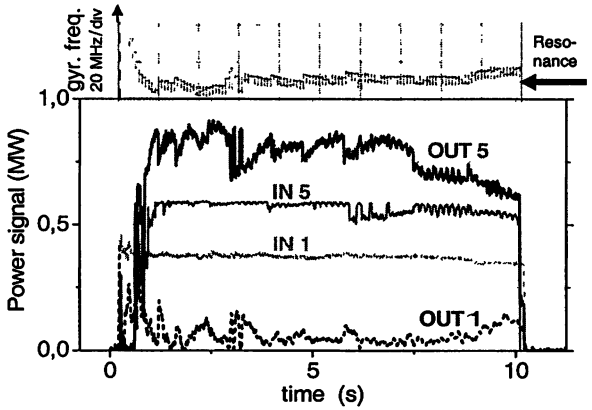

Fig. 6. Upper trace: frequency of gyrotron B1 with respect to the resonance frequency of the diplexer. Lower traces: IN1 and IN5: Power of gyrotrons B1 and B5, OUT1 and OUT5: output power from the diplexer coupled to the loads. Residual power in OUT1 is mainly caused by spontaneous frequency jumps of the B1 gyrotron and an increase of the B1 frequency during the end of the pulse. The frequency of B5 is far from the resonance, therefore, frequency stability of B5 is not critical. Note that the signals suffer somewhat from interference with stray radiation, and therefore are calibrated by comparing the averages over the pulse with corresponding calorimetric measurements.

Therefore, for the operation of any diplexer in an ECRH system, a remotely controllable, preferably automatic tuning of its frequency characteristics over one period of the transmission curve, i.e. $\Delta f_F = c/L$, is needed to match the gyrotron frequency and to compensate for thermal drifts. This means that one mirror in the resonator or delay line is equipped with a drive to move the mirror in normal direction over a distance of typically one wavelength. Fast and precise drive concepts for this purpose are in development [8]. Note that the misalignment due to this frequency tracking is negligible for all diplexer designs discussed here.

Two notes are added: (i) Triode-type gyrotrons are expected to allow a larger frequency shift with lower power modulation for a given voltage variation. Calculations performed for the Japanese 170 GHz ITER prototype gyrotron e.g. yield a frequency swing of more than 30 MHz at negligible power loss, when both the body and the gun anode voltage are used for modulation. An experimental proof of these calculations would be highly desirable. (ii) Once (frequency and phase-controllable) amplifiers with sufficient high power for ECRH purposes are available, the problems on frequency control are very much reduced.

4.2. Near-term plans for applications in ASDEX upgrade and FTU

At the new ECRH system for ASDEX Upgrade [15], the implementation of a resonant diplexer prototype is in preparation. This diplexer (Fig. 7) features a compact design within a rigid box providing stable alignment as well as microwave shielding. Corrugated waveguide inputs and outputs are matched to the resonator mode by HE_{11}-TEM_{00} mode converters, and polarizers in the mitre bends at the output waveguides are inserted to match the polarization to the launching conditions. A mirror drive allows the tuning of the resonator. The main application to be tested is AC-stabilization of NTMs by toggling of the power between two launchers, which aim at poloidal positions being displaced by 180° with respect to the phase of the NTMs; thus the driven EC current is always induced in the O-points yielding maximum NTM suppression [7]. A further application will be an in-line ECE system, where ECRH and ECE will be applied sharing the same launcher and thus a common line of sight [8].

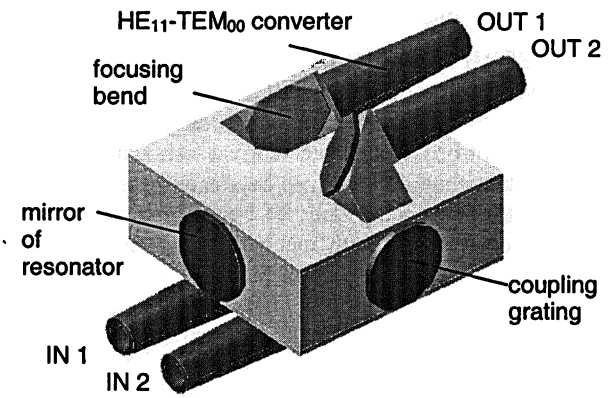

Fig. 7. Conceptual design of a compact resonant diplexer with corrugated waveguide ports, as designed for tests in the new ECRH system at ASDEX Upgrade.

At FTU, the frequency-to-voltage characteristics of the GYCOM gyrotrons is rather linear with a slope of about 9.8 MHz/kV [2], which is much steeper than the characteristics of the Thales gyrotrons. A diplexer/combiner is proposed as switcher between two poloidally symmetric antennas, in order to perform high-efficiency tearing mode stabilization experiments. Combining pairs of beams in a single line would also allow for fitting the 4 available sources into the new envis-

aged FTU ECRH launcher [16, 17] equipped with 2 antennas. The resonator version of Fig. 1*c* with squared corrugated waveguides [5] is designed for insertion in the long run of the 4 parallel transmission lines. Input matching optics converts beams to a smaller size before entering the combiner. The prototype, now in final design stage (Fig. 8), will undergo high-power qualification testing before it is installed in the FTU system.

Fig. 8. Sketch of the resonant diplexer/combiner made with 3 parallel squared corrugated waveguides (in dark-grey) and input/output optics (in grey) proposed for tests in the ECRH system at Frascati Tokamak Upgrade.

4.3. Options for applications and integration in the ITER ECRH system

The basic ITER ECRH system [18] will employ 24 170 GHz gyrotrons. It is assumed, that these will be free-running oscillators (although gyro-amplifiers and phase-locking schemes are under development, but at present do not provide sufficient power). The gyrotrons are connected via evacuated corrugated HE11 waveguide to 3 upper launchers [19] (UL; 8 beams each, mainly for NTM stabilization) and one equatorial launcher (EL; 24 beams, mainly for central heating and current drive). A central unit with mechanical waveguide switches allows connecting the gyrotrons either to the ULs or the EL.

During the development phase of the ITER ECRH system, a diplexer can be used for a test stand which is fed by two 1 MW gyrotrons, e.g. those which are developed in Japan [20]. This allows CW tests of the FADIS itself, the transmission lines, the dummy load, later on also for UL and EL with 2 MW.

In the ECRH system itself near to the generator hall, diplexers can be used as switches between transmission line and loads allowing gyrotrons in hot stand-by; they could also be used for power combination from two 1 MW gyrotrons on a common transmission line to reduce the number of waveguides.

The most essential modification, however, of the present ITER ECRH design would be the replacement of the mechanical waveguide switches between ULs and EL by diplexers. This would offer interesting and attractive options:

Firstly, this allows switching of the power from the EL to the UL by retuning of the diplexer as before, but without the need to switch off the gyrotrons during the switching process, as the power goes either way, but not to unknown or unwanted places. Note that power sharing with arbitrary fractions between the UL and EL is possible.

Secondly, efficient AC-stabilization of NTMs is possible as soon as a mode occurs: The gun anode or body voltage of the gyrotrons is modulated (by a few

kV only) with the mode frequency, and the diplexers are tracked such that the corresponding frequency modulation results in a maximum power modulation at the outputs for the ULs, synchronous to the rotation of the island. There is no waste of installed power at the modulated operation, as the asynchronous power is still available at the EL and can be used to continue the task as before the onset of the NTMs.

Thirdly, as the transmission lines are designed for a power of 2 MW and two gyrotrons could be fed into the inputs of the diplexer to provide power combination, the initial installation with only half the number of waveguides (12 to ULs, 12 to EL) between the 12 switches and launchers is possible. This would require only two UL plugs. Alternatively, if the launchers and waveguides are installed as foreseen at present, and 24 diplexers are installed as switches/combiners, one has the option to add (at a later stage) more gyrotrons to the system, by feeding them into the second inputs of the diplexers.

Several notes need to be added to these proposals. *Firstly*, although possibly all types of diplexers can be designed for arbitrary polarization, the different launching conditions for the EL and the UL will most probably require different polarizations. Therefore, for *fast* switching applications, the polarizers should be installed behind (down-stream from) the diplexers.

Secondly, for about 0.5 s after switch-on of the gyrotrons, where the frequency varies rapidly due to thermal cavity expansion, the routing of the power probably cannot be controlled. This has to be taken into account for start-up scenarios. It is, however, no problem for long-pulse experiments and for hot stand-by operation.

Thirdly, for combiner operation, one has to choose pairs of gyrotrons with a frequency difference (for optimal output in steady state operation) not equal to (a multiple of) the free spectral range of $\Delta f_F = c/L$, the ideal case being a difference of (an odd multiple of) roughly $\Delta f_F/2$ (cf. Fig. 1). The diplexer is tuned such that a resonance frequency f_2 coincides with $f_{A,0}$, the optimal frequency of gyrotron A; thus, the optimal frequency of gyrotron B, $f_{B,0}$, stays always non-resonant. To direct the combined power to the other output channel, the tracking of the diplexer resonance has to be switched to $f_{B,0}$. In case of operation as a fast switch and combiner, both gyrotrons are frequency modulated with sufficient Δf_S, and the diplexer is tracked that $f_{A,0}$ (or $f_{B,0}$) is coincident with f_2.

Fourthly, the various types of diplexers discussed here differ strongly with respect to the transmission characteristics, insertion loss, cross-talk, dimensions and requirements for system integration. Therefore, the diplexer concept chosen will depend on the concrete tasks to be performed, and on the experimental environment. Therefore, the development of an ITER compatible FADIS should be started soon, and in close cooperation with the design of the transmission line. A detailed discussion is beyond the scope of this paper.

5. Conclusions

It has been shown, that high-power diplexers are a valuable component, which can strongly increase the performance and flexibility of ECRH systems. The results obtained up to now in the development of several prototypes including the high-power demonstration of fast switching and power combination from two gyrotrons confirm the applicability of these devices. In conclusion, the results motivate the development of power combiners and fast switches until maturity, especially in view to applications in ITER and other advanced devices.

Further research is aimed to study other multiplexing schemes and arrays of phase-controlled gyrotrons. Gyrotron developers are encouraged to continue the development of frequency- or even phase-controlled gyrotrons, the availability of which would further extend the application palette of high-power diplexers.

This work is carried out in the frame of the virtual institute "Advanced ECRH for ITER" (collaboration between IPP Garching and Greifswald, FZK Karlsruhe, IHE Karlsruhe, IPF Stuttgart, IAP Nizhny Novgorod, and IFP Milano), which is supported by the Helmholtz-Gemeinschaft deutscher Forschungszentren.

References

1. *Petelin M. I. and Kasparek W.* Electrically controlled scanning of wave beam produced by gyrotron: Option for plasma fusion experiment // Proc. 6th Int. Vacuum Electronics Conference (IVEC 2005), Noordwijk, The Netherlands, p. 131.
2. *Kasparek W. et al.* Fast switching and power combination of high-power electron cyclotron wave beams: principles, numerical results and experiments // Fusion Sci. Technol. **52** (2007), 281–290, and references therein.
3. *Kasparek W. et al.* A fast switch, combiner and narrow-band filter for high-power millimetre wave beams // Nucl. Fusion **48** (2008), 054010.
4. *Smits F M A.* Power combiners for incoherent waves // Proc. of 8th Joint workshop on ECE and ECRH. Report IPP III/186. 1993. Vol. 2. P. 607–621.
5. *Bruschi et al.* Beam Combination and Routing at High Power with a Ring-type Waveguide Millimeter-Wave Resonator // Fusion Sci. Technol. **53** (2008), 97–103.
6. *Wubie W. et al* Numerical and experimental investigations of a diplexer for combination and switching of high-power millimeter waves // Int. Conf. on Infrared and Millimeter Waves, Pasadena, 2008.
7. *Maraschek M. et al.* Enhancement of the Stabilization Efficiency of a Neoclassical Magnetic Island by Modulated Electron Cyclotron Current Drive in the ASDEX Upgrade Tokamak // Phys. Rev. Lett. **98** (2007), 025005.
8. *Bongers W. et al.* Feedback Stabilization of Tearing Modes by Electron Cyclotron Current Drive controlled by in-line Electron Cyclotron Emission, submitted to Fusion Sci. Technol. (2008).
9. *Koshurinov Yu. I. et al.* Diplexer based on open cavity with corrugated mirrors // Tech. Phys. Lett. **31** (2005), 709–711.
10. *Petelin M I.* Quasi-optics in High-Power Millimeter-Wave Systems // 6th Workshop on High Energy Density and High Power RF, WV, USA, AIP Conference Proc. **691** (2003), 251–262.

11. *Kuzikov S V.* Wave beam multiplication phenomena to RF power distribution systems of high-energy linear accelerators // Int. J. Infrared Millimeter Waves, **19** (1998), 1523–1539.

12. *D'Arcangelo O. et al.* Tests of a 105 GHz prototype diplexer combiner based on square corrugated waveguide, accepted for publication, Fusion Eng. Design (2008).

13. *Erckmann V. et al.* Electron Cyclotron Heating for W7-X: Physics and Technology // Fusion Sci Technol. **52** (2007) 291.

14 *Erckmann V. et al.* Power Combination of Two 140 GHz Gyrotrons and Fast Switching of the Combined Beam, accepted for publication // Fusion Sci. Technol. **55** (2009).

15. *Wagner D et al.* The new multi-frequency electron cyclotron resonance heating system for ASDEX Upgrade // Fusion Sci. Technol. **52** (2007), 313–320.

16. *Bruschi et al.* A new Fast-steerable ECRH Launcher for FTU, accepted for publication, Fusion Sci. Technol. **55** (2009).

17. *Bin W. et al.* Design of a new ECRH launcher for FTU tokamak, accepted for publication, to Fusion Eng. Design (2008).

18. Design Description Document for the ITER ECRH System G 52 DDD 5 01-05-29 W 0.1.

19. *Heidinger R. et al.* Conceptual design of the ECH upper launcher system for ITER, submitted to Fusion Eng. Design (2008).

20. *Sakamoto K. et al.* High power 170 GHz gyrotron development in JAEA // Strong Microwaves. Sources and Applications: Proc. 7th Int. Workshop. Nizhny Novgorod, 2009. P. 7–14.

DEVELOPMENT AND APPLICATIONS OF THz GYROTRONS

T. Idehara, I. Ogawa, S. Mitsudo, Y. Tatematsu and T. Saito

Research Center for Development of Far Infrared Region, University of Fukui FIR FU)
3-9-1 Bunkyo, Fukui-shi 910-8507, JAPAN

A gyrotron with a 21 T pulse magnet achieved the breakthrough of 1 THz. This is the first result of high frequency operation in the world beyond 1 THz. In addition, new gyrotron series in FIR FU, University of Fukui, so-called Gyrotron FU CW Series is being developed. Such a present status of high power THz radiation sources – gyrotrons in FIR FU and their application to high power THz technologies will be introduced.

1. Introduction

Our previous Gyrotron FU Series has already achieved high frequency operation up to 0.89 THz by using a 17 T magnet and the second harmonic operation [1]. In addition, some gyrotrons included in the series achieved modulation of amplitude and frequency and highly stable operation in amplitude and frequency. After then, we have already applied these gyrotrons to plasma diagnostics and other high power far-infrared technologies. Recently, a gyrotron in FIR FU with a 21 T pulse magnet achieved the breakthrough of 1 THz [2]. For convenience of the application to high power THz technologies, CW gyrotrons (Gyrotron FU CW Series) is being developed. Gyrotron FU CW I has been developed and succeeded in the CW operation at 300 GHz under high power of 1.75 kW [3]. The next gyrotrons, Gyrotrons FU CW II and III are being developed. The parameters are as follows, 394 GHz, 100 W for FU CW II and 1 THz 100 W for FU CW III. Both gyrotrons operate in CW mode.

2. A THz gyrotron with a pulse magnet

A demountable gyrotron tube is installed on the center axis of 21 T pulse magnet. In the operation test, a high voltage pulse is applied to electron gun at around the maximum field intensity B. When B is changed, many cavity modes are excited at the fundamental and second harmonic of cyclotron frequency. Fig. 1 shows expected frequency of observed radiation as functions of B. The second harmonic radiation is separated from the fundamental by using a high pass filter. The maximum frequency is around 1.016 THz at the second harmonic operation of $TE_{4,12}$ cavity mode. Corresponding field intensity B is 19.1 T. Now we

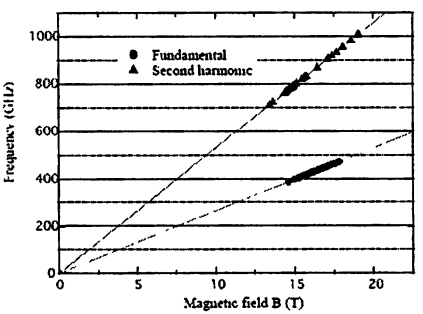

Fig. 1. Output frequencies as function of magnetic field intensity B

are trying to increase the frequency by increasing B. Similar study on development of a high frequency gyrotron with a pulse magnet is advancing in Institute of Applied Physics, Russian Academy of Science (IAP RAS) [4].

3. Gyrotron FU CW Series

Now, in FIR FU, we are developing high frequency CW gyrotrons named Gyrotron FU CW Series as high power THz radiation source. We have already developed Gyrotron FU CW I. The frequency is around 300 GHz, output power 1.75 kW, the operation is complete [3].

3.1. Gyrotron FU CW II

We have finished the construction of a next CW gyrotron, Gyrotron FU CW II and begun the operation test. Fig. 2 shows a cross section of the gyrotron and Fig. 3 the side view. The gyrotron consists of a 8 T He-free superconducting magnet, a demountable tube, a vacuum pump system and power supplies. The cavity is a simple cylindrical one whose diameter and length are 5.72 mm and 15 mm. The designed frequency is 394.6 GHz at the second harmonic operation of $TE_{0,6}$ cavity mode. After completing the operation test, the gyrotron will be used for enhancement of NMR sensitivity by use of dynamic nuclear polarization (DNP). 394.6 GHz is corresponding to ESR frequency at the field intensity of 7.1 T. The frequency of proton NMR at the field is 600 MHz.

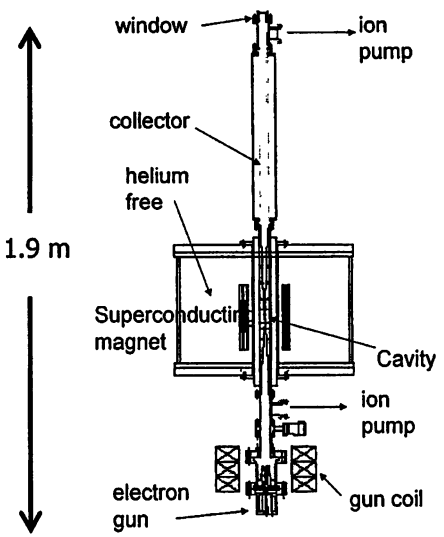

Fig. 2. The cross section of Gyrotron FU CW II

Fig. 3. Sideview of Gyrotron FU CW II

We have already succeeded to operate the gyrotron at many fundamental and second harmonic resonances. Cavity modes corresponding to almost all radiations resulting from fundamental and second harmonic operations are identified. We have found the operation at the $TE_{0,6}$ cavity mode whose frequency measured by a heterodyne system is 394.3 GHz. It is a little bit lower frequency than the designed frequency. Fig. 4 shows all of frequencies observed up to the present as functions of magnetic field intensity. Measured frequencies are distributed in the range from 61GHz to 209 GHz in the case of fundamental operations, while from 212 to 439 GHz in case of second harmonic operations. Now, we are measuring the output power of Gyrotron FU CW II. Typically, the output power is several hundred watt for fundamental operations and several tens watt for the second harmonic operations.

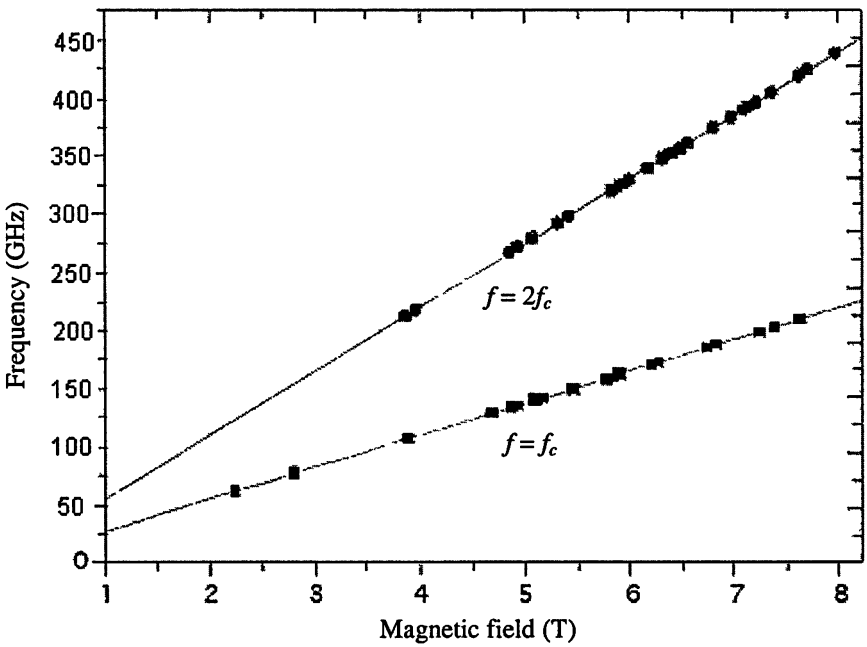

Fig. 4. All frequencies measured by a heterodyn detection system as functions of magnetic field

3.2. Gyrotron FU CW III

The third gyrotron, Gyrotron FU CW III with a 20 T superconducting magnet [5] has already been constructed and operated. In Table, main parameters of the gyrotron are shown. The gyrotron is optimized for the second harmonic operation of $TE_{4,12}$ at the frequency of 1013.7 GHz. The operation mode is complete

CW. This gyrotron will achieve the breakthrough of 1 THz in CW operation. In addition, it is expected that many other cavity modes will be excited by adjusting the field intensity at the optimum value for each cavity mode. As the results, it will achieve frequency step tunability in wide range covering sub-THz to THz frequency region.

Specification of Gyrotron FU CW III

Total height from electron gun to the window	2.4 m
Superconducting magnet	
Maximum magnetic field	20 T
Inner bore	50 mm
Cavity	
Radius	1.95 mm
Length	10 mm
Main cavity mode	$TE_{4,12}$
Frequency	1013.7 GHz at the 2nd harmonic
Q-factor	23720
Operation mode	Complete CW
Operating magnetic field	19.1 T for $TE_{4,12}$ mode
Triode-type electron gun	
Cathode radius	4.5 mm
Maximum cathode current	1 A
Cathode voltage	30 kV
Gun coil	
Maximum input current	300 A
Maximum magnetic field	0.183 T
Pumping bores	1. Near the electron gun. 2. Near the output window
Water cooling jackets	installed at a cavity and a collector regions

Fig. 5 and Fig. 6 show the cross section and a photo of Gyrotron FU CW III. Figure 7 shows measurement results of radiation power at fundamental operations and calculation results for starting currents of each cavity modes at both fundamental (dotted lines) and second harmonic (solid lines) operations. It is seen that almost all cavity modes at the fundamentals are excited at the optimum intensities of magnetic field.

For measurement of the second harmonic operations, we tried to observe a radiation power after high pass filter consisting of a narrow circular wave guide whose diameter is 0.3 mm. The corresponding cutoff frequency is 586 GHz. Up to the present, we have measured several second harmonic operation in the field intensity region below 18 T (Fig. 8). The maximum frequency estimated from the

corresponding field intensity is around 980 GHz. Fig. 9 shows all of frequencies observed at both fundamental and second harmonic operations as function of field intensity at the cavity region. As seen in the figure, Gyrotron FU CW III has achieved frequency step-tunability in a wide region from 140 GHz to 980 GHz. Output power is distributed from around 100 W to higher than 200 W at the fundamental operations and in several tens watt at the second harmonic operations. The operation mode is CW or long pulse with several hundred milliseconds.

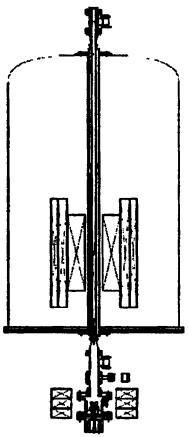

Fig. 5. The cross section of Gyrotron FU CW III

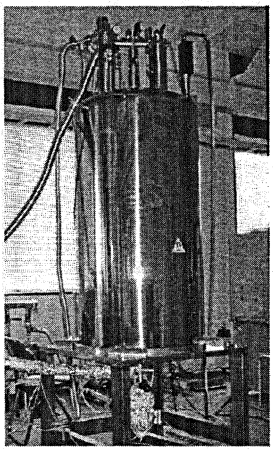

Fig. 6. Photo of Gyrotron FU CW III

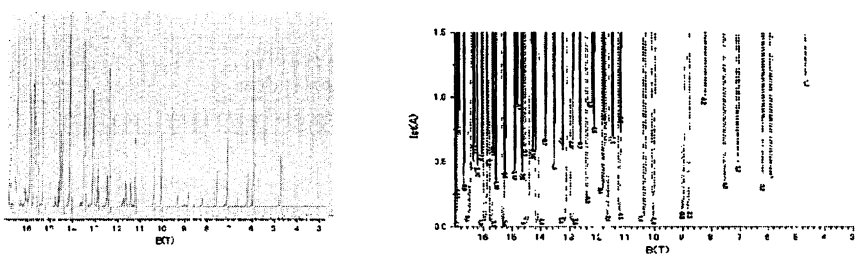

Fig. 7. A typical measurement result at the fundamental operations and comparison with calculation result for starting current of each cavity mode. *Upper figure:* Radiation power observed just after the output window as function of magnetic field intensity at the cavity region. *Lower figure:* Starting current for each cavity mode as a function of magnetic field intensity. Dotted lines show fundamental operations and solid lines second harmonic operations. Numbers indicated near calculated lines show mode numbers *m, n*. Comparing with the upper figure, it is seen that almost all cavity modes are excited at the optimum intensities of magnetic field for fundamental operations.

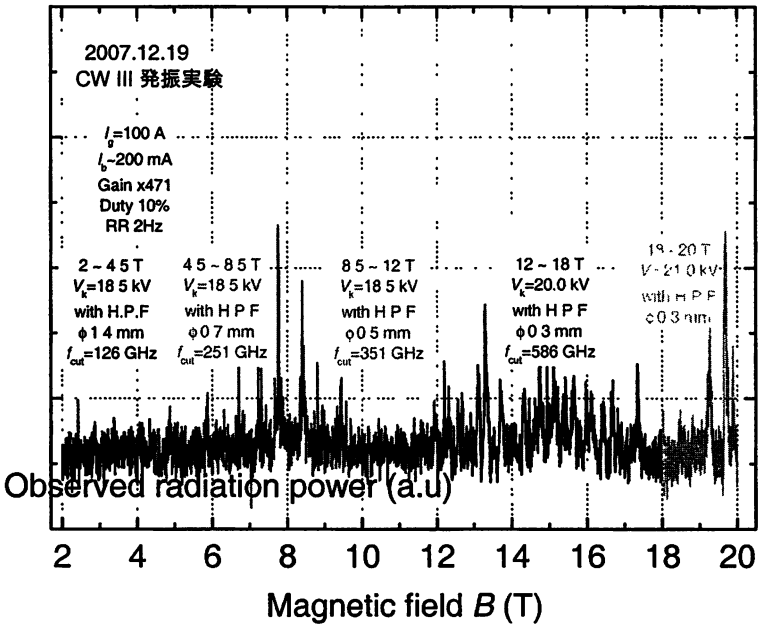

Fig. 8. Radiation power measured after high pass filters as a function of magnetic field intensity

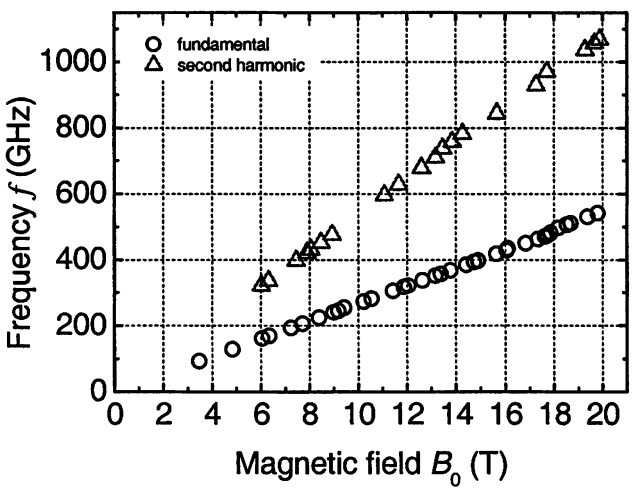

Fig. 9. Measured frequencies as functions of magnetic field intensity

4. Summary

Three CW gyrotrons, Gyrotron FU CW I, II and III operating in sub-THz to THz region are being developed. Operation test of FU CW I and II have already carried out. Gyrotron FU CW I is being used for material processing. Gyrotron FU CW II has been installed on a 600 MHz proton-NMR device at Institute of Protein Research, Osaka University for sensitivity enhancement of NMR spectroscopy by using Dynamic Nuclear Polarization (DNP). Gyrotron FU CW III will be used for development of high power THz technologies in future, after operation test is completed. These three gyrptrons have the advantages of complete CW operation and frequency step-tunability in addition to high frequency operation up to 1 THz.

Now, we are developing the fourth gyrotron of the series, Gyrotron FU CW IV with 10 T superconducting magnet. It will achieve continuously frequency-tunability for application to DNP-NMR. The fifth gyrotron Gyrotron FU CW V will be developed for application to accurate measurement of energy level difference of positronium. The frequency should be varied around 203.4 GHz. This is the first trial for direct measurement of the level difference.

Acknowledgement

This work is partially supported by a Grant in Aid from Japan Society for Promotion of Science (JSPS). For achieving the stable operation of electron gun, a 20 kV stable amplifier (20/20C) was supplied from TREK Japan Co. as a special cooperative support.

References

1 *Idehara T., Ogawa I., Mitsudo S., Pareyaslavets M., Nishida N., Yoshida K.* Development of frequency tunable, medium power gyrotrons (Gyrotron FU Series) as submillimeter wave radiation sources // IEEE Trans. Plasma Sci., 27, 340–354 (1999).

2. *Idehara T., Tsuchiya H., Watanabe O., La Agusu and Mitsudo S.* The first experiment of a THz gyrotron with a pulse magnet // Int. J. Infrared and Millimeter Waves, 27, 319 (2006).

3. *Idehara T., Ogawa I, La Agusu, Kanemaki T., Mitsudo S., Saito T., Fujiwara T., Takahashi H* Development of 394 6 GHz CW gyrotron (Gyrotron FU CW II) for DNP/proton-NMR at 600 MHz // Int. J. Infrared and Millimeter Waves, 28, 433–442 (2006).

4. *Glyavin M.*, private communication.

5. *La Agusu, Idehara T., Mori H., Saito T., Ogawa I., Mitsudo S.* Design of a CW THz gyrotron (Gyrotron FU CW III) using a 20 T superconducting magnet // Int. J. Infrared and Millimeter Waves, 28, 315–328 (2007).

HIGH-HARMONIC TERAHERTZ GYRODEVICES

I. V. Bandurkin, V. L. Bratman, Yu. K. Kalynov, V. N. Manuilov, S. V. Samsonov, and A. V. Savilov

Institute of Applied Physics, Russian Academy of Sciences, Nizhny Novgorod, Russia

Prospects of development and results of first experiments from gyro-oscillators and multipliers radiating at high cyclotron harmonics in sub-THz and THz frequency range have been discussed. The problem of selective mode excitation for both types of devices is significantly simplified in the case of using axis-encircling beams of electrons moving along helical trajectories with guiding centers near the cavity axis (configuration of Large Orbit Gyrotron, LOG). In a self-exciting gyro-multiplier, a 60 keV / 5 A / 10 μs axis-encircling beam simultaneously excited the 2nd-harmonic mode $TE_{2,2}$ and 4th-harmonic mode $TE_{4,3}$ of an azimuthally-corrugated cavity at the frequencies of 37.5 GHz and 75 GHz. An axis-encircling electron beam with parameters 80 keV / 0.7 A / 10 μs was obtained in a cusp gun and further compressed 3000 times in magnetic field increasing up to the operating value of 13.7 T. In the end of 2008, this beam was used for excitation of a 3rd-harmonic LOG that allowed for the first time obtaining radiation with frequency of 1 THz in this type of oscillators.

Introduction

Electron-vacuum devices can in principle satisfy any demands to sources of coherent sub-THz and THz radiation which have been ever made from applications [1, 2]. In the course of long duration, conventional Backward Wave Oscillators (BWOs [3]) have covered most of the requirements to relatively low-powerful oscillators. Having provided generation in the frequency range of 0.1–1.4 THz with power of 100–1 mW and very broad electrical frequency tuning they have been used in many fields of physics and technology. A remarkably higher power has been radiated or can be radiated at the frequencies 0.3–0.5 THz from other varieties of electron devices using interaction of rectilinear electron beams with slow waves, namely, BWOs with inclined electron beams (clinotrons [4]), Extended Interaction Klystrons [5] and orotrons [6] (or Diffraction Radiation Generators [7]). Devices using interaction of curvilinear electron beams with fast waves, namely Free Electron Lasers (FELs) [8] and gyrotrons [9–11] can deliver many orders of value higher power that opens new opportunities for many applications. FELs enable coherent and smoothly frequency-tuned radiation not only in whole THz region but also at much higher frequencies. However, they utilize ultrarelativistic electron beams and, hence, typically require large-size particle accelerators for their realization. That is why these devices can be only used in specialized research centers. Gyrotrons can use beams with significantly lower energy of 10–100 keV. Correspondingly, they are much more compact than FELs and available for many laboratories.

The first gyrotron with the wavelength less than 1 mm (330 GHz, CW, 1.5 kW) [12] was demonstrated many years ago. It should be, however, empha-

sized that even today realization of gyrotrons at submillimeter-wavelength and THz ranges is not easy because it requires very strong operating magnetic fields: e.g., 36 and 18 T at the fundamental and second cyclotron harmonics, respectively, for the radiation frequency 1 THz. Modern cryo-magnets provide magnetic field up to 20 T (up to 15 T for liquid-helium-free magnets) in sufficient volume, whereas pulsed solenoids are able to provide over 50 T in single-shot pulses. Cryo-magnet and pulsed-solenoid sub-THz gyrotrons were developed in Russia, USA, Japan, and Australia [13–15]. After a number of attempts, very recently, the 1 THz frequency threshold was at last successfully exceeded in pulsed fundamental-harmonic [16] and cryo-magnet second-harmonic gyrotrons [17]. However, sub-THz and THz gyrotrons still stay quite unique because of strong magnetic field required.

The operating field can be decreased in the case of higher ($s > 2$) operating harmonics, but it is complicated because of dense spectrum of eigenmodes and difficulty in discrimination of low-harmonic spurious modes [18, 19]. It is important in this connection, that for relatively low voltage acceptable for the most applications the electron-wave coupling decreases very fast with the increase of the cyclotron harmonic number [9–11]. Therefore, a high-harmonic operation requires a high Q-factor of the operating cavity. At that, one should also take into account a drastic decrease of Q-factors in the sub-THz and THz range caused by increase in Ohmic losses [20].

Thus, realization of high-harmonic THz gyrotrons requires special methods of mode selection. In this paper, we discuss two systems with strong additional selection, namely, Large Orbit Gyrotrons [21–24] and gyro-multipliers [9, 21, 25–30]. In LOGs, motion of the electrons along helical trajectories around the axis of an axially symmetrical microwave system (the axis-encircling electron beam) results in improving the electron-wave coupling at high harmonics and thinning the spectrum of competing modes. In gyro-multipliers, the selectivity of the high-harmonic radiation is provided by fixation of their frequency due to low-harmonic electron-wave interaction; the use of axis-encircling beams additionally improves the selectivity of gyro-multipliers.

Large-Orbit Gyrotron

Efficiency of high-harmonic gyrotrons can be in principle comparable with the fundamental-harmonic efficiency. However, as mentioned in Introduction, high-harmonic gyrotrons require relatively high operating currents and, generally speaking, suffer from excitation of low-harmonic spurious modes. It can be explained from the expression for the gyrotron starting current. For a circular gyrotron cavity and interaction at the s-th cyclotron harmonic the starting current of a $TE_{m,p}$ operating mode depends on main parameters as follows (see e.g. [10, 11]):

$$I_{st} \propto \frac{1}{G_{m,s}\beta_{\perp}^{2s}(L/\lambda)^2 Q}. \qquad (1)$$

Here

$$G_{m,s} = \frac{J_{m-s}^2(\nu_p R/a)}{(\nu_p^2 - m^2)J_m^2(\nu_p)} \qquad (2)$$

is the excitation factor, J_m and ν_p are the Bessel function and the p-th positive root of its derivative, J_m', R is the radius of the guiding electron centers of a tubular electron beam, a is the cavity radius, $\beta_\perp$ is the rotary electron velocity normalized to the speed of light, L and Q are the length and Q-factor of the cavity. Thus, the starting current increases with the increase of the cyclotron harmonic number as $\beta_\perp^{-2s}$, and this increase is fast for relatively low voltages and electron pitch-factors, when $\beta_\perp$ is significantly less than the unity. This effect could be compensated by an increase of the diffraction Q-factor of the cavity, but this possibility is limited by Ohmic losses. In order to decrease Ohmic losses, one should use operating modes with high radial indices, p, in spite of some complication of the mode competition.

The problems of parasitic mode discrimination and high starting currents at high cyclotron harmonics can be significantly mitigated by the use of an axis-encircling electron beam. All electrons of such a beam move along helical trajectories around the axis of the cavity. This results in improving of the electron-wave coupling at high cyclotron harmonics, as well as in significant thinning of the spectrum of competing modes. Actually, in this case $R = 0$, and, according to Eq. (2), the electron-wave coupling at the s-th harmonic is possible only for modes with $m = s$; at the same time, for these modes the excitation factor (2) reaches the maximum. This fruitful idea was successfully used in many experiments with LOGs and so-called harmonic converters [21–24, 27]. It is important to emphasize that an axis-encircling electron beams can not be produced in well-developed magnetron-injection gyrotron guns. Correspondingly, the most complicated problem for LOGs is the creation of electron-optical systems, which are able to produce axis-encircling beams possessing sufficiently high currents and pitch-factors, as well as small spreads in velocity and radii of electron guiding centers.

The experimental study of LOGs at the Institute of Applied Physics from the very beginning was aimed at generation of high-frequency radiation and developed, step by step, from mildly relativistic to more practical weakly relativistic electron beams, from explosive to thermionic cathodes, from cavity modes with small to high radial indices. Until recently, the highest radiation frequencies achieved in LOGs were 0.37–0.41 THz. It was obtained at the third cyclotron harmonic with power 10–20 kW in microsecond pulses [31]. In those experiments, we used a conventional gyrotron cavity in the form of a piece of a weakly-irregular cylindrical waveguide terminated with a cut-off narrowing at the cathode end (Fig. 1*a*). In all experiments with relatively long-wavelength and high-voltage LOGs, we used a quasi-Pierce gun forming a rectilinear (pencil) electron beam and a kicker, which was immersed in a region of a relatively weak mag-

netic field in order to impart an initial rotary electron velocity [31, 32]. Then, in the process of electron motion in the increasing magnetic field, the electron oscillatory velocity increased up to the operating value.

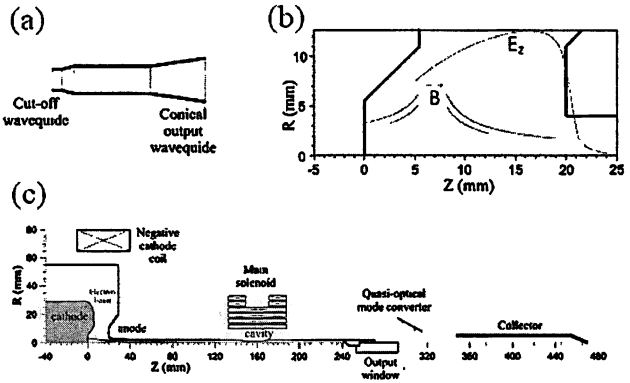

Fig. 1. Third-harmonic THz LOG: cavity (*a*), electron gun with magnetic field cusp (*b*), and general scheme of the LOG (*c*)

Evident disadvantages of the Pierce-kicker gun described above are caused by non-symmetry of the kicker's field and too high electron density close to the cathode; these factors can prevent obtaining high-quality beams. In addition, it is difficult to realize such a system in CW regime. These problems are significantly complicated with increasing the frequency and decreasing the operating voltage. Therefore, in a new, relatively low-voltage third-harmonic 1 THz LOG, we use a different electron-optical system, namely, a gun with magnetic field cusp [33, 34] in a close-to-cathode region. In this system, a cathode with a ring-type emitter is immersed in an axial magnetic field and produces a thin tubular beam (Fig. 1*b*). In the cusp region, the axial magnetic field goes to zero and, then, changes its sign. At that, under action of radial magnetic field electrons begin to rotate around the axis of the system, so that a cylindrical beam of rotating electrons (with radius coinciding with the electron Larmor radius) is formed. Then, in the process of electron motion in the increasing magnetic field, the rotary velocity increases adiabatically, whereas the beam radius decreases.

The third-harmonic 1 THz LOG (Fig. 1*c*) has been designed for operation at the relatively low-voltage of 80 kV with the electron current of 0.7 A, the pulse duration of 10 μs, and the repetition frequency of 0.1 Hz [35]. The magnetic field inside the cavity amounts to 13.7 T, whereas close to the cathode it is as small as –4.5 mT. A very high field compression, 3000, allows achieving a high enough current density inside the operating cavity, whereas emission density is not so high (4 A/cm^2). In order to decrease Ohmic losses, a mode with high radial index ($TE_{3,7}$) has been chosen; the corresponding diameter of the cavity is equal to

2.3 mm. A relatively high pitch-factor (1.4–1.5) and long-length cavity (7.2 mm, or 24 wavelengths) are required to excite this mode. A long length of the interaction region results in a very narrow (as compared to experiment [31]) frequency band of the cyclotron resonance. Due to this, the operating mode $TE_{3,7}$ should not be suppressed by the spurious mode $TE_{2,5}$ (Fig. 2). Simulations predict 1 THz operation with quite high (10 %) electron efficiency. However, Ohmic losses decrease the total efficiency down to 1.3 %; corresponding output power amounts to 0.7 kW.

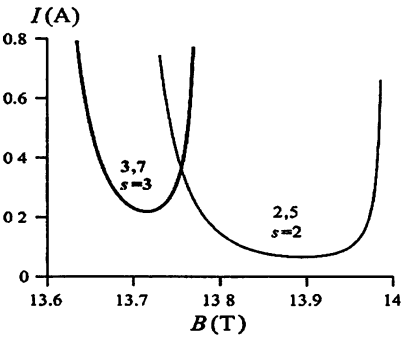

Fig. 2. Calculated starting currents for the operating 3rd-harmonic mode $TE_{3,7}$ and spurious 2nd-harmonic mode $TE_{2,5}$ in the 1 THz LOG

The electron-optical system of the 1 THz LOG was first tested in a low-current modeling regime. At various values and signs of the cathode magnetic field, three types of beam traces on the quartz scintillating target were observed (Fig. 3). It corresponds to Bush theorem, which gives the following expression

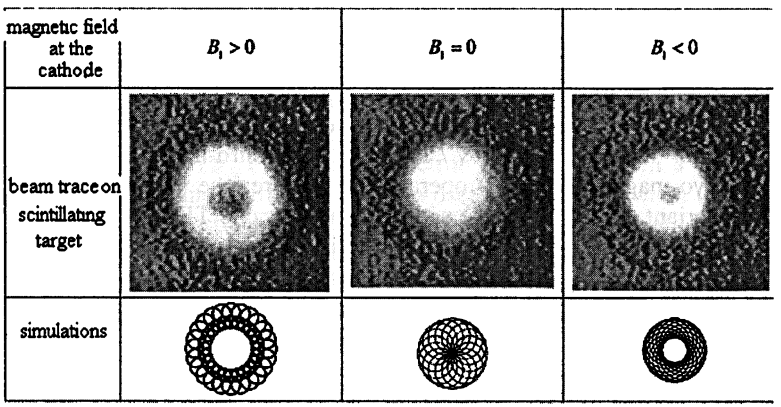

Fig. 3. Low-current modeling test of the cusp gun for the 1 THz LOG. Electron beam traces on the scintillating target and calculated electron trajectories for positive, zero, and negative magnetic fields at the cathode.

for the electron Larmor radius after transition through a fast jump of the axially-symmetrical magnetic field:

$$r = r_c \frac{B_2 - B_1}{2B_2} \,. \tag{3}$$

Here r_c is the radius of the electron emitter, and $B_{1,2}$ are the magnetic field at the cathode and in the region after the field reverse. In the first regime, when fields of the cathode coil and the main solenoid were co-directed (the cusp is absent), a ring-type spot was observed on the target; this corresponded to a multi-axis tubular beam. A decrease of the field B_1 resulted in an increase of the Larmor radii; simultaneously, the electron guiding centers were shifted to the center of the beam. When the cathode field was equal to zero, one observed a regime with large rotary velocities. In this regime, the radius of electron guiding centers was close to half of the Larmor radius, so that electron orbits filled in almost the whole beam cross-section. In the third regime B_1 was negative, so that the cusp was realized. In this case, an increase of $|B_1|$ leaded to increase of the electron Larmor radius and decrease of the radius of guiding centers.

In an ideal case, an axis-encircling electron beam is provided in the symmetrical cusp, $|B_1| = B_2$. In the experiment, the displacement of electron guiding centers was almost twice smaller than the Larmor radius.

In the end of 2008, the full-scale experiment with the 1 THz gyrotron was successfully carried out. A rather long cavity provided sufficient mode separation and single-mode operation at the 3rd and 2nd cyclotron harmonics. The modes $TE_{3,7}$ and $TE_{3,6}$ with radiation frequencies 1.00 and 0.87 THz and output power 0.4 and 0.3 kW, respectively, have been radiated at the 3rd cyclotron harmonic. The modes $TE_{2,5}$ and $TE_{2,4}$ with frequencies 0.68 and 0.55 THz and power 1.8 and 0.6 kW have been observed at the 2nd cyclotron harmonic. An output quasi-optical mode converter transforms all the modes into Gaussian wave beams.

Both simulations and mm-wavelength experiments have shown that the operating voltage of a LOG can be further decreased if the electron pitch-factor is increased. For instance, a 30 kV / 1 A / 0.4 THz third-harmonic LOG with a compact cryo-magnet ($B = 4$ T) operating in CW regime [36] seems as a very attractive variant. In this case, the same operating mode $TE_{3,7}$, is even more isolated from the spurious mode $TE_{2,5}$. According to simulations, a cusp electron gun is able to produce the electron beam possessing all required parameters. In the case of the cavity length of 15 mm, the calculated output power of the LOG amounts to 1 kW with the efficiency of 3.5 %.

Gyro-Multipliers

A well-known additional method of improving the gyrotron selectivity is synchronization of the high-frequency (HF) high-harmonic operation by a low-frequency (LF) wave, which interacts with electrons at a low cyclotron harmonic [21, 25–27]. Actually, due to non-linearity of the interaction electron bunching occurs at all harmonics of the frequency of the LF wave, ω_1, and stimulates the HF interaction at a multiplied frequency,

$$\omega = n\omega_1 . \qquad (4)$$

A high selectivity of a gyro-multiplier is caused not only by the frequency synchronization, but also by a spatio-temporal structure of electron bunches fixed by the LF wave. The latter imposes some limitations on the HF mode. In the case of an azimuthally-symmetrical microwave system and phase-mixed electron beam, the following relations for azimuthal indices of the LF and HF modes, as well as for numbers of cyclotron harmonics for these modes take place:

$$m = nm_1\,,\ s = ns_1\,. \tag{5}$$

Having used Eqs. (4), (5) and conditions of the cyclotron resonance between electrons and the waves

$$\omega \approx s\omega_B + hv_z,\ \ \omega_1 \approx s_1\omega_B + h_1 v_z\,, \tag{6}$$

one can also find relations between the axial wavenumbers, h and h_1 (the approximate character of Eqs. (6) is caused by a finite length of the interaction region). For a uniform magnetic field

$$h \approx nh_1\,. \tag{7}$$

For instance, in the case of a near-cutoff LF modulating signal ($h_1 << k_1$) the high-harmonic HF wave also should be near-cutoff ($h << k$). However, condition (7) is absent in the case of a profiled magnetic field, when resonance conditions (6) for the two waves are provided at different parts of the interaction region and different values of the magnetic field.

The LF modulation of the electron beam can be provided either by an external RF signal [21, 26, 27] or by a signal excited by the same electron beam. In the first case, the gyro-multiplier is analogous to the gyro-klystron. According to simulations [26], the multiplier with an external LF signal can provide a high efficiency and an improved selectivity as compared to a simple high-harmonic auto-oscillator. However, the optimal electron current for such a multiplier is close to the HF starting current in the auto-oscillator regime, when the input LF signal is absent. Correspondingly, at relatively low voltages, high-efficiency regimes can be achieved only at relatively low factors of frequency multiplication. In a more realistic case, when the current is significantly lower than the optimal value, the multiplier efficiency is proportional to the current and significantly lower compared to the case of the auto-oscillator.

In spite of their attractiveness, gyro-multipliers have been studied in a small number of experimental works, as their realization is complicated by a number of factors. In particular, one can mention here spurious excitation of the output cavity, which can take place for a pre-bunched beam even if the operating frequency is far from the cavity eigenfrequency. In addition, the use of multi-axis beams in gyro-klystron experiments leads to a weak electron-wave coupling at high cyclotron harmonics and to a large radius of the drift region, which makes possible the spurious low-frequency excitation of the whole gyro-klystron.

Suppressing low-frequency oscillations can be based on enhancement of the operating high-harmonic component of the electron current,

$$\rho_n = \left\langle e^{in\theta} \right\rangle \tag{8}$$

and simultaneous depression of the electron bunching at low harmonics [29, 37, 38]. In Eq. (8), θ is the electron phase with respect to the modulating LF signal, and <...> denotes averaging over the whole electron ensemble. If phases of all electrons are mixed uniformly over the interval $[0, 2\pi)$, then $\rho_n = 0$, whereas $|\rho_n| = 1$ corresponds to the "ideal" electron bunch. In the case of a short modulating cavity, the evolution of electron-current harmonics is described by the "klystron" formula

$$|\rho_n(z)| = J_n(n\chi z), \tag{9}$$

where factor χ is proportional to the amplitude of the modulating LF wave (Fig. 4*a*). Similar to the conventional klystron, the operating harmonic in the output cavity can be increased by the use of additional cavities inside the drift region, which are excited at low harmonics [29, 37]. The additional cavities significantly improve electron bunching at the high operating harmonic and depress low harmonics [37]. Forming a special axial structure of the RF field inside the first cavity can provide bunching only at selected harmonics [38].

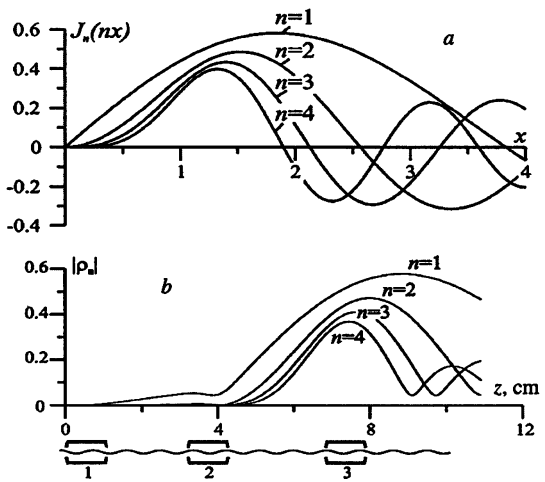

Fig. 4. Klystron-type gyromultipliers. Dependence of electron-current harmonics on the axial coordinate in the drift region of a gyromultiplier with a short input cavity (*a*), and results of simulations of a three-cavity gyro-multiplier operated at the 4th cyclotron harmonic (*b*).

Similar to LOGs, the use of axis-encircling electron beams is attractive in gyro-multipliers. It provides maximal electron-wave coupling at high cyclotron harmonics, improves the selectivity, and allows the use of a small-radius drift region. The latter leads to a good electrodynamical isolation of the cavities and, therefore, helps to avoid self-excitation of the long system of the multiplier. At the same time, as compared to LOGs, gyro-multipliers can operate at a significantly lower electron current that simplifies formation of electron beam.

Let us consider an example of a three-cavity sub-THz gyro-multiplier (Fig. 4*b*) with a low-current (0.1 A) weakly-relativistic (30 kV) electron beam (pitch-factor is equal to 1.2) and a CW low-power orotron (150 GHz, 100 mW) [39] used as a source of the input rf signal. In the first cavity, the $TE_{1,3,1}$ mode interacts with the electrons at the fundamental cyclotron resonance. In the second cavity, the modulated electron beam excites the same mode, $TE_{1,3,1}$; this provides an additional electron modulation, accelerates the electron bunching and helps to reduce significantly the length of the drift region. According to simulations, such scheme can provide fairly high power of 1 and 0.1 W, respectively, at the frequencies 0.6 and 0.75 THz when the output cavity is excited by the 4th or 5th harmonic of the electron current.

A different gyro-multiplier scheme, namely, a self-exciting two-wave oscillator [40–42], is especially attractive in the THz frequency range. In this scheme, both LF and HF waves are excited by the same electron beam. In a klystron-type multiplier, this scheme can be realized by using the auto-oscillator regime of the input cavity. However, such scheme can operate only when the electron current just slightly exceeds the starting current of the input cavity because high current harmonics increase with the axial coordinate faster and saturated earlier than the fundamental one (Fig. 4*a*). If the first cavity operates as a saturated fundamental-harmonic oscillator, then higher current harmonics are also saturated inside this cavity, so that their amplitudes in the output cavity are very small. As an example, one can mention the experiment with a gyromultiplier [43], where a multi-axis electron beam (24 kV and 0.3 A) excited two gyrotron cavities at the fundamental and third harmonics, respectively. The output power amounted to 30 W at the frequency of 285 GHz. A relatively low efficiency was possibly caused by a poor electron bunching inside the second cavity.

An additional disadvantage of the two-cavity scheme of the self-exciting gyro-multiplier is a strict requirement to synchronization of eigenfrequencies of the two high-Q cavities:

$$\frac{\omega - n\omega_1}{\omega} < \frac{1}{Q} + \frac{1}{Q_1},$$

where Q_1 and Q are the Q-factors of the cavities. This problem is additionally complicated by the fact, that one should provide the synchronization of the "hot" eigenfrequencies.

A possible mitigation of these problems is to provide both LF and HF interactions inside a single cavity [40–42]. In this case, the high harmonic is emitted from an optimally bunched electron beam and the system is less sensitive to manufacturing errors. However, there is still a problem of frequency synchronization of two modes inside a single cavity. In the case of a uniform magnetic field, the spectrum of operating modes is limited by conditions (4)–(7). Let us take into account that the spectrum of eigenmodes of a cavity with the circular cross-section is non-equidistant. Correspondingly, co-generation of two gyrotron modes is possible only at determined factors of the frequency multiplication, n,

and minimal possible factor is quite high, $n = 5$. In this case, the exact synchronization of "cold" frequencies of the two modes is provided, when the cavity length is relatively short (so that it is close to the starting value). The situation is complicated by the fact that since "hot" eigenfrequencies are sensitive to the magnetic field, their synchronization is achieved in very narrow (~0.1 %) magnetic field band.

The situation is slightly simplified for co-generation of a gyrotron LF wave and a traveling HF wave, when the latter has a small group velocity. Such a possibility arises in a short cavity due to the approximate character of resonance conditions (6) (which corresponds to a finite length of electron bunches). The difference in group velocities leads also to a possibility to close the LF wave inside the cavity, and, therefore, to separate the radiation of the two waves. In this case, the LF mode has a high Q-factor and can be excited in a short cavity. Such system allows frequency multiplication with $n = 2$ and $n = 6$. The first case is especially attractive, when the LF wave is excited at a high cyclotron harmonic.

The use of magnetic field profiling allows realizing of any factor of the frequency multiplication. In this case, the choice of pair of the operating modes is not limited by condition (7), as the cyclotron resonance is provided for different modes in different parts of the interaction region. In particular, a klystron-like interaction of electrons with the LF wave can be organized in the case of a two-step profile of the magnetic field, when the resonance with this wave is provided at input and output parts of the cavity (Fig. 5), which operate similar to the modulating and output cavities of a klystron. The middle (non-resonant) part of the cavity corresponds to the drift region of such LF "klystron"; simultaneously, this part can be used for the HF-wave generation.

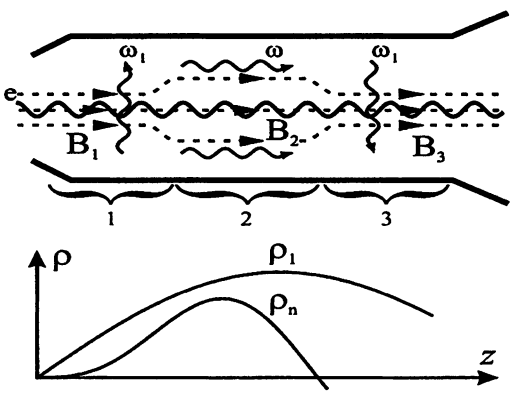

Fig. 5. Schematic of a single-cavity gyro-multipier with the "klystron-like" profiled magnetic field

Another method allowing an arbitrary multiplication factor is deformation of cavity cross-section. For instance, this can be done by periodic azimuthal

2 m-fold corrugation of cavity wall. Such a corrugation cancels frequency degeneration of all the modes with azimuthal index $m \neq 0$, splitting them in two azimuthally-standing waves with up- and down-shifted frequencies (Fig. 6). Choosing the corrugation amplitude one can regulate the value this frequency shift and satisfy all the conditions (4)–(7) for the LF and one of the split HF waves. It should be nevertheless mentioned that the price for such mode synchronization is halving of electron-wave coupling. On the other hand, the described cavity geometry provides the simple separation of LF and HF output waves. Indeed, since these waves have different group velocities when radiated into circular waveguide, one can choose such a narrow output waveguide that only HF wave propagates through it, whereas the LF wave is closed inside the cavity. This approach helps to modify the described above scheme with frequency doubling, so that interaction at both low and high harmonics took place with near-cutoff modes, which increases the efficiency of generation.

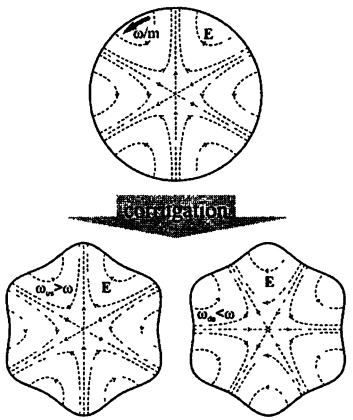

Fig. 6. Splitting of the $TE_{m,p}$ mode in the 2 m-fold azimuthally-corrugated cavity into two modes with up- and down-shifted eigenfrequencies, ω_{us} and ω_{ds}

In a modeling mm-range experiment having been carried out in IAP such a scheme with 8-fold corrugated cavity provides generation at the 4th cyclotron harmonic (mode $TE_{4,3}$, 75 GHz) using the axis-encircling 60 kV / 5 A electron beam. A rotating 2nd-harmonic mode ($TE_{2,2}$, 37.5 GHz) is used as the self-exciting LF wave. In the experiment, this LF wave is excited in a relatively wide range of magnetic field and accelerating voltage, whereas HF generation is observed only in a narrow sub-range of parameters. Evidently, this occurs when doubled "hot" LF frequency strikes in HF resonance. Together with the fact that the output HF radiation pattern corresponds to the $TE_{4,3}$ wave this confirms the realization of the described generation mechanism. It should be noted, that the starting current of the mode $TE_{4,3}$ in the cavity is 300 A, whereas the operation current is 60 times lower. At the first experiment, the output HF power measured by calorimeter amounts to 100 W.

References

1. *Bratman V. L., Suvorov E. V.* // Strong Microwaves in Plasmas: Proc. 6th Int. Workshop. Nizhny Novgorod, 2006. P. 76.
2. *Bratman V, Glyavin M., Idehara T. et al.* // Int. Journ. IEEE Trans. Plasma Sci. 2009. V. 37, is. 1. P. 36.
3. *Golant M. B., Alekseenko Z. T., Korotkova Z. S. et al.* // Prib. Tekh. Eksp. 1969. № 3. P. 231.
4. Clinotrons / ed by Usikov A. Ya. Kiev: Naukova Dumka, 1992 (in Russian).
5. *Steer B., Hyttinen M, Roitman A. et al.* // Strong Microwaves: Sources and Applications: Proc. 7th Int. Workshop. Nizhny Novgorod, 2009. P. 498–502
6. *Rusin F. S., Bogomolov G. D.* // Proc. IEEE. 1969. V. 57, № 4. P. 720.
7. Diffraction radiation generators / ed. by Shestopalov V. P. Kiev: Naukova Dumka, 1991 (in Russian).
8. *Deacon D A G., Elias L. R., Madey J. M. J. et al.* // Phys. Rev. Lett. 1977. V. 38. P. 892
9 *Gaponov A. V., Petelin M. I., Yulpatov V. K.* // Radiophys. Quantum Electron. 1967, V. 10. P. 794.
10. Gyrotron / ed. by Gaponov A. V. Gorky: Institute of Applied Physics, 1981 (in Russian).
11. *Nusinovich G. S.* Introduction to the Physics of Gyrotrons. Baltimore: Johns Hopkins University Press, 2004.
12. *Zaitsev N. I., Pankratova T. P., Petelin M I, Flyagin V. A.* // Radio Eng. and Electronic Phys. 1974. V. 19, № 5. P. 103.
13. *Flyagin V. A., Luchinin A. G, Nusinovich G. S.* // Int. J. Infrared Millimeter Waves. 1983. V. 4. P. 629.
14. *Spira-Hakkarainen S, Kreischer K. E., Temkin R J.* // IEEE Trans. Plasma Sci. 1990 V. 18. P. 334.
15. *Idehara T., Brand G. F.* Submillimeter wave gyrotron development and applications. Fukui University, printed by EXIT Co., LTD, 1995.
16. *Glyavin M. Yu., Luchinin A. G., Golubiatnikov G. Yu.* // Phys. Rev. Lett. 2008. V. 100. P. 015101.
17. *Idehara T., Saito T., Mori H et al.* // Int. J. Infrared and Millimeter Waves. 2008. V. 29. P. 131.
18. *Zapevalov V. E., Zarnitsyna I G., Nusinovich G. S.* // Radiophys. Quantum Electron. 1979. V. 22, № 3. P. 254.
19. *Antakov I I., Zapevalov V. E, Pankratova T. B., Tsimring Sh. E.* // in [10]. P. 192.
20. *Nusinovich G. S., Pankratova T. B* // in [10]. P. 169.
21. *Jory H.* Investigation of electronic interaction with optical resonators for microwave generation and amplification. R&D Tech. Report, Varian Associates, Paolo Alto, CA, ECOM-01873-F, 1968.
22. *McDermott D. B., Luhmann N C., Kupiszewski Jr. A., Jory H. R.* // Phys. Fluids. 1983. V. 26. P. 1936.
23. *Lawson W., Destler W. W., Striffler C. D.* // IEEE Trans. Plasma Sci. 1985. V. 13. P. 444.
24. *Bratman V. L., Fedotov A. E., Kalynov Y. K. et al.* // IEEE Trans. Plasma Sci. 1999. V. 27. P. 456.
25. *Zhurakhovskiy V. A* Nonlinear electron oscillations in magneto-guided beams. Kiev: Naukova Dumka, 1972 (in Russian).
26. *Belousov V. I., Ergakov V. S., Moiseev M. A.* // Elektronnaya Tekhnika Ser. 1. Elektronika. 1978. № 9. P. 41 (in Russian).
27. *Hirshfield J. L.* // Phys. Rev. A, 1991. V. 44. P 6845.
28. *Guo H., Chen S. H., Granatstein V. L. et al.* // Phys. Rev. Lett 1997. V 79. P. 515.
29. *Nusinovich G. S, Dumbrajs O.* // Phys. Plasmas. 1995. V. 2. P. 568.
30. *Aleksandrov A. F., Vlasov A. N., Galuzo S. Yu. et al.* // Relativistic HF Electronics. Gorky, Russia: Inst. Appl. Phys., 1983, Is. 3. P. 96 (in Russian).
31. *Bratman V. L., Kalynov Yu. K., Manuilov V. N., Samsonov S. V.* // Radiophys. Quantum Electron. 2005. V. 48, № 10–11. P. 731.
32. *Bratman V. L, Kalynov Yu. K, Manuilov V. N., Samsonov S. V.* // Tech. Phys. 2005. V. 50, № 12. P. 1611.
33. *Rhee M. J., Destler W. W.* // Phys. Fluids. 1974. V. 17. P. 1574.
34. *Gallagher D., Barsanti M., Scafuri F., Armstrong C.* // IEEE Trans. on Plasma Sci 2000. V. 28, № 3. P. 695.
35. *Bratman V. L., Bandurkin I. V., Dumesh B S. et al.* // High Energy Density and High Power RF. AIP Conf. Proc. 2006. V. 807. P. 356.

36. *Bratman V. L., Idehara T., Kalynov Yu. K. et al.* // Int. J. Infrared Millimeter Waves. 2006. V. 27, № 8. P. 1063.
37. *Bandurkin I. V., Savilov A. V* // Tech. Phys. Lett. 2007. V. 33, № 9. P. 795.
38. *Bandurkin I. V., Savilov A. V.* // Phys. Rev. ST Accel. Beams. 2005. V. 8. P. 010702.
39. *Bratman V. L., Gintsburg V. A., Grishin Yu. A. et al.* // Radiophys. Quantum Electron. 2006. V. 49, № 11. P. 866.
40. *Bandurkin I. V., Bratman V. L., Denisov G G. et al.* // Terahertz Science and Technology. 2008. V. 1, № 3. P. 169.
41. *Bandurkin I. V., Bratman V. L., Savilov A. V.* // Tech. Phys. Lett 2006. V. 32, № 1. P. 84.
42 *Bandurkin I. V., Bratman V. L., Denisov G. G., Savilov A. V.* // Strong Microwaves in Plasmas: Proc. 6th Int. Workshop. Nizhny Novgorod, 2006. P. 156.
43. *Antakov I. I., Gachev I. G., Denisov G. G. et al.* // Strong Microwaves in Plasmas: Proc. 6th Int. Workshop. Nizhny Novgorod, 2006. P. 162.

THE 10 MW, CW, ECRH-PLANT FOR W7-X: STATUS AND HIGH POWER PERFORMANCE

V. Erckmann[1], P. Brand[2], H. Braune[1], G. Gantenbein[3], W. Kasparek[2], H. P. Laqua[1], C. Lechte[2], N. B. Marushchenko[1], G. Michel[1], M. Thumm[3,4], Y. Turkin[1], M. Weissgerber[1], and the W7-X ECRH- teams at IPP Greifswald[1], IPF Stuttgart[2] and FZK Karlsruhe[3]

[1]Max Planck Institut für Plasmaphysik, EURATOM Association, Teilinstitut Greifswald, D-17491 Greifswald, Germany
[2] Institut für Plasmaforschung, Universität Stuttgart, D-70569 Stuttgart, Germany
[3] Forschungszentrum Karlsruhe, Association EURATOM-FZK, IHM, Hermann-von-Helmholtz-Platz 1, D-76344 Eggenstein-Leopoldshafen, Germany,
[4] Universität Karlsruhe, IHE, D-76131 Karlsruhe, Germany

ECRH is the main heating system for steady state operation of W7-X. A heating power of 10 MW with CW-capability at 140 GHz is required to meet the scientific objectives. The different heating- and current drive scenarios, which support W7-X operation at various magnetic fields and in different density regimes are briefly reviewed. The necesssary in-vessel components as well as the day-one set of diagnostics for rf-beam control and plasma absorption is presented. The ECRH power is generated by 10 gyrotrons with 1 MW power each. Integrated high-power CW tests of the transmission system including all optical elements except the launcher were performed and first results are presented.

1. Introduction

W7-X is the next step in the Stellarator approach towards magnetic fusion power plants. Stellarators have inherent steady state operation capability, because the confining magnetic field is generated by external coils only. W7-X is being built with superconducting modular coils, which generate the optimized 3-D magnetic field, and a continuously operating ECRH system. An actively pumped divertor with 10 MW heat removal capability for stationary particle and energy control will be installed after an initial exploration phase using a divertor with inertial cooling in pulsed operation. An ECR-heating power of 10 MW is required to achieve reactor relevant plasma parameters [1] at the design magnetic field of 2.5 T. The status of the gyrotron delivery and tests is reported in ref. [2], this volume, and will not be discussed here. Operation at lower magnetic field B is of interest in the commissioning phase of W7-X, and for physics studies, because B is a key parameter for confinement and high-ß operation. Experimental results on Gyrotron operation at reduced frequency are presented in Section 2, operation scenarios at nominal and reduced frequency are discussed in Section 3 together with the required in-vessel structures. Integrated high power tests of the transmission line are reported in Section 4.

2. Two-frequency operation

The W7-X gyrotrons are optimized for single frequency operation at 140 GHz [3]. The gyrotron diamond window has a resonant thickness of $4\lambda/2$ at 140 GHz and is also transparent at 105 GHz corresponding to $3\lambda/2$. Two modes, the $TE_{21,6}$ (103.6 GHz) and $TE_{22,6}$ (106.3 GHz) exist in the vicinity of the desired frequency. Both modes could be exited by proper tuning of the resonant magnetic field and by adjusting the operation parameters (I_{beam} = 40 A and U_{acc} = 62 kV). We have focused on the $TE_{21,6}$ mode operation, because the output beam was almost perfectly centered on the output window, whereas the beam from the $TE_{22,6}$ mode was located somewhat off center. A maximum output power of about 0.52 MW was achieved without collector voltage depression corresponding to an efficiency η = 21 %, which is compatible with the theoretical prediction. The output power drops with increasing depression voltage while the efficiency increases from 21 to 27 %. The corresponding collector loading at 0 and 8 kV depression voltage is 1.9 and 1.7 MW, respectively, which is incompatible with the collector-loading limit of 1.3 MW. Thus only operation with reduced beam current around 34 A (about 400 kW) can be handled safely by the collector. The RF-beam was transmitted through 7 mirrors of the quasi-optical transmission line into a calorimetric CW-load. Transmission losses of about 20 kW were measured, which compares well with the transmission loss fraction at 0.9 MW, 140 GHz operation. It is worth noting, that both the beam matching mirrors as well as the set of polarizers can be used without modification. Assuming, that all series gyrotrons behave similar to the prototype, ECRH for W7-X will be operated as a two-frequency system with a total source power of 4 MW at 104 GHz. The operation range of experiments can then be extended towards the resonant magnetic field of 1.86 T (X2 and O2 mode) and 1.25 T (X3 mode), respectively. The total operation space with X2, O2 and X3-mode as well as mode conversion heating with electron Bernstein waves (EBW) for both frequencies is sketched in Fig. 1.

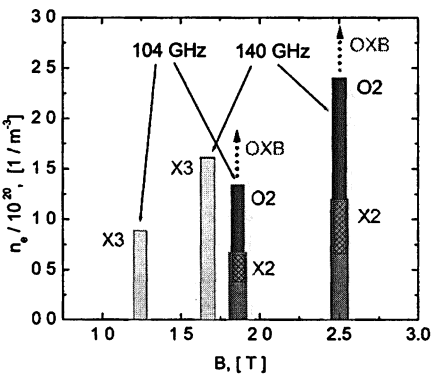

Fig. 1. Accessible Plasma density as a function of the magnetic field for both ECRH-frequencies at W7-X and different operation modes (second (X2) and third (X3) harmonic extraordinary mode and second (O2) harmonic ordinary mode. Electron Bernstein Wave heating via the OXB-mode conversion process is also indicated.

3. Operation scenarios and in-vessel components

The ECRH at W7-X has to fulfill many different requirements such as plasma start-up, heating and current control at different resonant magnetic fields. For plasma start-up and operation at low to intermediate density ($< 1.2 \cdot 10^{20}$ m^{-3}) heating with the second harmonic X-mode (X2) at 140 GHz is foreseen. This is a very robust scenario with almost complete single pass absorption up to the cut-off density. At low density an electron temperature exceeding 10 keV is calculated [4]. The heating power of 10 MW is expected to be sufficient to sustain a plasma at $1.0 \cdot 10^{20}$ m^{-3} with a central electron temperature of about 4 keV. Efficient divertor operation, however, may require an operation density well above the X2-cutoff density. In this range second harmonic O-mode heating (O2) with a operation density up to $2.4 \cdot 10^{20}$ m^{-3} is foreseen [4, 5]. In contrast to X2-heating the O2 single pass absorption is incomplete and 50–90 % are expected depending on density and temperature in the absorption region. A similar situation is found for X3-heating at $B_{res} = 1.66$ T, where $n_e < 1.6 \cdot 10^{20}$ m^{-3}, which is a promising scenario for operation at reduced magnetic field. An example for X3 single-pass absorption calculations with 10 MW input power is shown in Fig. 2 (left). The related electron- and ion temperatures resulting from the assumed transport model [4] are also shown.

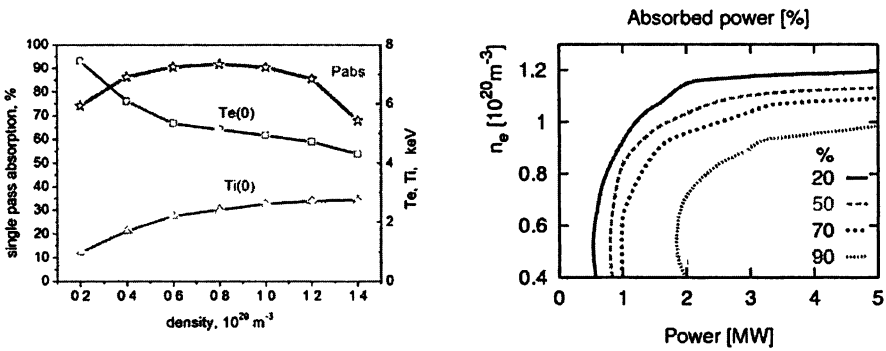

Fig. 2. *Left*: X3 Single-pass absorption P_{abs} at 140 GHz from ray-tracing calculations as a function of the plasma density. The central electron and ion temperatures $T_e(0)$, $T_i(0)$ are also shown. *Right*: O2 Triple-pass absorption at 104 GHz. Contours of constant absorbed power (in %) as a function of plasma density n_e and ECRH-power.

As the gyrotrons operate also at 104 GHz, the contours of constant absorbed power after three passes through the plasma are plotted for the O2 mode ($B_{res} = 1.89$ T) in Fig. 2 (right). An interesting operation regime with an absorption exceeding 90 % exists despite the reduced available power and the low magnetic field. The calculated electron temperatures range from 3.5 to 5 keV, depending on density and heating power.

Once plasma start-up could be achieved with the X3-mode, which is not clear yet, operation at 1.25 T is also of interest, because ECRH could then provide a target plasma for further heating with NBI for high-ß physics studies, which is most promising at low magnetic field.

The non-absorbed part of the ECRH beams in the O2 and X3 scenarios would, however, thermally overload the graphite tiles at the heat shield, which is installed at the inboard vacuum vessel wall opposite to the ECRH antennas. Therefore several selected graphite tiles will be replaced by specially shaped tiles made of a molybdenum alloy with small amounts of titanium and zirconium (TZM). These molybdenum reflectors have to sustain a microwave power of 0.5 MW on a surface of 120 cm^2 each in the worst case for O2 and X3 heating scenarios. High power tests (0.5 MW) of a prototype tile mounted on the original W7-X cooling structure showed an absorbed power fraction of 0.3 %, which is consistent with the theoretical value deduced from the material properties. With the resulting thermal load of 1.5 kW the tile reached a steady state temperature of 470 °C at the surface and 390 °C at the cooling plate, respectively, after 200 s for the maximum loading, which is acceptable for W7-X operation.

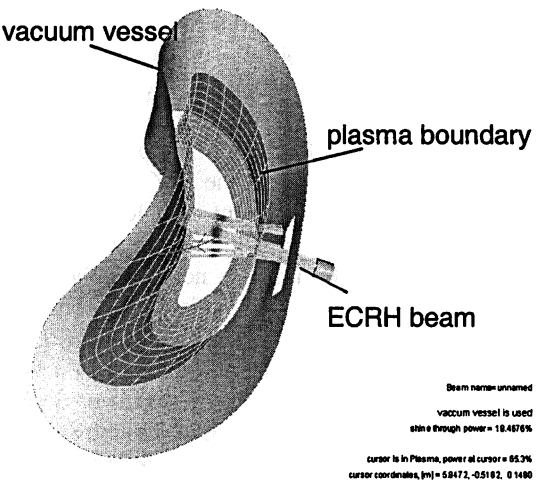

Fig. 3. Example of a three-pass ray tracing calculation for a beam with O2-mode polarization. The vacuum vessel is sketched together with the outer plasma contour and one selected ECRH beam.

These tiles reflect the beams in a well defined way for a second pass through the plasma center onto a water cooled stainless steel reflector panel at the outboard side of the vessel. This reflector will provide a third pass through the plasma as sketched in Fig 3. The ray tracing results as plotted in Fig. 2 (right) are

based on this geometry taking into account the individual launching position for each beam. The total absorption is substantially increased but for the expense of the beam steering capability. The same reflector system can be used for the X3 heating. The launch angle for both heating scenarios is about 12° at the most elongated plasma cross-section position. The beam deflection by plasma refraction is below 3 cm at the tiles, which can be easily compensated by the movable antennas.

Although strong ECCD is not needed in stellarators to generate the confining magnetic field and NTM stabilization is not an issue either, the control of the divertor strike point position requires the control of the edge rotational transform. In addition it should be taken care that the iota profile does not approach major low order rational resonances. Therefore ECCD will be used for residual bootstrap current [6] compensation and rotational transform control on a transient time scale. For long time scales (< 100 s) the iota can in principle be controlled by the coil system. Up to 300 kA current can be driven in the low-density branch at $1.0 \cdot 10^{19}$ m^{-3} by ECCD with the installed power of 10 MW and X2 heating. Even at $1.0 \cdot 10^{20}$ m^{-3} an ECCD current of up to 130 kA was estimated, which is sufficient to compensate the expected bootstrap current of about 80 kA.

A major challenge is the development of experimental operation scenarios, where the slowly developing bootstrap current is continuously compensated by external current drive. The ECCD capability in the O2-mode will not be sufficient to compensate the bootstrap current for all magnetic configurations and densities. Therefore scenarios have to be developed, where the expected steady state plasma current is already embossed by X2-ECCD during plasma start-up and density ramp up. With increasing bootstrap current the ECCD will be reduced until the current is taken over by the bootstrap current completely. The X2 polarization will then be tuned into O2 and continuous high-density operation will be established maintaining a plasma equilibrium with non-zero plasma net current. For operation at ultra high density above the O-mode cutoff density Bernstein wave heating via the OXB-mode conversion process is envisaged [7]. The transmission line and the equatorial port in-vessel antennas are designed to provide the required optimal launch angle of 55° with respect to the magnetic field direction.

The design of the front steering ECRH-antennas in the A- and E-type ports is compatible with full power CW requirements. Four antenna blocks are under construction and each block can handle 3 RF-beams (altogether 10 beam lines plus two spare for a possible later upgrade) as shown in Fig. 4 (top). The movable mirrors enable a poloidal steering range of ±25° and a toroidal steering range between ±15° and ∓35°, which complies with all relevant operation scenarios. The critical components like the ceramic bearings and the flexible tube spirals for the cooling water supply have been already successfully tested in a mechanical mock-up under vacuum conditions and in ECRH stray radiation environment. The mirror design is similar to the well-proven transmission line type. Most of the

antenna components are already manufactured and the assembly has started as seen from Fig. 4 (bottom).

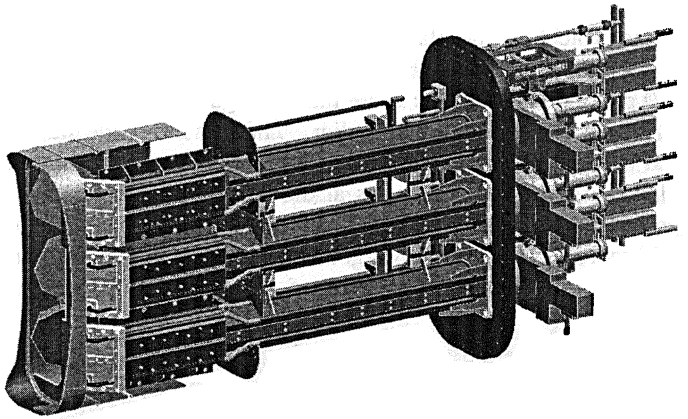

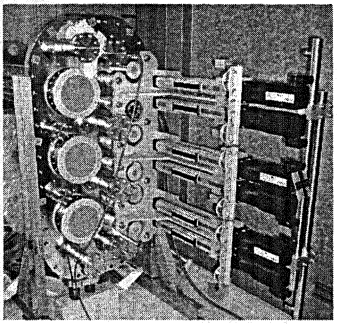

Fig. 4. The ECRH plug in antenna block. Top: CAD drawing. Bottom: Main flange with motor drives during assembly.

Two additional ports (N-type) are foreseen for special ECRH physics experiments with two RF-beams (2 MW). Here the beams are launched from the high field side and propagate along B = const surfaces, which allows the investigation of wave interaction with particles in different velocity regimes. In particular advanced ECCD scenarios with supra thermal electrons can be investigated by high field side launch. The N-port is also foreseen as the microwave injection port for the collective Thomson scattering diagnostics, because of the availability of neighboring ports with favorable orientation. The N-ports are very narrow and a remote steering scheme [8] will therefore be adopted, which is based on the imaging properties of a square corrugated waveguide. A 'long' solution with a bent waveguide was chosen, which eases the integration of the waveguides and leads to a lower antenna beam divergence because of the increased waveguide cross-section for this solution. This design, however, requires a thorough optimi-

zation of the position of the mitre bend and the vacuum valve in the waveguide. The conceptual design and first optimization calculations are presently being performed.

Reliable ECRH operation requires special ECRH-related diagnostics for both, machine protection and plasma physics. The beam position, the transmitted power and its polarization must be known with high accuracy and will be measured by 120 pick-up antennas (open circular waveguides), which are incorporated in the heat shield tiles as described earlier. These mono-mode waveguide tubes are grouped into four bundles, which run from the inboard side along the vacuum vessel wall towards four B-type ports at the outboard side, where the signal is transmitted through vacuum windows. A prototype of a waveguide bundle, with is pre-bended according to the in-vessel geometry is ready for a test assembly inside the W7-X vacuum vessel and is seen in Fig. 5.

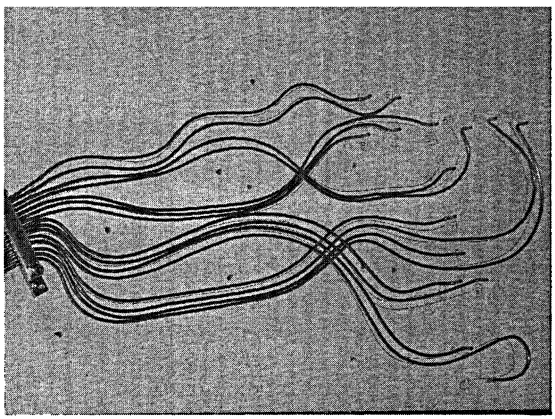

Fig. 5. Pre-shaped waveguide bundle prototype for assembly and routing tests inside the W7-X vacuum vessel.

Any deterioration of the original polarization, which is inferred by the many waveguide bends will be compensated by appropriate phase shifters in close vicinity of the rf-diodes.

The average non-absorbed power will be measured by at least five so called sniffer probes, which are installed in symmetrical poloidal positions in each of the five stellarator modules. These detectors measure the none-absorbed ECRH stray radiation, which is distributed inside the vacuum vessel. The sniffer probe signals will be used to detect any unintended reduction of ECRH absorption in order to avoid machine damage by direct beam irradiation or microwave stray radiation of in-vessel components. In addition it is planned to monitor the heat shield, which is installed at the inner vessel wall opposite to the ECRH antennas by infrared

cameras. An interlock signal will be derived from the thermal measurements, which turn off ECRH in case of local overheating and hot-spots.

4. Transmission line: High-power test results

The transmission line consists of single-beam waveguide (SBWG) and multi-beam waveguide (MBWG) elements. Each gyrotron is equipped with a matched beam conditioning assembly of five single-beam mirrors. Two of these mirrors match the gyrotron output to a Gaussian beam with the correct beam parameters, two others are used to set the appropriate polarization for optimum absorption of the radiation in the plasma. A fifth mirror directs the beam to a plane mirror array, the beam combining optics, which is situated at the input plane of a multi-beam waveguide [1].

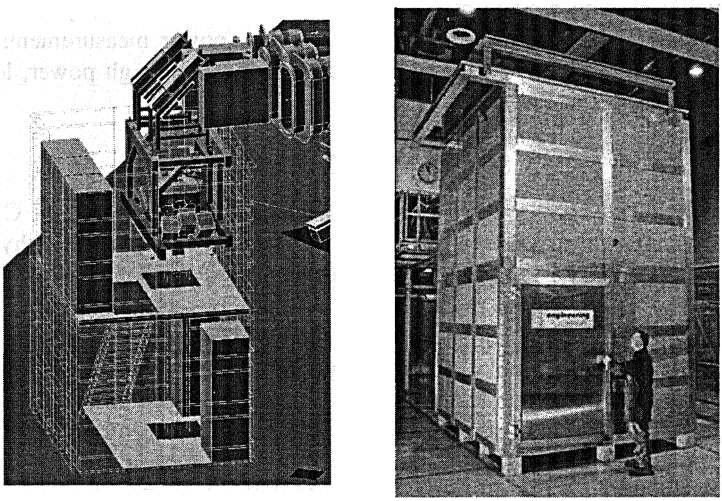

Fig. 6. *Left:* CAD-sketch of the beam distribution optics and control-racks inside the two-storey tower. *Right:* ECRH-tower with microwave absorbing granite-wall structure.

The MBWG is designed to transmit up to seven beams from the gyrotron area (entrance plane) to the Stellarator hall (output plane). A mirror array separates the beams again at the output plane and distributes them via CVD-diamond vacuum barrier windows to individually movable antennas (launchers) in the W7-X torus. Two symmetrically arranged MBWG's are used to transmit the total power.

The beam distribution optics module and the reflectors of type M13 and M14 are installed in two "towers" in front of the W7-X ports as sketched in

Fig. 6 (left). Both two-storey towers have a modular structure and are presently being equipped with the full set of remote control systems and water cooling for the mirrors and launchers. A photo of one tower is seen from Fig. 6 (right), the outer wall is made from granite plates, which serve as absorbers for microwave stray radiation and have a high mass like an optical bench.

Tests of the entire transmission line can only be performed, once the W7-X construction is completed and access to the main torus hall is provided. We have therefore installed retro-reflectors in the underground beam-duct in the image plane at half distance of the MBWG transmission line. Long distance transmission can be simulated and tested by transmitting the high power beams half way in forward direction and then back via the reflectors to the dummy load. First calorimetric high power measurements were performed and total losses of about 3 % were measured for 10 reflections on the 2×3 MBWG-mirrors and the 4 additional guiding mirrors over a total length of about 40 m [9]. Good agreement is found with calculations and previous low power measurements, which confirms the high quality of the quasi-optical concept for high power, long distance transmission.

5. Summary and Conclusion

The ECRH-system for W7-X is the most ambitious and largest CW-plant presently under construction. The system is designed to satisfy the physics demands for stationary heating and current drive at 2nd harmonic with X- and O-mode, 3rd harmonic with X-mode, as well as mode conversion heating in the high density regime with Bernstein modes. The 10 MW, CW ECRH-power is transmitted via a quasi-optical multi-beam waveguide system operating at atmospheric pressure, which is a unique feature of this system. The quasi-optical transmission offers favorable characteristics such as broadband transmission and a large margin for power handling. This allows operation of the system at two frequencies and with the option of a later power upgrade without modification of the transmission line. The most loaded components of the beam conditioning single beam section were tested and the losses were measured. Long-distance transmission through the multi-beam waveguide system was investigated. An excellent performance with low losses close to the theoretical losses was obtained under full power, CW conditions. The in-vessel structure is designed for a controlled 3-pass absorption of the O2 and X3-mode to ensure high total absorption. A set of diagnostics such as pick-up waveguide arrays, IR-cameras and sniffer probes are being prepared for installation in the W7-X vacuum vessel.

References

1. *Erckmann V., Brand P., Braune H., Dammertz G. et al.* Fusion Science and Technology. 2007. Vol. 52, № 2. P. 291–312.

2. *Thumm M., Braune H., Dammertz G., Ercknann V. et al.* 1 MW, 140 GHz series gyrotrons for the W7-X Stellarator // Strong Microwaves: Sources and Applications: Proc. 7th Int. Workshop. Nizhny Novgorod, 2009. P. 84–94.
3. *Damnertz G., Alberti S., Arnold A , Borie E. et al.* IEEE Trans. Plasma Science **30** (2002), 808–818.
4 *Turkin Y., Beidler C.D., Ercknann V., Laqua H.P., Maaßberg H., Marushchenko N.B. and W7-X Team* 34th EPS Conf. on Plasma Phys., Warsaw, ECA. 2007. Vol. 31F, P-1.148.
5. *Rome M., Ercknann V., Gasparino U., Karulin N* Plasma Phys. Control. Fusion **40** (1998), 511–530.
6. *Marushchenko N. B., Ercknann V., Laqua H.P., Maassberg H. and Turkin Y.* 34th EPS Conf. on Plasma Phys., Warsaw, ECA. 2007. Vol. 31F, P-5.129.
7. *Laqua H. P., Ercknann V., Hartfuß H. J., Laqua H., W7-AS Team, and ECRH Group* Phys. Rev. Lett. **78** (1997), 3467.
8. *Plaum B., Gantenbein G., Kasparek W., Schwörer K. et al.* Fusion Science and Technology. 2006. Vol. 50. P. 1–14.
9. *Ercknann V., Kasparek W., Gantenbein G., Hollmann1 F. et al.* Accepted for publ. in Fusion Science and Technology, 2009.

DIAGNOSTIC TESTS, UNUSUAL EXPERIMENTS AND PERFORMANCE ON THE DIII-D GYROTRON SYSTEM

J. Lohr[1], M. Cengher[1], I. A. Gorelov[1], P. B. Parks[1], D. Ponce[1], D. Young[2], P. Johnson[3], and K. Thompson[4]

[1]General Atomics, PO Box 85608, San Diego, California 92186-5608, USA
[2] National Renewable Energy Laboratory, Golden, Colorado, USA
[3] Butler University, Indianapolis, Indiana, USA
[4] University of Wisconsin, Madison, Wisconsin, USA

The gyrotron complex on the DIII-D tokamak now has been completed with the installation of six 110 GHz gyrotrons in the 1.0 MW class. The rf pulse lengths have been limited administratively to 5.0 s at full parameters, 40 A, 80 kV, and over 10.3 MJ per pulse at peak power, ~3.1 MW, has been injected into DIII-D for plasma experiments on a single shot using 5 gyrotrons. The reliability of the gyrotron performance has been 82 % over a three-year period and was 85.5 % in 2008.

A direct high power measurement of the transmission line efficiency has been made. The total efficiency averaged 74 % for the 31.75 mm diam. evacuated corrugated transmission lines carrying the $HE_{1,1}$ waveguide mode past 7 miter bends. Loss in the Matching Optics Unit (MOU) was 3.3–7.9 % and a fairly large loss, ~10 % was measured in the first sections of waveguide after the MOU.

Three materials experiments have been performed using the system. The power from one gyrotron was used to flash anneal amorphous silicon, forming aligned single crystals suitable as nucleation sites for CVD deposition of silicon leading to high efficiency photovoltaic conversion at low cost. A similar annealing of CMOS structures produced improved junctions accessing the 32 nm performance node. Finally, a gyrotron-pumped waveguide loaded with naptha and Ni powder is being used to investigate the possibility of creating high velocity frozen deuterium pellets driven by rapidly expanding gas heated by microwaves.

In this paper we report on the status, history and applications of the 110 GHz six gyrotron system installed on the DIII-D tokamak. The gyrotrons have been used with excellent reliability in a wide range of experiments and the installation has developed into a standard component of the auxiliary heating system on DIII-D, in use on most experimental days. The tubes have injected over 10 MJ on a single plasma shot, with rf pulses up to 5 s in length. The nominal pulse length limit is 10 s, however, as will be discussed later, the calculated collector fatigue lifetime depends not only on the number of pulses but also on their duration, therefore the pulse lengths used in experiments have been limited administratively to 5 s, which is consistent with present experimental requirements. All the tubes except one have been tested to 1.0 MW output. The sixth tube, for reasons believed to be connected with poor electron beam quality from the cathode, was only able to be operated at 750 kW output for 5 s pulses. One of the other tubes is being reconditioned to full power after repair of a vacuum leak.

Three of the gyrotrons, all the tubes in the first production run, experienced collector failures, which now are understood to have been due to excessive power

loading in the collector. New operating procedures and hardware are predicted to extend the collector lifetime to about 50000 pulses 5 s in length, which should be adequate for the long term experimental program on DIII-D.

The gyrotron and power supply installation will be described, including the results of direct measurements of the transmission line efficiencies. Alignment and setup procedures will be presented in connection with the efficiency measurements and system reliability data for the past five years, which demonstrate the high reliability in support of experiments will be shown. The collector failures and remedial steps will be discussed, followed by a description of launcher performance, including damage to one launcher mirror. The change in emphasis of the workshop from focusing on strong microwaves in plasmas to the broader subject featuring both sources and applications will be addressed in descriptions of a number of materials processing experiments, which have been done using the gyrotron installation during times when it was not being used for fusion research. Finally, the long term plans for enhancements to the DIII-D gyrotron installation will be presented.

System Description, Reliability and Transmission Line Efficiency

The gyrotron complex on the DIII-D tokamak has been described previously [1]. There are six gyrotrons, all in the 1 MW class at 110 GHz, which are connected to the tokamak with circular 31.75 mm diameter corrugated evacuated waveguides up to 100 m in length (Fig. 1).

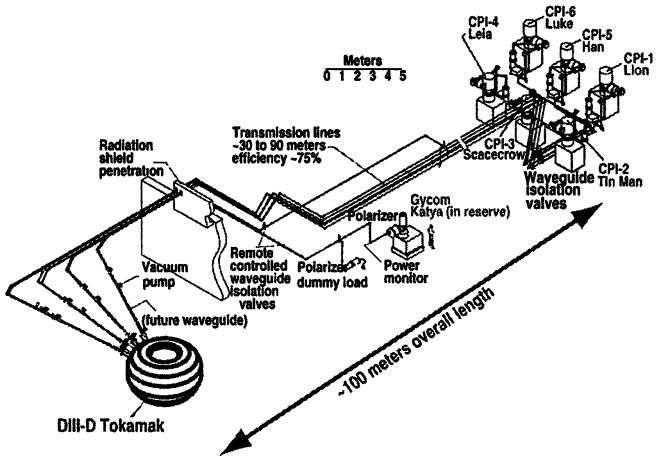

Fig. 1. Isometric layout of the DIII-D gyrotron complex. Six tubes are in operation, injecting >3 MW 110 GHz microwave power into the tokamak over a waveguide line up to 100 m in length with an average of 75 % transmission line efficiency. The long term plan calls for a total of eight gyrotrons, each of which will generate 1.5 MW.

The only window in a line is the gyrotron CVD diamond window. At the tokamak there are three launcher assemblies, each of which can independently direct the beams from two gyrotrons to anywhere in the tokamak upper half plane and ±20° toroidally for current drive.

The gyrotrons are all diode tubes [2] and are powered by vacuum tetrode modulator/regulators that provide a reproducible applied voltage of 80 kV ± 500 V dc and modulation frequencies up to 10 kHz. The power supply configuration is shown schematically in (Fig. 2). Because regulation at precise voltages is com-

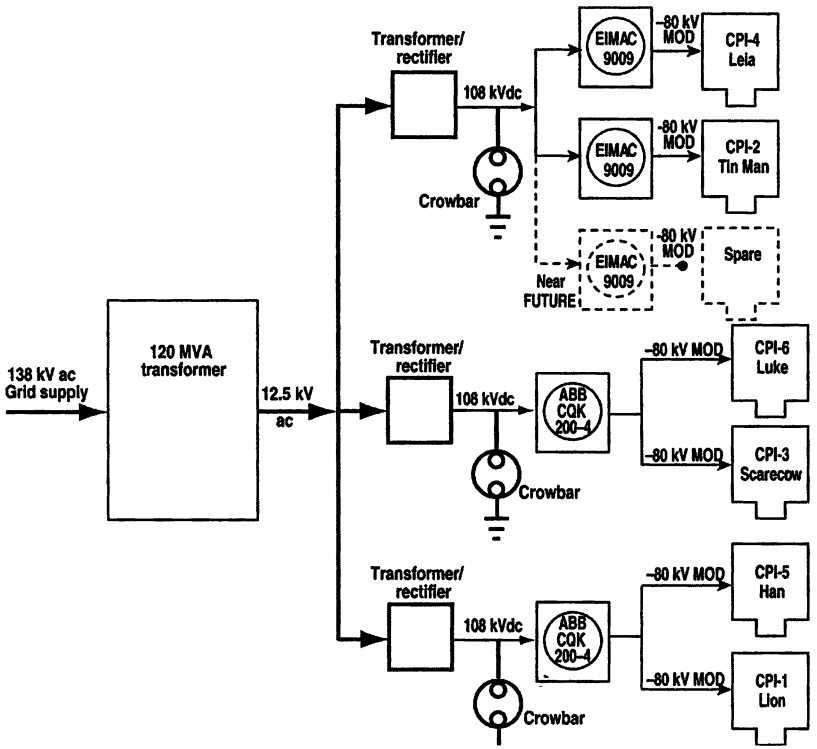

Fig. 2. Schematic diagram of the high voltage power supply system for the DIII-D ECH complex. Vacuum tetrodes are used, driving gyrotrons either singly or in pairs. Ignitron crowbars with microsecond response time and <10 J maximum arc energy protect the gyrotrons.

promised by changes in such factors as ambient temperature, changes in the unregulated kV supply voltage during plasma shots and pulse length, the gyrotrons must be tuned slightly for a given set of experimental conditions. This is done, for example, by making slight changes in the main magnetic field, by adjusting the filament voltage, by adjusting the magnetic field in the gun region or by

boosting the filament voltage at a predetermined time before the gyrotron pulse. Once the tuning is set, the gyrotron operation is rather reliable, achieving an overall average greater than 80 % success rate (defined as the number of times individual gyrotrons produced the pulse length requested divided by the total number of requests) over the past five years (Fig. 3). During acceptance testing the gyrotrons are operated at maximum possible output power, at about 31 % efficiency, and must achieve 10 consecutive 5.0 s pulses at $P_{gen} \geq 1.0$ MW without a fault to be accepted. But for plasma experiments, with changing pulse length requests, varying ambient conditions and uncontrollable pulse repetition frequencies based on experimental exigencies, the gyrotrons are operated with slightly detuned parameters. This is usually done by increasing the main magnetic field by as little as 0.2 % above the value that delivers peak power and reduces the generated power to about 900 kW.

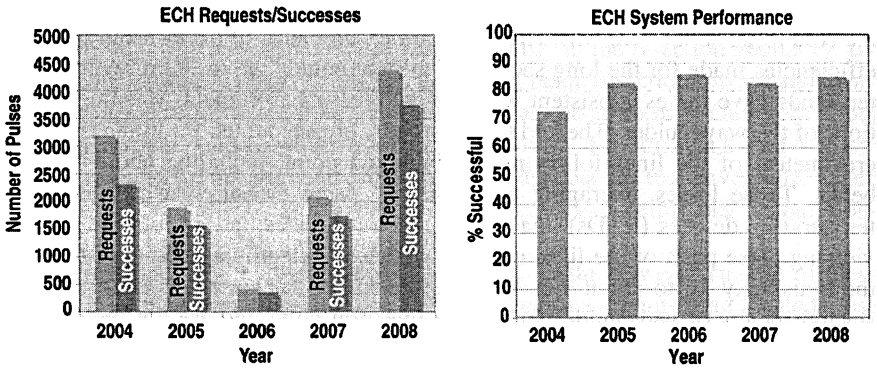

Fig. 3. The ECH system reliability has exceeded 80 % for 4 consecutive years despite the constant upgrades and power supply development. In 2008 there were over 4000 requests for individual gyrotron pulses and over 3500 successful pulses which satisfied the requests. A wide variety of pulse lengths, aiming and modulation combinations were used. The system is a regular part of nearly all experiment plans.

The long-term plan calls for an upgrade to 12 MW generated rf power. Two waveguide lines will be added, bringing the total to eight lines. A systematic replacement of the 1 MW class diode gyrotrons to 1.5 MW depressed collector units, all operating at 110 GHz, will then be accomplished.

During the recent experimental period, gyrotrons were added to the system as they became available and extensive modifications to the power supplies were constantly made, which contributed to lowering the reliability. With groups of two gyrotrons being operated from each of two high voltage power supplies, a fault in either gyrotron of a pair will terminate both gyrotron pulses. This reduces the reliability statistics disproportionately. During the 2008 DIII-D campaign, the gyrotron system was being used in support of experiments on most run days, with

4400 requests and over 3700 successes. The most common fault has been when rf generation stops, particularly for long pulses or when tuning up for modulation. A new fault processing system based on field programmable gate array (FPGA) technology is being installed and will permit retries after many of the common faults, which should improve the reliability.

The rf power delivered from each of the gyrotrons to the tokamak has been measured in a number of ways [3] and is the subject of continuing work to reconcile the theoretical waveguide efficiencies with experimental results. Low power tests on complete lines (Fig. 4) showed that, for a pure $HE_{1,1}$ waveguide mode, the line losses were about –1 dB, or 20 %, in good agreement with a theoretical estimate [4] of –0.84 dB calculated for a line having 12 miter bends with 1.6 % loss per miter. During these measurements, 10 m long sections of the waveguides were subjected to 1 m displacements with no detectable change in transmission efficiency. But for high power, the waveguide losses have been higher than for the cold tests, about –1.25 dB. High power measurements of the transmission line efficiencies made for the long section of the waveguide, up to 90 m, with 10 miter bends gave losses consistent with the cold test measurements on similar sections of the waveguides. The additional losses were accounted for in the first several meters of the lines following the injection point, including about 5 miter bends. These losses, averaging about 80 kW, were measured using resistance temperature devices (RTDs) attached to the waveguides and an infrared camera viewing these parts of the lines covered with black electricial tape used to bring the emissivity up to about 1.0. Because the additional losses occur in the first several meters of waveguide beyond the injection point and are not seen in low power tests when a pure $HE_{1,1}$ mode is excited, mode conversion to lossy modes occurring as a result of imperfect alignment or non-Gaussian content of the injected rf beam is suspected for the losses.

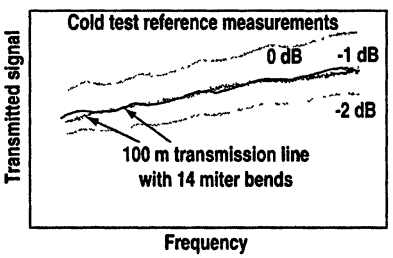

Present Hot Test Measurments			
Gyrotron	MOU loss	Calculated line loss	Total line loss
CPI-3 Scarecrow	3.8%	20.2% (-0.98 dB)	28.3% (-1.45 dB)
CPI-1 Lion	3.3%	20.2% (-0.98 dB)	26.0% (-1.30 dB)
CPI-4 Leia	7.9%	20.2% (-0.98 dB)	30.7% (-1.59 dB)
CPI-5 Han	4.5%	20.2% (-0.98 dB)	21.2% (-1.03 dB)

Fig. 4. Low power tests with pure $HE_{1,1}$ modes gave about –1 dB transmission line efficiency in agreement with theory. High power measurements on four of the systems, on the other hand, showed higher losses of about 0.5 dB, which are believed to be due to mode conversion arising from slight misalignment of the rf beam as it enters the waveguide. The frequency was swept for the low power tests to eliminate possible errors due to resonances.

When a gyrotron is first received, short rf pulses are launched into free space and the power profiles are measured at intervals of about 10 cm for the first meter after the beam exits the gyrotron window. These power profiles are then analyzed by a phase retrieval algorithm [5], which yields not only the mode mixture in the beam, but also the *x-y* offset of the peak of the Gaussian at the gyrotron window and its off-perpendicular propagation direction. Typically these are a few millimeters offset and $\leq 0.5°$ off-perpendicular. In order to place the center of the beam on the axis of the transmission line system, a specially designed spool piece with offset, non-parallel flanges is made, which aligns the beam and the MOU axis. The slight tilt in the whole MOU assembly with respect to horizontal which results from this process is accommodated by making the first 2 or 3 meters of waveguide slightly flexible by corrugating their outer surfaces. The cold tests previously described had shown that a slight bend over this distance made no detectable change in the propagation loss. But the use of a single coupling mirror makes it impossible to achieve complete flexibility in the injection geometry. By translating the single mirror along the original rf beam direction toward and away from the gyrotron it is possible to adjust the beam position in the horizontal, but not the vertical, plane, while tilting the mirror in the horizontal and vertical planes can change the angle at which the beam approaches the waveguide. When the beam is centered on the waveguide, therefore, it is possible that a small non-coaxiality in the vertical plane is present.

Assessment of the alignment is being made in three ways. The 1st of these will be real time measurements of power absorbed in a dummy load located close to the injection point, about 3 m and two miter bends after injection. The dummy load power should be maximized when the beam is well-aligned with the waveguide axis. The 2nd measurement technique uses the power radiated from a gap in the waveguide located at an odd multiple of one quarter of the beat wavelength between $HE_{1,1}$ and $HE_{2,1}$ propagating modes. The beat wavelength, L, in our 31.75 mm diameter waveguides at 110 GHz is 817 mm, therefore the measurement can be made using a waveguide gap power monitor [1] located, for example, at $5L/4$ or 1021.5 mm from the injection point. At this point, a 0.1° off-coaxial injection will result in a 10 % differential in the radiated power in the plane defined by the injected rf beam and the waveguide axis. The third measurement is a variation of the second in which the rf beam is relaunched into free space after propagating an odd multiple of one quarter of the beat wavelength described in the second technique. When the rf is relaunched into free space after traversing several meters of guide, the mode content can be determined using infrared power measurements and phase recovery analysis based on the power profiles. Alternatively, the coaxiality of the rf beam can also be inferred from the location of the beam center at any odd multiple of a quarter of the beat wave-

length from the injection point in free space, again using an infrared camera to locate the center of the rf beam with respect to the waveguide axis.

Using the more standard technique of simply measuring the power in the waveguide lines at two locations separated by long waveguide runs containing 8–10 miter bends, the transmission line efficiencies in Fig. 4 were determined. The losses in the lines measured in hot tests and cold tests are consistent with each other except that in hot tests there is an additional loss of about –0.5 dB, which is indicated by heating of the first few meters of waveguide and the first 4 or 5 miter bends. As discussed above, we believe that this loss arises from slight misalignment of the Gaussian beam at the input to the waveguide. For 31.75 mm diam waveguide at 110 GHz, a transverse offset of 1.0 mm with perfectly co-axial injection will result in 1 % mode conversion from $HE_{1,1}$ and a 0.1° deviation from perfectly co-axial injection with no transverse offset will result in 0.4 % mode conversion [6, 7]. In the real case, the injected rf beam will have a combination of these injection errors making it difficult to determine the exact mode structure, a combination of $HE_{1,1}$ and other modes, which will be excited in the guide. Although some of these modes, the $HE_{2,1}$ for example, will propagate in corrugated circular guide with nearly the same low loss as $HE_{1,1}$, they will lead to additional mode conversion at the first few miter bends in the lines, with heating of the waveguides in both the forward and reflected directions from the miters.

Collector and Launcher Mirror Failures

Initial operation of the 1 MW gyrotrons was done with allowable collector power loading up to 1 kW/cm^2. This loading turned out to be excessive and resulted in fatigue failures of the collectors on the first three gyrotrons placed in service. The electron beam footprint is smallest and the collector power density is highest when the electron beam is low in the collector during axial sweeping. Following the failures, the fatigue calculations were improved, with the result that a reduced standard for allowable collector loading, 600 W/cm^2, was determined. To achieve this, the electron beam was raised about 10 cm in the collector, increasing the footprint; the sweep frequency was increased from 4 to 5 Hz; and the dwell time at the limits of the sweep was reduced by a combination of an increase in the available output voltage of the power supply driving the sweep magnet to 200 V and by employing a sawtooth waveform for the sweeping magnetic field, which opposes the fringing field of the superconducting magnet. The fatigue lifetime is determined both by the number of single pulses and the number of repetitive sweep cycles, both of which contribute to the stress in the collector OFHC copper. Increasing the sweep frequency reduces the stress slightly, while increasing the number of sweep cycles per unit pulse length, resulting in a moderate improvement in lifetime. A direct measurement of the effect of these

measures on the sweeping magnetic field inside the gyrotron is shown in Figs. 5 and 6, indicating in particular that the dwell time at the low point in the sweep is reduced by ≈ 40 %. The new operational procedures have increased the predicted collector lifetime to 50000 pulses 5 s in length.

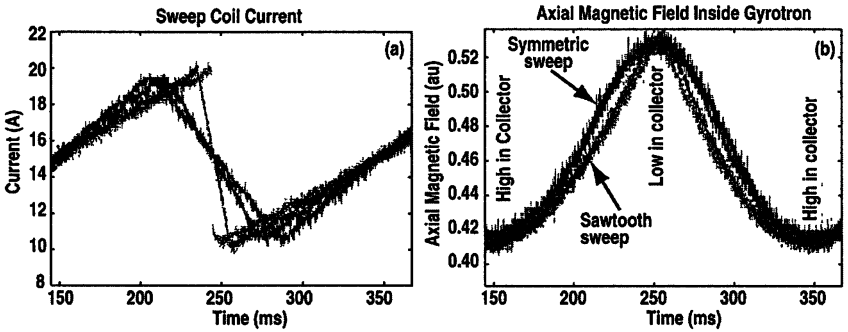

Fig. 5. Changing the sweep coil waveform from symmetric to a sawtooth reduced the dwell time of the electron beam at its lowest point in the collector by about a factor of two.

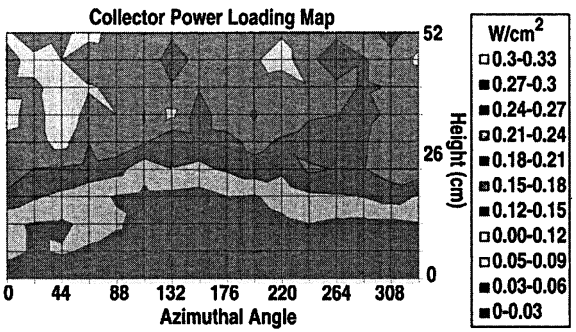

Fig. 6. The electron beam was also raised by about 10 cm in the collector, greatly reducing the power loading where the beam footprint is smallest and the power loading is greatest. The power loading is thus maintained <600 W/cm^2 everywhere in the collector.

The steerable launchers in the DIII-D system have two mirrors on each waveguide line. The rf beam expands from a 62.5 mm diam waveguide and is incident on a weakly focusing mirror at a 45° angle. From this mirror, the beam strikes a flat surface mirror, which can be moved so that the rf beam is directed over a range ±20° horizontally, in the current drive direction, and poloidally over the tokamak upper half plane, which also involves a 40° range of motion. The mirrors are cooled by radiation and conduction without active cooling. The focus mirrors are made from stainless steel with a thin, 0.125 mm, copper overcoating.

The steerable mirrors are made from a multi-layer laminate of stainless steel and copper with a thin copper-reflecting surface. The designs employ stainless steel to add strength and reduce forces during disruptions and copper to reduce resistive heating by the rf beam.

On both of these mirror designs, there is evidence of excessive heating and one of the focus mirrors failed with complete melting of the copper coating and of the stainless steel substrate over a surface area several mm in diameter. The rf power loading on the copper surface is about 100 W/cm^2 but on stainless steel it is about 5300 W/cm^2, so once the copper layer had melted and exposed the stainless steel, further damage was inevitable. Initial damage was noted during a short vent of the tokamak, but when the tokamak was opened for maintenance following a period during which 269 additional rf pulses had been fired on the damaged line, the damage was found to have spread to >1 cm diam and the stainless steel substrate was melted to a depth of 2 mm (Fig. 7). Heating of the steering mirror by plasma radiation is a significant effect [8], but the reflecting surfaces of the focus mirrors are facing away from the plasma and are not heated significantly by radiation. Although a test program leading to 10 s pulse lengths had been planned, the mirror damage necessitated a redesign effort and a delay in pulse extension beyond 5 s.

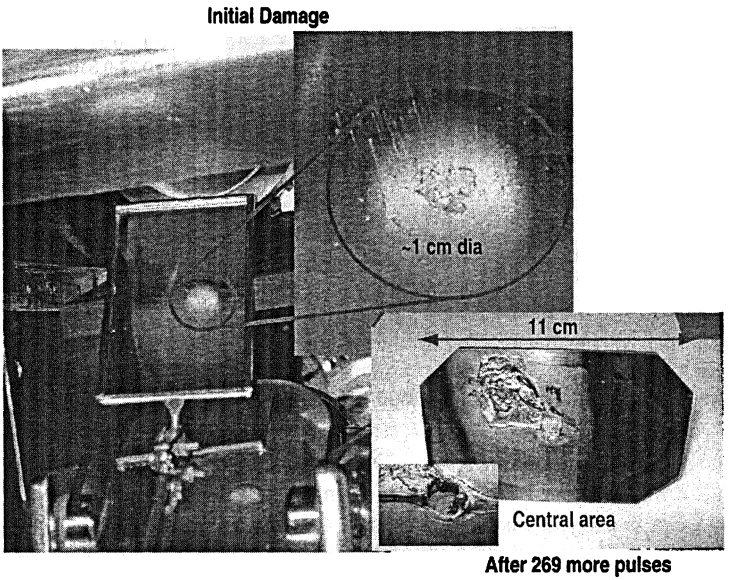

Fig. 7. Photographs of the melt damage to one of the focus mirrors. Once the copper overcoating was breeched, further damage was inevitable. The initial melting was observed in situ using a mirror.

Model calculations revealed that the melt damage could be explained if the braze of the stainless steel mounting stud (Fig. 8) on the back of the focus mirror had formed an incomplete bond to the stainless steel mirror body, thus reducing the conduction away from the center of the mirror. The new design for this mirror will use a Cr-Zr-Cu stud with additional care in making the braze. These measures are predicted to reduce the peak temperature of the mirror surface for 10 s pulses by about 200 °C, to a peak temperature for a 10 s pulse of 820 °C, providing a 200 °C margin against melting the copper.

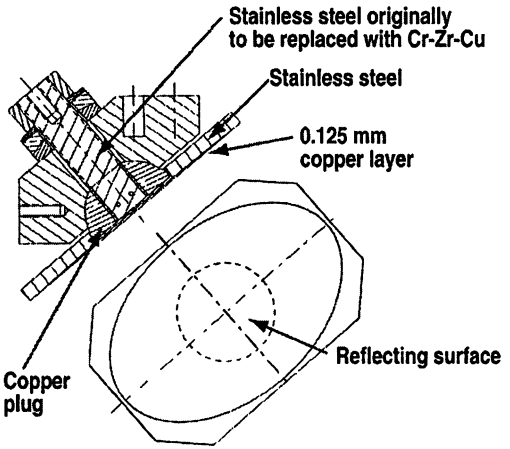

Fig. 8. The focus mirror stainless steel mounting stud will be replaced by Cr-Zr-Cu in the new design.

Microwave Annealing and Heating

Amorphous silicon. The DIII-D gyrotron complex has been used for a number of experiments unrelated to fusion, but which are connected to applications of strong microwaves. The most successful of these have involved rapid heating and crystallization of amorphous silicon leading to improved photovoltaic conversion efficiency and rapid annealing of CMOS structures formed by implantation.

For photovoltaic conversion, high efficiency at low cost is a key factor. Typical solar cells use amorphous silicon on a variety of substrates and have a conversion efficiency of ~8 %. With this efficiency, photo-voltaics cannot compete economically with other sources of electricity except in specific applications where the standalone capability of the cells to provide electricity, such as in remote locations or where power requirements are low, take particular advantage of the unique characteristics of the cells. If crystalline or polycrystalline silicon can be produced economically, the competitiveness of photovoltaics will improve,

since crystalline silicon has approximately twice the conversion efficiency of the amorphous state. We have subjected amorphous silicon layers on glass to rapid heating [9] using 110 GHz high power microwaves from the DIII-D ECH system and formed excellent silicon crystals in squat, egg shaped pillars about 20 μm in diameter distributed over the surface of the glass (Fig. 9). With these pillars serving as nucleation sites for additional CVD deposited silicon, it is possible that a low cost high efficiency solar cell can be fabricated.

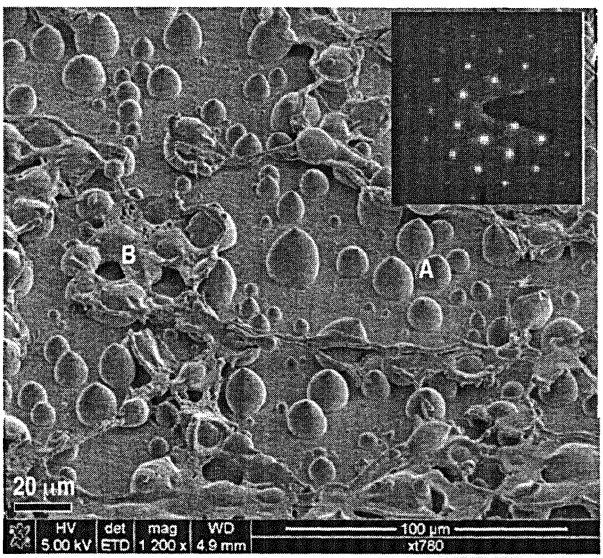

Fig. 9. Sample seen with field emission scanning electron microscopy following microwave annealing. The pillars have very high silicon crystalline quality as verified by the transmission electron microscopy picture shown in the inset. The pillars are about 20 μm in diameter. Target preparation on the glass substrate is indicated in the left side of the figure.

The glass substrates were prepared by coating with a ~120 nm layer of SiO_2 followed by a 1–2 μm thick layer of a-Si:H deposited by hot wire CVD from silane gas at a high rate of 10–100 Å/s. Square samples 2.5 cm on a side were placed in a vacuum chamber where microwave power launched from an open ended waveguide and reflected from a specially designed mirror to provide a flattened power profile irradiated the samples. The power density at the samples was ~40 kW/cm^2 and resulted in rapid heating, at 10^5–10^6 °C/s, of the silicon to melting temperature of ~1450 °C using pulses ≤8.5 ms in length. The samples were examined using a number of crystallographic techniques including field emission scanning electron microscopy, selected area diffraction and energy dispersive x-ray spectrocscopy. The pillars have excellent crystallinity with only

occasional structural defects and very large grain size, ~20 μm. This compares with a grain size of ~1 μm for traditional solid phase crystallization or low frequency microwave annealing

In the next series of experiments, attempts will be made to improve the wetting of the substrate surface by the molten silicon. The characteristics of silicon layers deposited onto the annealed substrates also will be investigated to determine if the annealed crystalline structures can force crystalline alignment of what would normally be an amorphous layer applied by CVD after formation of the pillars.

CMOS structures. A similar series of annealing experiments was performed on CMOS structures originally formed by low energy implantation [10]. During implantation, the specific range of dopants striking crystalline silicon can produce high performance junctions with very small-scale size capable of meeting the requirements of the 32 nm technology node planned for availability through 2013 by the International Technology Roadmap for Semiconductors (ITRS) [11]. But the implantation damages the silicon lattice structure, resulting in an increase in resistivity and decrease in device performance. The conventional solution to this problem is to anneal the structure using flash lamps, however if this is done over a time long compared with diffusion times of the dopants, the scale length of the junctions forming the source/drain and channel regions will increase during the annealing, dopant density will decrease, the performance will be impaired and the requirements of the roadmap cannot be met. One measure of device performance is the contact resistance, which must remain low, and the electrical isolation at small junction depth, which must remain high. Flash annealing of the structures by microwave heating provides a solution meeting the requirements.

The experiment was very similar to the silicon annealing work described above except that the targets were crystalline silicon with a variety of dopants and geometries. On DIII-D, one of the 110 GHz gyrotrons was easily able to provide heating rates to $5 \cdot 10^5$ °C/s up to and beyond the melting point of silicon. The optimum method found empirically was application of a 4.5 ms pulse providing 4 kW/cm^2, which heated the sample to ~1300 °C at about $2.75 \cdot 10^5$ °C/s. Subsequent analysis showed that little dopant diffusion occurred during this time period even if the sample was exposed to multiple pulses with a cooldown time between pulses. Electrical activation of the implanted dopants showed a sheet resistance, R_S, of 495–750 Ohms/square for junction depth between 14–2 nm and successive pulses resulted in continual improvements in R_S. The result was ultra shallow junctions which were superior to competing anneal technologies and which satisfied the ITRS requirements at least through 2013. Competing with the implantation/anneal technology is small-scale *x*-ray photolithography using wavelengths of 0.1–0.8 nm, which has the capability, particularly for the shorter wavelengths, of producing 3D structures. Both techniques can produce excellent performance.

Gyrotron pellet accelerator. A waveguide containing a substance that can be vaporized by microwaves could be used to generate high pressures and temperatures capable of driving pellets suitable for fueling in a fusion device [12]. A preliminary experiment was done using the DIII-D gyrotron complex. A waveguide with diameter 4 mm and length 25 mm was connected to a standard 31.75 mm diam corrugated waveguide using a downtaper. A diamond window in the larger waveguide isolates the test setup from the gyrotron. The small waveguide, isolated from the larger guide by a sapphire window, was filled with napthalene containing an admixture of 1–5 % Ni particles with scale size ~2 μm. This sealed waveguide was surrounded by a thick walled chamber hydro tested to 90 atm and capable of withstanding 680 atm. The microwaves, 500 kW, ~1–2 ms, were directed into the waveguide and were absorbed by the metal particles, which in turn heated the napthalene, which then vaporized producing high temperatures, >1000 °C, and pressures up to approximately 60 atm. In this experiment transducers measured the temperatures and pressures and following the termination of the rf pulse, the napthalene simply recondensed.

In the first attempt at the experiment, electric field enhancement at the interface between the napthalene and sapphire window isolating the small diameter waveguide resulted in arcing at the window surface, with damage to the window and protective termination of the rf pulse due to reflected rf power [13]. It is likely that the match can be improved by use of proper geometry at the window. This area will be redesigned and then the experiment will be tried again.

Conclusion

The ECH complex at DIII-D now has six operating gyrotrons, which have been used both for fusion and for materials experiments. Reliability has been very good and is expected to improve once all power supplies and other enhancements have been installed. The longer term plan is to add two more gyrotrons and waveguide lines with their ancillary equipment and then upgrade to 12 MW generated power by replacing the present group of 1.0 MW diode gyrotrons with depressed collector tubes having unit output power of 1.5 MW.

Acknowledgment

This work was supported by the U.S. Department of Energy under DE-FC02-04ER54698.

References

1. *Lohr J. et al.* Fusion Sci. Technol. **48**, 1226 (2005).
2. *Felch, Kevin et al.* IEEE Trans. Plasma Sci. **24**, 558 (1996).
3. *Cengher M. et al.* Proc. of 15th Joint Workshop on Electron Cyclotron Emission and Electron Cyclotron Heating, J. Lohr, ed., World Scientific, Singapore (2009).
4. *Doane J. L. and Moeller C. P.* Int. J. Electronics **77**, 489 (1994).
5. *Denison D. R. et al* IEEE Trans. on Plasma Sci. **27**, 512 (1999).

6. *Doane J. L.* Infrared and Millimeter Waves **13**, 123 (1985).
7. *Ohkubo K. et al.* Proc. of 10th Joint Workshop on Electron Cyclotron Emission and Electron Cyclotron Heating, T. Donné and T. Verhoeven, eds, World Scientific, Singapore, 597 (1997).
8. *Lohr J. et al.* Proc. Int. Workshop Strong Microwaves in Plasmas 2005, A. G. Litvak, ed., **2**, 434, Russian Academy of Sciences, Nizhny Novgorod (2006).
9. *Liu F. et al.* "Ultra-high Crystalline-quality Silicon Pillars Formed by Millimeter-wave Annealing of Amorphous Silicon on Glass," submitted to Nature Materials (2008).
10. *Thompson K. et al.* J. Vac. Sci. Technol. B **23**, 970–978 (2005).
11. International Roadmap for Semiconductors (ITRS), Presentations from the 2007 ITRS Winter Conference, Makuhari Messe, Japan, are available at http://www.itrs.net/Links/2007Winter/2007_Winter_Presentations/Presentations.html.
12. *Parks P. B. and Perkins F. W.* Proc. of 33rd EPS Conf. on Plasma Phys., ECA **30I** (2006) P-1.121.
13. *Callis R. W. et al.* Fusion Energy 2008 (Proc. 22nd Int. Conf., Geneva, 2008) (Vienna: IAEA) Paper FT/P2-23, http://www-pub.iaea.org/MTCD/Meetings/fec2008pp.asp.

1 MW, 140 GHZ SERIES GYROTRONS FOR THE W7-X STELLARATOR

M. Thumm[1,5], H. Braune[2], G. Dammertz[1], V. Erckmann[2], G. Gantenbein[1], S. Illy[1], S. Kern[1], W. Kasparek[3], H. P. Laqua[2], C. Lechte[3], F. Legrand[4], W. Leonhardt[1], C. Lievin[4], G. Michel[2], B. Piosczyk[1], O. Prinz[1,5], M. Schmid[1]

[1]Forschungszentrum Karlsruhe, Association EURATOM-FZK, Institut fuer Hochleistungsimpuls- und Mikrowellentechnik, Karlsruhe, Germany
[2]Max-Planck-Institut fuer Plasmaphysik, Teilinstitut Greifswald, Association EURATOM, Greifswald, Germany
[3]Universitaet Stuttgart, Institut fuer Plasmaforschung, Stuttgart, Germany
[4]Thales Electron Devices, Velizy-Villacoublay, France
[5]Universitaet Karlsruhe, Institut fuer Hoechstfrequenztechnik und Elektronik, Karlsruhe, Germany

A powerful electron cyclotron heating and current drive (ECH&CD) system with 10 MW mm-wave power at 140 GHz in CW operation is foreseen for the stellarator W7-X, being under construction at IPP Greifswald, Germany. The mm-wave power will be delivered by 10 gyrotrons, each capable of 1 MW, CW. Nine gyrotrons (cavity mode: TE28.8) are being manufactured by Thales Electron Devices (TED), Velizy, France, one gyrotron (cavity mode: TE28.7) was produced by CPI, Palo Alto, CA, USA. Testing of the TED gyrotrons is being performed in the test facility at FZK (pulse duration 3 min) and the final tests are being performed at IPP (pulse length 30 min).

Both, the first TED series gyrotron and the CPI gyrotron have passed the acceptance tests successfully. The first TED series tube yielded a total output power of 0.98 MW, with an efficiency of 31 % (with non-depressed collector) in short pulse operation and a power of 0.92 MW in pulses of 1800 s (efficiency of almost 45 % at a depression voltage of 29 kV). The Gaussian mode output power was 0.91 MW. The mm-wave power, measured in a calorimetric load at the end of a 24 m long quasi-optical transmission line with seven mirrors, was 0.87 MW.

The acceptance tests of the TED series gyrotrons are ongoing. The mm-wave output beam quality of all tubes tested so far is at a constant high level of about 96–97 % in the fundamental Gaussian beam. In short pulse operation (1 ms) all the gyrotrons have achieved the specified parameters. However, for long pulse operation the performance of some tubes decreases due to the occurrence of parasitic oscillations in the range of 119–132 GHz which are assumed to be excited by the electron beam in the beam tunnel close to the entrance of the cavity.

This contribution reports on the present status of the TED series gyrotrons.

1. Introduction

The stellarator W7-X at IPP Greifswald will use electron cyclotron heating and current drive (ECH&CD) as the basic heating and current drive system [1]. In the first stage W7-X will be equipped with a 10 MW ECH system operating at 140 GHz in continuous wave (CW). The mm-wave power will be delivered by ten gyrotron oscillators. The complete ECH system will be provided by Forschungszentrum Karlsruhe (FZK), including the design, development, construc-

tion, installation and integrated tests of all components required for stationary plasma heating on site at IPP Greifswald, e.g. gyrotrons, transmission lines, power supplies etc. FZK also coordinates contributions from IPF of the University of Stuttgart and from IPP Greifswald. Concerning gyrotron development, this project benefits from the collaboration with CRPP Lausanne, CEA in Cadarache and Thales Electron Devices (TED) in Velizy. After completion of the development phase seven series gyrotrons have been ordered from TED. First operation and long-pulse conditioning of these gyrotrons will take place at the test stand at FZK where pulses up to 3 minutes at full power and 30 minutes shots at reduced electron beam current are possible (limited by power supply). 30 minutes shots at full power are possible at IPP in Greifswald. The first TED series gyrotron has been tested successfully and has shown full performance on site at IPP Greifswald. One gyrotron has been developed at Communications and Power Industries, Palo Alto, USA (CPI). This gyrotron also achieved the specifications. Including the pre-prototype tube, the prototype tube and the 140 GHz CPI-tube, ten gyrotrons will be available for ECH&CD on W7-X.

2. Configuration of the TED gyrotron and experimental set-up

A DC-heated magnetron injection gun which works in the temperature limited region is used. It is designed as a diode-type gun (without modulation anode) and operates at an accelerating voltage of 80 kV creating a beam current of 40 A with a current density at the dispenser cathode of 2.5 A/cm2. The average velocity ratio of the electrons ($v\perp/v\|$) is 1.3. The gun cavity region (beam tunnel) is equipped with stacked copper and RF-absorbing ceramic rings in order to avoid spurious oscillations which could degrade the beam quality and lead to excessive thermal loading.

The cavity is a standard cylindrical design, optimized for the mode TE28,8. In order to minimize mode conversion at the transition from the input taper to the cylindrical section and to the output taper these sections have been smoothed, resulting in a mode purity of 99.9 %. The realistic thermal peak wall loading of the cavity is less than 2 kW/cm^2. The electron beam is placed at the first radial maximum of the electrical field of the TE28,8 mode to ensure a strong interaction of the electrons with the design mode. The nominal value of the magnetic compression ratio (B_{cavity}/B_{gun}) of the electron beam is 23.5.

The mm-wave output launcher and quasi-optical mirror system are optimized to convert the rotating TE28,8 cavity mode into a fundamental Gaussian beam with high efficiency [2, 3]. From calculations a conversion efficiency of the TE28,8 mode to the fundamental Gaussian beam TEM00 of more than 98 % is expected.

The output vacuum window is a single, edge-cooled CVD-diamond disk with an inner aperture of 88 mm, mounted under a small angle with respect to the out-

put beam. To minimize reflections at the window a resonant thickness for 140 GHz has been chosen (two wavelengths inside the material). Due to the low loss tangent of diamond the absorbed power for a 1 MW beam is only 400–700 W. The very high thermal conductivity limits the central temperature increase in CW operation to about 60 °C.

The isolation of the collector from the cavity region allows the application of a decelerating voltage. This measure reduces the residual energy of the spent electrons and lowers the thermal load of the collector, resulting in a higher overall efficiency. During operation the collector is at ground potential, the cathode voltage is set to a negative value of 52–54 kV and the cavity voltage to 27–29 kV. To equalize the thermal loading of the collector, watercooled solenoidal coils sweep the electron beam across the surface in axial direction with a repetition frequency of 7 Hz. An advanced 50 Hz sweeping system using transverse fields has the advantage of a further reduction of the peak wall loading. This system is presently under investigation [4].

Possible stray radiation in the gyrotron and along the transmission line to the CW load is measured calorimetrically. The thermal loading of the gyrotron components and transmission line is monitored continuously.

3. Experimental results of TED series gyrotrons

3.1. Operation of SN1 at full performance

All TED-gyrotrons are pre-tested in the test facility at FZK prior to shipment to IPP, where they undergo the final full performance tests. TED-gyrotron SN1 showed an almost linear dependence of output power versus beam current at constant magnetic field. The saturation in power as measured in the prototype was absent indicating the azimuthally homogeneous emission of the cathode. An output power of 1 MW at 40 A and 1.15 MW at 50 A was measured in short pulse (ms) operation. The corresponding efficiencies without depressed collector were 31 % and 30 %, respectively.

In long-pulse operation up to 3 min, which is the test stand limit at FZK for a beam current > 30 A, the power was measured calorimetrically in an RF-load. The RF-beam is directed and focused by two matching mirrors and two polarizers into the load, which is located at a distance of about 6 m from the gyrotron window. The polarizers generate a circularly polarized wave to homogenize the power loading on the surface of the load. The first matching mirror possesses a grating surface, which directs a small amount of the RF-beam towards a horn antenna with a diode detector to get a power proportional signal. The gyrotron was operated with a typical depression voltage in the range 25–30 kV to limit the collector loading and optimize the efficiency. The highest measured directed power inside the load for a 3 min pulse was 906 kW. Including the external stray radiation, which was determined by calorimetric measurements inside the mi-

crowave chamber, the total gyrotron output power was 920 kW with an efficiency of almost 45 %. Thus the specified value of > 900 kW for the power in the directed beam has been achieved. No arcing in the quasi-optical transmission line has been observed.

After the successful tests at FZK, the tube was delivered to IPP Greifswald for final tests in 30 minutes operation and the year 2005 saw the successful full performance tests of gyrotrons from both manufacturers, TED and CPI at IPP. Fig. 1 shows the TED-gyrotron and super-conducting (SC) magnet in the installation at IPP Greifswald.

Typical time traces of the output power and the gyrotron pressure (IGP-current) for an experimental sequence of one short (4 min) and one longer pulse (30 min) are shown in Fig. 2. The slow rise and fall times of the RF-power trace are determined by the characteristic time constant of the CW-calorimeter. The small steady increase of the gyrotron pressure as seen from Fig. 2 (bottom) indicates, that the tube has not yet reached steady state after 30 min, although all other measured parameters became stationary. Power modulation was demonstrated up to 20 kHz by modulating the body voltage [5]. An almost linear dependence of the output power on the body voltage was measured. The RF-power vs. acceleration voltage characteristics for the CPI-gyrotron is plotted in Fig. 3 (top) for 10 min pulses [4]. It provides a very convenient voltage range for the power control. The operating cavity mode in this tube is $TE_{28,7}$.

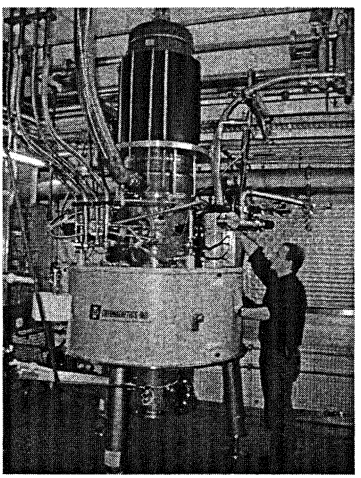

Fig. 1. TED-gyrotron SN1 at IPP Greifswald

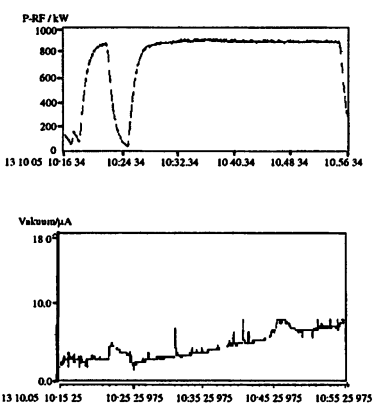

Fig. 2. Example of a 30 min shot for the TED gyrotron SN1 (with a 5 min shot as precursor). RF-power (top) and gyrotron vacuum (IGP-current, bottom) as a function of time (h, min, s).

An example for a beam-current scan for TED-gyrotron SN1 is shown in Fig. 3 (bottom), each data point was taken in pulses with 1–5 min pulse duration. The scan was performed up to a maximum output-power of 0.96 MW with an efficiency of 44 %, indicating the full gyrotron capability.

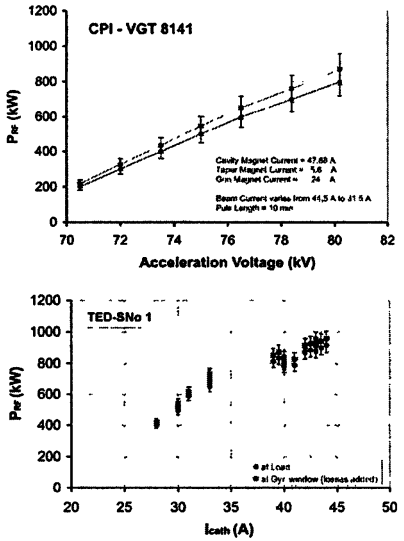

Fig. 3. Top: Output power (squares) and RF-power to load (dots) as a function of the acceleration voltage (CPI-gyrotron). Bottom: Same quantities as a function of the beam current for the TED-gyrotron SN1.

We have chosen somewhat more conservative parameters for the 30 min operation, which is the target plasma discharge length of W7-X. The gyrotrons were operated at a power in the directed beam of about 0.9 MW (CPI) and 0.92 MW (TED), the related power measured in the calorimetric CW-load was 0.83 MW (CPI) and 0.87 MW (TED).

Note, that due to the inherent mode filtering capability of a beam waveguide only the Gaussian mode content of the gyrotron beam reaches the CW-load. The total transmission losses after seven mirrors were estimated in the range 50–70 kW. Since at the time of commissioning the parameters of the Gaussian output beam for the CPI-gyrotron were not known with the required accuracy, slightly higher losses (70 kW) resulting from an imperfect Beam-Matching-Optics (BMO) unit had to be accepted as compared to the TED-gyrotron (50 kW). The CPI-gyrotron opened a collector vacuum leak after having passed the acceptance test and was returned to the manufacturer for repair. The TED gyrotron SN1 was mothballed after the acceptance tests.

3.2. Operation of SN2 and SN3

A short-pulse output power of 1 MW has also been achieved with SN2 and SN3. However, with both tubes, it was not possible to increase the pulse length

and to find parameters of good performance. To avoid competition with the parasitic mode oscillation, the beam voltage had to be reduced to low values which resulted in an unacceptable power and efficiency of SN2 and SN3.

The dependence of the output power on the accelerating voltage is shown in Fig. 4 for SN3 in short pulse operation (3 ms). The output power has been measured for different combinations of the cavity magnetic field and beam radius in the cavity, the beam current was 41–44 A. However, at longer pulses (1 s) the performance of SN3 was similar to SN2 and the maximum achievable output power was considerably reduced (650 kW in pulses of 3 min).

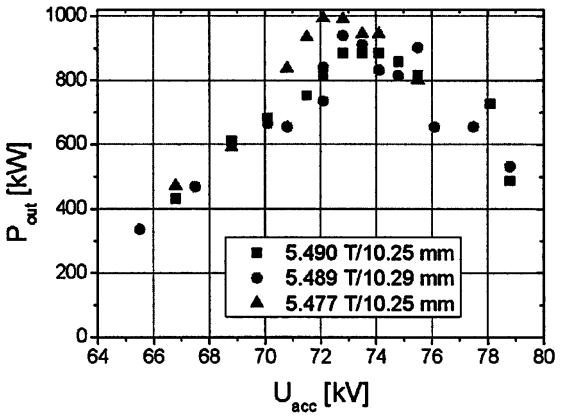

Fig. 4. Output power of TED-gyrotron SN3 versus accelerating voltage for different combinations of cavity magnetic field and beam radius in the cavity.

Both gyrotrons have been opened at TED and subjected to a visual inspection. The beam tunnel has been examined very carefully. This component consists of sandwiched copper and lossy ceramic rings which have a decreasing inner diameter towards the cavity. Several ceramic rings and brazings close to the entrance of the electron beam to the cavity were damaged due to thermal overloading. These observations strongly support the assumptions that parasitic oscillations are excited in the beam tunnel. Since SN1 operated satisfactorily, this effect seems to be at its threshold.

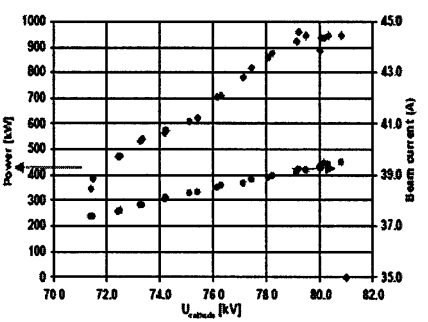

Fig. 5. Influence of accelerating voltage on output power and beam current in short pulse operation of SN2A.

The operating parameters of series gyrotron SN2A with repaired but not modified beam tunnel have been opti-

mized in short pulses of a few ms. Fig. 5 shows the dependence of the output power on the cathode voltage and the increasing beam current at constant heating power of the electron gun. The output power can be varied from 350 kW up to 950 kW by changing the voltage from 72.5 kV to 80.5 kV. At higher voltage the gyrotron oscillates in a wrong cavity mode.

The specified output power (1 MW) of the gyrotron has been achieved with a beam current of 41 A. This is demonstrated in Fig. 6 which also shows a saturation of output power with increasing beam current (at constant B-field), in particular at a beam current above 40 A.

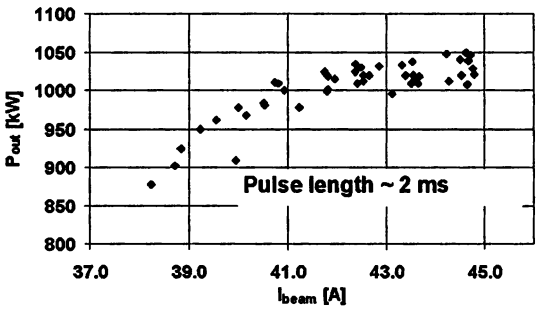

Fig. 6. Saturation of output power with increasing beam current measured with SN2A.

Operation of the tube was possible with currents of up to 50 A. Fig. 7 shows the maximum achieved output power at 50 A (≈ 1200 kW) in dependence of the magnetic field and optimized cathode voltage (76–81 kV). Since the gyrotron is operated with non-depressed collector in short pulses the corresponding efficiency varies from 25.4 to 30 % which is in good agreement with results of previous gyrotrons.

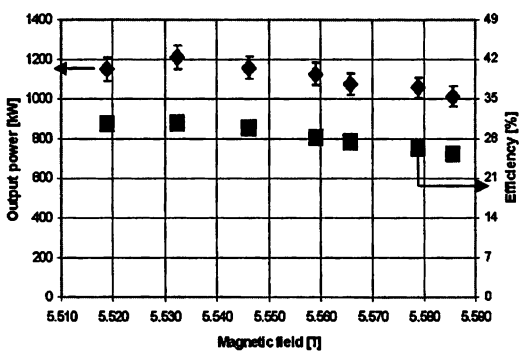

Fig. 7. Output power and efficiency of SN2A achieved with 50 A beam current.

In long-pulse operation gyrotron SN2A and the repaired SN3A both delivered only 650 kW in pulses of 3 min due to the performance limitations by parasitic beam tunnel oscillations.

Precise measurements have been performed to monitor possible frequencies which may originate from interactions in the beam tunnel. It has been found that several frequencies in the range of 119–132 GHz have been excited simultaneously with the main mode at 140 GHz.

At the mirror box of the W7-X gyrotrons a relief window with a calorimeter is installed which offers the possibility to measure the level of stray radiation in the gyrotron. This measurement is given in Fig. 8 which shows the output power and the relative stray radiation through the relief window versus the accelerating voltage. It is clearly visible that those operating points where only the desired 140 GHz was observed show a smaller amount of relative stray radiation. As soon as additional parasitic oscillations occur, the level of relative stray radiation is increased significantly.

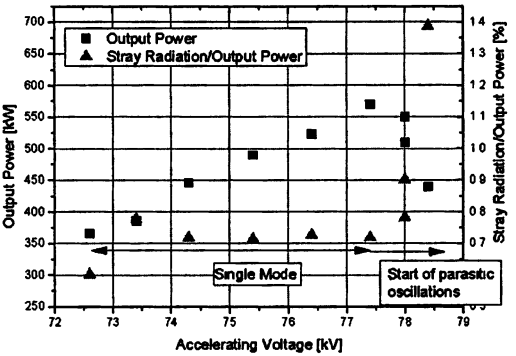

Fig. 8. Output power and relative stray radiation measured at the relief window of SN3A versus accelerating voltage.

3.3. Operation of SN4 at full performance

The series gyrotron SN4 was taken into operation and tested at FZK with short and long pulses. The total RF output power has been measured by a short pulse calorimetric load which is mounted close to the output window of the gyrotron. In the experiments given in Fig. 9 the beam radius has been varied from

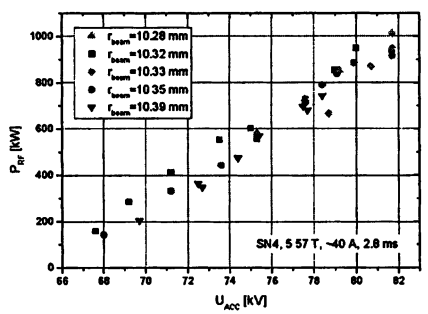

Fig. 9. Output power of series gyrotron SN4 in short pulse versus accelerating voltage at different electron beam radii in the cavity.

10.28 mm to 10.39 mm. In short pulses (2.8 ms) it shows a stable output power of up to 1 MW at the design values.

For medium pulse length (≈ 0.1 s) and long pulses (several seconds up to 30 minutes) a CW load with massive water cooling is used in combination with an optical transmission system. At pulses longer than ≈ 0.1 s the gyrotron is usually operated with depressed collector. The efficiency of the gyrotron was around 42 % for beam currents from 28 A up to 40 A with a maximum of 43 % (see Fig. 10). This indicates a good performance of the electron gun and a sufficient electron beam quality. Safe operation of the gyrotron under CW conditions was

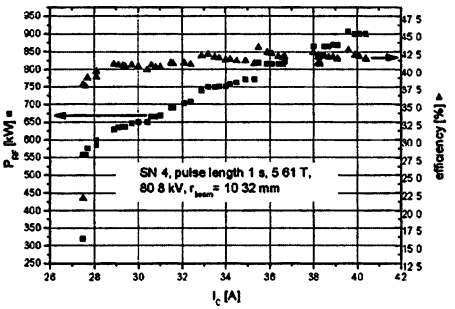

Fig. 10. Output power and efficiency of series gyrotron SN4 in dependence of beam current.

possible in the current range from 27 A up to 44 A with a depression voltage of up to 28 kV. Pulses have been performed up to 30 minutes, however with a reduced beam current (< 30 A) due to a limitation in the power supply at FZK. The output power obtained was about 500 kW. At maximum RF-power (910 kW) repetitive operation of the gyrotron was possible with a pulse length of 3 minutes. Fig. 11 shows the thermographic image (PVC target) of the Gaussian output beam with a mode purity of 97 % and a beam waist of approximately 18 mm. During the site acceptance test at IPP Greifswald a loss-of-cooling accident happened, so that the tube had to be shipped to TED for repair.

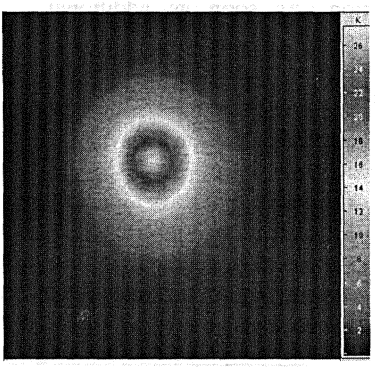

Fig. 11. Thermographic image of the Gaussian output beam of series gyrotron SN4 (Gaussian mode content: 97 %, beam waist 18.3 mm).

4. Summary

In this contribution we have reviewed experimental results of the series gyrotrons for the ECH&CD system of the stellarator W7-X. In general, the short-

pulse operation of the gyrotrons shows acceptable results with respect to output power and efficiency. All tested gyrotrons have a high quality Gaussian output beam (Table). The prototype gyrotrons and the series gyrotrons SN1 and SN4 worked well and achieved the specified output power also in long pulse operation.

Gaussian output beam parameters of the series TED-gyrotrons calculated from measured patterns [4] employing a phase retrieval and mode-analysis code

Gyrotron	w_{0x}; w_{0y}	z_{0x}; z_{0y}	Beam center offset $\Delta x;\Delta y$ at window	φ_{hor}; θ_{vert} [mrad]	TEM_{00} [%]
Maquette	19.3; 17.4	–82.8; 61.2	0.0; 4.9	8.1; –23.8	95
Prototype	18.6; 21.3	202; 71	18.2; 16.4	3.5; –1.7	97
TED SN1	17.7; 21.6	126.9; 126.0	–7.0; 8.0	12; –2	97.5
TED SN2	20.2; 22.5	103.5; 39.8	10.0; 9.0	7; 7	97
TED SN2A	18.7; 22.2	127.0; 30.0	3.4; 11.9	8.5; 6.7	95
TED SN3	17.5; 20.6	130; 90	5.4; 9.0	0.1; 13	97
TED SN3A	17.6; 20.5	24; 77	6.0; 3.0	–1; 17	96
TED SN4	18.1; 18.5	105; 51	–1; 2	–4; 5	97

Although the design of the beam tunnel is basically the same for all gyrotrons tested so far, the occurrence of parasitic oscillations may depend on small variations of material properties (e.g. RF absorption of the ceramic rings). A more robust design of the beam tunnel with respect to avoidance and suppression of these undesired oscillations is required.

A possible improvement towards a more stable single frequency operation in the high power regime has to take into account that the starting current of the parasitic oscillations must be increased as much as possible. This can be achieved by destroying the residual azimuthal symmetry, for example by introducing longitudinal slits in the Cu rings. A different solution has been reported by [6]: the authors successfully replaced the beam tunnel with a solid SiC ceramics cylinder which absorbs RF radiation on the one hand, and which is a semiconductor on the other hand, thus avoiding the build-up of electrical charges.

Acknowledgement

This work, supported by the European Communities under the contract of Association between EURATOM and Forschungszentrum Karlsruhe, was carried out within the framework of the European Fusion Development Agreement. The views and opinions expressed herein do not necessarily reflect those of the European Commission.

References

1. *Ercknann V., Brand P., Braune H., Dammertz G., Gantenbein G., Thumm M., Turkin Y., Weissgerber M. and Weller A.* Fusion Science and Technology, **52**, 291–312 (2007).
2. *Thumm M., Alberti S., Arnold A., Brand P., Braune H., Dammertz G., Illy S., Kasparek W., Laqua H. P., Legrand F. Leonhardt W., Lievin C., Michel G., Neffe G., Piosczyk B., Schmid M., Schworer K., and Tran M.Q.* IEEE Trans. on Plasma Science, **35**, 143–153 (2007).
3. *Dammertz G., Alberti S., Arnold A., Bariou D., Brand P., Braune H., Ercknann V., Dumbrajs O., Gantenbein G., Giguet E., Heidinger R., Hogge J. P., Illy S., Jin J., Kasparek W., Koppenburg K., Laqua H. P., Legrand F., Leonhardt W., Lievin C., Michel G., Muller G., Neffe G., Piosczyk B., Prinz O., Rzesnicki T., Schmid M., Thumm M., Tran M. Q., Yang X., and Yovchev I.* IEEE Trans. on Plasma Science, **34**, 173–86 (2006).
4. *Thumm M., Brand P., Braune H., Dammertz G., Ercknann V., Gantenbein G., Illy S. Kasparek W., Laqua H. P., Lechte C., Leonhardt W., Michel G., Neffe G., Piosczyk B., Schmid M., and Weissgerber M* IEEE Trans. on Plasma Science, **36**, 341355 (2008).
5. *Dammertz G., Alberti S , Fasel D. Giguet E., Koppenburg K., Kuntze M., Legrand F., Leonhardt W., Lievin C., Muller G., Neffe G., Piosczyk B., Schmid M., Sterk A., Thumm M., Tran M. Q. and Verhoeven A. G. A.* Fusion Eng. Des., **66–68**, 497–502 (2003).
6. *Shoyama H., Sakamoto K., Hayashi K., Kasugai A., Tsuneoka M., Takahashi K., Ikeda Y., Dariya T., Mitsunaka Y., Imai T.* Jpn. J. Appl. Phys., **40**, L906–L908 (2002).

TEST RESULTS OF 170 GHz / 1 MW / 50 % GYROTRON FOR ITER

L. G. Popov[2], S. V. Usachev[2], M. V. Agapova[2], A. V. Chirkov[1], G. G. Denisov[1], A. Ph. Gnedenkov[2], V. I. Ilyin[3], V. N. Ilyin[2], A. N. Kostyna[2], A. N. Kuftin[1], A. G. Litvak[1], S. A. Malygin[2], V. I. Malygin[1], V. E. Myasnikov[2], V. O. Nichiporenko[2], Yu. V. Roschin[3], V. G. Rukavishnikova[2], E. A. Soluyanova[2], E. M. Tai[2], A. N. Yakunin[2], Yu. M. Yashnov[2], V. E. Zapevalov[1]

[1]IAP RAS, Nizhniy Novgorod, Russia
[2]GYCOM Ltd., Nizhniy Novgorod, Russia
[3]INF RRC "Kurchatov Institute", Moscow, Russia

During last years large efforts at IAP / GYCOM were exerted to improve design and performance of 170 GHz / 1 MW / 50 % / CW gyrotron for ITER. The paper presents new results in development of gyrotrons for ITER including test of 170 GHz / 1 MW / 50 % gyrotron and test of short-pulse gyrotron mock-up with output power over 1.5 MW. On the threshold of gyrotron delivery for ITER issues of gyrotron reliability and life time are discussed.

Introduction

On the threshold of gyrotron delivery for ITER more and more attention is paid to gyrotron reliability. Detailed analysis of electron gun assembly has shown that probability of arcing could be reduced further by improving of electrostatic field distribution due to correct shaping of electrodes in vicinity of HV ceramic insulator. The test of gyrotron with modified gun unit has been carried out since December 2007. In all other aspects tested gyrotron was manufactured following conventional GYCOM 170 GHz / 1 MW / CW gyrotron design [1].

Gyrotron pumped mock-up with high spatially developed cavity mode $TE_{28\,12}$ was tested in summer 2008 to verify possibility of output power enhancement to ~1.5 MW.

Estimation of actual gyrotron life time concerning its future run in ITER is becoming the problem of the day.

Test results of production prototype of regular ITER gyrotron

At operational beam voltage of 76.5 kV at increasing of beam current to 54 A as is shown at Fig. 1 output power attained 1.2 MW which was measured at 100 ms pulse duration. Under measurement calorimetric load was moved 30 cm away from output window to absorb neat Gaussian beam power.

In Fig. 2, gyrotron output power and efficiency are plotted as a function of retarding voltage. Total efficiency of 52 % was reached at output power over 1 MW.

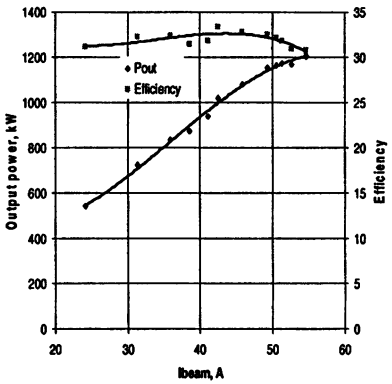

Fig. 1. Output power & efficiency vs. beam current at beam voltage of 76.5 kV

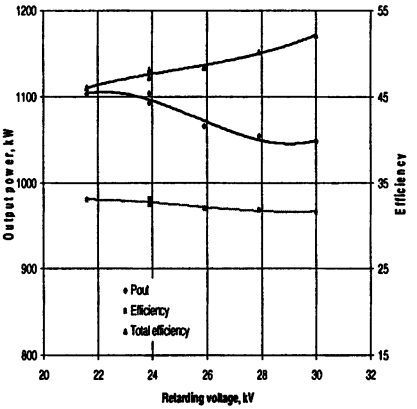

Fig. 2. Output power & efficiency vs. retarding voltage at beam current of 46 A

In long-pulse test gyrotron after some initial conditioning demonstrated very reliable operation with negligible amount of HV arcing verifying utility of made modification. Gyrotron output radiation formed finally by 2 mirrors of matching optics unit (MOU) was directed to the terminal load through the set of phase-correcting mirrors situated at atmospheric pressure. Small fraction of wave beam was derived to RF detector and small calorimetric load for power monitoring. There were also measured fractions of stray radiation absorbed in MOU (~5 %) and emanating through relief window (~3 %). Diamond window losses were determined as ~0.1 %.

Present test facility was upgraded several times to extend its testing capabilities and to approach them to ITER specifications. High-voltage pulse as designed could last up to 5 min if voltage of main power supply does not exceed 50 kV and beam current is less than 50 A. 5 min pulse duration was attained early for ~0.5 MW output power at cathode voltage of 46 kV and beam current of 25 A [2]. 50 kV / 50 A combination is nearly typical for gyrotron 1 MW regime but in the same time it is very close to the designed limit of the power supply. This limit was felt during long-pulse test as necessity of frequent retuning of power supply operational regime.

On the another hand long-pulse gyrotron operation was found strongly limited by arcing in the terminal load and overheating of metallic sheets shielded the

beam transporting channel. Additional absorbers installed in beam channel enabled to extend pulse to 203 s at power of 830 kW and to 116 s at power of 1020 kW. Signal traces corresponding to the longest pulse are shown in Fig. 3.

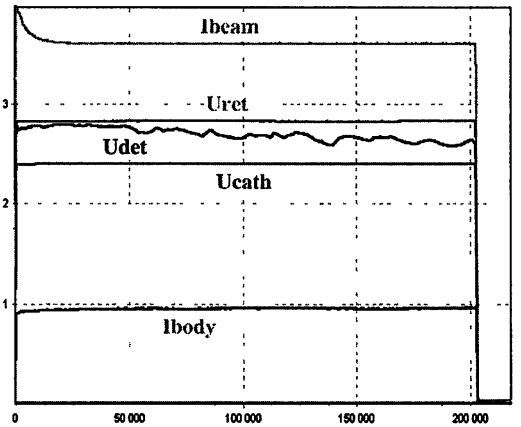

Fig. 3. Signal traces monitored in 830 kW / 203 s pulse

All signals were very stable. Stability of beam current was provided by feedback embedding to heater power source. Operational frequency showed good stability as well. Total frequency drift during the pulse is typically less than 100 MHz. Change of vac-ion current indicating gyrotron internal pressure did not exceed 1–2 μA.

Sometimes body current could deviate during a pulse between two stable values. Lower one was of 3–5 mA while upper one was about 20 mA higher. Deviation of body current led to minimum perceptible change of beam current and output power and has no another influence on gyrotron behavior.

Some of gyrotron pulses were terminated by oscillation cut-off happened after a few tens of seconds from the pulse start which looked inexplicable against a background of stability of gyrotron voltage, current and internal pressure.

Temperature rise of DC break ceramic insulator did not come to steady-state value but was noticeably reduced by forced air cooling. Air flow was rather weak and more intense air cooling or especially oil cooling would solve the problem. Possibility of oil cooling is envisaged in design of modified ITER gyrotron which will be ready to test by the end of this year.

After improvement of beam transporting channel arcing in MOU arose as a main problem. It was caused by overheating of movable cylindrical part connecting MOU to gyrotron flange. Evidently switch to evacuated waveguide provided for ITER will thoroughly solve a problem of RF arcing. New power transmission line of this kind included evacuated wave guide and evacuated load has mounted in the new testing facility which is under setting-up in Kurchatov Institute now. 80 kV / 50 A main power supply of new test facility will provide gyrotron operation in CW regime. Considering 50 kV voltage of recuperation power supply total accelerating voltage up to 130 kV will be available. It may be useful for gyrotron with increased power level. New facility is expected to operate in full-scale regime in the end of this year.

Testing of 1.5 MW gyrotron mock-up

To explore 170 GHz gyrotron capability for production of about 1.5 MW output power pilot gyrotron mock-up was designed and tested. Gyrotron cavity mode had to meet 3 conflicting objectives. Firstly, it has to secure reasonable cavity losses at desired power level. Secondly, it should win mode competition in start-up scenario. Lastly, it has to interact with electron beam which could be formed by electron gun fitted in the largest size to 160 mm diameter of cryomagnet bore. Finally, $TE_{28.12}$ mode was chosen as an operating one.

To provide high-performance interaction electron beam quality was preliminary analyzed. Three versions of electron gun were investigated with usage of special beam analyzer under gun optimization for higher pitch factor, lower velocity spread and easy control in wide beam parameter range.

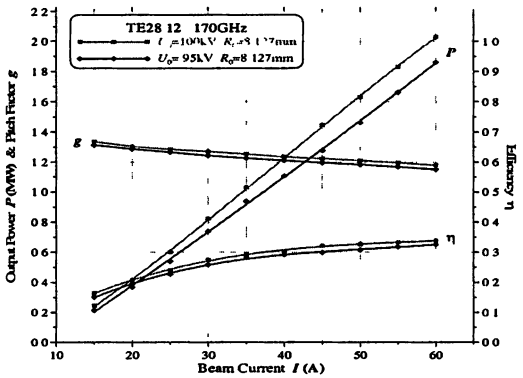

Fig. 4. Output power, efficiency & pitch-factor vs. beam current at two values of beam voltage

In the pumped gyrotron mock-up electron gun having the best parameters was installed. In Fig. 4, gyrotron output power, efficiency and pitch-factor are shown as a function of beam current. As one can see output power as high as 2 MW was attained at efficiency ~32 %.

Life time issue of ITER gyrotron

ITER IO team did not set yet any specifications related to H&CD gyrotron life time. Nevertheless, those who are concerned with future gyrotron run in ITER installation underst and that life time is to be estimated at few thousands of running hours. To convert these running hours into calendar time one should know operation schedule, namely pulse duration, duty factor, amount of pulses per day and amount of workdays per year etc, which as well are not announced yet.

No problems with collector of ITER gyrotron were met in Gycom but few recent collector failures of CPI gyrotrons have served as incentive to look at collector more precisely as at the most heavily loaded gyrotron unit. Collector performance is being now intensively analyzed using set of computer programs to calculate collector loading under impact of swept electron beam and ANSYS code to calculate collector mode of deformation. Furthermore, efforts are made to elaborate reliable criteria for estimation of collector life time.

Conclusions

In short-pulse test of 170 GHz gyrotron over 1 MW output power at total efficiency of 52 % was attained according to ITER requirements. Up to now maximal pulse duration of 203 s at power over 0.8 MW and of 116 s at power over 1 MW was limited by arcing of terminal load and MOU operated under atmospheric pressure.

Testing of ITER gyrotron will be continued after debugging of new test facility in Kurchatov Institute having evacuated transmission line and power supplies capable to provide CW gyrotron operation.

New modified ITER gyrotron is manufacturing now and will be ready to test to the end of this year.

Under testing of gyrotron pumped mock-up with $TE_{28.12}$ cavity mode output power of 2 MW was attained.

Considering soon gyrotron delivery to ITER gyrotron life time is becoming issue of the day.

References

1. *Agapova M. A. et al.* Development of 1 MW and 1.5–1.7 MW / 170 GHz gyrotrons for ITER // Proc. of the Int. Workshop on Strong Microwaves in Plasmas, 2006, July 25 – August 1, Nizhny Novgorod, Russia, p. 107–112.
2. *Usachev S V. et al* New test results of 170 GHz / 1 MW / CW gyrotron for ITER // Conf. Digest of 32th Int. Conf. on Infrared and Millimeter Waves and 15th Int. Conf. on Terahertz Electronics, 2007, Sept. 2–7, Cardiff, UK, p. 44–45.

STEP-TUNABLE EXPERIMENTAL GYROTRONS AT 75 GHz AND 140 GHz RANGES

I. V. Kazansky[1], *A. V. Kruglov*[1], *S. A. Malygin*[1], *V. B. Orlov*[1], *E. A. Solujanova*[1], *E. M. Tai*[1], *V. I. Belousov*[2], *A. V. Chirkov*[2], *G. G. Denisov*[2], *V. I. Malygin*[2], *A. B. Pavelev*[2], *E. V. Sokolov*[2]

[1] Gycom Ltd, Nizhny Novgorod, Russia
[2] Institute of Applied Physics, Nizhny Novgorod, Russia

Two step-tunable gyrotrons have been manufactured and tested at 0.1 s pulse duration. In the both, boron nitride windows of 120 mm diameter were used. The first gyrotron delivered 600–700 kW at 12 frequencies within 104–143 GHz band. The second one delivered 700–800 kW at 3 frequencies within (75 ± 3) GHz band.

Several-frequency gyrotrons worked long ago. Their operation was based on the transparency of output window on several frequencies due to the discrete relation between window disk thickness and gyrotron radiation wave length in the window material. Frequency spectra of such gyrotrons are dense, co-ordination of optimal helical electron beam properties and window conditions is complex. A magnetron-injection electron gun forms an electron beam with fixed radius in area of gyrotron cavity and fixed value of relative oscillating velocity. The parameters can be corrected using a cathode magnetic coil and changing operating voltages, but not in wide limits. The cavity operating mode is selected among the number of Bessel functions, which can be exited by electron beam in the range of it possible adjustment. Mostly modes optimal for HF interaction turns out to be not transportable throug the window. Therefore several-frequency gyrotrons are optimized for a main frequency and have relatively low efficiency at other ones. One of the way to solve the problem is creation of the window transparent in a wide frequency band.

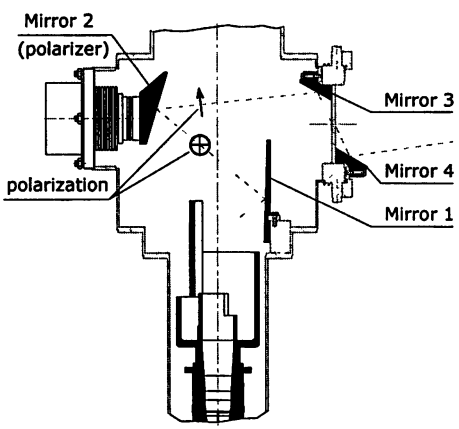

Fig. 1. Scheme of the multifrequency gyrotron

The article is dedicated to experimental investigation of gyrotrons with the Brewster window, which transparence doesn't depend on frequency. A scheme of the gyrotron is shown at Fig. 1. The peculiarity of the scheme is a polarizer mirror which changes the wave polarization for the Brewster effect.

In the gyrotron, a microwave beam is radiated in the quasi-gaussian form from inner waveguide converter and propagates through the mirror line and then through the window with the Brewster angle for BN window 65.2°. For insertion in frame of window unit mirrors near the window appeared to be quite small even in case of maximum window clearance diameter 120 mm. As a result, high power density in window area and high diffraction on mirror edges cause high danger of near-window HF discharge. Therefore gyrotron design must provide good screening of different heterogeneities in mirrors-window region, especially in case that a diamond window is used. It is seen from the Fig. 1, after the last mirror (number 4) the microwave beam propagates at an angle to the horizontal direction. Its further transportation requires an additional external mirror line.

The gyrotron was designed for the frequency range 105–150 GHz. Its possible mode spectrum is shown in Fig. 2. At this diagram, the lines corresponding to different modes are shown versus the frequencies at their band of excitation. Top and bottom points of the lines correspond to 90 and 10 % levels of a structure factor of interaction between the electron beam and HF electromagnetic field The middle of line corresponds to the maximum interaction.

Operating voltages at the diagram are normalized by one of the 140 GHz $H_{22,10}$ mode optimal interaction (~ 90 kV in the gyrotron).

During experimental investigation twelve modes were excited in the gyrotron: $H_{23,10}$ (143.08 GHz), $H_{22,10}$ (140.09 GHz), $H_{21,10}$ (137.07 GHz), $H_{22,9}$ (132.08 GHz), $H_{20,10}$ (134.08 GHz), $H_{21,9}$ (129.07 GHz), $H_{21,9}$ (129.07 GHz), $H_{20,9}$ (126.12 GHz), $H_{20,8}$ (118.06 GHz), $H_{19,8}$ (115.11 GHz), $H_{18,8}$ (112.13 GHz), $H_{18,7}$ (104.10 GHz). Output power from 600 kW up to 800 kW dependently on the mode was observed. The maximum power 800 kW was achieved at frequency 140 GHz, it was limited by current of the power supply.

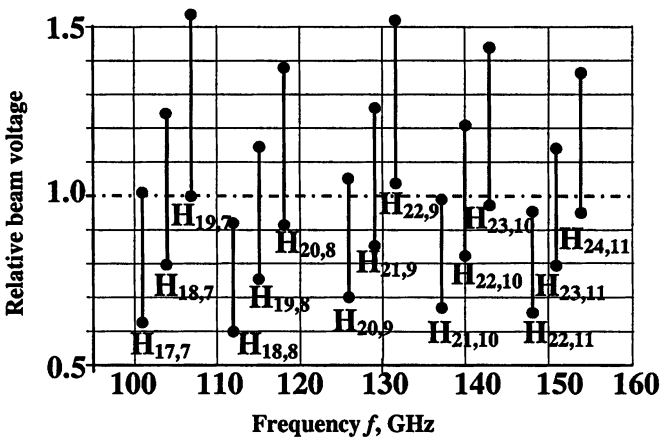

Fig. 2. Diagram of mode excitation

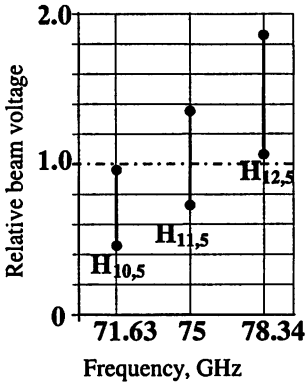

Fig. 3. Operating frequency triplet of 75 GHz gyrotron

The next gyrotron was created for 3-frequency operation at the stellarator L-2 of Institute of Common Physics in Moscow. Its central frequency is 75 GHz ($TE_{11.5}$ mode). The additional frequencies are 71.63 GHz ($TE_{10.5}$ mode) and 78.34 GHz ($TE_{12.5}$ mode). A diagram of themode excitation is shown in Fig. 3. Here operating beam voltage is normalized on the optimal voltage for the main mode. High efficiency of operation is the feature of this gyrotron.

The gyrotron was designed with boron nitride output window with disk clearance diameter 120 mm. Its operating regimes in the experimental investigations are listed in Table. The maximum pulse duration 0.1 s was defined by the Customer. It should be uderlined that 75 GHz gyrotron had very high efficiency at its total frequency range.

Operating regimes of 3-frequency 75 GHz gyrotron

Frequency, GHz	F	71.49	74.81	78.15
Cathode voltage, kV	U_o	–49.8	–58.0	–53.6
Anode voltage, kV	U_a	+23.0	+23.6	+23.2
Beam current, A	I	25.6	24.4	24.0
Cathode coil current, A	I_k	+0.75	+1.0	–0.6
Output power, kW	P	717	805	704
Pulse duration, s	τ	0.1	0.1	0.1
Efficiency, %	η	56.2	56.9	54.7

Conclusion:

- The multifrequency gyrotron with the Brewster output window was investigated experimentally. In it the maximum output power 800 kW was achieve at 140 GHz frequency. At other 11 modes in 104–143 GHz frequency range the maximum output power was 600–700 kW.
- In the 3-frequency 75 GHz range gyrotron output power 700–800 kW at 0.1 s pulse length was achieved.

RESEARCH ON MAGNETRON INJECTION GUNS

R. L. Ives [1], D. Marsden [1], G. Collins [1], G. Miram [1], P. Borchard [2]

[1] Calabazas Creek Research, Inc, San Mateo, CA, USA
[2] Consultant, CA, USA

Research is in continuing to improve the performance of magnetron injection guns for gyrotrons and gyroklystrons. Recent measurements indicate that problems still exist with emission uniformity. Techniques are presented to address this problem.

Calabazas Creek Research, Inc. (CCR) is continuing research to improve the performance of magnetron injection guns (MIGs). This paper reports on recent measurements of cathodes that exhibit unacceptable emission variations as a function of azimuthal position. It appears that these are caused by both temperature and work function variations. Techniques to address these issues are presented.

Introduction

Within the past few years, several facilities developed equipment for measuring the performance of magnetron injection guns independent of the RF source. One is located in St. Petersburg, Russia, where the electron emission in a gyrotron can be measured at the cathode and in the collector [1]. MIT developed a special collector where the electron beam can be sampled after transmission through the RF cavity. Calabazas Creek Research, Inc. (CCR) developed a facility that can measure both electron emission and temperature from the cathode surface. This paper describes research and development at CCR using its test facilities.

Recent measurements in Russia and the United States indicate that the quality of MIGS suffers from serious emission problems. In particular, all laboratories are measuring significant variations in emission as a function of azimuthal position. Recent measurement of a MIG for MIT indicated variations in temperature of 30 °C with 4:1 variations in current emission.

CCR is investigating cathode heater designs that provide better temperature control with a configuration that can be modified to correct problems. This design uses a tungsten wire heater attached to ceramic supports. The heating profile can be modified, and the heater can be repaired if necessary. The emitter is a separate assembly that can be replaced if the desired work function performance is not obtained. This design is described and experimental results presented.

Test Facilities

Test facilities at CCR include a vacuum bell jar for initial cathode processing and spot measurement of cathode temperature and heater power. The facility

consists of a scroll pump, turbo pump, VacIon pump, and residual gas analyzer (RGA). A photograph of the equipment is shown in Fig. 1.

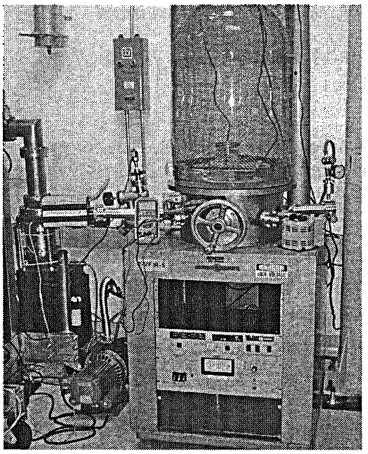

Fig. 1. Vacuum Bell Jar

The other facility is the MIG Test Chamber, shown in Fig. 2. This facility consists of scroll, turbo, and VacIon pumps and an RGA. The chamber includes current probes that span the width of the cathode strip and a temperature probe that views the center of the cathode strip at the same location where current measurements are obtained. There is also a view port that allows visual observation of the cathode strip with the ability to make pyrometer measurements of the temperature. The base pressure of this chamber is approximately $1.8 \cdot 10^{-8}$ Torr.

Cathodes for testing are mounted on a support structure that can be inserted and removed from the test chamber. The support structure provides water cooling for the cathode stem and a stepper motor for rotating the cathode past the current and temperature sensors. The support structure also contains the probes, allowing precision alignment prior to insertion in the vacuum chamber.

A computer-controlled data acquisition system controls rotation of the cathode and operation of the pulsed power supply. The probe signals are amplified and transmitted to an analog to digital converter in the computer. The stepper motor can be advanced in increments as small as 0.5 degrees. A Mikron 680 infrared temperature acquisition system measures the cathode temperature. The system includes a graphical user interface to facilitate set up and operation. A photograph of the computer system with typical display is shown in Fig. 3.

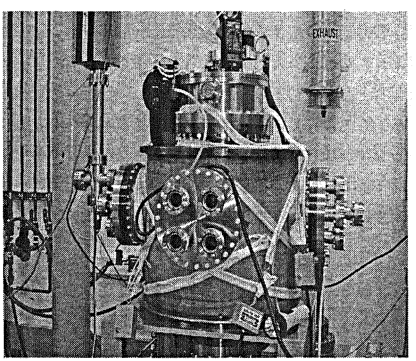

Fig. 2. MIG Test Chamber

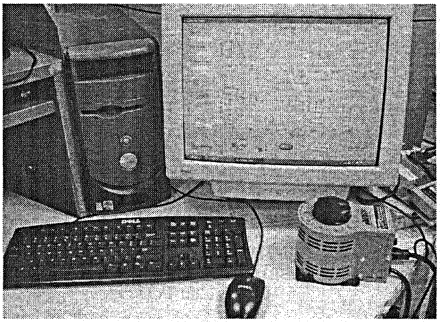

Fig. 3. Computer control system
and typical display

During operation, the high voltage power supply applies a user selected, voltage to the cathode of 200–5000 V. This voltage is applied as a series of microsecond pulses at a repetition rate of several hertz. Cathode current is collected on the individual current probes which capacitively store the accumulated charge. After termination of the voltage pulse and power supply transients, the voltages on the probes are recorded and stored. Typically, ten current readings from each probe are averaged to provide the reading at each azimuthal position.

Experimental Meaurements

Several cathodes were recently measured to determine the expected performance. Initially, cathodes are processed in the vacuum bell jar where the temperature can be measured as a function of heater power. This also allows spot measurement of the temperatures around the cathode. These can later be compared with more detailed measurements from the MIG chamber to verify the performance. Figure 4 shows measurements of a cathode both in the bell jar and from the MIG chamber. Both measurements confirm a significant temperature variation around the cathode. This variation would imply a 2 to 1 variation in emission current.

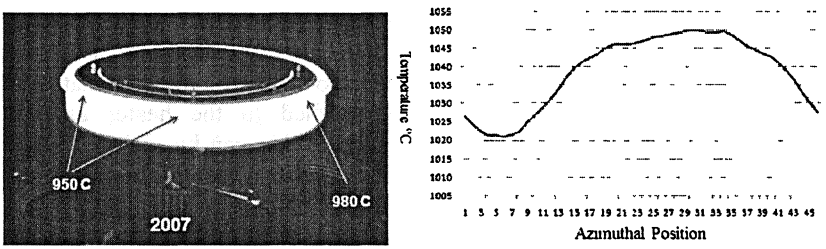

Fig. 4. Temperature measurement of a cathode in the bell jar (*left*)
and from the MIG Chamber

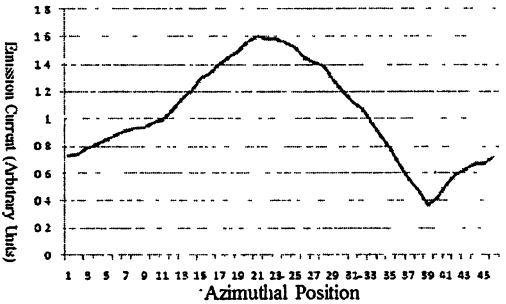

Fig. 5. Emission current as a function of azimuthal position for cathode shown in Fig. 4

The current probe measurement for this cathode is shown in Fig. 5. Note that the emission current varies by a factor of four around the cathode; however, the variation is not totally consistent with the temperature variation shown in Fig. 4. This indicates that there are variations in the cathode work function in addition to the temperature variation. Consequently, the performance of this cathode in a gyrotron would probably not be accepable.

Improved Heater Cathode Design

To address the type of problems in the cathode above, CCR is developing an alternative fabrication process that allows correction to temperature variations and economical replacement of cathodes with non-uniform work function. The design consists of separate heater and cathode assemblies. In the heater assembly, the heater winding is not potted, but supported on a series of ceramic spacers. The number of turns between ceramic supports can be adjusted to control the heat deposited in sections around the cathode. A photograph of this assembly is shown in Fig. 6.

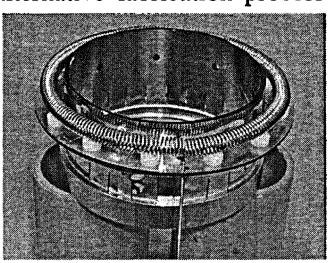

Fig. 6. Heater assembly with winding supported by ceramics standoffs

The emitter assembly consists of the tungsten cathode mounted to a support that is mechanically attached to the heater assembly. Since these are completely separate assemblies, either can be replaced without impact on the other assembly. This allows defective heaters or cathodes to be replaced without loss of the entire heater-cathode assembly.

Figure 7 shows the temperature and current measurements of the CCR cathode design. There is a 10 °C variation in temperature and approximately a 3:1 variation in emission. The localized variations in emission are not understood but would appear to be variations in work function. The temperature variation can be

corrected by adjustment of the heater coil, as described above. It may be prudent to replace the emitter assembly to obtain more uniform emission.

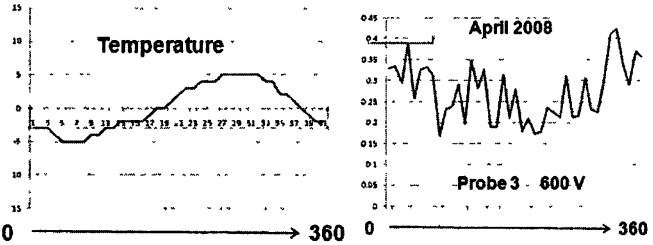

Fig. 7. Temperature variation (*left*) and emission variation (*right*) as a function of azimuthal position for CCR heater – cathode assembly

Summary

Variations in emission with angular position are still a problem in MIG cathodes. Research is continuing to develop techniques to eliminate this problem. A new assembly process was developed that allows simple repair or correction of problem heater-cathode assemblies.

Acknowledgements

This research was supported by U.S. Department of Energy grant number DE-FG02-04ER83918.

References

1. *Louksha O. et al.* "Experimental Study of Gyrotron Efficiency Enhancement by Improvement in Electron Beam Quality," Joint 32 Intern. Conf on Infrared and Millimeter Waves, and 15th Intern. Conf on Terahertz Electronics, Cardiff, UK, September 2007, p. 880–881.

1.3 THz GYROTRON WITH A PULSED MAGNET

M. Yu. Glyavin, A. G. Luchinin

Institute of Applied Physics RAS, Nizhny Novgorod, Russia

A demountable compact THz gyrotron tube with operating voltage about 30 kV has been designed constructed and tested at IAP RAS. The tube used improved pulsed solenoid with magnetic field up to 50 T. At the magnetic field close to 38.5 T, the $TE_{17,4}$ mode was excited at 1.022 THz frequency. The radiation power averaged over the pulse was 1.5 kW and the microwave energy was 75 mJ in single shots. The frequency 1.3 THz has been obtained at 48.7 T magnetic field with the several hundreds watts averaged power.

Introduction

One of the most important areas of the present microwaves investigations is development of radiation sources in the sub-Terahertz and Terahertz frequency bands ($f \geq 0.3$ THz). Gyrotrons are capable of producing high-power coherent electromagnetic radiation in the millimeter wavelength ranges and looks promising for submillimeter and terahertz bands.

Development of compact, simple and reliable sources of high-power coherent sub-THz and THz radiation is important for numerous applications such as plasma diagnostics, electron-spin resonance spectroscopy, enhancement of NMR sensitivity using Dynamic Nuclear Polarization (DNP), standoff detection and imaging of explosives and weapons, new medical technology, atmospheric monitoring, chemical technologies, production of high-purity materials, deep space and special satellite communication, etc. Currently, the most widespread and frequently used devices in the frequency range up to 1.4 THz are low-voltage and small-size Backward Wave Oscillators (BWOs) that provide an output power of several milliwatts in the CW regime at the highest admissible frequencies. There also exist other low-voltage vacuum sources based on stimulated Cherenkov and Smith-Purcell radiation of rectilinear electron beams, as well as solid-state devices delivering sub-THz and THz radiation at a power level up to one milliwatt; quantum cascade lasers already provide a power of hundreds of milliwatts at frequencies down to 4.4 THz. At the same time, the power of coherent radiation that can be delivered by vacuum devices based on the stimulated Bremsstrahlung radiation of curvilinear electron beams (Free Electron Lasers (FELs) and gyrotrons) can be higher by many orders of magnitude, which opens new opportunities for many applications. High-power radiation is produced in FELs and gyrotrons, due to advantage of using interaction of electrons with fast electromagnetic waves instead of slow waves in "conventional" electron devices. FELs can provide coherent and smoothly frequency-tuned radiation not only in the entire THz frequency region, but also in the bands of much higher frequencies, presumably up to *X*-rays. However, FELs utilize ultrarelativistic electron beams and, hence,

typically require large-size particle accelerators for their realization. That is why these devices can be used only in special research centers. Unlike FELs, gyrotrons can operate with electron beams having significantly lower energies of 10–100 keV. Correspondingly, they are much more compact than FELs and available for many laboratories.

For all that, it should be noticed that providing cyclotron resonance between gyrating electrons and fast waves in sub-THz and THz gyrotrons is not an easy task, since it requires a very strong magnetic field, specifically, one exceeding 35 T for the fundamental harmonic interaction at a radiation frequency of 1 THz. At the same time, the magnetic field, which can be typically produced in cryomagnets with a sufficiently large inner bore, does not exceed 15–20 T. A stronger magnetic field can be produced with the use of pulsed solenoids. In principle, efficient operation can be obtained in gyrotrons not only at the fundamental cyclotron resonance, but also at high cyclotron harmonics. The latter regime is very attractive, because it requires a weaker operating magnetic field which is inversely proportional to the harmonic number. However, realization of high-harmonic short-wave gyrotrons at high ($s \geq 2$) harmonics, in its turn, runs into rather complicated problems of mode competition and ohmic losses, which take many efforts to overcome.

Brief historical review of sub-THz frequency gyrotrons investigations

First gyrotron experiments at sub-THz waves were carried out at IAP as early as in the beginning of 1970s, when 326-GHz CW generation was obtained at the second cyclotron harmonic with an output power of 1.5 kW and an efficiency of 6.2 % [1]. Later, also at IAP, a fundamental-harmonic gyrotron with a strong pulsed magnetic field up to 25 T was realized [2]. In these experiments, a frequency up to 650 GHz with a power of 40 kW was obtained for pulse duration of 50 μs and step frequency tuning from pulse to pulse.

It should be emphasized that at the sub-THz and THz frequencies ohmic losses in gyrotron cavities become drastically important for the operation and efficiency of the device. There is a known way to diminish the role of this factor, namely, enlargement of the transverse cavity size and a corresponding increase in the radial index of the operating mode. A basic opportunity of single-mode operation at the $TE_{6,5}$ mode with a rather high radial index in a conventional gyrotron cavity has been demonstrated in Reference [3]. Another important achievement at the first stage of high-frequency gyrotron development was realization of the possibility to change the cavity size mechanically, which opened the basic opportunity for broadband and smooth frequency tuning [4].

Successive development of medium-power high-frequency FU Series gyrotrons at Fukui University demonstrated frequency step-tunability in a very wide range, namely, from 38 to 889 GHz, including the excitation of the highest frequency (889 GHz) at the second cyclotron harmonic in 17 T solenoid, as well as

the modulation of the amplitude and frequency and stabilization of the output radiation [5]. At the beginning of this century the second harmonic pulsed (20 T) magnetic field gyrotrons has been developed at FIR FU. At this gyrotron first successful experiments with 1 THz generation was realized at relatively low power level (about 1–10 W) and single shots operation regime (1 pulse per 20 minutes) but relatively long pulse duration (about 1 ms) [6,7]. Second-harmonic low-power gyrotrons with frequencies 150–600 GHz based on cryomagnets were also demonstrated in joint experiments of the FIR and the University of Sydney [8]. In collaboration between IAP RAS and FIR FU the CW 300 GHz gyrotron with output power 2.3 kW has been developed based on 12 T superconducting magnet [9].

A high output power of 375 kW at the frequency of 327 GHz has been obtained in 3-μs pulses in the Massachusetts Institute of Technology (MIT) [10]. Current MIT efforts in the THz frequency range are basically concentrated on gyrotron development for DNP experiments [11]. In this direction, CW operation at a frequency of 233 GHz with the power 10 W at the lowest voltage of 3.5 kV was demonstrated at the fundamental harmonic. In addition, broadband and continuous frequency tuning of the fundamental-harmonic gyrotron over a range of more than 2 GHz, which was based on the excitation of opposite waves and smooth transitions between the axial modes of a low-Q cavity during variations of the magnetic field, was demonstrated. A similar method was also used for the 140-GHz gyrotron with the $TE_{1,2}$ operating mode at FIR FU.

A so-called Large Orbit Gyrotron (LOG) with an axis-encircling electron beam is capable of higher-harmonic operation due to its better mode selectivity. The axis-encircling electron beam can resonantly excite only modes whose azimuthal indices are equal to cyclotron harmonic numbers. The third-harmonic LOG with a 250 keV / 4A / 10 μs electron beam has been realized at IAP RAS [12]. The power up to 10 kW in single-mode regimes at the operating modes $TE_{3,8}$ and $TE_{3,9}$ with high radial indices and frequencies 371 and 414 GHz, respectively, was radiated (20 kW / 369 GHz at the $TE_{3,5}$ mode).

Despite all these achievements, the problems of creating strong magnetic fields and discriminating parasitic modes made the gyrotron operation at the THz band with high output power level problematic. So, the main goal of the reported project was essentially increase gyrotron power at THz frequency band and develop pulsed kW level THz power source.

Solenoid and gyrotron design

A demountable THz gyrotron tube with a pulse magnet has been designed, constructed and tested at IAP RAS. This work is based on the previous results obtained with gyrotrons using pulsed solenoids [2] and on the development of an improved pulsed solenoid [13], producing up to 50 T magnetic fields. In the design of this gyrotron a number of specific requirements for gyrotrons operating with pulsed

magnetic fields were taken into account. First, to provide cyclotron resonance condition accurately enough, magnetic field should be reproducible from pulse to pulse and its value during the microwave radiation pulse should vary by less than 0.1 %. Second, conductivity of a resonator wall should meet contradicting requirements: on the one hand, this conductivity should be rather poor to allow varying magnetic field to penetrate into the resonator; on the other hand its inner surface should have conductivity high enough to provide reasonably low level of ohmic losses. Then, as in conventional gyrotrons, magnetic field distribution on axis should be uniform in the interaction space. Finally, the tube and the solenoid should be robust enough to withstand mechanical stresses caused by high pulsed magnetic fields.

The solenoid (Fig. 1) was made of a composite cable consisting of a 40%Nb-60%Ti alloy mechanically reinforced in an outer copper shell. For reducing ohmic heating and stabilizing the operation, the solenoid was cooled by liquid nitrogen, which reduces the resistance by a factor of 7 in comparison with the room temperature resistance. The cable was wired directly on a thin stainless steel gyrotron body. This allowed for significant reduction of the solenoid inner bore diameter (up to 6 mm) and the energy required for obtaining the necessary magnetic field. Magnetic field was produced in the course of discharge of a bank of capacitors. The voltage and the coil current in 1.5 ms pulses did not exceed 2.5 kV and 6 kA, respectively (total storage energy was about 5.6 kJ). The pulse-to-pulse reproducibility of the magnetic field was within 0.05 %. Due to limitations caused by cooling the pulsed solenoid, the repetition rate was limited by one shot in a minute. After more than 2500 pulses with magnetic fields above 30 T no signs of solenoid deterioration had been observed. The oscilloscope trace of solenoid current is show in Fig. 2. The current is not a half of sinusoidal due to power supply with energy recovery – after maximum current the process of capacitor bank recharge was started. For this purpose two pair of automatically controlled thyristors plug in the opposite direction was used.

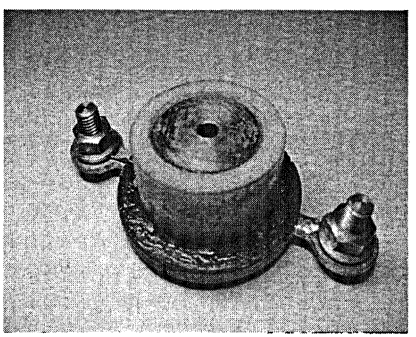

Fig. 1. Prototype of 50 T coil

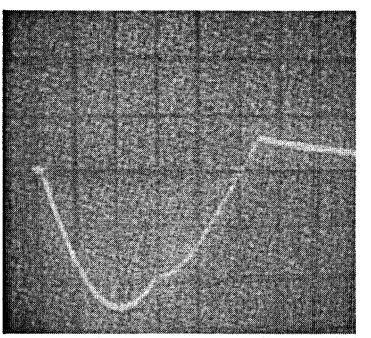

Fig. 2. Oscilloscope trace of coil current (pulse duration 2.5 ms)

Gyrotron photo is shown in Fig. 3 and block diagram of the experimental facility is shown in Fig. 4.

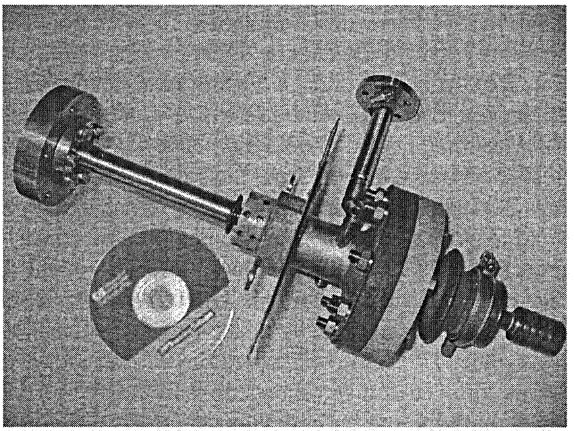

Fig. 3. Photo of the gyrotron with pulse solenoid producing 50 T magnetic field. Electron gun is on the right and the output window is on the left.

Gyrotron components included the conventional cylindrical cavity (3 mm diameter and 3 mm length of a straight section) and the diode-type magnetron injection gun (accelerating voltage 20–25 kV, beam current up to 5 A, pulse duration 50 microseconds). The cavity was made of a beryl bronze; its diffractive and ohmic Q was estimated as 2500 and 8200, respectively. The high-voltage pulse was synchronized with the peak of the pulsed magnetic field as shown in Fig. 5*a*.

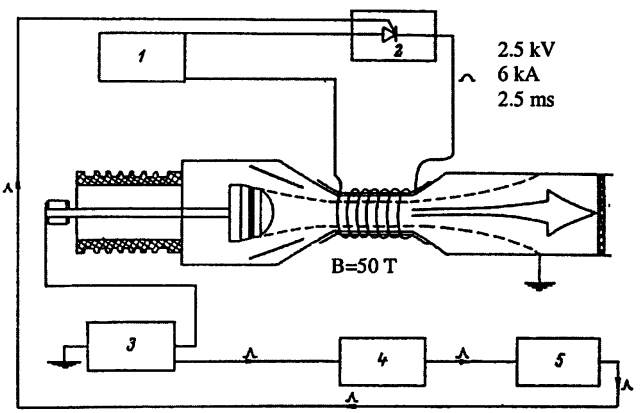

Fig. 4. Block diagram of the experimental facility: *1* – capacitor bank, *2* – thyristor switch, *3* – high voltage power supply, *4* – delay unit, *5* – control unit

Experimental results

Experimental results were obtained for high frequency operation at the fundamental cyclotron resonance. Detection of microwave power was made by a silicon point contact diode and by the dummy load. In our experiment, the calorimeter with the sensitivity allowing for detecting the microwave energy in single shots at a 10 mJ level [14] were used. By varying the magnetic field, a number of various modes with frequencies close to 1 THz and the output power at about 1 kW level were excited in a step-tunable manner. At the magnetic field close to 38.5 T, the transverse-electric ($TE_{17,4}$) mode was excited at 1.022 THz frequency. The microwave pulse of this mode is shown in Fig. 5*b*. The radiation power averaged over the pulse was 1.5 kW [15] and peak power was 2.7 kW. This power level for a 24 kV, 3 A electron beam corresponds to 2.2 % output efficiency. From the relation between diffractive and ohmic quality factors it follows that this value corresponds to the interaction efficiency (for a reasonable value of the orbital-to-axial velocity ratio about 1.2–1.3) of about 5 %. The main reason for a relatively low efficiency is the cavity length which is about two times longer than the optimal one. However, in a gyrotron with so long cavity the start current is much lower than the beam current that ensures the excitation of the desired mode.

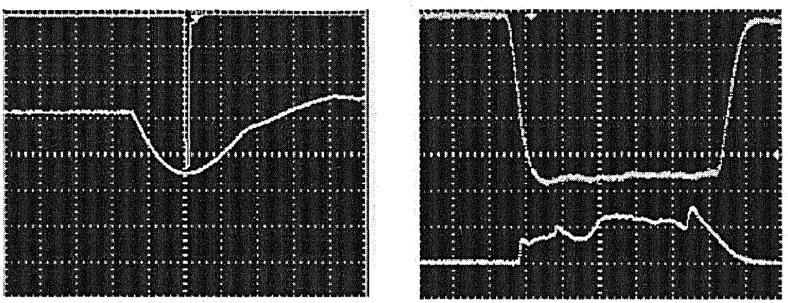

a *b*

Fig. 5. The 50 μs high-voltage pulse (*a*) synchronized with the peak of the pulsed magnetic field. Horizontal scale is 500 μs per division. The microwave pulse of the $TE_{17,4}$ operating mode (*b*). Upper trace – high voltage pulse, lower trace – microwave signal from detector. Horizontal scale is 10 μs per division.

To measure the THz frequency in a device operating in single shots is a serious problem because of the absence of standard instruments. The preliminary measurements were made by cut-off waveguide. Unfortunately, for 0.88 THz diameter of cut-off waveguide is 0.2 mm only and it looks difficult to manufacture this waveguide with high enough accuracy. Nevertheless, the measurements indicates the signal after cut-off section during high voltage pulse and no signal if waveguide input closed by metallic plate. It means that the detected signal is the real one, not the foil. The accurate method of frequency measurements was based

on mixing the gyrotron signal with the signal from a millimeter-wave frequency synthesizer. The block diagram of the frequency measurement section of the experimental setup is shown in Fig. 6. The measurement method is closed to the one described in [16]. The distinction is in the fact that in our experiment the gyrotron frequency was slightly varied from pulse to pulse. Therefore, to get the intermediate frequency (IF) in a relatively narrow frequency band of the IF amplifier (1 GHz) the frequency of the backward-wave oscillator (BWO) shown in Fig. 6 was swiped during the microwave pulse several times. Then, by gradually narrowing the bandwidth of BWO frequency modulation it was possible to determine the radiation with the precision determined by the bandwidth of the IF amplifier given above. The typical oscilloscope traces are shown in Fig. 7. The measured frequency 1.022 THz was close to the cyclotron frequency defined by the magnetic field which is equal to 1.024 THz. Brief estimation of the frequency bandwidth based on experimental data is about 10 MHz. The mistake of frequency definition from power balance is about 2 % from measured frequency which means good design and technology of solenoid and gyrotron cavity manufacturing.

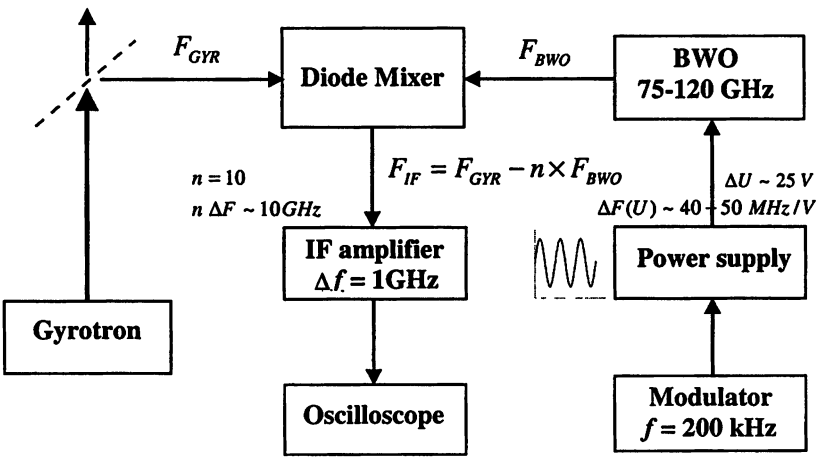

Fig. 6. Block diagram of the frequency measurement section of the experimental setup and example of oscilloscope trace.

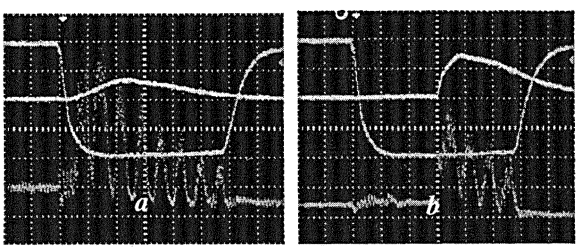

Fig. 7. The oscilloscope trace of frequency measuring system. If the intermediate frequency is inside IF amplifier band (1 GHz), the output signal is differ from zero.

So, in the first experiments with a gyrotron operating in pulsed magnetic field, coherent THz radiation with the microwave power of 1.5 kW and the microwave energy 75 mJ in single shots was obtained. After success of the first experiments the storage energy of power supply was improved to increase the current (generally speaking, up to maximum current closed to coil destruction). For this purpose the capacitor bank was increased from 1.8 mF to 2.3 mF. As a result maximum magnetic field equal 50 T was achieved and no any problem during operation was observed after several hundreds pulses with magnetic field higher than 45 T.

The oscilloscope traces of coil current for 40 T and 50 T operation regimes are shown in Fig. 8. Due to coil cooling limitation the repetition frequency was reduced to one shot per five minutes. The oscillation frequency estimation was made based on coil current value. The highest for gyrotrons generation frequency 1.3 THz with averaged over the pulse radiation power about 0.5 kW has been obtained at the magnetic field 48.7 T.

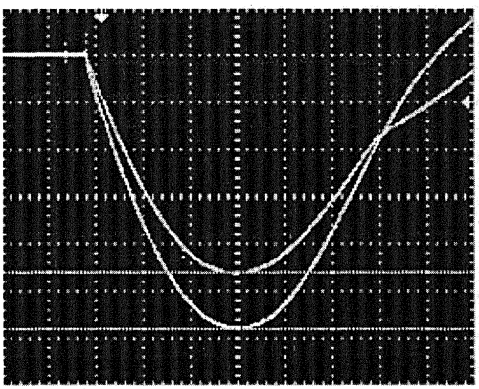

Fig. 8. The coil current oscillograms for 40 T (–0.9 V) and 50 T (–1.17 V) regimes

The experimental results are summarized in the Table.

Main output parameters of pulsed magnetic field gyrotron

Magnetic field, T	34.2	35.4	36.9	37.5	38.3	48.7
Oscillation frequency, THz	0.914	0.945	0.984	1.002	1.024	1.300
Microwave pulse energy, mJ	60	63	62	87	60	10
Pulse duration, μs	40	40	50	40	40	20
Average power, kW	1.46	1.58	1.25	1.75	1.58	0.5
Operating mode	$TE_{2,9}$	$TE_{15,4}$	$TE_{16,4}$	$TE_{6,8}$	$TE_{17,4}$	$TE_{24,4}$

There are some plans to developed improved solenoid cooling based on active pumping of liquid nitrogen. The new version of solenoid is under construction now. Also there are plans to developed similar gyrotrons with internal mode converter

and modified cooling system allowing for operation with higher repetition rate (up to two Hz) and high average power.

This work was supported by CDRF Grant RUP1-2688-NN-05, RFBR-JSPS Grant 06-02-91176 and RFBR Grant 08-08-01058. The authors are grateful to V. Malyshev, G. Golubyatnikov and Yu. Rodin for their help during experiments preparation and tests.

References

1. *Zaytsev N. I, Pankratova T. B., Petelin M. I., Flyagin V. A.* Radio Eng. Electron Phys., **19**, 103 (1974).
2. *Flyagin V. A., Luchinin A. G., Nusinovich G. S.* Int. J. of Infrared and MM Waves, **4**, 4, 629 (1983).
3. *Pankratova T. B., Nusinovich G. S.* Sov. Phys., Tech. Phys., **34**, 8, 912 (1989).
4. *Antakov I. I., Gintzburg V. A., Zagryadskaya L. I., Nikoleav L. V.* Electronnaya Tekhnika, Ser. Electronica SVCh, **8**, 20 (1975).
5. *Idehara T. [et al.]* IEEE Trans. on Plasma Science, **27**, 2, 340 (1999).
6. *Idehara T. [et al.]* Int. J. IRMM Waves, **27**, 3, 319-331, (2006).
7. *Idehara T. [et al.]* Int. J. IRMM Waves, **29**, 2, 131 (2008).
8. *Hong K., Brand F., Idehara T.* J. Ap. Phys., **74**, 8, 5250 (1993).
9. *Saito T.* Joint 33 Int. Conf. on IRMM Waves and 16 Int. Conf. on Terahertz Electronics, Pasadena, USA, F2A3.1207, 2008.
10. *Kreischer K., Grimm T., Guss W., Temkin R.* Technical Digest of the Int. Electron Devices Meeting, 751 (1989).
11 *Hornstein M. K. [et al.]* IEEE Trans. Electron Devices, **52**, 798 (2005).
12 *Bratman V. L. [et al.]* AIP Conf. Proc. of 7th Workshop on High Energy Density and High Power RF, **807**, 356 (2006).
13. *Luchinin A. G., Glyavin M. Yu., Malyshev V. A.* Abstracts 6 Int. Workshop "Strong microwaves in plasmas", N. Novgorod, Russia, S40 (2005).
14. *Belousov V. I. [et al.]* Instr. and Experim. Techniques, **39**, 402 (1996).
15. *Glyavin M., Luchinin A., Golubiatnikov G.* Phys. Rev. Lett., 100, 015101 (2008).
16 *Tretyakov M., Kalynov Yu.* Instrum. and Experim. Techniques, **49**, 661 (2006).

DEVELOPMENT OF 260 GHz SECOND HARMONIC CW GYROTRON WITH HIGH STABILITY OF OUTPUT PARAMETERS FOR DNP SPECTROSCOPY

V. E. Zapevalov, A. Sh. Fix, E. A. Kopelovich, A. N. Kuftin, O. V. Malygin, V. N. Manuilov, M. A. Moiseev, A. S. Sedov, N. A. Zavolsky

Institute of Applied Physics, Russian Academy of Sciences,
Nizhny Novgorod, Russia
GYCOM Ltd. Nizhny Novgorod, Russia

The results of development of CW 260 GHz gyrotron with an output power 100–200 W and its magnetic system are presented. Numerical optimization of the gyrotron key subsystems was considered. Dependences of efficiency and output power of gyrotron on magnetic field and electron beam parameters were studied. Mode interaction effects at fundamental and second harmonics of gyro-frequency were investigated. Requirements for stability of parameters of high voltage power supply and current were specified.

Introduction

The interest for the source of coherent electromagnetic radiation of frequency range of 200–400 GHz with an output power level of 10–200 W has been recently grown with regard to various scientific and technical applications such as diagnostics of dense plasma, the dynamic nuclear polarization spectroscopy (DNP) of atoms and molecules and others [1–3]. In this frequency range one of the most promising sources of this power level are gyrotrons. The majority of such gyrotrons are designed for operation at high harmonic of cyclotron frequency due to the difficulty of creating of high magnetostatic fields. These gyrotrons usually use relatively low operating modes, an accelerating voltage 10–30 kV and beam currents up to 1 A.

This paper is devoted to design of 258.6 GHz middle-power (≈100 W) gyrotron at the second harmonic of the gyro-frequency for DNP spectroscopy. Choice of the best operating modes, limited by the allowable density range of parasitic modes and by the possibility of electron beam creation by magnetron-injection gun (MIG) [4, 5], was presented. An optimization of the cavity profile was considered. Efficiency of gyrotron with operating mode the $TE_{-2,3}$, with the acceleration voltage 15 kV and current of electron beam up to 0.5 A was determined. Mode interaction effects at fundamental and second harmonics of gyro-frequency were considered as well. Requirements for gyrotron power supplies parameters and cooling system, that are to provide the stability of output power and frequency on the level of 10 % and 10^{-5} correspondingly, were determined. For this gyrotron especially designed magnetic system described below. Numerical optimization of electron gun was produced also.

1. Magnetic system

The main part of the magnetic system for the gyrotron is a superconducting cryomagnet. The maximum intensity of the longitudinal component of the magnetic field induction is 5 T and the length of homogeneous section is about 36 mm (accuracy is 0.2 %). Diameter of the "warm" aperture is 47 mm and its length is 620 mm. Additional normal-conducting ("warm") coil is used for the fine adjustment of the magnetic field in the electron gun region.

2. Optimization of the cavity

Selection of the most suitable operating modes is limited by the allowable density of specter of parasitic modes frequencies, and by the capability of helical electron beam (HEB) formation systems [4, 5]. Using the $TE_{-2,3}$ and $TE_{-6,5}$ as the operating modes with a guiding radius of the electron beam 0.984 mm, the current could be expected up to $I = 0.5$–0.7 A (here and below negative azimuthally index means that mode has a counter-rotation direction to the electron beam). Considered modes have relatively rare parasitic modes spectrum including the most dangerous ones, which are excited at the fundamental harmonic of gyrofrequency. Those operating modes have previously been used in experimental gyrotrons [5, 6], where efficiency of 4–6 % and output power 300–700 W had been achieved. With further increase of the beam radius and using higher operating modes, for example the $TE_{-8,5}$, the range free of parasitic modes is quickly compressed and there appears the risk of self-excitation of mode at the fundamental gyro-frequency. Here we consider only operating mode the $TE_{-2,3}$, selected on the basis of mutual requiring characteristics, with an accelerating voltage $U_0 = 15$ kV and beam current up to $I = 0.5$ A.

The optimization of the high-quality factor cavity of middle-power gyrotron at the second harmonic of the gyro-frequency differs fundamentally on the optimization of the cavity of powerful gyrotrons at the fundamental gyro-frequency because of two main reasons. The first one is dominant influence of ohmic losses (relation of the total quality of the cavity to ohmic quality $Q / Q_{ohm} > 0.5$) on the efficiency. Quality factor of the cavity is determined by the following expression $Q = Q_{duf} \cdot Q_{ohm} / \left(Q_{dif} + Q_{ohm}\right)$, where $Q_{ohm} = 680 \cdot \nu_{mp} \left(1 - m^2 / \nu_{mp}^{\ 2}\right) \sqrt{\lambda(mm)}$ – is the ohmic quality of cavity made of copper, taking into account the empirical factor 0.5 to the real properties of walls, Q_{dif} is the diffraction quality. The second reason is the possibility to ignore the restriction on the limiting specific ohmic load due to its relative smallness ($P_{ohm} < 0.5$ kW/cm^2), and so cavity does not require the use of intense cooling. The optimization of cavity profile mainly consists in finding an effective length of the cavity and minimization the ratio Q/Q_{ohm} for achievement high efficiency.

The cavity profile with cylindrical section with the length L_p and input down-tapering section were considered. Fig. 1 shows dependences of output power (at the cavity output) and oscillation frequency on magnetic field for accelerating voltage $U_0 = 15$ kV, several values of beam current $I = 0.2$–0.5 A and pitch-factor $g = 1$.

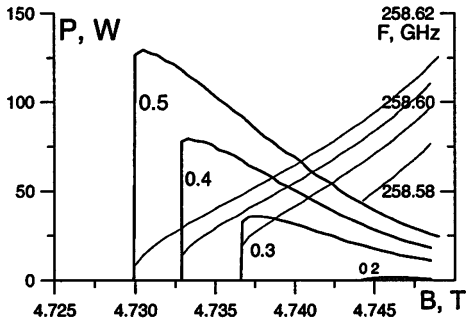

Fig. 1. Dependences of output power and frequency on magnetic field for beam currents $I = 0.2 - 0.5$ A and $U_0 = 15$ kV.

3. Map of oscillating modes of gyrotron

For stability of operation of the gyrotron at the second harmonic of the gyro-frequency main danger is self-excitation of modes that are synchronous to the fundamental harmonic. Their starting currents are greatly smaller than the currents of modes at the second harmonic of the gyro-frequency [4]. Self-excitation of modes at the third harmonic and above is excluded because their starting currents are greatly bigger. Fig. 2 shows map of oscillating modes for the gyrotron with optimized cavity. The map includes zones of oscillation of operating mode the $TE_{-2,3}$ and parasitic modes, limited by starting currents, and also the dependence of efficiency from the magnetic field $\eta(B)$. Starting currents of parasitic modes are shown by solid lines for velocity spread of HEB $\delta v_\perp = 0.3$ and dotted lines for $\delta v_\perp = 0$. It should be noted that parasitic mode $TE_{3,1}$, with a frequency distant from the critical one (traveling wave), synchronous with the electron beam at the fundamental harmonic of gyro-frequency self-excited for the calculating model without velocity spread (which doesn't consider the dispersion of electron beam). However parasitic mode the $TE_{3,1}$ not self-exited in advanced simulating model, taking into account

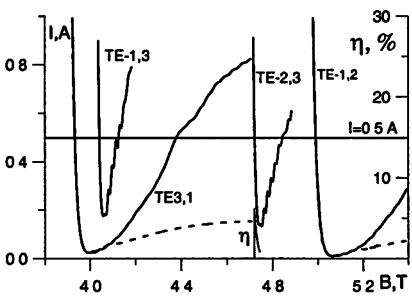

Fig. 2. Map of oscillating modes of gyrotron

HEB velocity spread $\delta v_\perp = 0.3$, i.e. with the relative value close to reality for millimeter wave gyrotrons [2, 3].

In some cases, reduction in the accelerating voltage greatly simplifies the using of middle-power gyrotrons and makes the system as a whole be cheaper. Fig. 3 shows the dependences of efficiency and output power, optimized for the magnetic field, on the accelerating voltage for the beam current $I = 0.5$ A and different pitch-factors. The calculations show that the efficiency is relatively weakly dependent on accelerating voltage, especially when $g = 1.2$, power of 100 W is reached at $U_0 = 5$–6 kV.

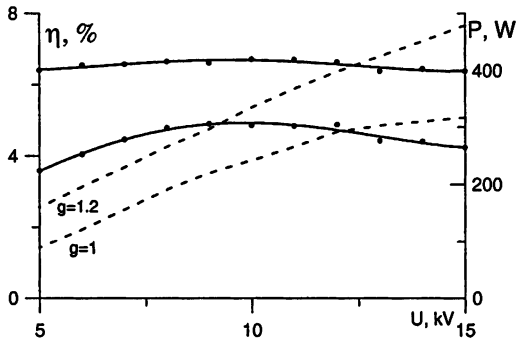

Fig. 3. Efficiency and output power on accelerating voltage

4. Electron gun

For the creation of HEB gyrotron magnetron-injection gun of the triode-type is chosen. It gives the possibility to correct parameters of HEB, changing regardless anode and accelerating voltage and allows to adjust (or stabilize) the operating frequency and power of gyrotron. Calculated parameters of electron gun are the following: accelerating voltage $U_0 = 15$ kV, anode voltage $U_a = 12$ kV, beam current – up to 0.5 A, cathode radius – 5 mm, pitch-factor of electrons $g = 1.1$, the relative spread of transverse velocities is 0.3–0.4. In order to achieve required parameters electrodes' profiles of electron gun were optimized numerically by means of the trajectory analyses of HEB.

5. Stability of gyrotron output radiation

One of the main requirements for this gyrotron is maintaining the output power and operating frequency stability at the level of 10 % and $\Delta f/f = 10^{-5}$, correspondingly. Table 1 summarizes maximum deviations of parameters of required power supplies providing relative changes of operating parameters which does not exceed declared values. Thus, it was necessary to develop a set of new power supplies for gyrotron system in order to execute given conditions.

Table 1

χ_i	$U_0 / U_{0,st}$	$U_a / U_{a,st}$	I / I_{st}	$B_0 / B_{0,st}$
$dP/d\chi/P_{st}$	5.0	–4.1	0.384	–136.6
$df/d\chi/f_{st}$	$1.4 \cdot 10^{-3}$	$1.9 \cdot 10^{-3}$	$1.32 \cdot 10^{-3}$	$3.9 \cdot 10^{-2}$
$\Delta\chi_i$	$7.1 \cdot 10^{-3}$	$5.2 \cdot 10^{-3}$	$7.6 \cdot 10^{-3}$	$2.6 \cdot 10^{-4}$

In addition to fluctuations of the power supplies' parameters, changes in profile of the cavity, defined by the work of the cooling system leads to the frequency instability. In the presence of average ohmic load on the walls of cavity 100–200 W/cm^2 and ohmic power losses of about 1 kW the cavity requires a continuous flow of cooling water 0.25 L/s with its heating at 1 °C. Heating of the cavity at 0.5 °C means the relative frequency drift 10^{-5} because of the diameter increase, in accordance with the coefficient of thermal expansion of copper $\approx 1.7 \cdot 10^{-5}$. Cooling system has to ensure the continuity of temperature cavity block with an accuracy of better than 0.5 °C.

Conclusions

Preliminary analysis and optimization of the 258.6 GHz gyrotron design demonstrate the possibility of reaching 5–8 % efficiency and power up to 350–400 W, with the acceleration voltage 15 kV and beam current 0.5 A. There is no evident risk of the self-excitation of parasitic modes when gyrotron use the operating mode the $TE_{-2,3}$. The relative stability of the frequency of 10^{-5} is achieved with relatively fluctuations parameters: no more than 0.5 % for voltage, 0.5 % for the beam current and 0.02 % for magnetic field. Gyrotron cavity does not require intense cooling because its ohmic load does not exceed 100–200 W/cm^2, but the cooling system has to keep the stable temperature of the cavity with an accuracy of less than 0.5 °C.

References

1. *Gaponov-Grekhov A V. and Granatstein V. L.* Applications of High-Power Microwaves, Artech House, Norwood, MA. (1994).
2. *Thumm M.* State-of-the-Art of High Power Gyro-Devices and Free Electron Masers. FZK Karlsruhe, 2006.
3. *Saito T., Nakano T., Hoshizuki H. et al.* Perfomance test of CW 300 GHz Gyrotron FU CW I // Int. J. Infrared and MM Waves. 2007. V. 28. P. 1063.
4. *Nusinovich Gregory S.* Introduction to the physics of gyrotrons, The Johns Hopkins University Press, 2004.
5. *Zaitsev N, Pankratova T., Petelin M. et al.* Millimeter and submillimeter wave giritron // Radiotekh. I Electron. Int. 1974. V. 19. P. 1056.
6. *Spira S., Kreicher K., Temkin R.* Submillimeter gyrotronfor space based radar // Discrimination & Signal Processing & Superconducting Materials & Instrumentation. 1988. V. 879. P. 58.

METAL MESH BASED QUASI-OPTICAL SELECTIVE COMPONENTS FOR THZ-, SUBMM-WAVE AND MICROWAVE APPLICATIONS

S. A. Kuznetsov[1,2], A. V. Arzhannikov[1,2], P. V. Kalinin[2], V. V. Kubarev[2], A. V. Gelfand[3], N. I. Fedorinina[3], Yu. G. Goncharov[4], B. P. Gorshunov[4], M. Sorolla[5], M. Navarro-Cia[5], M. Beruete[5], M. Aznabet[5]

[1] Novosibirsk State University, Research-and-Education Centre "Nanosystems and Modern Materials", Novosibirsk, Russia
[2] Budker Institute of Nuclear Physics SB RAS, Novosibirsk, Russia
[3] Institute of Semiconductor Physics SB RAS, Novosibirsk Branch "TDIAM", Novosibirsk, Russia
[4] A. M. Prokhorov General Physics Institute RAS, Moscow, Russia
[5] Millimeter and Terahertz Wave Laboratory, Universidad Pública de Navarra, Pamplona, Spain

We describe results of development and application of passive quasi-optical selective devices based on single- and multi-layer metal mesh structures with subwavelength topology of mesh cells designed for filtering radiation at frequencies from a few tens GHz up to ten THz: frequency filters, polarizers, metastructures.

Introduction

Intense study of quasi-optical properties of planar periodic arrays comprised by densely packed metallized elements (metal mesh structures or MMS) was initiated in the end of 1960s by phenomenological works of R. Ulrich who first investigated in details frequency response of different MMS for the purpose of their application in long-wave FIR filters [1]. It became clear that currents induced by the incident EM-wave on the MMS surface strongly depend on mesh topology that enables effectively control amplitude, phase and polarization response of MMS opening up possibilities for creating versatile selective devices. Easily fabricated by a well-tailored photolithographic and other micromachining techniques of micron accuracy the single- and multi-layer MMS serve as the best alternative for controlling radiation beams from microwave to terahertz frequencies.

In this report we briefly consider phenomenological properties of MMS for frequencies below the diffraction onset and present results of MMS development for different applications: spectral analysis of radiation from 4mm-wave FEM, submm-$2\omega_p$-radiometry of hot turbulent plasma at GOL-3 facility, harmonics filtering at Novosibirsk THz-FEL, realization of left-handed EM-metamaterials.

MMS Terminology and Phenomenology

It is accepted to divide MMS into *capacitive* (C) and *inductive* (I) ones which differ either mesh cells are electrically isolated or not on a wavelength λ (or

smaller) scale respectively. For complimentary geometry C-MMS and I-MMS manifest complimentary frequency response, and at low frequencies ($\omega << 1$, where $\omega = g/\lambda$, g – attice parameter) C-MMS is radiation-transparent while I-MMS is opaque that in LC-transmission line representation means capacitive or inductive mesh reactance respectively (Fig. 1*a*). As ω grows, the $|S_{12}|^2$-parameter increases steadily for a simple I-MMS up to the point $\omega_{res} \approx (LC)^{-1/2}$ of resonant transmission (or reflection for C-MMS) lying slightly below the diffraction onset ω_{diff}, which for a thin MMS on the dielectric (n_1, n_2)-interface is derived from the equation $\omega_{diff} = \min[1/(n_2+n_1\sin\theta),\ 1/(n_1+n_1\sin\theta)]$. Above ω_{diff} $|S_{12}|^2$ drops due to diffraction losses that limits application of MMS at higher frequencies.

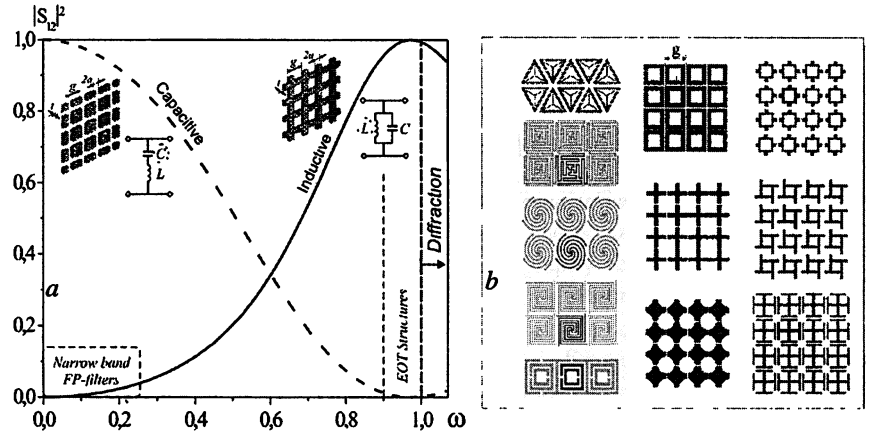

Fig. 1. Qualitative transmittance behavior for simple inductive and capacitive PEC meshes (*a*) and examples of sophisticated FSS (*b*).

A simple MMS with regular-polygon-shaped cells has only one resonance ω_{res} close to ω_{diff}, caused by a "plasmon-polariton-like" mechanism resulting from mesh periodicity and explained by near-field amplification and constructive far-field interference from radiating apertures. Underlying for the extraordinary transmission (EOT) phenomenon [2] this effect is very sensitive to oblique incidence that limits application of simple MMS in band-pass or band-stop filtering although their employment as high-pass or low-pass filters is very effective [1]. Suppression of incident angle dependence in band-selective filtration is realized due to shifting ω_{res} to lower frequencies by increasing MSS intra- or inter-cell capacitance & (or) inductance. Such MMS with more sophisticated topology, which specifies a type, form and number of desired LF LC-resonances, are known as *selfresonant* MMS or *frequency selective surfaces* (FSS) [3] (Fig. 1*b*). In most cases the fundamental resonance of FSS nevertheless is of order of cell size ($g \sim 0.3 \div 0.7\lambda_{res}$) like in photonic crystals. Last years intense studies are devoted to search of FSS with $g << \lambda_{res}$ appropriate for realizing the concept of *left-*

handed metamaterials which exhibit negative values of effective "bulk-like" permeability & (or) permittivity at desired frequencies that generally is unachievable in natural media (see e.g. [4]).

Narrow-band Fabry–Perot and EOT Filters

As for inductive MMS the reflectance R is high at $\omega << 1$ (Fig. 1*a*) this operation mode is very suitable for realizing narrow-band band-pass filtration by employing two-layer MMS in a Fabry–Perot configuration. We have successfully developed and applied such interference filters in a 4-channel spectral system for analyzing radiation from a planar 75 GHz-FEM (ELMI-device, BINP [5]), Fig. 2. Each MMS with CA-size 100×100 mm was created by a printed-circuit-card production technique and had the following geometrical parameters: g = 1 mm, a = 0.32 mm, t = 0.018 mm, Δ = 0.9 mm, $L \equiv$ 8 mm. It provided $R \approx 0.9$ at 73–77 GHz resulted in averaged values of filter's FWHM and contrast 0.68 GHz and 25 dB respectively. The frequency shift ~0.95 GHz for adjacent spectral channels was tuned by 100 μm-variation of the inter-mesh gap L.

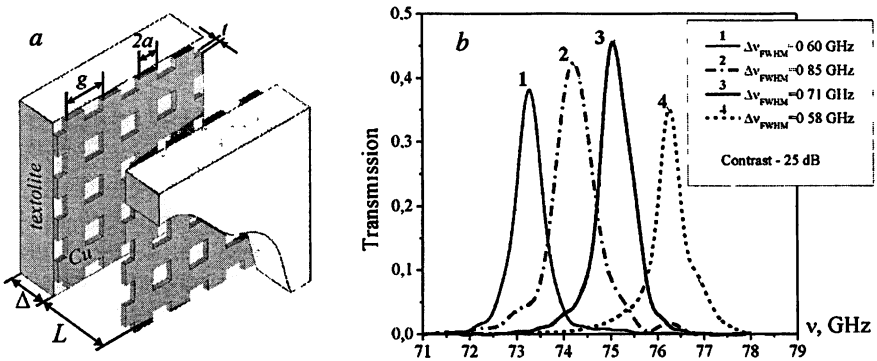

Fig. 2. Implementation of Fabry–Perot filters for the 4 mm-wave region (*a*) and frequency response of four filters standing in a quasi-optical transmission line of the 4-channel spectral diagnostics (*b*).

Alternative to Fabry–Perot MMS, narrow-band selectivity can be realized as well by a single-layer inductive MMS of a "hole array" type with parameters satisfying the EOT operation regime: $\omega \approx \omega_{diff}$, $\omega_{hole's\ cut\text{-}off} > \omega_{diff}$. In this case the effect of multiple amplification of the E-field near MSS surface compensates its small "geometric" transparency that provides close to unity transmission in EOT-resonance. Fig. 3 illustrates simulated response of EOT-arrays optimized for filter applications at the ELMI-device. A numerical milling technique is used for fabricating such MMS.

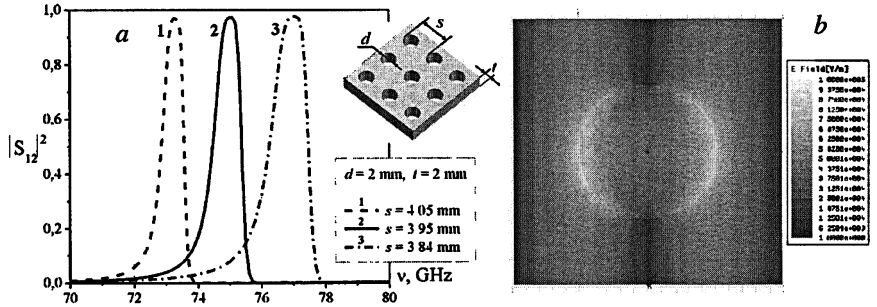

Fig. 3. Simulated in Ansoft HFSS™ spectral transmittance of three narrow-band single-Al-plate EOT-filters at normal incidence (*a*) and E-field magnitude surface distribution at 75 GHz for the filter #2 (*b*).

Polymeric film backed FSS

For subterahertz and terahertz frequencies the topological size of MMS micro-pattern becomes of order ~ 1–100 μm that is very suitable for micro-pattern creation by a well-tailored contact photolithography technique (CPhLT) employed in semiconductor industry. The key problem of non-self-bearing (sub)THz-MMS is the lack of appropriate low absorbing and low dispersive substrates supporting MMS and fitting for CPhLT. We have chosen two polymers as substrate materials for (sub)THz-MMS: polyimide (PI) and polypropylene (PP). PI is ideal for CPhLT, has high fastness and thermostability, while PP exhibits the best optical properties.

Using CPhLT we have fabricated a set of 3.5μ-PI- and 20μ-PP-film-based single-layered 1D- & 2D-MMS (metallization: 0.5μm-Al; CA-size 80 × 80 mm): (sub)THz-polarizers (Fig. 4 *a, d*) and FSS-filters with topology of "inductive crosses" (Fig. 4 *b, c*) and "capacitive rings" (Fig. 4 *e, f*) optimized for filtering radiation harmonics of Novosibirsk terahertz FEL [6, 7]. The inductive FSS (*b, c*) were designed for band-pass selection of the 2nd and 3rd harmonics ($\nu_{II} \approx 4$ THz, $\nu_{III} \approx 6$ THz) against a background of the fundamental generation frequency $\nu_I \approx 2$ THz, whereas capacitive FSS (*e, f*) were optimized for resonant rejection of ν_I at 2.25 THz. At the initial stage of design optimization the resonant wavelengths for "cross" (+) and "ring" (o) topologies were estimated from approximate relations: $\lambda_{res\ (+)} \approx 2L \cdot n_{eff}$, $\lambda_{res\ (o)} \approx \pi d \cdot n_{eff}$ ($n_{eff} = [(\varepsilon+1)/2]^{1/2}$, ε – substrate permittivity).

From Fig. 4*c* it can bee seen that in spite of small thickness absorption in PI limits its application in multilayer structures due to fast degradation of transmittance. In contrast to PI, PP is most suitable for application in multilayer FSS-filters and metastructures.

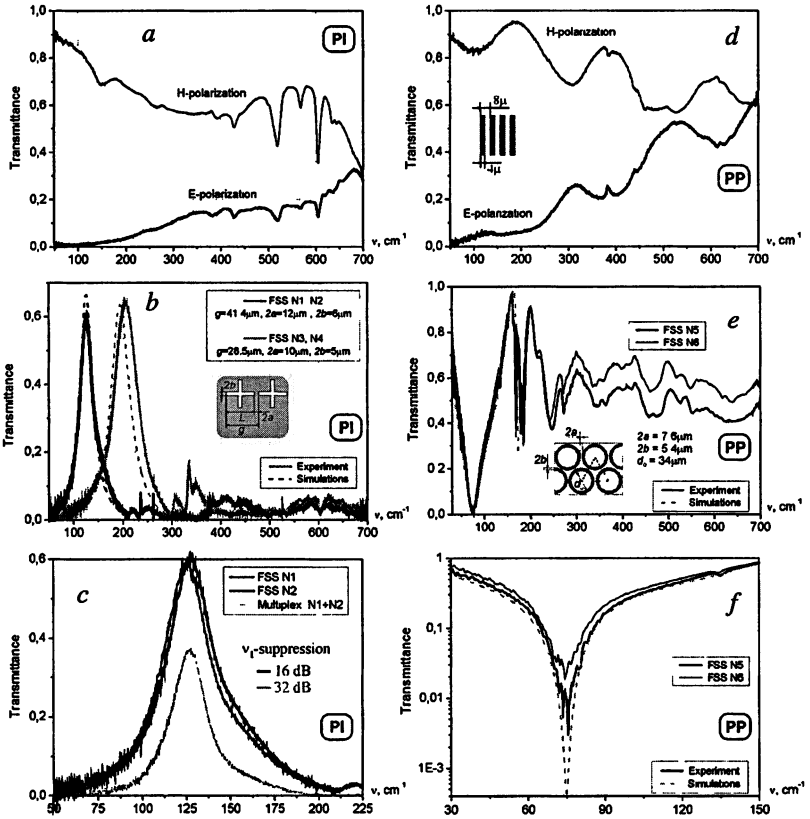

Fig. 4. The results of "Bruker IFS 66v/s" FT-characterization of 3.5μm-PI-backed 4 × 8μ-polarizer (*a*) & "inductive crosses" FSS (*b, c*) and 20μm-PP-backed 4 × 8μ-polarizer (*d*) & "capacitive rings" FSS (*e, f*)

Fig. 5 illustrates our first results on development of 2-layer submm band-pass filters based on PP-film-backed FSS designed for application in a 4-channel $2\omega_p$-radiometric spectral diagnostics of 250–450 GHz emission from hot & turbulent plasma at the GOL-3 nuclear fusion facility [8]. FSS with anisotropic topology ("inductive slots") were used to provide ~ 40 GHz frequency shift in transmission band positions for *X*- and *Y*-polarized radiation. It let us to employ only two FSS-structures for realizing 4 spectral channels that reduced fabrication costs. A hot lamination technique was used to fuse HQ 40μm-PP-films for creating (*a*)-configuration, while non-HQ 170μm-PP-films were used for the "fast & cheap" "cold" (*b*)-configuration (see [8]). At present, we master aforementioned approaches for fabricating low-cost PP-based subTHz LH-metamaterials. The first positive experience was gained by developing single-layer metasurfaces with

topology of split ring resonators (SRR) and their complimentary structure (CSRR), Fig. 6, [4]. The most important regime for such FSS is realized at co-polar excitation in the vicinity of the lowest-frequency quasi-static resonance where a negative effective permeability concept is expected to be feasible.

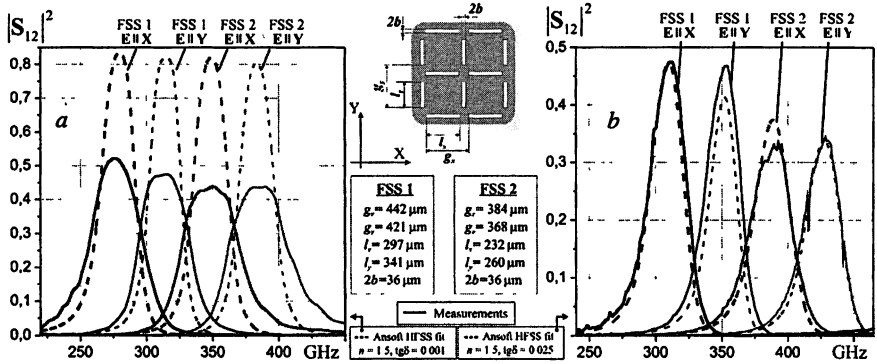

Fig. 5. The results of BWO-characterization for 2-layer FSS-filters of different configurations:
a – 8 × 40μmPP + ***FSS*** + 4 × 40μmPP + ***FSS*** + 8 × 40μmPP; *b* – ***FSS*** + 170μmPP + ***FSS***

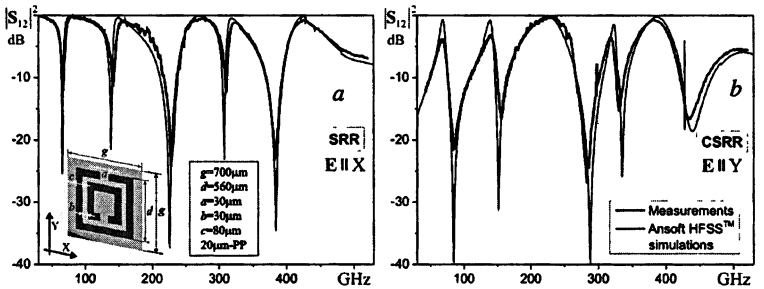

Fig. 6. Co-polar transmittance of subterahertz SRR- (*a*) and CSRR- (*b*) metasurfaces

References

1. *Ulrich R.* Applied Optics **7** (10), 1987–1996 (1968).
2. *Martín-Moreno L. et al.* Phys. Rev. Lett. **86**, 1114–1117 (2001).
3. *Munk B.* Frequency Selective Surfaces: Theory and Design. NY: Wiley, 2000
4. *Aznabet M. et al* Opt. Express **16**, 18312–18319 (2008).
5. *Arzhannikov A. V et al.* NSU Bulletin: Physics **1** (2), 71–81 (2006).
6. *Bolotin V. P. et al.* Nucl. Inst. and Meth. **A543**, 81–84 (2005).
7. *Kuznetsov S. A. et al.* J. Surface Investigation **6**, (2009) (in press).
8. *Kuznetsov S. A. et al.* Guide of "IRMMW-THz'2008" Int. Conf. Paper M3B4. 1743.

PARAMETRIC INSTABILITY IN THE AUTOOSCILLATOR WITH THE DELAYED LOAD REFLECTION

Yu. V. Novozhilova, M. I. Petelin, A. S. Sergeev

Institute of Applied Physics, Nizhny Novgorod, Russia

The number of one-frequency states – longitudinal modes – increases with the growth of the reflection coefficient and the length of the delay line. A mode of this kind can be unstable in some parameter regions. There can be two types of perturbations: a) the perturbations resulting in a slow evolution of principal mode amplitude and frequency; b) the perturbations in the form of two satellites which frequencies are symmetric from that of the principal mode. Relative to the 1st type of the perturbations frequencies of stable and unstable modes alternate. The satellites instability can take place only for modes situated near edges of the set of all stationary frequencies.

1. Introduction

Any auto-oscillator connected by a waveguide with a load (Fig. 1) represents a distributed system with an infinite number of degrees of freedom. As the system parameters are time-independent, relevant self-consistent equations admit existence of stationary single-frequency states (modes). At a sufficiently large magnitude of the negative conductivity of the active element R in Fig. 1, some of these modes may have non-zero amplitudes. The number of admitted stationary modes depends on the waveguide length and the reflection from the load.

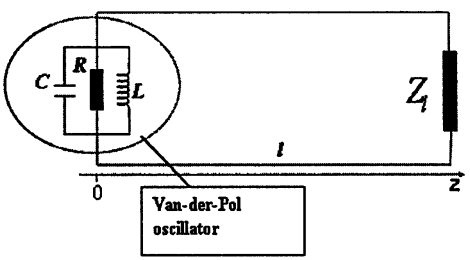

Fig. 1. A Van-der-Pol oscillator connected with a remote load

At some region of the system parameters, stationary modes may be unstable [1], resulting in an auto-modulation up to a chaos [1–11].

This paper is aimed to study the stability of single-frequency states analytically, scrutinizing the perturbations spectrum in detail.

2. The main limitations

For the model shown in Fig. 1, assume

1. the active element negative conductivity being voltage-quadratic: the voltage $\hat{U}$ and the current $\hat{I}_R$ are related by

$$\hat{I}_R = -\hat{U}(1-\nu\hat{U}^2)/R_0\,,\ R_0>0; \qquad (1)$$

2. the load impedance Z_l being close to the line wave impedance ρ

$$Z_l = \rho(1+\delta), \quad |\delta| << 1 \tag{2}$$

(the reflection coefficient is $\delta/2$);

3. the Q-factor of the auto-oscillator resonator being high enough

$$\rho, \ R_0 >> \sqrt{L/C}, \tag{3}$$

so all frequencies are close to the eigen-frequency of the circuit

$$\omega_0 = 1/\sqrt{LC}. \tag{4}$$

3. One-frequency operation

According to (3), (4) the frequency of the active element voltage $U \approx \widehat{U}_c = \mathrm{Re}\left(U_c e^{i\omega_c t}\right)$ is close to the circuit frequency:

$$|\alpha| << 1, \tag{5}$$

$\alpha = \bar{\omega}_{\tilde{n}} - 1$, $\bar{\omega}_c = \omega_c/\omega_0$. For the RF current harmonics situated within the resonator band, the Kirchhoff rule $I_L + I_R + I_C = U_c/Z_2$ gives

$$2\alpha + i\mu\left(1 - \left|\bar{U}_c\right|^2/4\right) = i\left(\eta - re^{-2i\vartheta_c}\right), \tag{6}$$

$\vartheta_c = \omega_c l/c$. is the phase delay at the frequency ω_c, l is the line length, $Z_2 = \left(i\rho\mathrm{tg}\vartheta_c + Z_l\right)/\left(1 + iZ_l\mathrm{tg}\vartheta_c/\rho\right)$ is the load impedance translated to the cross-section $z = 0$ at the frequency ω_c, $\bar{U}_c = \sqrt{3\nu}U_c$, $\mu = \sqrt{L/C}/R_0$, $\eta = \sqrt{L/C}/\rho$, $r = \delta\eta$. At $r = 0$ the equation (5) turns into that for the usual Van-der-Pol oscillator [12].

4. Start modes

According to the equation (6), at small RF fields, $U \to 0$, modes situated within the resonance band (5) are shifted relative to the conservative resonator eigen-frequency (4) by

$$\alpha = i\left(\eta - \mu - re^{-2i\vartheta_c}\right)/2. \tag{7}$$

As at the start stage the reflection from the load, according to (2), may be neglected, all near-resonance modes are self-excited ($\mathrm{Im}\,\alpha < 0$) at

$$\eta < \mu, \tag{8}$$

i.e. when $R_0 < \rho$.

5. Stationary modes

At $\mu > \eta$ the equation (6) may admit a solution at a real frequency

$$2\alpha = -r\sin(2\vartheta_c), \tag{9}$$

with a constant oscillation amplitude

$$\left|\bar{U}_c\right|^2/4 = \left(\mu - \eta + r\cos(2\vartheta_c)\right)/\mu. \tag{10}$$

This amplitude is perturbed insignificantly by the wave reflection from the load: $\left|\bar{U}_c\right|^2 \approx 4(\mu-\eta)/\mu$. The power transmitted to the load is maximal when the active resistance R_0 is a half of the line wave impedance ρ, i.e.

$$\mu \approx 2\eta. \tag{11}$$

The number of admitted stationary modes in the system is determined by the product of the reflection coefficient and the line length: $|r|\vartheta_0$. If the product is small

$$|r|\vartheta_0 < 1, \tag{12}$$

there is only one admitted stationary mode. At

$$|r|\vartheta_0 > 1 \tag{13}$$

several stationary modes are admitted. With the increase of $|r|\vartheta_0$, a new mode appears at

$$r\vartheta_0\cos(2\vartheta_c) = -1, \tag{14}$$

which corresponds to the touch of the straight line and the sinusoid in Fig. 2. The new mode at the touching condition is degenerated and at the further increase of $|r|\vartheta_0$ splits into two ones (Fig. 2*c*).

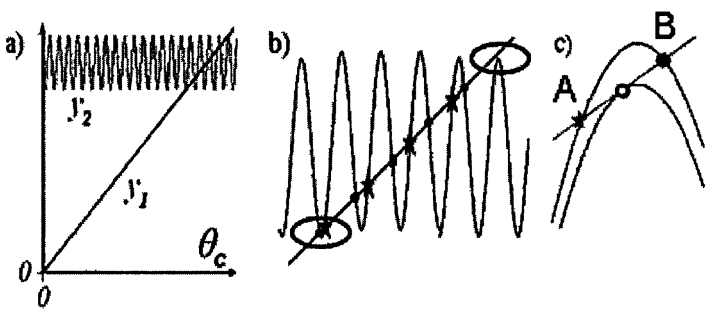

Fig. 2. Graphic solution of the Eq. (9): *a*) the stationary states are the intersections of graphs $y_1(2\vartheta_c) = 2\vartheta_c$ and $y_2(2\vartheta_c) = 2\vartheta_0 - r\vartheta_0\sin(2\vartheta_c)$; *b*) the fragment of Fig. 2*a*, ovals indicate the stationary states, which can be unstable relative to satellites decay (p. 8); *c*) the appearance of the new mode. Self-stable modes is marked by the black circles, self-unstable modes – by the stars, neutral mode – by the grey circle.

Let us emphasize that the equation (6) can be used to describe any one of stationary modes, but not a combination of stationary modes which would be admitted to co-exist simultaneously.

6. The equations of the perturbations

Assume that a stationary mode is admixed with a small $\left(|U_+|/|U_c| \ll 1\right)$ perturbation $\widehat{U}_+ = \mathrm{Re}(U_+ e^{i\omega_+ t})$ at a frequency ω_+. In this case, the active element nonlinearity (1) results in appearance of a current and a voltage at the frequency ω_- symmetrically shifted from the principal mode frequency:

$$2\omega_c = \omega_+ + \omega_-^*, \tag{15}$$

and the Kirchhoff rule gives a relation between satellite amplitudes

$$\left(-1+\bar{\omega}_\pm^2 + i\mu\bar{\omega}_\pm\left(1-\frac{|\bar{U}_{\tilde{n}}|^2}{2}\right) - i\bar{\omega}_\pm\eta\frac{2+\delta-\delta e^{-2i\vartheta_\pm}}{2+\delta+\delta e^{-2i\vartheta}}\right)\bar{U}_\pm = \frac{i\bar{\omega}_\pm\mu\bar{U}_c^2\bar{U}_\mp^*}{4}, \tag{16}$$

here $\bar{U}_\pm = \sqrt{3\nu}U_\pm$, $\vartheta_\pm = \omega_\pm l/c$ are the delayed phases, $\bar{\omega}_\pm = \omega_\pm/\omega_0$.

The equation (15) admits, in particular, a case when real parts of perturbation frequencies are equal to the principal mode frequency:

$$\mathrm{Re}\,\omega_+ = \mathrm{Re}\,\omega_- = \omega_c. \tag{17}$$

Such perturbations represent slow evolution of the principal mode amplitude and frequency.

If

$$\left|\delta e^{-2i\Omega\vartheta_0}\right| \ll 1, \tag{18}$$

where $\Omega = \omega_+ - \omega_{\tilde{n}}$ is the satellite frequency shift relative to the principal mode frequency, the equation (16) has two solutions:

$$\Omega_1 \approx iw, \tag{19}$$

$$\Omega_2 \approx i\left(\chi^2 + 2w\chi\cos(2\vartheta_c)\right)\Big/(4w), \tag{20}$$

where $w = \mu|\bar{U}_c|^2/4$, $\chi = r\left(1-e^{-2i\Omega\vartheta_0}\right)$, and $w >> |r|, |\chi|$ (see (2)). The solution (19) is compatible with the limitation (18), only if the wave reflection from the load back to the oscillator is exponentially small. As for the equation (20) which has an infinite set of roots (including the trivial one $\Omega_2 = 0$ corresponding to an arbitrary time shift), it is valid at any reflections from the load, if a perturbation is growing in time. The latter case is, obviously, most interesting.

Below, growing perturbations satisfying the condition (17) are called the "self-instability"; and growing perturbations satisfying the condition (15) at $\mathrm{Re}\,\omega_+ \neq \mathrm{Re}\,\omega_-^*$ are called the "satellite instability"(the latter parametric effect can be interpreted as a decay of two photons of the strong principal mode into photons of two side satellites).

7. "Self instability" of the stationary state

For perturbations described with the equation (20) under the condition (17) we have:

1) if the product of the reflection coefficient and the line length is small to satisfy (12), the corresponding single stationary state is stable;

2) under the condition (14), the degenerate mode (Fig. 2*c*) has zero increment: $\mathrm{Im}\ \Omega_2 = 0$;

3) at the subsequent increase of $|r|\vartheta_0$ described with Fig. 2*c*, the mode B, which amplitude is increased due to the load reflection, is stable, and the mode A, which amplitude is decreased due to the load reflection, is unstable: the effect reduces to the locking of the auto-oscillator by the weak external force [12];

4) at $|r|\vartheta_0 >> 1$, when the number of equilibrium states is large, self-stable and self-unstable states are alternating (Fig. 2*b*).

8. "Satellite instability" of the stationary state

Perturbations described with the equation (20) at $\mathrm{Re}\,\omega_+ \neq \mathrm{Re}\,\omega_-^*$ depend on 3 parameters: 1) $r = \eta\delta$, which is proportional to the reflection coefficient and inversely proportional to the Q-factor; 2) delay phase ϑ_0 at the eigen-frequency of the circuit, ϑ_0 is proportional to the waveguide length; 3) w, which equals to the relative excess over the start current divided by the Q-factor: $w = (I - I_{st})/(I_{st}Q)$. For a fixed mode, in the r, w, ϑ_0 space we find a surface at which $\mathrm{Im}\,\Omega_2 = 0$. If a dot (r, w, ϑ_0) crosses this stability surface, the sign of $\mathrm{Im}\,\Omega_2$ reverses (the method of D-partition, [13]). The condition $\mathrm{Im}\,\Omega_2 = 0$ applied to the equation (20) gives

$$\Omega = -r^2 \sin(2\Omega\ \vartheta_0)/(2w), \qquad w\cos(2\vartheta_c) = r\cos(2\Omega\vartheta_0). \qquad (21)$$

As it follows from (21) the stationary state can have real frequency satellites only if the number of all stationary states is large: $|r|\vartheta_0 >> 1$, and the principal mode is situated near the edge of the set of all stationary frequencies (Fig. 2*b*). At the optimal load condition (11), the $\mathrm{Im}\ \Omega_2 = 0$ boundaries are shown in Fig. 3.

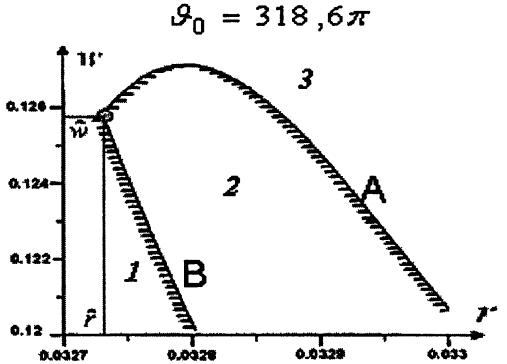

Fig. 3. The boundaries of the satellite-stability regions for the states A and B, shown in Fig. 2*c*. Satellite-unstable regions are hatched. Degenerate mode ($r = \hat{r}$) at $w = \hat{w}$ is neutral relative to both types of the perturbations. At $r < \hat{r}$, A and B modes do not exist. At $r > \hat{r}$ (in the regions 1, 2, 3) the mode A is stable relative to self-perturbations, B is unstable relative to them. Besides, in the region 1 the modes A and B both are unstable relative to satellite decay; in the region 2 the mode A is unstable, B is stable relative to satellite decay; in the region 3 the modes A and B both are stable relative to satellite decay.

9. Conclusion

It seems natural to assume that the "satellite" instability taking place at a certain region of the system parameter space may result into a self-modulation of an auto-oscillator connected with a remote reflecting load [1–11].

References

1. *Landa P. S.* // Regular and Chaotic Oscillations. Springer-Verlag (2001).
2. *Kuznetsov S. P.* // The Dynamic Chaos. Moscow (2001).
3. *Trubetskov D. I.* // The Chaos and the Structures. Moscow (2004).
4. *Grigor'eva E. V., Kashenko S. A.* // New in Synergy. Moscow (2002).
5. *Ryskin N. M., Shigaev A. M.* ZhTPh. **72**, № 7, 1 (2002).
6. *Losson J., Mackey M. C.* Phys. Rev. E. **52**, № 1, 115 (1995).
7. *Ginzburg N. S. et al.* Tech. Phys. Lett. **28**, № 5, 395 (2002).
8. *Airila M. I. et al.* Nucl. Fusion. **43**, № 11, 1454 (2003).
9. *Grudiev A et al.* Int. J. of Infr. and Mill. Waves. **24**, № 4, 429 (2003).
10. *Kulik V. V. et al.* J. of Infr. and Mill. Waves. **19**, № 3, 427 (1998)
11. *Glyavin M. Yu. et al.* Radioph. and Quant. Electr. **43**, № 5, 396 (2000).
12. *Rabinivich M. I., Trubetskov D. I.* // Oscillations and Waves in Linear and Nonlinear Systems. Kluwer Academic, Dordrecht. 1989.
13. *Neimark Yu. I.* Stability of Linearized Systems // L-d. War-Air Ac. (1949).

THE SECOND HARMONIC GYROTRON WITH RECORD EFFICIENCY

Yu. V. Bykov, G. G. Denisov, M. Yu. Glyavin, A. L. Goldenberg, A. G. Luchinin, M. V. Morozkin, D. I. Sobolev

Institute of Applied Physics RAS, Nizhny Novgorod, Russia

The second harmonic 24 GHz gyrotron with the efficiency of 60 % at 6.2 kW CW output power was developed and tested. High efficiency has been achieved using the energy recovery of the spent electron beam. The single stage of a collector potential depression scheme was realized. An internal mode converter with the efficiency of 99.9 % was developed using a synthesis method to minimize the microwave power leakage through an insulator separating the gyrotron body and collector. According to the experimental data, the minimal returning potential value was about 0.2 of the electron beam accelerating voltage, which was in accordance with the result of the theoretical simulation.

Introduction

Gyrotrons are the highest-power sources of millimeter and submillimeter waves witch have many promising practical applications in material processing. A series of 24–28 GHz 3–30 kW CW gyrotrons for technological applications has been developed by the Institute of Applied Physics Russian Academy of Science (IAP RAS) in collaboration with GYCOM Ltd. [1]. These devices have demonstrated efficiency up to 50 %. In continuation of the successful development, operation and application of these tubes, a novel high-efficiency gyrotron with a collector potential depression (CPD) system was developed. Energy recovery of a spent electron beam is one of the most effective ways to enhance significantly the gyrotron efficiency [2–4]. Currently, CPD systems are used in all high-power fundamental-harmonic gyrotrons for fusion. The presented results are the first experimental data for the second harmonic CPD gyrotrons.

The numerical simulation of the electron beam energy spectrum

The efficiency of the energy recovery depends on the minimal electron energy in the collector region. The value of the minimal energy can be calculated by the numerical methods given below.

The simulation is based on the well-known model with a so-called "fixed" structure of the microwave field in a resonator [5]. The electron beam energy can be found by solving the following differential equation written in its standard form (see, for example, [6]):

$$\frac{dp}{d\zeta}+\frac{i}{n}p\left(\Delta+|p|^2-1\right)=if\left(p^*\right)^{n-1}F. \qquad (1)$$

Here p is the electron transverse momentum with the initial condition $p(0)=\exp(i\vartheta_0/n)$, where ϑ_0 is the initial phase of the electron-$(0\le\vartheta_0<2\pi)$, n is the harmonic number, $\zeta=\pi g\beta_\perp z/\lambda$ is the dimensionless longitudinal coordinate (z is the longitudinal coordinate), $0\le\zeta\le\zeta_{out}=\sqrt{3}\mu$, $\mu=\zeta(L)$ is the dimensionless cavity length, c is the velocity of light, $\beta_\perp=v_\perp/c$, $g=v_\perp/v_\parallel$ ($v_\perp$ and $v_\parallel$ are orbital and longitudinal electron velocities, respectively), λ is the wavelength, $\Delta=\frac{2}{\beta_{\perp 0}^2}\frac{(\omega-n\omega_c)}{\omega}$ is the frequency mismatch between the electron cyclotron frequency

$$\omega_c=\frac{eB}{m\cdot c\gamma_{rel}}\ (\gamma_{rel}=1+\frac{U(kV)}{511},B$$

is the operating magnetic field, e is the elementary charge and m is the electron mass) and frequency of gyrotron oscillations ω, F is the microwave field amplitude. The microwave field structure in the resonator with radius R and length L is described by the Gaussian distribution $f(\zeta)=\exp[-\left(2\zeta/\mu-\sqrt{3}\right)^2]$. The electron efficiency without energy recovery is $\eta_{el}=\eta_\perp g^2/(1+g^2)$ and $\eta_\perp=1-\frac{1}{2\pi}\int_0^{2\pi}|p(\zeta_{out})|^2\,d\vartheta_0$ is the orbital efficiency [5].

At the input to the interaction region, all electrons are assumed to have the equal initial energy W_0. For the electron beam without a velocity spread, the maximum efficiency is achieved for fixed parameters: $\mu=\mu_0$, $\Delta=\Delta_0$ and $F=F_0$. These parameters are functions of the voltage and current of the electron beam, the operating magnetic field and the cavity length. To take into account a velocity spread, many (several tens) electron beam fractions with different pitch-factors are used. For each velocity fraction, we recalculate the corresponding parameters μ, Δ and F, which enter Eq. (1), and then calculate the energy spectrum $n(W)$ at the cavity output, the efficiency and the minimal residual energy of electrons W_{min}. The calculated value of the minimal electron beam energy for the second-harmonic 24 GHz CW gyrotron for technological applications [1], which was used at CPD experiments, is slightly more than $0.2W_0$ for the typical 20 % velocity spread in the 6 kW operation regime (U = 17.5 kV, I = 0.75 A).

The experimental tests of the second-harmonic CPD gyrotron

The second harmonic CPD gyrotron has been designed using the standard gyrotron with 47 % efficiency as a prototype. The main parameters of the operation regime are given in Table.

Main parameters of the experimental gyrotron

Operating mode (second-harmonic operation)	TE_{12}
Operating frequency, GHz	24.15
Output power, kW	6.2
Accelerating voltage, kV	17.5
Beam current, A	0.75
Magnetic field, T	0.46
Output efficiency without energy recovery, %	47
Output efficiency with energy recovery, %	**60**

The electron gun and the cavity of the CPD gyrotron was the same as of the prototype tube and the efficiency enhancement was achieved only due to the energy recovery.

The collector of the CPD gyrotron was electrically insulated from the body by a ceramic insulator. To minimize the leakage through the gap in the waveguide, a high-efficiency (with losses less than 0.5 %) mode converter was designed using the method of microwave component synthesis developed at IAP RAS [7, 8]. The converter transformed the gyrotron operating TE_{12} mode to a mixture of the TE_{11} (6.3 %) and TE_{12} (93.7 %) modes with zero electric field at the boundary (see Fig. 1).

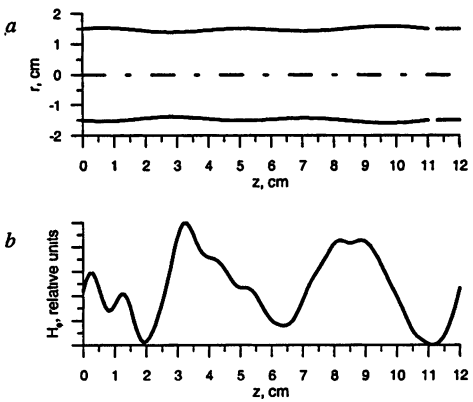

Fig. 1. Waveguide mode converter profile (*a*) and dependence of the azimuthal component of magnetic field (*b*) on the longitudinal coordinate

The operation of a CPD gyrotron requires two high-voltage power supplies (HVPS). The main HVPS is connected between the ground and cathode. Its current is equal to the beam current and its voltage is less by the value U_D than the voltage in the scheme without the energy recovery. The second, low-power (due to close to zero current of reflected electrons) HVPS has the voltage U_D.

In these proof-of-principle experiments the decelerating voltage U_D was produced using a variable resistor, which connected the collector with the ground

(the experimental scheme is similar to that in [9]). The body of the gyrotron was grounded. The gyrotron operation conditions in this case were the same as in the CPD scheme with two power supplies. The total efficiency with regard to the energy recovery is $\eta = \eta_{out} U_0/(U_0 - U_R)$. Here $\eta_{out} = W_{out}/(U_0 I_0)$ is the measured efficiency of the gyrotron, U_0 – accelerating voltage, I_0 – beam current, $U_D = U_R$ – a drop voltage across the resistor and W_{out} – output power.

The output power was measured using a dummy load, which was also insulated from the collector by a teflon spacer. There could be a small leakage of the microwave power through the spacer, and the measured power could be slightly less than the actual output power of the gyrotron.

The experimental data obtained are shown in Fig. 2. With an increase in the decelerating potential, the total gyrotron efficiency first increases until the decelerating voltage becomes close to the minimal returning potential. The subsequent collector voltage increase results in the reflection of electrons and the decrease in the efficiency. According to the experimental data, the minimal returning potential is about 0.2 of the electron beam accelerating voltage and agrees with the calculated value.

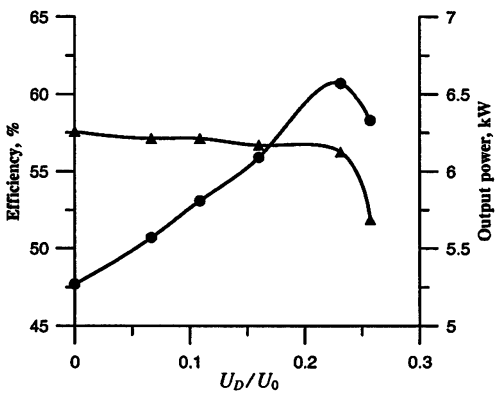

Fig. 2. Output power (triangles) and efficiency (circles) of the gyrotron versus a ratio of the decelerating voltage U_D to the electron beam voltage U_0 ($U_0 = 17.5$ kV, $I_0 = 0.75$ A)

The experimental results demonstrate the highest, achieved to this date, efficiency of the 2nd harmonic CW gyrotrons, although the tested device has not been optimized for the operation in the depressed collector regime. The gyrotron had the cavity length corresponding to the maximum electron efficiency at high output power operation without the CPD. This resulted in low residual energy of the electron beam, thus making energy recovery not efficient enough. The results of preliminary calculations indicate that the cavity length for the CPD operation should be increased to achieve the maximum total efficiency [10].

Conclusion

The second-harmonic 24 GHz 6 kW CW gyrotron for technology application with the efficiency of 60 % has been developed and tested. Significant enhancement of efficiency was obtained using the energy recovery of the spent electron beam.

It is worth noting that the advantages of the CPD operation of the gyrotrons designed for applications are not limited to an increase in the efficiency of the microwave power oscillations and the reduction of the energy consumption only. It is important that the CPD system reduces significantly the thermal load on the collector, thus making it possible to simplify the cooling system. Additionally, the use of the CPD system increases the capabilities of controlling the gyrotron oscillation regime by a low-power HVPS and makes it possible to modulate the output microwave power when it is needed by an application.

This work was partially supported by the RFBR Grants 06-08-00585, 08-08-01058.

References

1. *Bykov Yu. et al.* IEEE Transactions on Plasma Science, **32**, 1, 67 (2004).
2. *Sakamoto K. et al.* Nature Physics, **3**, 411 (2007).
3. *Denisov G. et al.* IEEE International Vacuum Electronics Conference, IVEC07 (2007).
4. *Thumm M.* FZKA 7298, Karlsruhe (2007).
5. *Gaponov A. et al.* Int J. Electronics, **51**, 4, 277 (1981).
6. *Dumbrajs O., Koponen J. P. T.* Physics of plasmas, **6**, 6, 2618 (1999).
7. *Sobolev D. I., Denisov G. G.* Proceedings of VI Int. Workshop Strong Microwaves in Plasmas (N. Novgorod, Russia, 2005), **1**, 342 (2006).
8. *Denisov G., Samsonov S., Sobolev D.* Radiophysics and Quantum Electronics, **49**, 12, 961 (2006).
9. *Glyavin M et al.* Int. J. IRMM Waves, **18**, 11, 2129 (1997).
10. *Glyavin M., Morozkin M.* Radiophysics and Quantum Electronics, **51**, 7 (2008).

CONTINUOUSLY TUNEABLE COAXIAL GYROTRONS

O. Dumbrajs[1], M. Yu. Glyavin[2], T. Idehara[3], Z. C. Ioannidis[4], V. I. Khizhnyak[2], A. G. Luchinin[2], M. V. Morozkin[2], T. Saito[3], I. G. Tigelis[4]

[1]Helsinki University of Technology, Association Euratom-Tekes, P.O. Box 2200, FIN-02015 HUT, Finland
[2]Institute of Applied Physics RAS, 603950, Nizhny Novgorod, Russia
[3]Research Center for Development of Far-Infrared Region, University of Fukui, Bunkyo 3-9-1, Fukui 910-8507, Japan
[4]National and Kapodistrian University of Athens, Faculty of Physics, Department of Electronics, Computing, Telecommunications and Control, 15784 Athens, Greece

The continuous tuning of coaxial gyrotrons is achieved by moving the linearly tapered inner conductor in the axial direction in combination with the proper adjustment of the operating magnetic field. We consider two continuous frequency tuneable CW coaxial gyrotron oscillators: the 330 GHz gyrotron with 3 GHz bandwidth and the 395 GHz gyrotron with 8 GHz bandwidth for scientific applications. The output power of these gyrotrons is several hundreds of watts.

1. Introduction

Frequency step-tunable gyrotrons for Electron Cyclotron Resonance Heating (ECRH) of magnetically confined fusion plasmas and for Electron Cyclotron Current Drive (ECCD) in plasmas were considered in [1, 2]. In recent years, new exciting applications of gyrotrons have emerged beyond fusion plasma applications. For example, Dynamic Nuclear Polarization (DNP) to enhance signal to noise ratio in Nuclear Magnetic Resonance (NMR) [3, 4] and Electron Spin Resonance (ESR) spectroscopy experiments [5]. In these applications, the possibility of tuning the gyrotron frequency is a great advantage.

There are several possibilities to vary the frequency of a gyrotron oscillator by changing: i) the accelerating and modulation voltages (electrical tuning), ii) the magnetic field (magnetic tuning) and iii) the physical dimensions of the oscillator using a split cavity structure or a movable piston (mechanical tuning) (see e.g. [1] and references therein). Recently, an operation in the higher order axial modes was proposed [6, 7] for a smooth variation of frequency within a particular axial mode and between adjacent axial modes. It should be emphasized however that as long as the cavity geometry is not changed during the operation, the tuning is possible only in discrete steps, which are determined by the difference between the eigenvalues of the modes. The exception is the so-called frequency pulling by changing the electron beam parameters while keeping the oscillating mode [8]. However, the latter method has no practical applications, because the bandwidth is proportional to $1/Q_{diff}$ and thus extremely small.

Coaxial cavity gyrotrons open new possibilities in tuning the frequency in a truly continuous way. This is achieved by moving a tapered inner conductor in the axial direction [9, 10] as shown in Fig. 1.

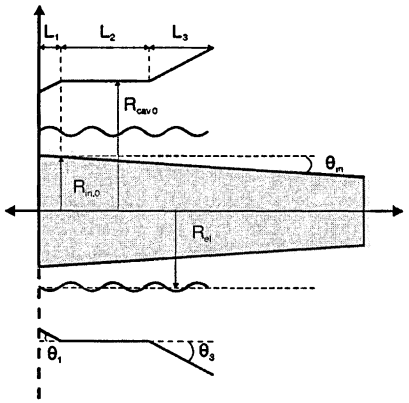

Fig. 1. The geometry of a coaxial cavity with an axially movable tapered insert

By moving the conical insert to the left the outer to inner radii ratio $C = R_{cav,0}/R_{in,0}$ decreases, leading to a relevant change to the resonance frequency f_0 and the diffractive quality factor Q_{diff}, which strongly depends not only on the radii ratio, but also on the slope of insert.

2. The 330 GHz gyrotron for NMR experiments

A 330 GHz step frequency tuneable gyrotron with the operating mode $TE_{+6,2}$ is presented in [6]. This gyrotron has a conventional cavity and its resonance frequency varies by fixed values that are determined by the distance of the axial $TE_{6,2,n}$ modes. Here, we consider a similar coaxial cavity with the geometrical details given in the first and second column of Table. The last three columns of the table show the dependence of the frequency and the quality factor on the axial displacement of the insert (positive displacement values correspond to the movement of the insert to the left). Here as the cavity geometry changes, the magnetic field is readjusted to remain in resonance with the given mode and to maintain the optimum coupling between the electron beam and the RF field.

It is evident that for the maximum shift of 35 mm (value being chosen arbitrary) the frequency decreases by 3.173 GHz. Since the quality factor of the cavity is high in the whole tuning range, one can expect high efficiencies at all frequencies. Indeed, the calculations with the operating parameters similar to those considered in [6], i.e., $V = 20$ kV, $I = 50$ mA, pitch factor $\alpha = 2$ and $R_{el} = 1.2$ mm, confirm this and predict high output power for the whole tuning range, as shown in Fig. 2.

Geometrical characteristics, resonance frequencies and quality factors of the cavity with the linear insert

Geometrical parameter	330 GHz gyrotron for NMR applications	Shift (mm)	f_0 (GHz)	Q_{diff}
$R_{cav,0}$	1.62 mm	0	332.880	1382
$R_{in,0}$	0.961 mm	5	332.166	1543
L_1	2.73 mm	10	331.539	1742
L_2	11 mm	15	331.008	1986
L_3	8 mm	20	330.560	2287
θ_1	3°	25	330.200	2660
θ_2	3°	30	329.914	3126
θ_{in}	–0.1°	35	329.707	3696
R_{el}	1.2 mm			

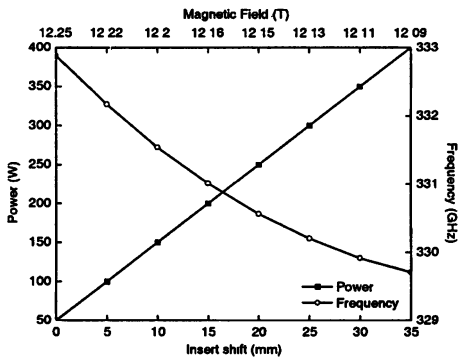

Fig. 2. Dependence of the frequency, the output power and the optimal magnetic field on the axial shift of the linear inner conductor

It should be emphasized that the results presented in this figure have been obtained with a fixed operating current 50 mA. With larger currents it should be possible to maintain constant output power in the entire tuning range. It should be noted that the proposed tuning is genuinely continuous in contrast to "pseudo-continuity", which can be achieved by the method proposed in [6]. The tuning range is limited by the length of the insert and by the mechanical feasibility of the proposed design, which should be optimized for any specific inverted Magnetron Injection Gun (MIG), whose emitter is fixed, but the coaxial insert movable.

The realization of a cavity with a movable insert, such as shown in Fig. 1, could be constrained by the length of the insert. A possible solution to this problem is the use of a non-linear tapering profile, for which the movement to the left will result in a combined change of the radii ratio and the tapering slope [11].

3. The 395 GHz gyrotron for NMR experiments

The cavity of this gyrotron is shown in Fig. 3. Here the insert has longitudinal corrugations, which allows one to reduce ohmic losses [12].

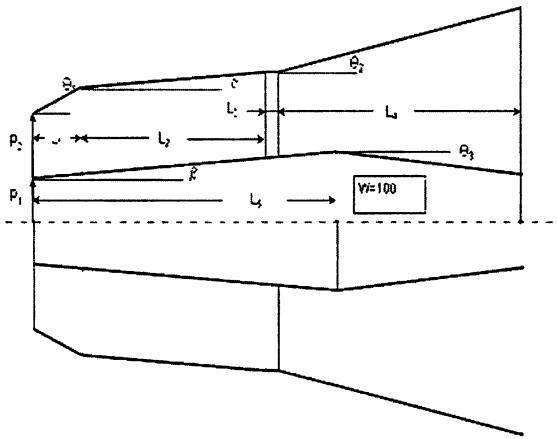

Fig. 3. The cavity profile for $TE_{10\,5}$ operating mode ($f_{average}$ = 394.6 GHz). The main cavity parameters are: L_1 = 5 mm, L_2 = 19 mm, L_3 = 1 mm, L_4 = 25 mm, L_5 = 30 mm, $\Theta_1 = 3°$, $\Theta_2 = 3°$, $\Theta_3 = 1.5°$, $\alpha = \beta = 0.25°$, R_1 = 2.4 mm and R_2 = 4 mm.

The dependence of Q_{diff} and f on the axial shift of the inner conductor for V = 15 kV and I = 1 A is shown in Fig. 4 and the dependencies of the output power P, efficiency and density of ohmic losses J on the beam current is shown in Fig. 5.

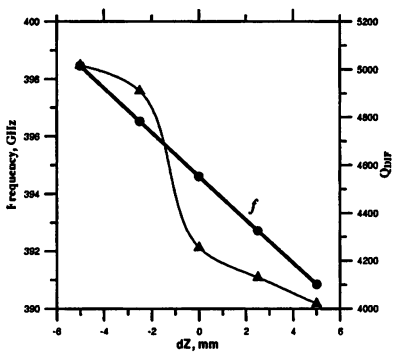

Fig. 4. The calculated value of f (circles) and Q_{diff} (triangles) on the axial shift of the inner conductor for beam voltage V = = 15 kV and I = 1 A

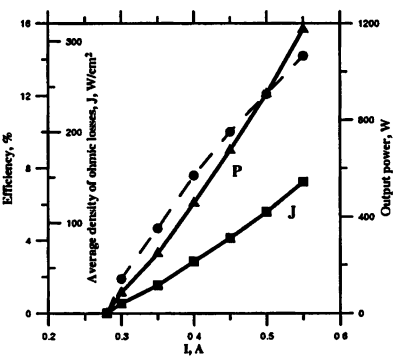

Fig. 5. Output power (triangles), efficiency (circles) and peak ohmic loss density (squares) as a function of beam current for V = 15 kV

The central frequency 394.6 GHz corresponds to 14.5T operating magnetic field. The effective frequency tuning is about 8 GHz. The "–" values correspond to the shift towards the cathode and "0" marks the central (initial) position of the insert. It should be emphasized that the obtained frequency tuning is much larger than needed for DNP experiments. Thus shorter shifts can be used which can simplify manufacturing of the insert. The output efficiency is about 10 % in the whole frequency range and the output power is several hundreds watts. For the output power higher than 1 kW the peak density of ohmic losses J is about 100 W/cm^2 at the external wall. In the case of the use of an insert without corrugations the maximum density of ohmic losses is about 200 W/cm^2 at the internal cavity wall which is still acceptable for CW operation. However in this case the insert diameter becomes larger for desired frequencies and the distance between the electron beam and the cavity wall becomes smaller (by the factor about 0.95) which makes the alignment more difficult.

4. Conclusions

The genuinely continuous tuning of coaxial gyrotrons by moving the tapered inner conductor in the axial direction and by adjusting the operating magnetic field has been demonstrated for two cases. In both cases, the remains high in the whole frequency range and it is possible to retain constant the output power by increasing the beam current properly.

The length of the inner conductor can be significantly shortened by increasing the slope of the tapering or by using a non-linear profile as discussed in [11]. The use of a more sophisticated cavity geometry (Fig. 3) allows further reduction of the needed shift to ±1.5 mm to achieve the frequency band ± 0.5 GHz required for DNP experiments. It should be possible to manufacture such a system using corrugated pipe elements.

References

1. *Dumbrajs O., Heikkinen J. A., and Zohm H.* Nuclear Fusion **41**, 927 (2001).
2. *Zohm H. and Thumm M.* J. Phys. Conference Series **25**, 274 (2005).
3. *Becerra L. R. et al.* Phys. Rev. Letters **71**, 3561 (1993).
4. *Bajaj V. et al.* J. Magn. Reson. **160**, 85 (2003).
5. *Mitsudo S. et al.* Int. J. Infrared Millim. Waves **21**, 661 (2000).
6. *Sirigiri J. R., Shapiro M. A., and Temkin R. J.* 2004 Joint 29th Int. Conf. on Infrared and Millimeter Waves and 12th Int. Conf. on Terahertz Electronics, pp. 621–622.
7. *Sabchevski S., Idehara T., Mitsudo S., and Fujiwara T.* Int. J. Infrared Millim Waves **26**, 1241 (2005).
8. *Antakov I. I., Zasypkin E. V., and Sokolov E. V.* Int. J. Infrared Millim. Waves **14**, 1001 (1993).
9. *Dumbrajs O., Möbius A., and Mühleisen M.* Patentanmeldung 19532785, Anmeldetag: 06.09.95. Deutsches Patentamt, München, 17. April 1997, (1997).
10. *Dumbrajs O. and Möbius A* Int. J. Electronics **84**, 411 (1998).
11. *Ioannidis Z. C., Dumbrajs O., and Tigelis I. G.* Int. J. Infrared Millim. Waves. **29**, 416 (2008).
12. *Glyavin M., Khizhnyak V., Luchinin A., Idehara T., and Saito T.* Int. J. Infrared Millim. Waves **29**, 641 (2008).

CONTROL OF GYROTRON BY MODULATED REMOTE REFLECTOR

A. Fernandez[1], N. Kharchev[2], G. Batanov[2], Yu. Bondar[2], L. Kolik[2], Yu. Novojilova[3], M. Petelin[3], K. Sarksyan[2], A. Tolkachev[1]

[1] Laboratorio Nacional de Fusión, EURATOM-CIEMAT. Madrid, Spain
[2] General Physics Institute, RAS, Moscow, Russia
[3]Institute of Applied Physics, RAS, Niznhny Novgorod, Russia

We have studied interaction of a gyrotron with a remote low-reflection oscillating membrane. After the ending of transient processes, which character and duration depend on the sequence of gyrotron and acoustic modulator switching on, the power turns modulated at the frequency of the load oscillations. When the membrane shifts along the wave ray at a half wavelength, the scenario of generator-load interaction is reproduced

1. Introduction

The sufficient broadening of a gyrotron spectrum under the influence of small reflection from plasma fluctuations was observed in [1]. This effect was explained as the gyrotron locking by the reflected wave. In order to study in detail the effect of the reflection from the non-stationary load on a gyrotron the using of the oscillating reflector (membrane) with fixed amplitude and frequency was suggested [2]. In present paper we describe the results of this study.

Let us consider the system, composed of the auto-oscillator, the delay line and the load. When one of the system parameters changes periodically, the auto-oscillator power and frequency turn modulated with the same period after the some time. The settling time and the steady-state modulation depth depend on the reflection coefficient and the phase shift of radiated and reflected waves at the auto-oscillator output. For quasi-monochromatic process the reflector shift at a half wavelength results in the reflected signal phase shift at 2π, so the system behavior is reproduced.

2. The theoretical estimations of the auto-oscillator and the low reflected load interaction effects

Let us consider a case of constant system parameters and small load reflection coefficient R [3, 4]

$$|R|\vartheta_0 < Q, \qquad (1)$$

when there is a single stable mode in the system. Here ϑ_0 is the delay phase of the reflected wave. We can note that in [3, 4] the model of Van-der-Pole oscillator without the susceptance of active medium (an electron beam in a gyrotron) was studied. But in accordance to Kramers–Kronig relations any medium has both conductance and the susceptance, which are the values of the same order. So, the condition (1) up to a constant factor of the order of unity remains valid for any real auto-oscillator.

Let us estimate the frequency and the Q-factor shifts under the influence of the reflected wave for the operating mode. It is known, that the gyrotron cavity is a piece of weakly-irregular metal tube, conjugated with the output waveguide (Fig. 1). The suitable method to find the corrections of the frequency and Q-factor was suggested in [5]. This method is based on the finding of reference cross-section in the output waveguide (Fig. 1).

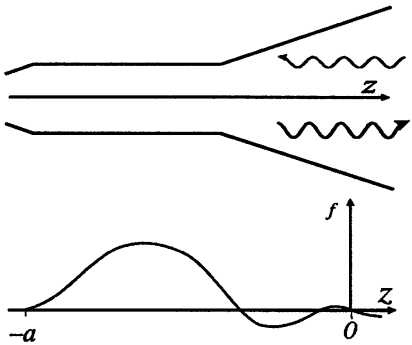

Fig. 1. The gyrotron cavity and the output waveguide; the structure of field, excited by the external monochromatic source, and the reference cross-section at z = 0.

The reflection from the remote load is equivalent to specification of the complex reflection coefficient $R = |R|e^{-i\varphi}$ in this reference cross-section. If the reflection is small: $|R| << 1$, then in the frame of perturbation method the corrections of the principal mode frequency and Q-factor are proportional to the magnitude of the reflection coefficient $|R|$:

$$\Delta Q / Q = -2|R| \cos\varphi, \; \Delta\omega / \omega = |R| \sin\varphi / Q. \qquad (2)$$

It should be noted that the reflection coefficient in (1), (2) is meant the relative amplitude of the reflected wave with the same structure as the operating auto-oscillator mode, including the same rotation direction.

If the load (a reflected membrane) shifts along the wave propagation direction, the phase of the reflected wave will shift too, and the phase φ of the reflection coefficient in the reference cross-section changes at the same value. Specifically under the shift of the remote reflector at a half wavelength the reflected wave phase and the reflection coefficient phase φ change at 2π. In this case the system will return to the initial state, as it follows from (2).

As the Q-factor of electrodynamic system enters to the equation

$$P = \omega W / Q \qquad (3)$$

(W is the field energy stored in the cavity), the change of the Q-factor results in the change of radiated power P.

The hereinabove theory remains valid until the time scale of any parameter variation much more than the transient processes duration. But at small reflection coefficient the auto-oscillator locking by the reflected wave turns the most prolonged transient process, as the locking time is inversely proportional to the reflected wave amplitude [6–9]. At that the usability condition of the stationary theory is violated, though the steady-state power is modulated at the same frequency as the parameter. The locking time is equal to

$$\tau_{lock} \sim Q_{difr} / (|R|\omega). \qquad (4)$$

3. The experimental results

The equivalent scheme of the experiment is represented in the Fig. 2. The mica plate (*6*) with the amplitude reflection coefficient 17.3 % was situated at the angle of 45° to the wave beam in the path of the gyrotron (*1*) which worked at the water dummy load (*5*). The gyrotron frequency was 51.7 GHz. After the reflection from the mica plate the wave come to the aluminum foil (membrane) pasted-in the acoustic modulator diaphragm (*7*). The acoustic modulator was fed by the ac voltage at fixed frequency that resulted in the foil harmonic oscillations. The acoustic modulator could move along its own axis, so the foil mean position could change up to 150 mm. Its amplitude and frequency could change consistently: the more frequency, the less amplitude. The amplitude could change from 0 to 13 mm, the frequency – from 100 Hz to 1200 Hz.

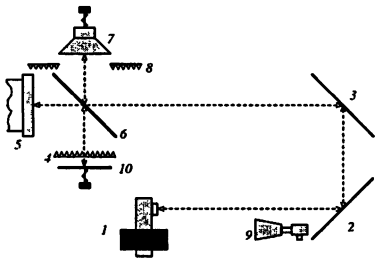

Fig. 2. The experimental set-up: *1* – gyrotron, *2–3* – quasi-optical line mirrors, *4, 8* – absorbed diaphragms, *5* – water load, *6* – mica plate, *7* – the acoustic modulator, 9 – the diagnostic diode, 10 – additional mirror

The diode (*9*) was used for the gyrotron power measuring. The gyrotron radiation through the QTL mirrors come to the mica plate, the most part of radiation passed through the mica and absorbed in the water load, the small part was reflected from the mica, then was reflected from the oscillating membrane (foil), being moved back along the quasi-optical path.

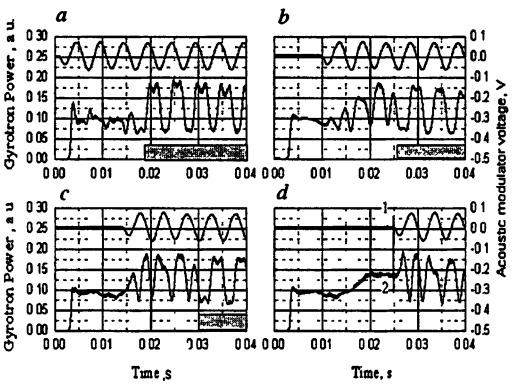

Fig. 3. Gyrotron power dependence (low curves) and the acoustic modulator voltage (top curves). The delay of acoustic modulator switching on was 0, 10, 15, 25 ms in Fig. 3 *a–d* correspondingly. The vertical line 1, 2 at Fig. 3*d* denotes the time of the membrane oscillations beginning. The grey rectangles mark the steady-state modulation.

The transient processes character depended on the sequence of the gyrotron and the acoustic modulator switching on as well as the time delay between their switching on (Fig. 3). After the gyrotron switching on the cavity was heated and expanded. So, the gyrotron frequency changed. Until it changed sufficiently

quickly the gyrotron couldn't be locked by weak reflected wave, as the locking time and the heating time were comparable (Fig. 3*d*). When the gyrotron frequency became stable, it was locked and the regime of periodically modulated power was formed.

For the fully heated gyrotron the transient time to locked state was about 12 ms (Fig. 3*d*). As the diffraction Q-factor was about 1000, the mica reflection coefficient was $R_{mica} = 0.03$ (as the wave was reflected twice), we can estimate the transformation coefficient T of the reflected wave into the wave, having the same structure as the operating mode (including the azimuthal number). It was about $T \sim 10^{-4} \div 10^{-5}$. The reflection coefficient, which enters in the formulas (1), (2), (4)

$$R = R_{mica} T \qquad (5)$$

was about $|R| \sim 10^{-6}$.

The time dependencies of the gyrotron power at different mean membrane positions under the modulation frequency 400 Hz, oscillations amplitude 0.22 mm are shown in the Fig. 4. As the pair of figures – 4 *a*, *d* differs at roughly half wavelength, they looks similar. In accordance with above stationary theory if the membrane (foil) oscillations amplitude was much less than the wavelength ($\lambda = 5.8$ mm), the power modulation shape reproduced the shape of the foil oscillations (Fig. 4). If the foil oscillations amplitude and the wavelength were comparable, the power modulation shape differed from the foil oscillations shape, though they both remained periodic (see Fig. 3, 6, where the foil oscillations frequency was 200 Hz, foil amplitude was 1.3 mm).

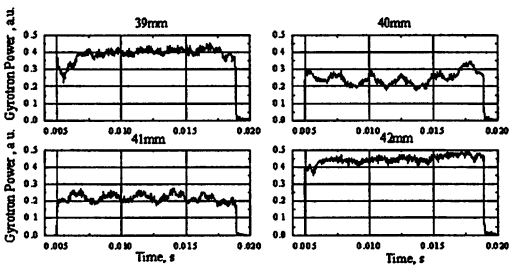

Fig. 4. The gyrotron power at different mean membrane coordinate

The cross-correlation coefficient

$$K = \frac{1}{T}\int_{-T}^{T} \left(\Delta P_{gyr} U_{acoust}\right) \Big/ \left(\sigma_{gyr}\sigma_{acoust}\right) dt \qquad (6)$$

between the gyrotron and the acoustic modulator powers depended on the mean foil position z_{refl} periodically, period was equal to $\lambda/2$ (Fig. 5). Here σ_{gyr}, σ_{acoust} – roof-mean-square deviations of gyrotron power and modulator voltage.

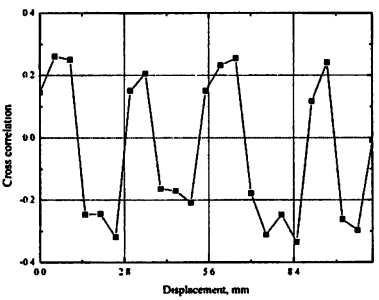

Fig. 5. The cross-correlation coefficient between the gyrotron power and acoustic modulator power oscillations

The variations of the gyrotron cryo-magnet field resulted in the frequency changes, and therefore, in the phase shift of the reflected wave. So the modulation depth differs in Fig. 6.

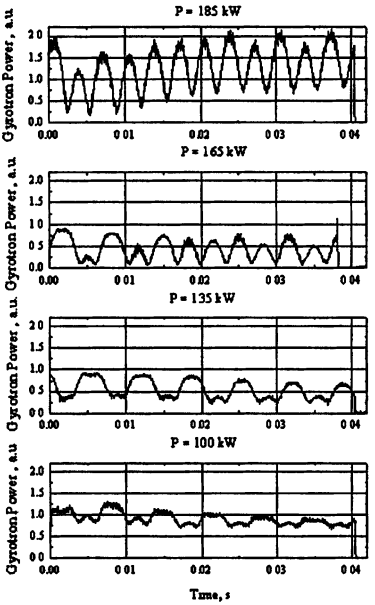

Fig. 6. Gyrotron power time dependence at different gyrotron cryo-magnet fields and constant reflector parameters

4. Conclusions

In our experiments with a gyrotron influenced with reflection from an oscillating foil, we have seen, in accordance to the theory, that:

- after a transient process, the gyrotron power turned modulated with the period of the reflector oscillations;
- when the oscillating foil mean position shifted at the half-wavelength, the gyrotron power modulation pattern was reproduced;
- if the reflector oscillations amplitude was of the order of the wavelength, the power modulation pattern differed from the reflector oscillation pattern;
- the wave coming from the load into the gyrotron is transformed to the operating cavity mode with coefficient $T \sim 10^{-4} \div 10^{-5}$.

The work was supported by the RFBR, grant № 06-02-16272.

References

1. *Batanov G. M. et al.* Technical Physics, **46(5)**, 596 (2001).
2. *Fernandez A. et al.* Int. J. Infr. and Mill. Waves, **28(9)**, 705 (2007).
3. *Landa P. S. et al.* Radiotech and Electr. (rus), 31(4), 730 (1986).
4. *Novozhilova Yu. V. et al* Abst. of VII Int. Work. "Strong Microwaves: Sources and Applications", Nizhny Novgorod, 54 (2008).
5. *Kovalev N. F. et al.* Radiphys. and Quant. Electr, **10/11**, 875 (2007).
6. *Rabinovich M. I., Trubetskov D I.* Oscillations and Waves in Linear and Nonlinear Systems, Kluwer Academic (1989).
7. *Novozhilova Yu. V. et al* Proc. of Int. Work. "Strong Microwaves in plasmas". Nizhny Novgorod, **1**, 173 (2006).
8. *Pikovsky A. et al.* Synchronization. A universal concept in nonlinear sciences. Cambridge Univ. Press, N. Y. (2001).

ADVANCED TRANSVERSE FIELD COLLECTOR SWEEPING FOR HIGH POWER GYROTRONS

H. Braune[1], V. Erckmann[1], S. Illy[2], H. P. Laqua[1], F. Noke[1], F. Purps[1], M. Schmid[2]

[1] Max-Plank-Institut für Plasmaphysik, EURATOM Association, Teilinstitut Greifswald, Germany

[2] Forschungszentrum Karlsruhe, Association EURATOM – FZK, IHM FZK, Karlsruhe, Germany

The collector of MW-class CW gyrotrons is a critical component, which is sometimes limiting the gyrotron performance. A higher safety margin and/or an increase of the output power are feasible with a smooth power distribution profile at the collector surface. The W7-X gyrotrons operate with an RF-power of typically 0.9 MW at 140 GHz in CW-mode with an efficiency of 42–44 %. In this range of efficiencies 1.3 MW power remains in the spent electron beam after the electron-wave interaction as waste power and must be dissipated in the collector. The W7-X gyrotrons are equipped with a commonly used and well-established "Vertical Field Sweeping System" (VFSS). The power deposition profile obtained with a VFSS only displays pronounced maxima with almost equal power density at both the upper and lower turning points of the electron beam. An advanced collector sweep system was successfully tested on the "Thales Electron Devices" gyrotrons, which creates an almost homogenous heat loading-profile. This system is based on the "Transverse Field Sweep System" (TFSS). The TFSS consists of 3 pairs of TF-coils, which are powered with a 3-phase a.c. thyristor controller thus generating a transverse field, which rotates with 50 Hz. The electron strike area forms a rotating ellipse. In case of a slow amplitude modulation (up to 10 Hz) of the a.c. coil current with typically 50 % modulation depth the tilt angle of the rotating strike line ellipse follows this modulation and smoothes out the power peaks at the turning points. This system is of particular interest for next generation gyrotrons with an output power up to 2 MW.

Introduction

The collector of MW-class CW gyrotrons is a critical component, which is sometimes limiting the gyrotron performance. Such high-power collectors are generally made from copper and have strong sophisticated water-cooling systems for continuous operation. The W7-X gyrotrons operate with an RF-power of typically 0.9 MW at 140 GHz in CW-mode with an efficiency of 42–44 % [1]. In this range of efficiencies 1.3 MW power remains in the spent electron beam after the electron-wave interaction as waste power and must be dissipated in the collector. The W7-X gyrotrons are equipped with a commonly used and well-established Vertical Field Sweeping System (VFSS) [1]. The CW-operation at maximum output power of the W7-X gyrotrons is limited by the maximum permissible collector temperature. A higher safety margin and/or an increase of the output power are feasible with a smooth power distribution profile at the collector surface. A Transverse Field Sweep System (TFSS) have been investigated, which generates a smooth power deposition profile.

Basics of collector sweeping

The electron beam in gyrotrons is axis-symmetric and hollow. The electrons enter the interaction region with energy of typically 80–100 keV and are guided by an axis-symmetric strong (typically 5–6 T) stationary magnetic field.

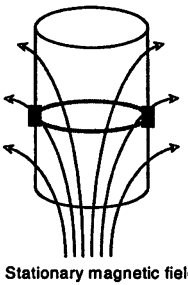

Fig. 1. Strike area

The axis-symmetric collector has a cylindrical shape in the simplest case. The diverging magnetic field lines and thus the drifting electrons intersect at a certain vertical position with the collector wall. The strike area forms a horizontal ring with a vertical dimension of about 50 mm, as shown in Fig 1. The typical power density, e.g. for the W7-X gyrotron is 20 MW/m², which is beyond existing cooling technology and would lead to melting of the collector. High power gyrotrons are therefore equipped with a magnetic field sweeping system, which sweeps the electron-beam over the collector surface.

Vertical versus transverse field sweeping

The power deposition profile obtained with a VFSS displays pronounced maxima with almost equal power density at both the upper and lower turning points of the electron beam. The VFSS has a weak electrical efficiency because the copper collector represents a single turn, short-circuited coil, which is shielding the sweep magnetic field very efficiently (typically 80 %). The sweeping is thus restricted to low frequencies in the range of 5–10 Hz.

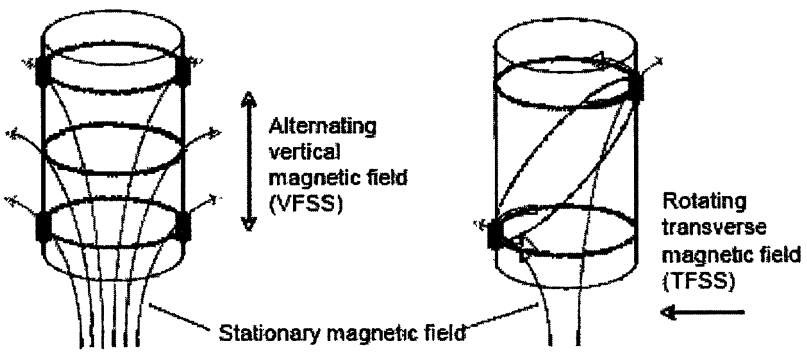

Vertical magnetic Field Sweep System

The top and bottom rings mark the upper and lower turning points with collector sweeping. The central ring is the intersection area without sweeping.

Transverse Field Sweep System

The intersection area is an ellipse, which rotates with the sweep frequency.

Fig. 2. VFSS versus TFSS

The "Transverse Field Sweep System" (TFSS) as invented in Russia [2] and further investigated at FZK [3] and at the Institute of Applied Physics (IAP) [4] consists of 3 pairs of TF-coils. The coils are powered with a 3-phase AC-supply thus generating a transverse field, which rotates with 50 Hz. The coil pairs are positioned direct below the collector. The gyrotron wall consists of stainless steel in this region, which has lower damping losses concerning the eddy currents. An additional DC powered coil is horizontal placed immediate at the top of transverse field coils.

Three commercial types of amplitude modulated three-phase current power supplies are available.

- Three-phase a.c. controller based on thyristor or triac.
- Frequency converter.
- Power supplies based on the PSM principle (Pulse Step Modulation) with IGBT modules.

The three-phase a.c. controllers are reliable and not as expensive as frequency converters or PSM-power supplies. Therefore a three-phase a.c. controller has been investigated in connection with the coil pair array. The modulation was always performed with a sinusoidal control voltage.

Influence of the modulation and the DC field on the intersection area

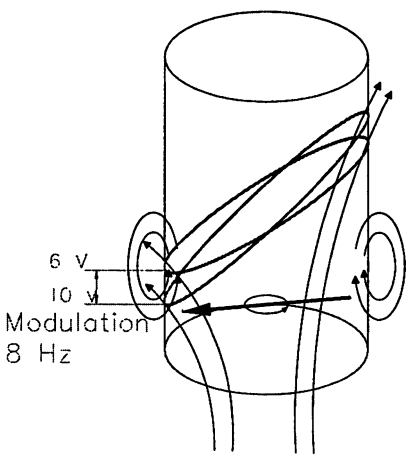

The rotating field modulation changes the tilt and the diameter of the elliptical intersection area on the collector wall.

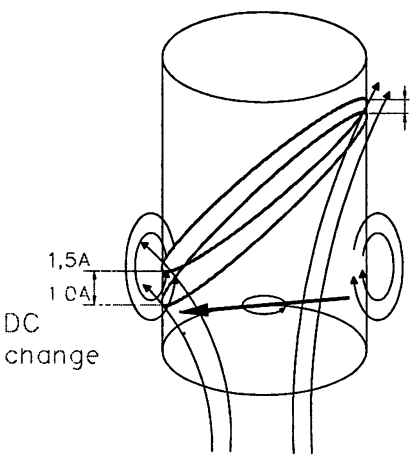

The current modification of the horizontal DC coil shifts the elliptical intersection area on the collector wall up or down. The diameter changes marginal.

Fig. 3. Modulation

Advanced transverse collector sweeping results

The first experiments were performed without collector cooling in order to get pictures of the collector surface temperature recorded with an infrared camera as shown in Fig 4. (pulse time 100 ms, beam current 12 A).

The experiments with modulated rotating field and the overlaid DC powered field were performed with collector cooling. (pulse time 1000 ms, beam current 15.8 A).

The measurements are taken with an array of 49 thermocouples mounted at equal distances along the vertical direction of the collector and at three positions in the azimuthally direction. Some thermocouple connections didn't work very well.

The reinforcement bars of the concrete wall near the gyrotron have an influence on the diverging magnetic field lines. Therefore the strike area on the collector wall isn't horizontal. The compensation is performed with some iron rods close to the gyrotron opposite to the concrete wall.

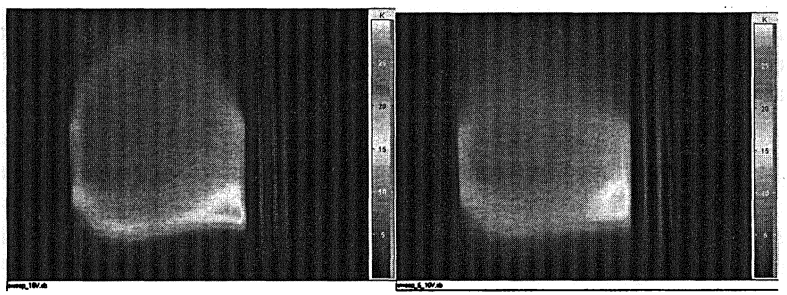

Fig. 4. TFSS without modulation (*right*) and with modulation (*left*). The compensation iron rods cause the hot spots.

The amplitude modulation of the rotating field without DC field reduces the maximum at the lower point of the electron beam strike area but does not smooth the power deposition profile perfectly.

An additional vertical DC field shifts the electron beam strike area towards the top of the collector and the electrons don't intersect the collector wall at the range of the high magnetic field density. The power deposition profile is smoothed (blue track in Fig. 5) with the DC field and a modulation depth of 50 percent. Only the correct combination of modulation depth and DC offset smoothes the power deposition profile perfectly.

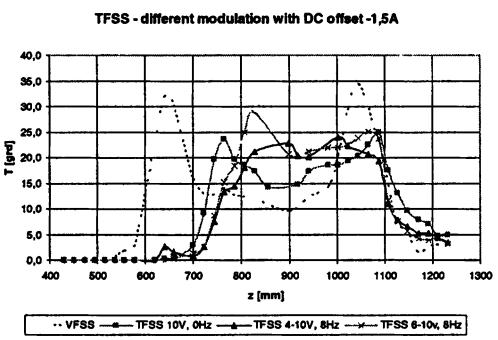

Fig. 5. Power deposition profiles

Summary and Outlook

The conventional VFSS, which is state of the art in present day high power CW-gyrotrons, generates an unfavorable power distribution profile along the collector surface. Strong local power peaking at both, the upper and lower turning points has been measured.

TFSS reduces the power peaking at the upper turning point, but the peaking at the lower turning point remains. The advanced TFSS - method with slow modulation of a fast rotating field and an overlaid static horizontal field has been investigated and a homogenous collector power distribution has been achieved.

A three-phase a.c. controller operates successfully in connection with the coil pair array. The modulation capability and the current threshold of the tested power supply meet the requirements of the investigated advanced collector sweeping method.

The advanced collector sweeping with a low frequency modulated TFSS power supply reduces the complexity and the costs compared with the conventional VFSS.

The next step of the advanced collector sweeping investigation will be the replacement of the long DC powered coil with a shorter one. A combination of a modulated rotating field and a marginally modulated static field will be tested with the new coil in order to increase the usable power deposition collector surface. This system is of particular interest for next generation of gyrotrons with an output power up to 2 MW.

References

1. *Thumm M. et al.* EU Megawatt-class 140-GHz CW gyrotron // IEEE Trans. Plasma Sci. 2007. Vol. PS-35. P. 143–153.
2. Private communication.
3. *Dammertz G., Illy S., Piosczyk B., Schmid M., Bariou D.* Collector Sweeping Systems for high power Gyrotrons // Conf. Digest Joint 30th Int. Conf. on Infrared and Millimeter Waves and 13th Int. Conf. on Terahertz Electronics. Williamsburg, USA, 2005.
4. *Manuilov V. N., Smirnov D. A., Malygin S. A., Soluyanova E. A.* Numerical simulation of the Gyrotron Collector System with Rotating Magnetic Field // Conf. Digest Joint 29th Int. Conf. on Infrared and Millimeter Waves and 12th Int. Conf. on Terahertz Electronics. Karlsruhe, Germany, 2004.

GENERATION OF POWERFUL COHERENT RADIATION IN FEM EXPLOITING TWO-DIMENSIONAL DISTRIBUTED FEEDBACK

N. S. Ginzburg[1], N. Yu. Peskov[1], A. S. Sergeev[1], V. Yu. Zaslavsky[1], A. V. Arzhannikov[2], P. V. Kalinin[2], S. L. Sinitsky[2], V. D. Stepanov[2], S. A. Kuznetsov[2], A. W. Cross[3], W. He[3], I. V. Konoplev[3], A. D. R. Phelps[3], C. W. Robertson[3], K. Ronald[3], C. G. Whyte[3] and M. Thumm[4]

[1] Institute of Applied Physics, Russian Academy of Sciences, Nizhny Novgorod, Russia
[2] Budker Institute of Nuclear Physics, Russian Academy of Sciences, Novosibirsk, Russia
[3] SUPA, Department of Physics, University of Strathclyde, Glasgow, UK
[4] University of Karlsruhe, IHE, Karlsruhe, Germany

A two-dimensional distributed feedback is an effective method of production ultra-high power spatially-coherent radiation from spatially extended relativistic electron beams of sheet and annular geometry. The paper describes progress in the investigations of planar and coaxial FEMs based on the novel feedback mechanism. Theoretical analysis was conducted in the frame of the coupled-wave approach and agrees well with the experimental data obtained in "cold" and "hot" tests. As a result, the effective transverse (azimuthal) mode selection has been demonstrated under the transverse size of about 20–25 wavelengths and narrow-frequency microwave pulses of multi-MW power have been generated in the FEMs operating in Ka- and W-bands.

Introduction

Two-dimensional (2D) distributed feedback [1], which is realized in Bragg resonators having double-periodic shallow corrugation in two perpendicular directions, is an effective method of producing spatially coherent radiation in relativistic masers driven by large-size electron beams of sheet [1, 2] and annular [1, 3] geometry. This mechanism can be considered as a development of 1D distributed feedback based on the traditional single-periodic Bragg structures [4]. Spatially-extended over one of the transverse coordinates interaction space allows significant increase of the total microwave power (up to GW powers) while keeping RF-power and current densities at moderate level.

High selectivity of the 2D Bragg resonators of planar and coaxial geometry was demonstrated for large Fresnel parameters in the frame of coupled-wave theory and in direct 3D simulations as well. Results of the theoretical analysis are validated by data obtained in "cold" microwave measurements [5, 6]. Computer simulations demonstrated high potential of 2D distributed feedback to achieve single-mode single-frequency oscillations in FEM when the transverse size of the beams in orders exceeds the radiation wavelength [1–3].

Experimental studies of FEMs based on novel feedback mechanism are performed in Ka-band (coaxial geometry) at the University of Strathclyde (Glasgow)

and in W-band (planar geometry) at the BINP RAS (Novosibirsk) in collaboration with the IAP RAS (N. Novgorod) and University of Karlsruhe. As a result of this work, narrowband microwave generators of multi-MW power level were realized. In these experiments an effective mode control over the transverse (azimuthal) index was demonstrated with oversize parameter of the resonators of about 20–25 wavelengths. The present paper is devoted to the results of simulations and experimental studies of these novel FEM schemes.

Planar 75 GHz FEM with a hybrid Bragg resonator

The 2D distributed feedback is based on the mutual scattering of the four partial wave fluxes

$$\vec{E} = \vec{E}_0 \, Re\left\{\left[A_+ e^{-ihz} + A\_e^{ihz} + B_+ e^{-ihx} + B\_e^{ihx}\right] e^{i\omega t}\right\}, \qquad (1)$$

propagating in forward (in respect with the electron beam propagation), backward and transverse $\pm x$ directions. These additional (in comparison with traditional 1D Bragg structures) fluxes act to synchronize different parts of sheet electron beam. Such feedback scheme is realized in planar 2D Bragg structures having double-periodical corrugation

$$a = a_{2D}\left[\cos \overline{h}_{2D}(z-x) + \cos \overline{h}_{2D}(z+x)\right], \qquad (2)$$

where $4a_{2D}$ is the corrugation depth ($a_{2D} << a_0$, $a_{2D} << \lambda$), under the Bragg resonance condition $h \approx \overline{h}_{2D}$.

To demonstrate operability of this novel feedback mechanism 75-GHz planar FEM was elaborated. Electrodynamic system of the generator is a hybrid resonator consisting of 2D and 1D Bragg structures [7] (Fig. 1*a*). The spatial synchronization of radiation in the transverse (x) direction is achieved in the input (cathode-side) 2D Bragg reflector due to the above-described scheme of coupling of the four partial waves (1). Interaction with the magnetically-guided electron beam oscillating in the planar wiggler mainly takes place in the regular part of the resonator. A conventional 1D Bragg mirror at the output of the system reflects a small amount of the

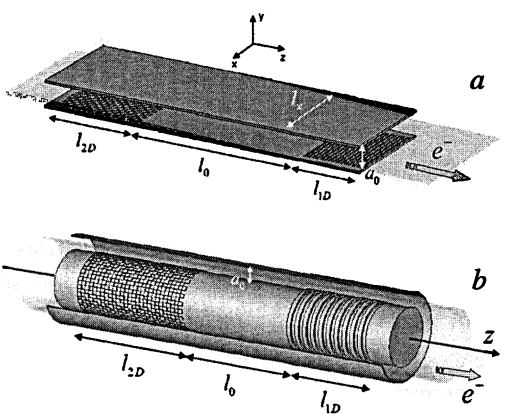

Fig. 1. Scheme of interaction space of FEM with a hybrid resonator consisting from 2D and 1D Bragg reflectors of (*a*) planar and (*b*) coaxial geometry

RF-energy into backward direction, thus providing the conditions for self-excitation of the generator.

In the frame of the coupled-waves approach dynamics of FEM with 2D distributed feedback can be described by the system of equations for the partial wave amplitudes [1, 2]:

$$\left(\frac{\partial}{\partial Z}+\beta_{gr}^{-1}\frac{\partial}{\partial\tau}\right)A_+ + i\alpha_{2D}\left(B_+ + B_-\right)=J,\quad J=\frac{1}{\pi}\int_0^{2\pi}e^{-i\theta}d\theta_0,$$
$$\left(\frac{\partial}{\partial Z}-\beta_{gr}^{-1}\frac{\partial}{\partial\tau}\right)A_- + i\alpha_{2D}\left(B_+ + B_-\right)=0, \qquad (3)$$
$$\left(\frac{\partial}{\partial X}\pm\beta_{gr}^{-1}\frac{\partial}{\partial\tau}\right)B_\pm + i\alpha_{2D}\left(A_+ + A_-\right)=0.$$

The forward wave A_+ synchronous with the electrons is excited by the beam and RF-current J can be found from the electron motion equations

$$\left(\frac{\partial}{\partial Z}+\beta_{\|}^{-1}\frac{\partial}{\partial\tau}\right)^2\theta = Re\left\{A_+e^{i\theta}\right\}, \qquad (4a)$$

$$\theta\big|_{Z=0}=\theta_0\in[0,2\pi),\quad \left(\frac{\partial}{\partial Z}+\beta_{\|}^{-1}\frac{\partial}{\partial\tau}\right)\theta\big|_{Z=0}=\Delta, \qquad (4b)$$

where θ is the electron phase in the respect to the synchronous wave.

The output traditional 1D Bragg reflector possesses single-periodical corrugation (Fig. 1*a*) $a=a_{1D}\cos(\bar{h}_{1D}z)$, where $2a_{1D}$ is the corrugation depth, $\bar{h}_{1D}=2\pi/d_{1D}$ and d_{1D} is the corrugation period. This structure provides mutual scattering of two counter-propagating partial waves $A_\pm$, which can be described by the equations

$$\left(\frac{\partial}{\partial Z}+\beta_{gr}^{-1}\frac{\partial}{\partial\tau}\right)A_+ + i\alpha_{1D}A_- = J,\quad \left(-\frac{\partial}{\partial Z}+\beta_{gr}^{-1}\frac{\partial}{\partial\tau}\right)A_- - i\alpha_{1D}A_+ = 0. \qquad (5)$$

Amplification of the synchronous wave A_+ in the regular section of the resonator is also described by Eqs. (5) in which $\alpha=0$, since the coupling is absent.

In Eqs. (3)–(5) the following variables are used $Z=zC\bar{\omega}/c$, $X=xC\bar{\omega}/c$, $\tau=tC\bar{\omega}$, Δ is the initial mismatch of the electron-wave synchronism, $(A_\pm,B_\pm)=(A_\pm,B_\pm)ek\mu/\gamma mc\bar{\omega}C^2$, $k=\beta_\perp/\beta_\|$ is the electron-wave coupling parameter, $\mu\approx\gamma^{-2}$ is the bunching parameter [4], $C=(I_0\lambda^2e\mu k^2/8\pi mc^3\gamma a_0)^{1/3}$ is the gain parameter, I_0 is the linear beam current and $\alpha_{2D,1D}$, are the wave coupling coefficients for 2D [1–3] and 1D [4] Bragg structures respectively.

Results of the simulation for the microwave system geometry and the electron beam parameters close to the experimental conditions at the high-current accelerator "ELMI" (BINP) are shown in Fig. 2 and demonstrate the establishment of a

steady-state single-frequency regime. The synchronous partial wave A_+ has practically uniform field distribution over the x coordinate that ensures the same conditions for the energy extraction from all parts of the beam and, a result, rather high electron efficiency.

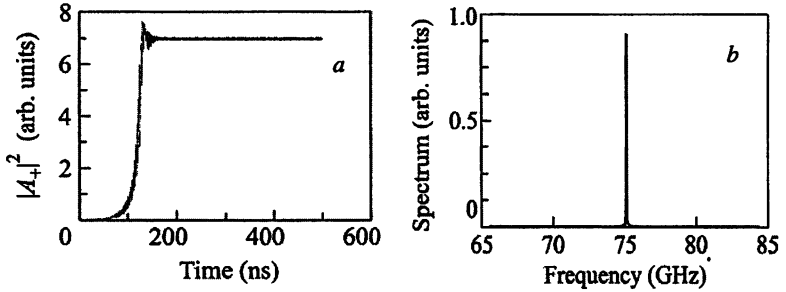

Fig. 2. Simulation of synchronization in a planar FEM with hybrid Bragg resonator: (*a*) time dependence of the normalized output power and (*b*) output radiation spectrum in the steady-state regime

In the planar FEM with 2D distributed feedback driven by the high-current accelerator "ELMI" [8] a sheet relativistic electron beam 0.8 MeV / 3 kA with the transverse cross-section of 0.4 × 7 cm was used. This beam was transported in a strong (up to 1.4 T) guide magnetic field inside a planar vacuum channel with the cross section of 0.95 × 10 cm and pumped by the wiggler of a period of 4 cm and an amplitude of the transverse field of up to 0.2 T. The resonator was composed from the input 2D and output 1D Bragg reflectors and regular section of a rectangular waveguide of length $l_0 = 32$ cm. The input reflector of length $l_{2D} = 19$ cm had a chessboard corrugation with a depth of 0.02 cm and a spatial period of 0.4 cm along the x and z coordinates. Theoretical analysis and "cold" measurements [6] showed that the electrodynamical properties of the Bragg structure with a chessboard corrugation are close to 2D sinusoidal corrugation (2). The transverse energy fluxes in the two-dimensional Bragg reflector were scattered outside the resonator by additional metal plates (scatterers) with irregular surface profiles. Since the radiation is amplified by the electron beam mainly after the 2D mirror, the energy losses due to this scattering are rather small. The output Bragg reflector of length $l_{1D} = 19$ cm had a corrugation in the form of parallel rectangular grooves with a period of 0.2 cm and a depth of 0.007 cm. A Bragg deflector having 1D corrugation at a 45° angle to the axis was used at the output of the Bragg resonator to direct the radiation into a parallel channel and to split the output radiation and the powerful electron beam traveling to collector.

In the experiments precise analysis of the FEM radiation spectrum was performed using heterodyne diagnostic with an additional bandpass interference filter to determine the sign of frequency shift of the mixed signal with respect to the master oscillator. Typical oscilloscope traces of the voltage at the accelerating diode, the electron current, and the signal from the RF-detectors are shown in

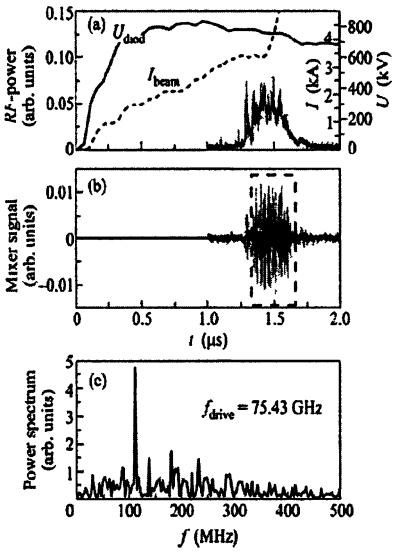

Fig. 3. Typical oscilloscope traces in planar 75-GHz FEM: (*a*) the diode voltage, beam current and RF-pulse, (*b*) the heterodyne signal and (*c*) radiation spectrum

Fig. 3*a*. Microwave radiation was observed when the beam current exceeded 1 kA which is in good agreement with the calculated starting current for the FEM-oscillator. A narrowband generation at a frequency close to the frequency of one of the eigenmodes of the hybrid Bragg resonator was obtained for a large number of pulses. In Fig. 3 radiation spectrum is localized near a frequency of 75.3 GHz during an almost entire 300-ns duration of the RF-pulse and demonstrated realization of a single-mode oscillation regime. In some other shots the generation at frequencies of 74.9, 75.1, and 75.5 GHz, which corresponded to the excitation of other longitudinal modes of the resonator, was observed. According to the simulation results, the possibility of excitation of different resonator modes is due to variations in the electron beam energy and beam current during the pulse, as well as pulse-to-pulse jitter of the beam parameters. The analysis of the time behavior of the optical emission from plasma at the beam transport channel, which was registered by means of fiber-optic waveguides, indicates that the total duration of the microwave pulse is limited due to the arrival of the collector plasma into the wave-beam interaction region. A total radiation power of about a few tens of megawatts was measured using the calorimeter and the hot-carrier calibrated detectors. Angular pattern of the output radiation was obtained by a neon bulb panel illumination positioned at various distances from the output window of the FEM.

Coaxial 37 GHz FEM with 2D distributed feedback

In this section we consider a co-axial scheme of FEM with a hybrid Bragg resonator (Fig. 1*b*) [7] which is investigated experimentally at the University of Strathclyde [9, 10]. The 2D Bragg structure represents a section of coaxial waveguide of length l_{2D}, distance between the conductors a_0 and the mean radius r_0 (Fig. 1*b*) having a corrugation in the form of two helices of opposite rotation

$$a = \frac{a_{2D}}{4}\left[\cos(\bar{h}_z z - \bar{M}\varphi) + \cos(\bar{h}_z z + \bar{M}\varphi)\right], \qquad (6)$$

where $\bar{h}_z = 2\pi/d_z$, d_z is the corrugation period along z axis, $\bar{M}$ is the azimuthal number of the corrugation. We assume the waveguide to be of a small curvature

$r_0 >> \lambda$, $r_0 >> a_0$. Similar to a planar system the RF-field in the coaxial system under such conditions can be presented as a superposition of the four coupled waves propagating in the longitudinal $\pm z$ directions and the azimuthal $\pm \varphi$ directions. For the coaxial geometry the partial waves must obey the cyclicity conditions $A_{\pm}(x+l_x,z,t) = A_{\pm}(x,z,t)$, $B_{\pm}(x+l_x,z,t) = B_{\pm}(x,z,t)$, where $x = r_0\varphi$ is the transverse coordinate directed along the waveguide azimuth, $l_x = 2\pi r_0$ is the resonator perimeter. These conditions allow the Fourier expansion

$$A_{\pm}(x,\ z,\ t) = \sum_{m=-\infty}^{\infty} A_{\pm}^{m}(z,t); B_{\pm}^{m}(z,t) e^{2\pi i m x / l_x}, \qquad (7)$$

where each harmonic can be considered as a resonator mode with azimuthal index m. Equations for the wave amplitudes in the quasi-optical approximation can be presented in a form

$$\begin{aligned}
&\left(\frac{\partial}{\partial Z} + \beta_{gr}^{-1}\frac{\partial}{\partial \tau}\right) A_{+}^{m} + \sigma A_{+}^{m} + i\alpha_{2D}(B_{+}^{m} + B_{-}^{m}) = J^{m},\\
&\left(-\frac{\partial}{\partial Z} + \beta_{gr}^{-1}\frac{\partial}{\partial \tau}\right) A_{-}^{m} + \sigma A_{-}^{m} + i\alpha_{2D}(B_{+}^{m} + B_{-}^{m}) = 0, \qquad (8)\\
&\left(\frac{iC}{2}\frac{\partial^2}{\partial Z^2} \pm ism + \beta_{gr}^{-1}\frac{\partial}{\partial \tau}\right) B_{\pm}^{m} + \sigma B_{\pm}^{m} + i\alpha_{2D}(A_{+}^{m} + A_{-}^{m}) = 0,
\end{aligned}$$

where J^m is the azimuthal harmonic of RF-current, $s = 2\pi / L_x$, σ is the ohmic losses parameter. For the partial waves $B_{\pm}$ circulating along the azimuthal directions we apply the radiation boundary conditions at the edges of 2D corrugation. In the output 1D Bragg reflector mutual scattering of partial waves $A_{\pm}$ can be described by the Eqs. (5).

Simulations were carried out for parameters close to those realized in the Strathclyde FEM: l_{2D}= 10.4 cm, l_{1D}= = 6 cm, l_0 = 65 cm, a_0 = 1 cm, the gain parameter C ≈ 0.007. This corresponds to normalized section lengths: L_{2D} = 0.6, L_{1D} = 0.4, L_0 = 4 respectively. For a resonator made from copper the parameter of ohmic losses σ = 0.01. For optimized corrugation depths a_{2D} = 0.05 cm and a_{1D} = 0.1 cm the waves coupling coefficients were taken as α_{2D} = 0.5, α_{1D} = 0.35. The zones, in which various regimes of oscillation are established, are shown in Fig. 4 on the plane: normalized perime-

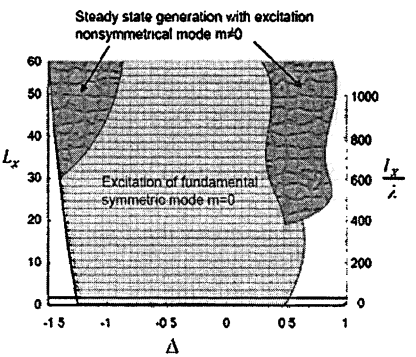

Fig. 4. Simulation of coaxial FEM with hybrid resonator: zones of stationary generation regimes corresponding to excitation of mode with different azimuthal indexes m. Solid line corresponds to the perimeter of Strathclyde FEM.

ter L_x versus the electron synchronism detuning Δ. While the perimeter is smaller than the value $L_x \approx 20$ the excitation of a single axial-symmetric mode $m = 0$ with the frequency close to the Bragg resonance frequency at all the variation range of parameter Δ (i. e. at any value of the electron energy from the zone of self-excitation) takes place. The 37 GHz Strathclyde FEM is driven by an annular electron beam with radius of 3.5 cm (i. e. perimeter of about 22 cm), which corresponds to the dimensionless perimeter $L_x = 1.2$. Thus, in the millimeter wave band the use of a hybrid Bragg resonator allows to realize single-mode single-frequency oscillation regime practically for any existing electron beams. Zones of excitation of modes with high azimuthal indexes appear only at the normalized perimeter $L_x > 20$. But even in these zones a steady-state regime of generation, which corresponds to the synchronization of radiation from the different parts of a large-size electron beam, is also established.

In the simulations, the field distribution of partial waves in the steady-state regime shows that the main amplification of the forward wave takes place after the input mirror. Thus, the amplitudes of the quasi cut-off waves $B_{\pm}$ excited in the 2D Bragg structure are relatively small. Correspondingly, the ohmic and diffraction losses associated with these waves are also rather small and up to 95 % of RF-energy extracted from the beam is radiated by the forward wave A_+. Note for comparison that in the coaxial FEM scheme with two 2D Bragg reflectors [9, 10] (i. e. 2D structure is used both as input and output mirrors) more than a half of RF-energy was dissipated inside the resonator. Exploiting a hybrid scheme [7] allows increase in the output radiation power in several times keeping the electron efficiency on the level of 20 %.

The coaxial FEM based on 2D distributed feedback, which has been developed at the University of Strathclyde, utilizes an axially symmetric wiggler with period of 4 cm and solenoid of length 2.5 m and guide field strength of up to 0.6 T. The FEM was driven by a annular electron beam 0.5 MeV / 0.5 kA with diameter of 7 cm [9]. A Ka-band coaxial 2D Bragg structure had the chessboard corrugation at inner conductor of the period along axis of 8 mm, number of azimuthal variations of 24 and depth of 0.08 mm. The "cold" tests of these structures [5] demonstrated effective 2D Bragg scattering zone in the vicinity of 37 GHz, which corresponds to the fundamental azimuthally-symmetrical mode ($m = 0$) formed from the four waveguide partial waves: forward and backward waves of TEM-type and two counter-rotating whispering-gallery waves of $TE_{24,1}$-type. The first experiments [9, 10] were conducted with a two-mirror resonator in which 2D Bragg reflectors of length 10.4 cm and 5.6 cm were used at the input and output of the system respectively with 86 cm long regular section between them. In these experiments azimuthal mode selection was achieved. In the radiation spectrum (Fig. 5*b*) a maximal spectral line at 37.3 GHz was presented that proves the achievement of azimuthal mode control. The presence of several spectral lines with the frequency distance ~ 40 MHz corresponds to excitation of modes with different longitudinal indexes (distance between modes with different azimuthal indexes was about 2 GHz). Note also that according to the simula-

tions the limitation of measured output power by 15 MW is associated with strong ohmic losses in the output 2D Bragg mirror.

In the present stage of the experiment a hybrid resonator consisting from input 2D Bragg reflector and output 1D Bragg reflector separated by a regular section was utilized with the parameters described above. Result of the spectrum measurements is shown in Fig. 5*c* and demonstrates the establishment of a single-mode oscillation regime including both azimuthal and longitudinal mode control. The output power in this configuration was estimated to be about 60 MW. Thus, the replacement of the 2D Bragg output mirror by a 1D mirror provides the possibility for drastic decrease of ohmic losses.

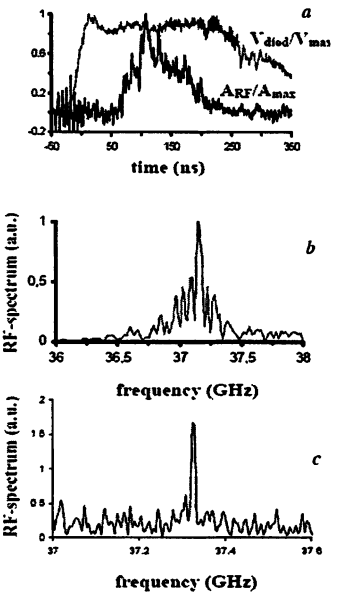

Fig. 5. Typical oscilloscope traces in 37-GHz coaxial FEM: (*a*) the diode voltage and RF-pulse and output radiation spectrum in the case of (*b*) two-mirror 2D Bragg resonator and (*c*) hybrid Bragg resonator

Conclusion

Modeling of nonlinear dynamics of planar and coaxial schemes of FEMs demonstrates possibility of the use of 2D distributed feedback for spatial synchronization the radiation of sheet and hollow electron beams having transverse size of up to 10^2–10^3 wavelengths. Results of the theoretical analysis are corroborated by the experimental studies carried out at Budker INP RAS (planar 75 GHz FEM) and Strathclyde University (coaxial 37 GHz FEM). Both experiments demonstrate effective mode control under the oversized parameter of 20–25 wavelengths. As a result, a narrowband radiation of multi-MW power level is obtained.

References

1. *Ginzburg N. S. et al.* Opt. Comm. **112**, 151 (1994).
2. *Ginzburg N. S. et al.* Phys. Rev. E, **60**, 935 (1999).
3 *Ginzburg N. S. et al.* J. Appl. Phys. **92**, 1619 (2002).
4. *Bratman V. L. et al.* IEEE J. Quant. Electr. **QE-19**, 282 (1983).
5. *Cross A. W. et al* Appl. Phys. Lett. **80**, 1517 (2002).
6. *Ginzburg N. S. et al.* Appl. Phys. Lett. **92**, 103512 (2008).
7 *Ginzburg N. S. et al.* Tech. Phys. Lett. **26**, 701 (2000).
8. *Arzhannikov A. V. et al.* JETP Lett. **87**, 618 (2008).
9. *Konoplev I. V. et al.* Phys. Rev. Lett. **96**, 035002 (2006).
10. *Konoplev I. V. et al.* Phys. Rev. E, **76**, 056406 (2007).

MICROWAVE AMPLIFIERS WITH HIGH-CURRENT ELECTRON BEAMS

E. Abubakirov

Institute of Applied Physics, RAS, Nizhny Novgorod, Russia

Presently, most of HPM sources are free running oscillators: they need not input microwave drivers and are relatively simple from the mode selection problem. Meanwhile, for a number of applications HPM amplifiers are more attractive. Development of amplifiers driven with high-current relativistic electron beams in IAP is based on application of oversized waveguides, so the main attention is always paid to development of appropriate methods of mode selection and filtration. In the most success line of powerful amplifiers suppression of spurious oscillation was provided with sectioning of the interaction space of a relativistic electron microwave device. Following the concept realization of enhanced versions of the amplifiers with output power up to GW level became possible.

Modern state of art of microwave relativistic electronics demonstrates that the main part of R&D works in the area is devoted to oscillators, which are, definitely, more simple in practical materialization than amplifiers. Besides that there are obvious demands for development of microwave sources with controlled amplitude and phase of output radiation. Promising application fields of them may be particle acceleration in supercolliders, high resolution radars and others.

Controlled microwave sources can be implemented as either amplifier or synchronized oscillators. Both cases provide control with an input microwave signal, but in an amplifier output radiation drops to zero when input signal is switched off, while a synchronized oscillator in this situation continue operation on its own frequency. These approaches have equal potential for the most part of applications, however synchronization requires greater amplitude of controlling signal.

Design and development of high-power microwave device requires solving of a set of problems, which appear because of high intensity of electron flows and microwave radiation used in relativistic electronics. It seems that the most significant tasks for development of a high-power amplifier:

– elimination of high-frequency breakdowns;
– minimization of stray radiation;
– providing of operation with shot pulses;
– achievement of high gain.

The most reliable way to avoid high-frequency breakdown is decreasing of intensity of electric field inside the microwave system of the device, and at pre-breakdown fields the only opportunity to enhance the RF power is to increase the cross-section of microwave devices. However, in the oversized system, where transverse cross-section is large in comparison of squared wavelength $S >> \lambda^2$, the intense electron beam can excite several modes with different frequencies and spatial structures, that means the loss of coherence. So suppression of parasitic excitation of an amplifier becomes in relativistic electronics even more serious

and complicated than in classical case, because of various mechanisms of the excitation, which include not only reflection of the operating wave from the edges of the microwave system, but also excitation of backward waves. Let us note that the last case shall be considered as the most dangerous, because the backward wave can be excited without any reflection and the oversized microwave systems practically always realize synchronous interaction of electron beam with modes of this kind.

A stray radiation in tubes driven with explosion-emitted electron guns can appear also because of amplification of inherent noises of the electron beam. The origin of the noise is connected with discrete mechanism of formation of the beam, when electrons are emitted by small cathode areas within relatively short time. As a result the beam consists of great number of current portions and due to that it possesses noticeable large-scale shot noise. The noise level is not too high but it may be comparable with input signal because of large gap between anticipated output power of the relativistic amplifier and power of input driver based on a conventional microwave source.

Obviously these circumstances produce contradictive requirements to design of the powerful amplifier and lead to necessity of compromise solutions between high amplification and resistance to parasitic self-excitation, narrowing of the operation frequency band to reduce the influence of beam noise and stability of operation with respect to random variations of the beam parameters etc.

Some notes should be made on the basic mechanisms of stimulated electron radiation, which can be applied for the amplifier design. Rectilinear electron beams are produced with more simple electron guns and carry much power than curvilinear (helical or spatially oscillating) ones. So the most powerful amplifiers employ transient and Cherenkov emission of radiation rather than Bremsstrahlung radiation or wave scattering.

Looking through the world experience in research and development of HPM amplifiers (see Table) one may notice that the most powerful experimental designs use sectioned schemes of operation. Longitudinal sectioning of the interaction space of electron devices is often used for efficiency enhancement, but in powerful electronics the method is more attractive for mode selection and suppression of parasitic excitation.

Experimental HPM amplifiers

Device	F, GHz	P, MW	τ, ns	eff, %	G, dB	U, kV	J, kA
Klystron [1]	1.3	3000	60	35	38	500	16
TWT [2]	8.8	100	100	11	35	850	1
2 beam twystron [3]	30	600	10	20	10	600	5
2 sect. TWT [4]	36.4	100	4	10	44	500	2
BWA+TWT [5]	9.1	100	10	20	70	500	2

Continued

Device	F, GHz	P, MW	τ, ns	eff, %	G, dB	U, kV	J, kA
BWA+TWT [6]	9.1	1100	70	20	47	800	6
Plasma TWT [7]	9.1–13	50	100	5	30	500	2
FEM [8]	33.3	60	25	27	30	750	0.3
FEM [9]	35	1000	30	34	45	3000	1
CARM [10]	36.6	10	25	4	30	500	0.5
CARM [11]	35	12	20	6.5	30	1500	0.13

Coupling between parts in a sectioned device is in strong dependence on spatial structure of high-frequency fields in sections. So, the conjoint action of the device in a whole is realized only at a definite set of modes in sections. A spectral density of these sets will drop with increasing of number of sections, and it gives a principal opportunity to reach a selective operation of the device. TWT with severing gives an example of realization of the method in classical electronics (Fig. 1). The absorbing insert in the tube provides electrodynamic isolation of

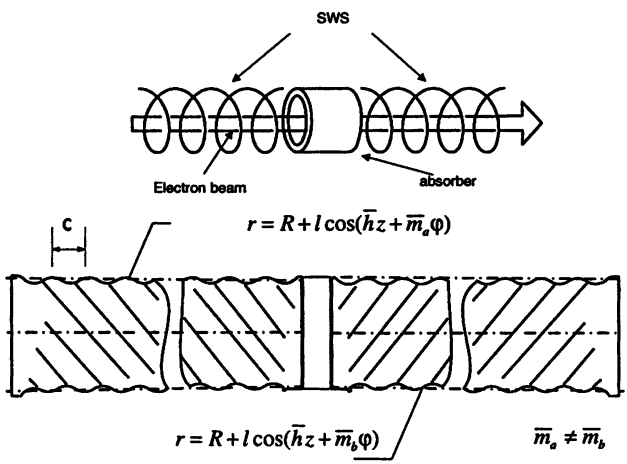

Fig. 1. Sectioned microwave systems: slow-wave structure with sever (top); corrugated oversized waveguides with common spatial harmonics (bottom)

device parts, which can be coupled by the common electron beam only. Modification of the method for oversized microwave systems employs for every part of the device orthogonal modes. Their coupling is provided by spatial harmonics of the modes, synchronous to the electron beam piercing the sections. Such interaction is possible if

$$\begin{aligned} h_a + \bar{h}_a &= h_b + \bar{h}_b, \\ m_a - \bar{m}_a &= m_b - \bar{m}_b, \end{aligned} \tag{1}$$

where $\overline{h}_i = 2\pi / d_i$, d_i and $\overline{m}_i$ are period and angular symmetry of corrugation of the slow wave structure respectively, h_i is longitudinal wave propagation constant, m_i is azimuth index of the mode.

Application of backward wave amplifying (BWA) section is another very useful feature for achievement of high gain in an amplifier. An advantage of the BWA is arisen because of realization of regenerative amplification regime near its self-excitation threshold. It permits:

- to realize the high gain $G \sim (1 - J/J_{st})^{-1}$, when operating current J aproaching to the starting one J_{st};
- to provide narrow amplification frequency band $\Delta f/f \sim (1 - J/J_{st})$ that is means for mode selection and for reduction of noise of the electron beam;
- to provide an electrodynamic decoupling between sections since amplified electromagnetic signal, is extracted from BWA to the direction of the cathode, whereas the following amplifying elements extract an output signal to the opposite direction.

A research interest to HPM amplifiers appeared in IAP practically simultaneously with development of relativistic electron oscillators. Several versions of amplifiers were developed and studied experimentally. At the first stage the problem of high gain was "bypassed" with application of powerful relativistic BWO served as master oscillator. The device was based on two coaxial beam design [3] (Fig. 2), where inner electron beam excited the BWO. Its output radiation drove a twystron-like amplifier operating at more powerful outer beam. The gain of the amplifier was relatively small (10 times) but it was enough to reach high output power (about 600 MW in Ka-band).

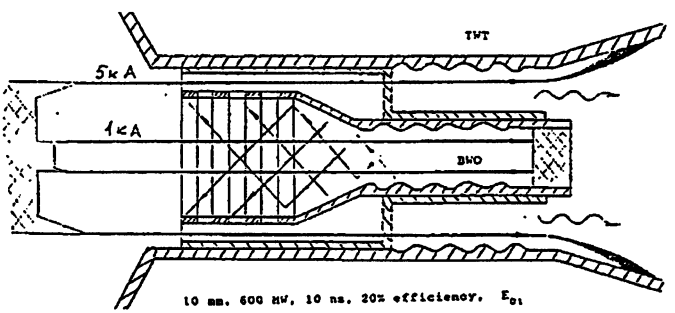

Fig. 2. Relativistic high-current twystron [3]. Master oscillator is driven by inner beam.

Using of TWT with sectioned slow wave system gave possibility to realize a high-gain amplifier driven with an ordinary magnetron master oscillator [4] (Fig. 3). A characteristic feature of the Ka-band amplifier was application of quasi-optical input of controlling signal.

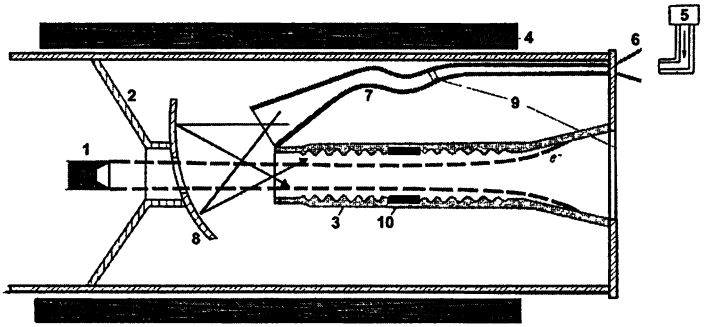

Fig. 3. Scheme of the sectioned TWT [4]: *1* – field-emission cathode, *2* – anode, *3* – slow wave structure, *4* – magnetic coil, *5* – magnetron, *6* – attenuator, *7* – mode converter, *8* – input mirror, *9* – vacuum windows, 10 – microwave absorber

The most powerful device were realized on a base of concept of a combination of BWA and TWT sections connected in series with a common electron beam and operated at different eigen modes [6]. The design provided more than 1 GW of output power in X-band and demonstrated reliable phase and frequency control of output microwave radiation.

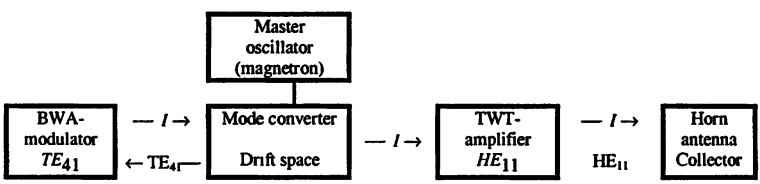

Fig. 4. Block diagram of the GW X-band amplifier [6]

The modern researches of amplifiers are aimed to enhance possibilities of controlling of output radiation parameters. First of all it concerns amplification band which is rather narrow especially in a case of application of a regenerative BWA. Enlargement of the band with preservation of high gain can be provided, for example, with two sequential BWA sections. On the other hand, there is a possibility of slow (from pulse to pulse) shifting of the frequency band by means of change of interaction conditions in the operating space of the amplifier. It may be mechanical change of parameters of the electrodynamic structure of the tube or electrical control of electron beam properties, in particular, induced by variation of focusing magnetic field in the vicinity of cyclotron resonance. The approach was demonstrated experimentally in oscillators [12], where about 5 % of frequency agility was achieved. Similar value of frequency tuning provided with change of magnetic field was observed experimentally in the X-band amplifier [6].

The prospects and future researches of HPM amplifiers are determined mostly with possible application requirements and expected to be focused on pulse-periodic operation mode, enlargement of the amplification band and amplification of composite signals.

References

1. *Friedman M., Krall J., Lau Y. Y., and Serlin V.* Rev. Sci. Inst. **61**, 171 (1990).
2. *Shiffer D., Nation J. A., Kerslick G S.* IEEE Trans. on Plasma Science, PS-18, 546 (1990).
3. *Bratman V. L., Gubanov V. P., Denisov G. G. et al.* Pisma JTF, **14**, 9 (1988).
4. *Abubakirov E. B., Botvinnik I E., Bratman V. L. et al.* JTF, **60**, 186 (1990).
5. *Volkov A. B , Zaitsev N. I., Ilyakov E. V. et al.* Pisma JTF, **18**, 6 (1992).
6. *Abubakirov E. B., Denisenko A. N., Fuks M. I. et al.* IEEE Trans. on plasma science, PS-30, 1041 (2002).
7. *Ponomarev A. V., Strelkov P. S.* Phys. Pl. **30**, 66 (2004).
8. *Conde M. E., Bekefi G.* IEEE Trans. on plasma science, PS-20, 240 (1992).
9. *Orzechovski T. J. et al.* IEEE Journal of Quantum Electronics, QE-21, 831 (1985).
10. *Bratman V. L., Denisov G. G., Korovin S. D. et al.* Relativistic microwave electronics, IAP, AS USSR, Gorky, **6**, 206 (1990).
11. *DiRienzo A., Bekefi G., Wurtele C. J.* Preprint MIT PFC/JA-90-40 (1990).
12. *Abubakirov E. B., Denisenko A. N., Soluyanov E. I. et al.* Pisma JTF, **26**, 14 (2000).

SMSA-2008: PULSE-PERIODIC GIGAWATT BWOS WITH LOW IMPEDANCE AND QUICK BUILD-UP

M. B. Goykhman[1], A. B. Gromov[1], V. V. Kladuhin[2], A. V. Kluchnik[3], N. G. Kolganov[1], N. F. Kovalev[1], A. V. Palitsin[1], V. N. Tulpakov[3]

[1] Institute of Applied Physics of RAS, Nizhny Novgorod, Russia
[2] Institute of Electrophysics of RAS Urals Division, Ekaterinburg, Russia
[3] Moscow Radiotechnical Institute of RAS, Moscow, Russia

Our research was aimed to enlarge average power of pulse-periodic relativistic BWOs by increase in the electron current without increase in the gun voltage. The periodic structure profile and matching of the structure with the output waveguide were optimized to shorten the BWO build-up time and to enlarge the overall efficiency. S-band and X-band BWOs were driven with 400–650 keV pulses of ~20 ns duration. The pulse repetition rates were up to 0.5 kHz. About 1 GW RF powers with efficiencies 20–30 % were obtained.

Investigations in the field of relativistic microwave electronics utilizing high current electron beams have been conducted during several tens of years, nevertheless the scopes of this promising branch of electronics are not clarified still. Full understanding is absent in basic issues as well as in specific technical aspects. Some of these problems are given in Table 1.

Table 1. Main problems in high power microwave (HPM) electronics

1. Electron gun • backward current, • exhaustion of emission, • cathode restoring time, matching of gun with power supply	**3. RF interaction space** • electric durability, • static space charge, electrostatic wiggler, • RF space charge, • build-up dynamics
2. Magnetic system and collector • cryomagnets, • cooling, • erosion and plasma recombination time, • reflected electrons	**4. RF output** • mode conversion, • horn and vacuum window, • RF output measurements

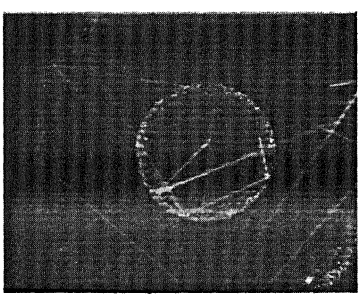

Fig. 1. Luminous drops in workspace

Existing situation is resulted from complexity of experimental research as well as from the lack of diagnostic tools. Difficulties are rising rapidly with increasing of output microwave power and especially in the case of development and research of oscillators operating in pulse periodic regimes with high repetition rate. As an exotic example on Fig. 1 it's shown the photograph of oscillator's working space made through the optically transparent vacuum window.

The camera exposition started approximately 10 ms after working pulse and shot time also was about 10 ms. As evident from Fig. 1 the working space isn't fully restored even after some milliseconds and the originated luminous drops can influence strongly on the following microwave pulses.

The questions related to elimination of high-frequency surface or space breakdowns in many aspects remain undecided. As an example we present some photographs of different breakdowns in Fig. 2–3. The space breakdown in the air is shown in Fig. 2*a*, situation including breakdown on surface of vacuum window – in Fig. 2*b*. Figure 3 presents a breakdowns on dissipative elements of calorimeter. The last picture illustrates difficulties in creation of diagnostic systems for relativistic microwave electronics.

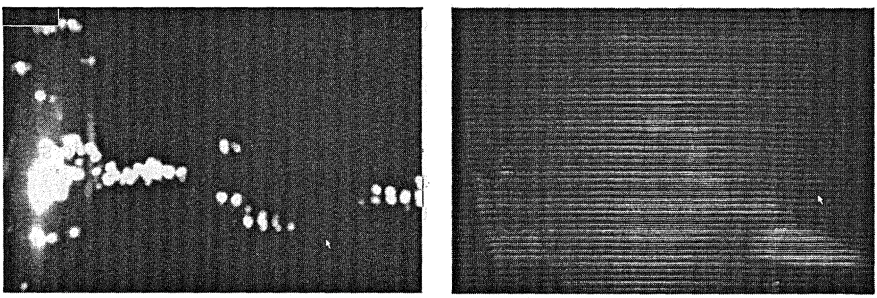

a *b*

Fig. 2. Air and surface breakdowns behind vacuum window

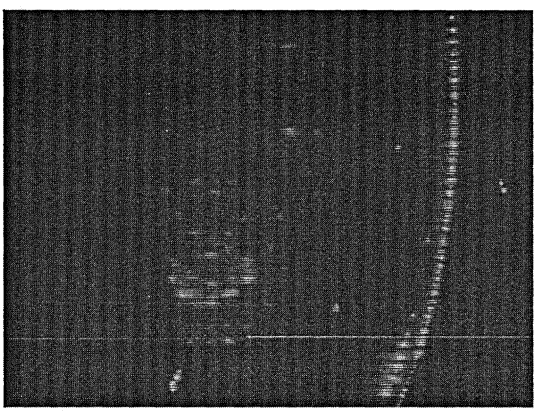

Fig. 3. Breakdowns on dissipative elements of calorimeter

The primary aim of the work is to confirm early achieved results and to define more correctly the aggregate of basic parameters attained by now as applied to relativistic BWOs. In experiments we used axisymmetric BWO with thin-

walled strongly magnetized electron beam emitted from magnetically insulated edged graphite cathode of a coaxial diode gun. The gun was placed in converging magnetic field, so the electron beam was compressed and the beam diameter can be changed by longitudinal displacement of cathode. A metal shield installed before cathode was used to decrease inverse electron beam current and has profile following magnetic field lines. A quarter-wave modulating resonator was used as reflector for experimental BWO prototype. The using of such reflecting resonators is confined by breakdowns. This reason limits output microwave power to 1–1.5 GW in case of accelerating pulse duration not more then 20 ns (for chosen BWO construction and obtained from analytical estimates and modeling experiments).

BWO workspace was weakly irregular and divided into two sections of corrugation, their dispersive curves are shown on Fig. 4. The corrugation profile was rectangular due to following reasons:

- it doesn't reduce total resistance to breakdown determined by resonance reflector;
- it decreases unwanted influence of high-frequency and quasistatic space charges fields for high magnetized electron beams;
- rectangular corrugation appreciably simplifies BWO's construction and matching of different junctions such as diffraction output or drift tube with corrugated section.

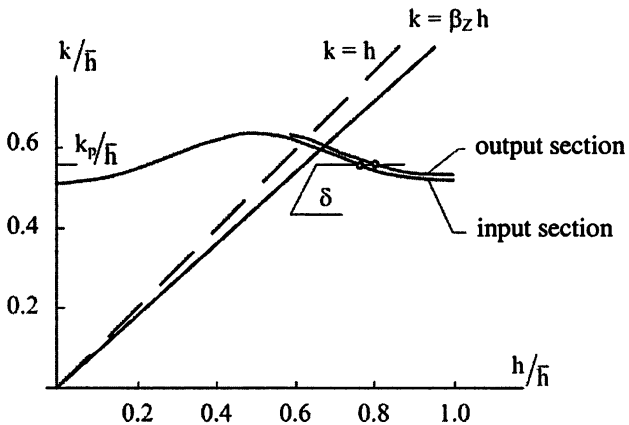

Fig. 4. Brillouin diagram of weekly irregular BWO

Two sets of BWO's (X- and S-band) were developed and manufactured. Sinusoidal corrugation and quarter-wave resonance reflector were used in S-band, rectangular corrugation and radial resonance reflector – in X-band. Electrodynamic systems of both sets were axisymmetric with operating axisymmetric wave of TM type, bent waveguide converters were used in output waveguide channels.

Here we present part of results related to pulse periodic regime and accordingly, to the stability of generation. Fig. 5 shows 200 successive pulses of X-band BWO operating in 2 Hz pulse periodic regime. As one can see, several pulses are missed, that is concerned with elongated rise time of some accelerating pulses. Besides this missed pulses the repeatability of the generation after first 30 pulses is rather high. In order to improve the reliability of results the number of series and total number of pulses were increased. Two pulses with maximum and minimum amplitudes in series are given in Fig. 6. These pulses correspond to the center of directivity diagram. At the diagram periphery the pulse form differs (Fig. 7) but, what is important, the stability of pulse form is rather high, that indicates fine spatial coherence ratio of output microwave radiation.

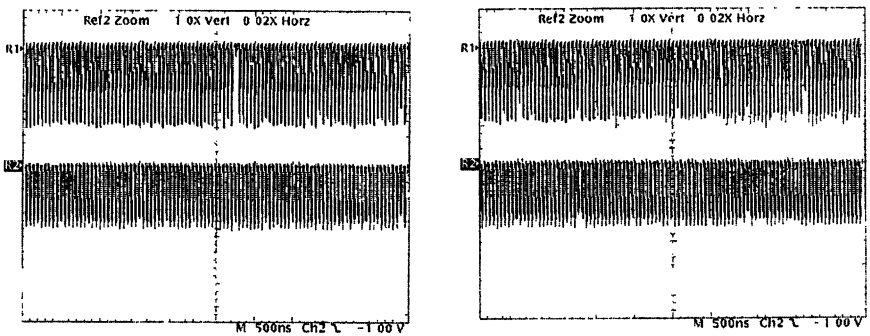

Fig. 5. Repetitive regime of BWO with irregular electrodynamic system. R1 – envelopes of microwave pulses, R2 – accelerating voltage.

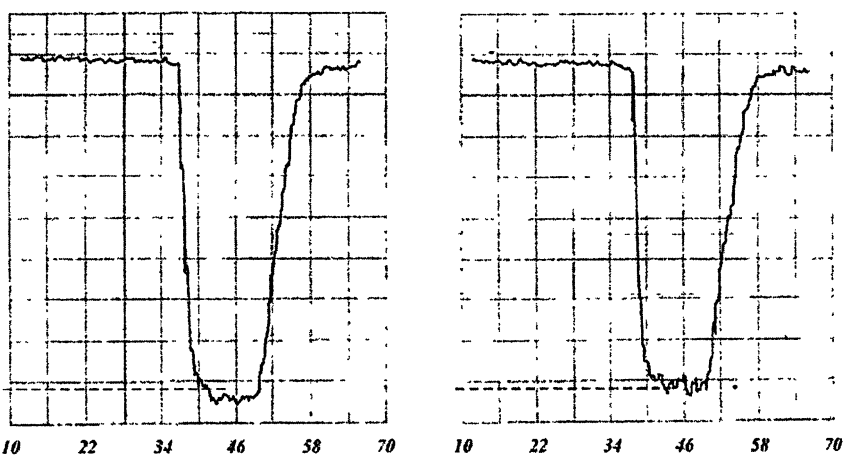

Fig. 6. Two pulses with maximum difference (5 series, 900 pulses per series, duration of pulse series 3 s)

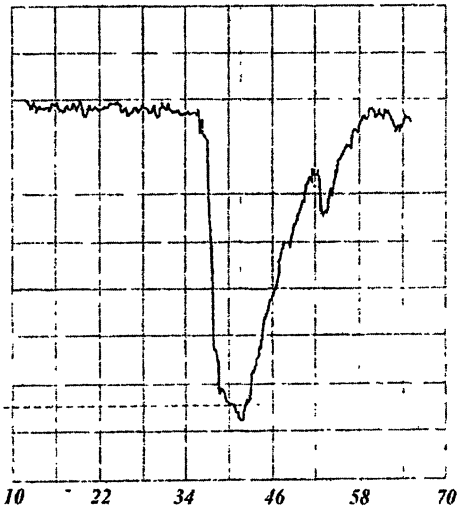

Fig. 7. HPM pulse envelope on the boundary of directivity diagram

The space coherence was observed by means of absorbing fibrous linen intercepting output wave beam. The photos of it's luminosity with and without mode converter are shown in Fig. 8.

Developed oscillators were tested in pulse burst regime. Fig. 9 is related to X-band BWO, Fig. 10 – S-band BWO. Both accelerators were not matched with electron guns, so afterpulses appeared. Afterpulses lead to generation of additional microwave pulses with reduced frequencies corresponding to synchronism of the wave to low-energy electrons. It evidences the absence of discharges in working space of microwave oscillators, which may lead to appearance of long-lived plasma. In accordance with oscillograms in Fig. 9–10 the microwave pulse's envelope stability is very high. Phase stability was also high since in X- and S-bands transient times were short (several microwaves periods). Short transient time leads to high energy efficiency – one of the most important consumer properties of oscillators.

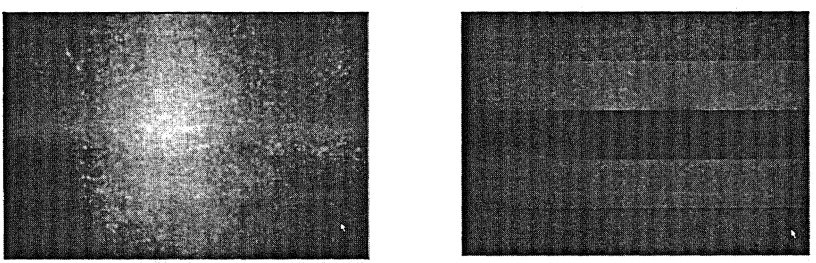

Fig. 8. Luminosity of absorbing fibrous linen intercepting output wave beam

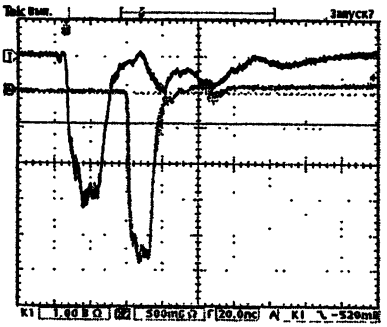

accelerating voltage	up to 700 kV
matched load	80 Ω
duration	20 ns
rise time	4 ns
repetition rate	up to 500 Hz
duration of pulse series	up to 5 s
Tesla's transformer efficiency	50 %

Fig. 9. Repetitive regime of 1 GW X-band BWO (rectangular corrugation). Channel 1 – accelerating voltage, Channel 2 – envelopes of microwave pulses.

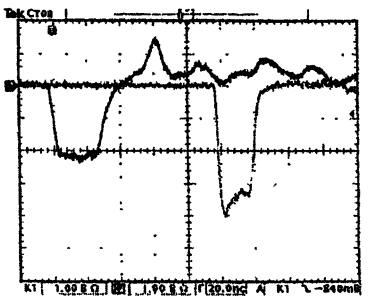

accelerating voltage	450–500 kV
matched load	50 Ω
duration	30 ns
rise time	5 ns
repetition rate	up to 700 Hz
duration of pulse series	up to 3 s
Tesla's transformer efficiency	55 %
Total accelerator efficiency	40%

Fig. 10. Repetitive regime of 0.6 GW S-band BWO (sinusoidal corrugation). Channel 1 – accelerating voltage, Channel 2 – envelopes of microwave pulses.

As a result of two experimental series we can conclude that it's possible to produce relativistic BWO's with aggregate of basic parameters, given in Table 2.

Table 2

Impulse microwave power	~ 1 GW
Pulse duration	~ $2 \cdot 10^{-8}$ s
Pulse repetition rate	~ 1 kHz
Accelerating voltage	~ 0.5 MV
Electron beam power	~ 4 GW

Both types of oscillators (X- and S-band) allow obtaining energy efficiency more than 20 %. Pulse series duration and time gap between them are determined by thermal conditions especially on collector. In accordance with simple estimations and experimental results in oscillators of considered type it is possible to archive the average power up to 100 kW without taking recuperation into account.

NON-STATIONARY NUMERICAL MODEL FOR SIMULATION OF COUPLED CAVITY MICROWAVE TUBES

V. N. Titov, A. V. Yakovlev, N. M. Ryskin

Saratov State University, Saratov, Russia

A computer code for non-stationary nonlinear simulation of a coupled cavity traveling wave tube is presented. The model is based on the non-stationary discrete theory of excitation of a periodic waveguide. It allows simulation of processes in the center of the slow wave structure pass band, as well as near cutoff/stopband. Results of numerical simulations of amplification in small-signal and large-signal regimes are presented. Non-stationary dynamics near cutoff including complicated transient processes of self-excitation is discussed.

Introduction

High-power sources of microwave radiation often operate in essentially time-dependent, non-stationary regimes, especially when utilizing high current relativistic beam with pulsed power supply. The development and optimization of such devices depends on the availability of effective tools for non-stationary numerical modeling. In this paper, we report development of the approach based on the non-stationary discrete theory of excitation of a periodic waveguide [1]. The basic equations of the theory are thoroughly reviewed in [2, 3] along with its implementations to finite-length periodic structures. According to [1–3], we represent a periodic slow-wave structure (SWS) by a chain of coupled microwave cavities. This approach precisely fits the SWS dispersion, takes into account interaction with all spatial harmonics and allows simulation of beam-wave interaction in the center of the SWS pass band as well as near cut-off/stopband. It is applicable for modeling of various microwave electronic devices such as multiple cavity klystrons, extended interaction klystrons, coupled cavity traveling wave tubes (TWTs) and backward wave oscillators (BWOs), etc.

Consider a finite-length periodic structure comprised of N cavities connected by uniform input and output waveguides with a driving signal source and an output load (Fig. 1). This model correctly takes into account the reflections from the couplers [2, 3], allowing simulation of self-excitation due to end reflections.

The beam-wave interaction is given by the 1D electron motion equations that are solved by "particles in cells" method [4] and the excitation equation

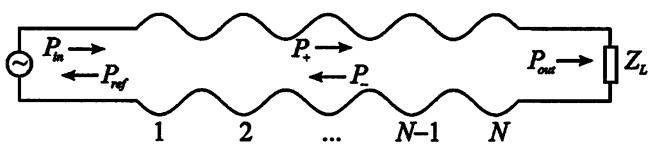

Fig. 1. Schematics of the SWS connected to input and output waveguides

[1–3], which in the simplest case of only single SWS eigenmode taken into account and coupling with only nearest neighbors takes the form

$$\frac{dC_n}{dt} - i\omega_0' C_n + \frac{i\Delta\omega}{2}\left(C_{n+1} + C_{n-1}\right) = -\frac{\omega_0 Z_0}{2V_0^2}\int_x I(x) E_0^*(x - nd)\,dx. \qquad (1)$$

Here ω_0 is cavities resonant frequency, $\omega_0' = \omega_0\left(1 + i/2Q\right)$, Q is quality factor, Z_0 is shunt impedance, V_0 is beam dc voltage, $I(x,t)$ is beam current, $E_0(x)$ describes cavity field profile, and d is the SWS period. Coupling parameter $\Delta\omega$ determines the SWS bandwidth.

The total field is expressed as a sum over the fields of all cavities:

$$E(x,t) = \sum_n C_n(t) E_0(x - nd). \qquad (2)$$

Numerical results

We selected CC TWT parameters similar to that of the TWT described in [6] (see Table).

Parameters of the coupled-cavity TWT

Beam voltage	11–20 kV
Operating band	5.7–7.3 GHz
Period	0.85 cm
Number of cavities	13–40
Shunt impedance	88 Ω

Calculations of small-signal gain in the case of non-relativistic dynamics [2, 4] in kinematic limit showed good agreement with the Pierce's linear TWT theory [7] considering long SWS with one forward harmonic dominating. However, for the moderate number of cavities the discrete nature of interaction is significant and no agreement with the wave theory is observed. Fig. 2 shows small-signal gain for the TWT consisting of 13 cavities. The gain curve exhibits strong ripples caused by the end reflections.

Analysis of self-excitation near cutoff is a challenging task due to the singularity of reflection factor at cutoff frequency [8–11]. The model developed in

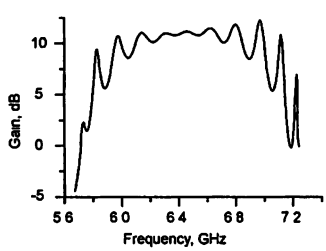

Fig. 2. Small-signal gain vs. frequency for TWT with 13 cavities, $V_0 = 18.3$ kV, $I_0 = 0.77$ A

this paper accounts for that phenomena [3]. Fig. 3 shows the self-excitation boundary on the beam voltage – beam current parameter plane near the upper cutoff (2π-mode). The voltage $V_0 = 11.26$ kV corresponds to synchronism at the cutoff frequency. For $V_0 < 11.26$ kV the beam interacts mainly with backward waves, and the system behaves as a BWO with strong end reflections (resonant BWO). Therefore the left branch of the boundary is shaped as a sequence of generation zones. Each zone corresponds to resonance with one of the high-Q axial eigenmodes of the SWS with strong end reflections. Fig. 4 shows typical distributions of the electromagnetic field along the system that establish after transient process. One can see that in different generation zones axial modes with different number of humps are excited. When the voltage shifts off from the cutoff, the starting current increases as the reflections diminish.

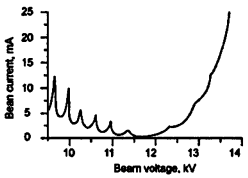

Fig. 3. Self-excitation current vs. beam voltage near upper cutoff

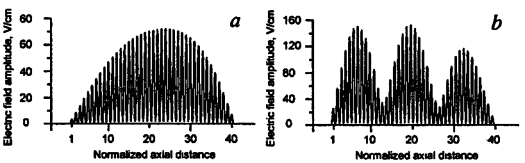

Fig. 4. Field distributions along the system above the self-excitation threshold for *a*) $V_0 = 11.65$ kV, $I_0 = 3$ mA; *b*) $V_0 = 10.725$ kV, $I_0 = 3{,}5$ mA

Voltages $V_0 > 11.26$ kV correspond to preferable interaction with forward wave, as in a resonant TWT. Excitation of the fundamental axial mode is observed after long transient process shown in Fig. 5. One can see strong mode competition effects with subsequent excitation of modes with higher frequencies. Such effects are typical for the resonant TWT and BWO interaction. After the transient process, the fundamental axial mode survives.

These results are in good agreement with the theory developed in [8–11]. However, the approach developed in [8–11] is valid only in the vicinity of the cutoff frequency and thus is less general.

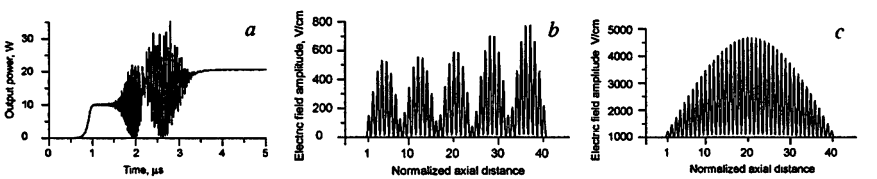

Fig. 5. Output power waveform of the transient process near cutoff, $V_0 = 13.2$ kV, $I_0 = 15$ mA (*a*). Field distributions in different moments of time: $t = 1$ μs (*b*), 3.4 μs (*c*).

Conclusion

The non-stationary discrete numerical model of coupled-cavity tubes has several important advantages. It is applicable for modeling processes in the center of the SWS pass band, as well as near cut-off/stopband, and describes both forward and backward-wave interaction. The theory takes into account frequency-dependent reflections from input and output couplers and suitable for simulation of coupled cavity TWT, BWO, multiple cavity klystron, extended interaction klystron, etc. The numerical model is fully non-stationary since no assumptions are made about the spectrum of the signal. Thus, it allows modeling of complicated non-stationary self-excitation processes, such as the nonlinear drive-induced excitation near upper cutoff (2π-mode) predicted in [10, 11].

The plans for further development of this numerical model include account of 2D electron motion and higher-order passbands, in particular, the slot mode in coupled cavity TWT.

Acknowledgements

The authors wish to thank A. G. Rozhnev and S. P. Kuznetsov for helpful discussions.

This work is supported by the Russian Foundation for Basic Research under grant № 08-02-00621. NMR is also indebted to the "Dynasty" foundation.

References

1. *Kuznetsov S. P.* Sov. J. Comm. Technol. Electron. **25**, 419 (1980).
2. *Ryskin N. M., Titov V. N.* IEEE PPPS Tech. Digest, 1185 (2007).
3. *Ryskin N. M., Titov V. N., Yakovlev A. V.* Modeling in Applied Electrodynamics and Electronics. № 8, 46. Saratov Univ. Press, 2007.
4. *Ryskin N. M., Titov V. N., Yakovlev A. V.* Modeling in Applied Electrodynamics and Electronics. № 8, 57. Saratov Univ. Press, 2007.
5. *Hockney R. W., Eastwood J. W.* Computer simulation using particles. New York: McGraw–Hill, 1981.
6. *Collier R. J. et al.* Bell Syst. Tech. J. **42**, 1829 (1963).
7 *Pierce J. R.* Traveling wave tubes. New York: Van Nostrand, 1950.
8. *Bulgakova L. V., Kuznetsov S. P.* Radiophys. Quant. Electron. **31**, 155 (1988).
9. *Bulgakova L. V., Kuznetsov S. P.* Radiophys. Quant. Electron. **31**, 452 (1988).
10. *Bulgakova L. V., Kuznetsov A. P., Kuznetsov S. P., Rozhnev A. G.* Sov. Electron Tech Microwave Electronics. № 3, 7 (1988).
11. *Kuznetsov A. P et al* Radiophys Quant. Electron. **47**, 356 (2004).

ADVANCED CATHODE RESEARCH AT CALABAZAS CREEK RESEARCH

R. L. Ives[1], K. L. Falce[1], G. Miram[1], Philipp Borchard[2], Ross Wilcox[2], Kim Gunther[3], Marc Curtis[3], Steve Schwartzkopf[4], Ron Witherspoon[4]

[1] Calabazas Creek Research, Inc, San Mateo, CA, USA
[2] Consultant, CA, USA
[3] HeatWave Laboratories, Inc., Watsonville, CA, USA
[4] Ron Witherspoon, Inc., Campbell, CA, USA

Research is in progress to improve the performance of dispenser cathodes for vacuum electron devices. Two approaches include the use of sintered tungsten wires to create controlled porosity cathodes and scandate to lower the emission work function. Progress in these two areas is reported.

Calabazas Creek Research, Inc. (CCR) and its associates are developing advanced cathodes for vacuum electron devices. These include development of controlled porosity cathodes using sintered tungsten wires [1] and scandate to lower the work function of the emission surface. CCR is also pursuing a combination of these two approaches. Results from this research are reported.

Tungsten Wire Cathodes

CCR began development of tungsten wire cathodes using a sintering technique described by Alexander and Balluffi in 1957 [2]. In this technique the tungsten wire is wound around a spool in a tightly packed array and sintered to create a material where the gaps between wires become pores that penetrate entirely through the material. The pattern appears similar to the pore structure in plants. CCR wound 20 μm diameter wire on a moly spool, sintered the material at 2075 °C for 75 min, and sliced the material to form caps for reservoir cathodes. Figure 1 shows a photograph of the face of the sintered material.

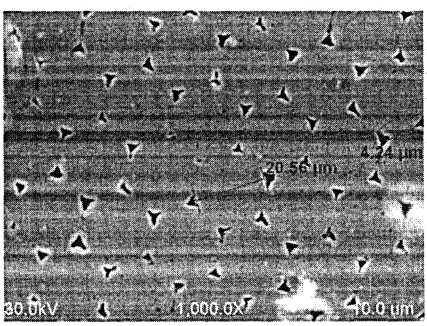

Fig. 1. Sliced surface from sintered tungsten wire

The reservoir cathode was fabricated by bonding a 0.025 in thick, 0.138 in diameter slice of the sintered material into one end of a molybdenum cylinder. The cylinder was filled with a mixture of barium oxide, calcium oxide, and aluminum oxide and bonded to another cylinder that contained a cathode heater. Figure 2 shows a photograph of the assembled cathode.

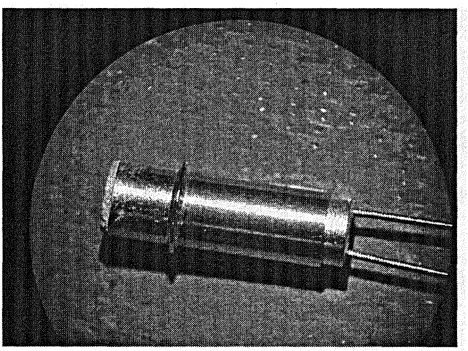

Fig. 2. Reservoir cathode with cap from sintered tungsten wires

Figure 3 shows the barium diffusion rate. The rate appears consistent with that required for a cathode emission current density of 50 A/cm^2.

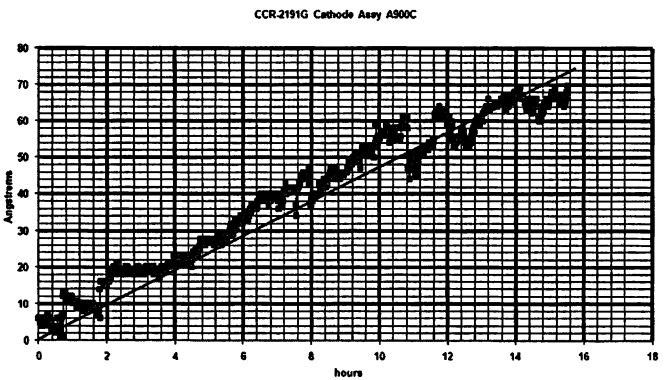

Fig. 3. Measured barium diffusion rate for sintered tungsten wire cathode

The cathode was installed in a device designed for cathode life testing. After life testing for 660 h, the cathode performance was measured in a Miram Curve Generator at an emission current density of 4 A/cm^2. The resultant rolloff curve is shown in Fig. 4. Since this cathode does not have a coated emission surface, it is a B-type cathode. The results indicate that the sintered wire cathode achieves or exceeds the best of class results for B-type cathodes. CCR is now fabricating

M-type cathodes with the goal of demonstrating 50 A/cm^2 cathode emission with long life. The cathode shown in Fig. 2 is now undergoing life testing.

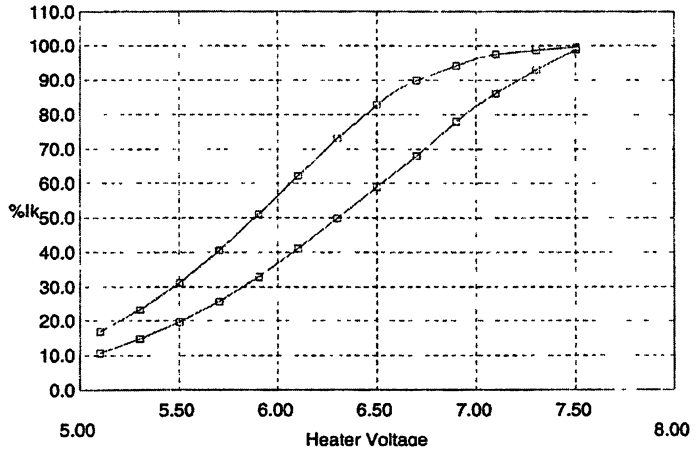

Fig. 4. Miram curve of sintered tungsten wire cathode with emission current density of 4 A/cm^2

Scandate Cathodes

Research in the 1980s indicated that scandium lowered the work function of cathodes, resulting in increased emission current densities at nominal operating temperatures [1, 2]. More recent developments by the Chinese renewed interest in this research [5, 6, 7]. Measurements at Stanford Linear Accelerator Center demonstrated 100 A/cm^2 emission at normal cathode temperature [8]. The primary issue with scandate cathodes, however, is related to the lifetime. It is well known that nano-particles of scandium on the surface leads to increased current emission at these locations. The issue arises when the scandate particles are removed from the surface by back ion bombardment or other erosion processes. The scandium is relatively immobile when bonded to tungsten. Consequently, particles removed from the surface are not easily replaced by migration of subsurface particles. This results in decreased performance with time.

CCR investigated three techniques for insuring sufficient scandate on the cathode surface for the lifetime of the cathode. Two processes were specific to the tungsten wire cathodes described earlier. The first technique involves bonding of the tungsten wires with scandium instead of sintering. This would provide an extremely large quantity of scandium on the surface and within a few microns of the surface. Initially, the approach was to sinter scandium wires in addition to tungsten wires; however, scandium melts around 1600 °C, which is far to low to sinter tungsten.

Figure 5 shows an photograph of tungsten wires brazed with scandium. The key requirement was that the scandium not close the pores between the tungsten wires. As can be seen, the pores are still open to provide a diffusion path for barium in a reservoir cathode.

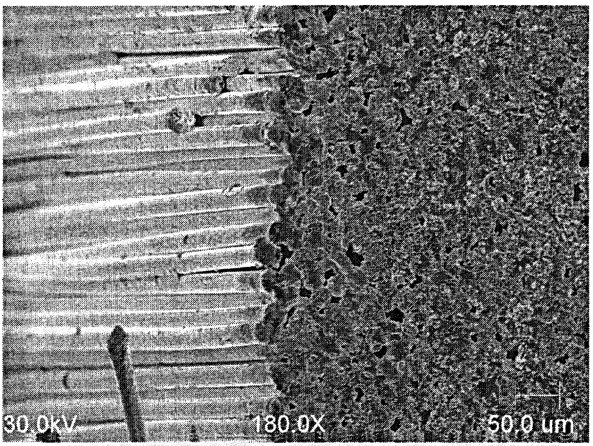

Fig. 5. Microscope photo of tungsten wires brazed with scandium

A second technique specific to the tungsten wire cathodes is to incorporate scandium powder into the reservoir with the barium compound. There would be two potential processes that could transport scandium to the surface. Since the reservoir is between the cathode and the heater, the temperature will be considerably higher than at the surface. If the temperature exceeds 1600 °C, the scandium could vaporize and be transported through the reservoir cap to condense on the surface. A second process could be direct transport of scandium particles with the barium as it diffuses to the surface. This would require the scandium particles smaller than the 4 μm micron pore size. CCR is currently pursing nano-size scandium to explore this technique.

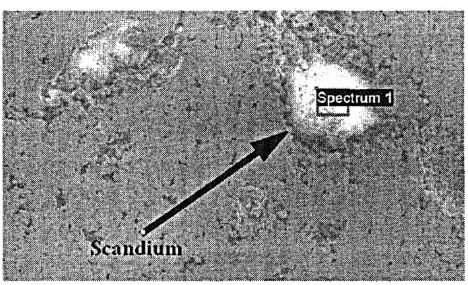

Fig. 6. Scanning electron microscope photograph of scandium on tungsten surface. The deposit is approximately 150 μm in diameter.

The final technique, which applies to both tungsten wire and sintered powder cathodes, involves chemical vapor deposition and insertion (CVD/CVI) of scandium. This technique was tested with sintered powder material. The goal was to deposit significant amounts of scandium on and below the sintered tungsten surface. The goals was to deposit sufficient scandium to survive erosion processes for the life of the cathode.

Figure 6 shows deposition of a large amount of scandium on the surface, and Fig. 7 shows deposition of subsurface scandium. Scandium was measured at depths approaching 1 mm below the surface. This represents a significant deposition of scandium. Life testing will be required to determine if this amount would be sufficient for long life cathodes.

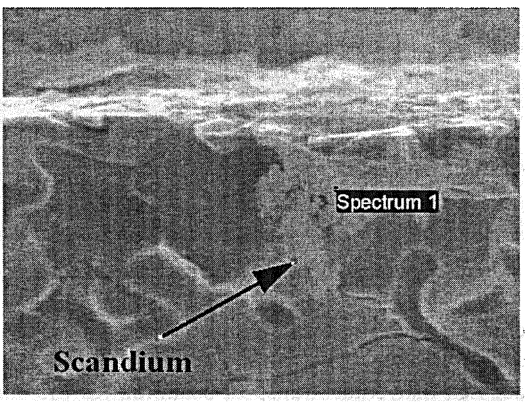

Fig. 7. Scanning electron microscope photo of subsurface scandium. The scandium extends approximately 10 μm below the surface.

Summary

Research is in progress to develop improved thermionic dispenser cathodes. A tungsten wire cathode was fabricated and tested with extremely encouraging results. Additional cathodes will be built and tested in the coming months. Techniques were developed for deposition and replenishment of scandium on the surface of scandate cathodes to achieve long life performance. These techniques will be tested with the tungsten wire cathodes.

Acknowledgements

This research was supported by U.S. Department of Energy grant number DE-FG03-03ER83827 and U.S. Air Force contract number FA9550-07-C-0063.

References

1. *Ives R. L., Falce L., Schwartzkopf S., Witherspoon R.* Controlled Porosity Cathodes From Sintered Tungsten Wires // IEEE Trans. on Electron Devices. 2005. Vol. 52, № 12, December. P. 2800–2805.

2. *Alexander B. H. and Balluffi R. W.* Acta Met., 1957, 5 (11), 666–677.
3. *Hasker J., Van Esdonk J., and Crombeen J. E.* Properties and manufacture of Top-Layer Scandate Cathodes // Applied Surface Science, 26 (1986), 173–195.
4. *Yamamoto S., Taguchi S., Watanabe I. and Kawase S.* Electron Emission Properties and Surface Atom Behavior of an Impregnated Cathode Coated with Tungsten Thin Film Containing Sc2O3 // Japanese Journal of Applies Physics. 1986. Vol. 25, № 7, July. P. 971–975.
5. *Jiang D., Hong S., Zhou C., Wang D., Liu X.* Preparation of Impregnated Barium Scandate Cathode and Its Application // Proc. 5th International Vacuum Electron Sources Conference, September 2004. P. 206–207.
6. *Shuguang W.* Scandate Cathode for TWT // Proc. 5th International Vacuum Electron Sources Conference, September 2004 P. 224–225.
7. *Yuan H., Gu X., Pan K., Wang Y., Liu W., Zhang K., Wang J., Zhou M., Li J.* Characteristics of scandate-impregnated cathodes with sub-micron scandia-doped matrices // Applied Surface Science, 251 (2005) P. 106–113.
8. *Schietrum G., Caryotakis G., Luhmann N., Wang Y., Li J., Miram G., Vancil B* 100 A/cm^2 Tungsten-Scandate Nanopowder Thermionic Cathode Testing at SLAC // Multidisciplinary University Research Initiative Annual Review, Monterey, CA, April 2006.

FAST OPTICALLY CONTROLLED MICROWAVE SWITCHES

G. G. Denisov, M. L. Kulygin, S. V. Kuzikov, A. A. Vikharev

Institute of Applied Physics, Russia Academy of Science, Nizhny Novgorod, Russia

Switches, based on induced photoconductivity, are considered as attractive devices for fast control of microwave radiation at very different frequencies (10–1000 GHz) [1–3]. The main advantage of such switches, based on semiconductors, is a fast time of switching due to the use of short-pulse lasers. In the paper we consider several types of switches in dependence of microwaves to be switched: high peak power, low peak power, and high average power.

Introduction

Semiconductor-based switches of microwave radiation are considered to be used for switching of microwaves in different electronic devices including particle accelerators, radars, spectroscopy modulators etc. The switching effect is reached due to a fast (much less than pulse duration) appearance of a thin photoconductive layer created by means of laser light which quant energy is close to semiconductor band gap. In order to be influent to microwaves, the concentration of free carriers in such a layer should be high enough (e.g. higher than critical value for a given frequency).

Let us consider main properties of semiconductor switches using as an example a so-called 180° phase shifter. In order to switch a phase of the reflected beam, the semiconductor of the proper thickness could be placed on metal mirror (Fig. 1).

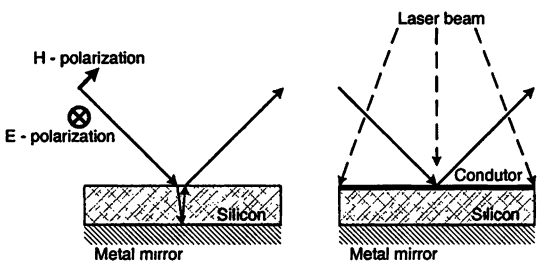

Fig. 1. Principle of phase switching by semiconductor irradiated by laser

Small tangent losses, a high concentration of free carriers in photoconducting layer and fast growth of this concentration ("metallization") under laser light are typical requirements to switches. One of attractive materials is a silicon ($\tan \delta = 10^{-2}$–10^{-6}). The band gap of silicon (1.1 eV) is close to most popular laser wavelengths, such as Nd:YAG with $\lambda = 1064$ nm at first harmonic and $\lambda = 532$ nm at second harmonic, and Ti:Sa with $\lambda = 795$ nm wave length.

Calculations of the scheme (Fig. 1) by means of strong-collision plasma model [4] in the conducting layer show possibilities to provide the full reflection of 30 GHz microwaves with the desired 180° phase shifting. The graphs in the Fig. 2 show a reflection and phase of reflection as a function of free carrier's concentration. While the concentration is less than critical concentration, the reflection is low (Fig. 2*a*), and the phase is far from the needed 180° (Fig. 2*b*). These are explained by high absorption in a low-density plasma created in the photo-conducting layer. As soon as the concentration reaches ~ 10^{18} cm^{-3}, the reflection comes to 100 %, and the phase goes to 180°.

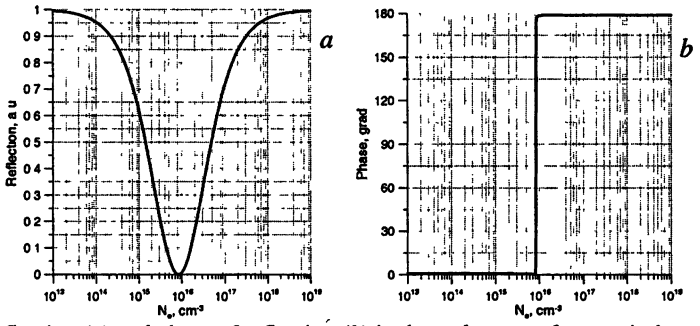

Fig. 2. Reflection (*a*) and phase of reflection (*b*) in dependence on free carrier's concentration in conducting layer

In order to show a possibility to reach the necessary concentration level by accessible lasers, we have carried out preliminary experiments at low RF power level at 30 GHz (Fig. 3*a*). The best results in these experiments were achieved with a silicon doped with gold and Ti:Sa laser (10 ns pulse duration, energy in pulse up to 10 mJ). The observed reflection immediately after laser pulse was ~ 0.9–0.95. Typical reflection rise time was less than 1 ns, which was also independently measured by means of 70–80 fs laser pulses. Other mentioned lasers did not provide so high reflection level. As an explanation, for 532 nm laser the absorption depth (~1 μm) is too thin in comparison with the skin depth at 30 GHz, and for 1064 nm laser the absorption depth is too thick (about 1 mm).

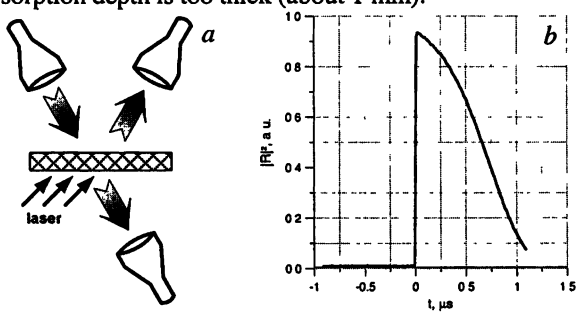

Fig. 3. Scheme of preliminary tests (*a*), reflection from silicon slab irradiated by Ti:Sa laser (*b*)

The measured relaxation time for the doped silicon (~500 ns) was much less than this value for the pure silicon.

High peak power microwave switches

High peak power level of microwaves due to breakdown limitation ($E \leq 100$ kV/cm [5]) requires a big surface of semiconductor to avoid self-breakdown and leads to quasi-optics and accordingly to powerful lasers. In particular, a 30 GHz 180° fast phase-shifter, designed and tested at IAP for a high-power pulse compressor in CERN, was based on wide-aperture Gaussian optics. An active element of this switch consisted of a copper plane mirror with a silicon plate (∅ 100 mm) on it. The Ti:Sa laser (λ = 795 nm, τ = 10 ns) was used with energy up to 10 mJ [2].

For testing of phase switch a special diagnostic resonator with variable length for frequency tuning was used (Fig. 4). This test modeled passive compression (for example, see [6]). Due to fast 180° phase switching the power reflected by an iris of the resonator is added in phase to the power leaked from within this resonator. This leads to increase of total reflection (e.g. compression). The used resonator with $Q_{coupling} = 2Q_{load}$ allowed the maximum power gain equaled 4. This value was just measured in the described experiment under laser energy exceeding 5 mJ (Fig. 5).

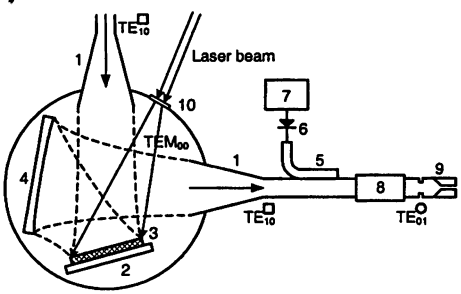

Fig. 4. Scheme of phase switch test: *1* – horns, *2* – flat copper mirror, *3* – silicon disk, *4* – focusing copper mirror, *5* – directional coupler, *6* – detector, *7* – oscilloscope, *8* – Marier converter, *9* – diagnostic resonator, *10* – lens

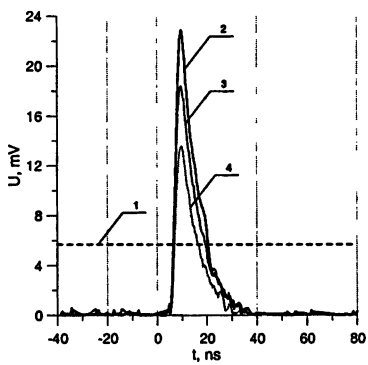

Fig. 5. Pulse compression by diagnostic cavity at laser energy: *2* – 8 mJ, *3* – 5 mJ, *4* – 2 mJ. *1* – level of incident wave.

Low power microwave switches

At low peak power microwaves, when the electric field is much less than threshold value, so-called resonant switches are promising. These switches (to be shaped by high-Q resonators) are operated by means of resonance's destroying due to "metallization" of photoconductive layer as well as absorption in it. A resonator allows decreasing the necessary carrier's concentration and the laser power. Requirements to spatial quality of the laser spot on semiconductor are also reduced. Because of the essential reduction of light power, cheap laser diodes are able to substitute more expensive lasers.

Let us consider a model of resonant switch based on the silicon disk covering the metallic mirror (Fig. 6*a*). The semitransparent grating placed above semiconductor (Fig. 6*a*) makes the resonator for the radiation traveling between the mirror and grating. The reflection (Fig. 6*b*) as well as phase of reflection (Fig. 6*c*) is sensible to the length of the resonator. The incoming laser light changes this effective length and, of course, causes absorption. Calculations of the 30 GHz switch with Ohmic losses taken into account show that necessary light energy can be reduced by at least 100 times in comparison with the energy needed for full "metallization".

The waveguide version of the resonant switch with an expansion filled by silicon is shown in Fig. 7. This switch on TE_{01} mode of circular cross-section waveguide works as a power modulator. Without lasing the expansion provides near to full RF reflection. However, the light power is able to increase dramatically the transmission coefficient.

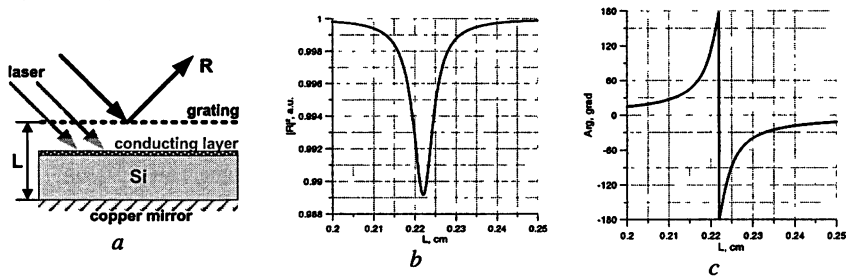

Fig. 6. Resonant switch (*a*) and its characteristics: reflection (*b*) and phase of reflection (*c*) in dependence on distance between grating and silicon

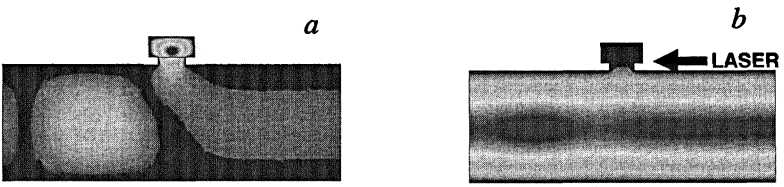

Fig. 7. Field structure in case of light absence (*a*) and in presence of light (*b*)

High average power microwave switches

At high average power of microwaves it seems natural to use components based of self-switching due to heating of semiconductor by microwave radiation. Because of the temperature rise, the concentration of free carriers is higher than the room temperature concentration. Calculations, carried out by FDTD technique, show that a relatively low-power laser in this case might be used only for ignition of "metallization" effect [7]. The power level of microwave radiation for such scenario corresponds to the field ≤100 kV/cm, which is close to breakdown threshold. That is why, high power tests are necessary.

Conclusion

Quasi-optical principles allow efficient switching of high peak power microwaves. According to these principles fast optically controlled 100 MW phase switch was designed and manufactured. Low power experiments showed efficient phase switching at 30 GHz.

For low peak power applications resonant switches seem most preferable ones. Cheap low power laser diodes could be used for switching in this case.

For high average power microwaves switches could be designed to work in regime of self-switching with a control by laser ignition.

References

1. *Tamura F. et al.* Phys. review letters special topic: Accelerators and beams, vol. 5, 062001, 2008.
2. *Vikharev A. et al.* Radiophusics and Quantum Electronics. 2007. Vol. 50, № 10/11. P. 786–793.
3. *Fujita T. et al.* Con. Digest of the Joint 31st Int. Conf. on IRMMWs and 14th Int. Conf. on Terahertz Electronics, Shanghai, China, 2006, p. 462.
4. *Sze S. M.* Physics of semiconductor devices. New York: John Wiley & Sons Inc., 1981.
5. *Tamura, Fumihiko and Tantawi, Sami G.* Phys. Review special topic: Accelerators and beams, vol. 5, 062001, 2002.
6. *Tantawi S. G., Dolgashev V. A., Nantista C. D.* Proc. of LINAC 2004, Lubeck, Germany, 2004, p. 852.
7. *Denisov G. G., Kocharovsky Vl. V., and Kulygin M. L.* Bulletin of the Russian Academy of Sciences: Physics. 2009. Vol. 73, № 1. P. 91–95.

TO THE IMPROVEMENT OF RESONANCE DIPLEXER

S. N. Vlasov, E. V. Koposova

IAP RAS, Nizhniy Novgorod, Russia

An improvement of diplexer to make it available for work on waves with any polarization is suggested. The grating having identical factors of reflection (on a power and on a phase) into zero mount for both polarizations of electromagnetic field is found and presented. The reduction of ohmic losses may be reached in multi-mirror diplexer by returning to a plane configuration of it and using the E-polarization of electromagnetic field.

The resonance diplexer which represents four-mirror symmetric resonator having two opposite plane corrugated mirrors and two opposite parabolic mirrors [1] (Fig. 1) was used at experiment on combine of two beams of gyrotron power successfully carried out in Germany not long ago.

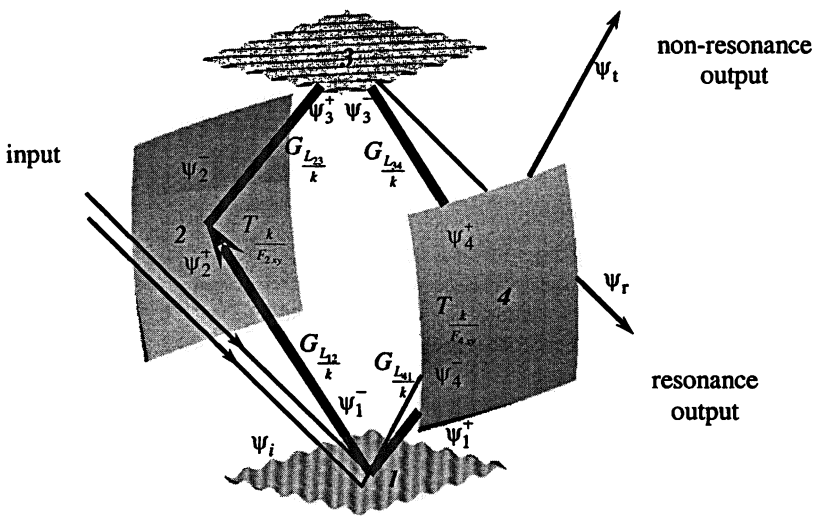

Fig. 1

Corrugated mirrors were intended for input and output of radiation from diplexer by scattering of incident wave to specular direction and –1 Littrow mount. A working eigenmode – the Gaussian beam with linear polarization had a plane phase front on corrugated mirrors. The direction of corrugation had an angle 45° with a central plane of the resonator, the directions of corrugation for the upper and lower mirrors differed on 90°. Such cross orientation of corrugated mirrors does not change eigenmode polarization of the resonator (electric *E* or magnetic *H* field relative to the corrugation). Usually the eigenmode with electric *E* field along corrugation is used for the purpose of the better electro strength. Non-

resonance frequency simply reflects from corrugated mirror to the specular mount and leaves the diplexer. But resonance frequency reflects from corrugated mirror to the –1 Littrow mount and cycles into resonator. It leaves from the opposite mirror in direction differed from non-resonance output.

The theory of 4-mirror diplexer

The theory of diplexer based on the solution of quasi-optical integral equations [2], built in terms of the method of operators, suggested by V. I. Talanov in 1965.

Let's consider the beam of electromagnetic waves, having hybrid polarization in general case, so each wave may have two components of polarization and describes by two amplitudes A_E, A_H – the amplitudes of E and H polarizations at beam relative to grating respectively. Each wave has a structure $\psi^{\pm}_{E,H\,n} = A^{\pm}_{E,H\,n}\, f^{\pm}_n(x,y)$, depending on transversal coordinates at the plane, perpendicular to the propagation direction. Index n is a number of mirrors. «+» means beam incoming to mirror, «–» means beam leaving from mirror. Input to the resonator beam, resonance and non-resonance output from the resonator beam are described by indices «*i*», «*r*» and «*t*» (see Fig. 1).

The amplitudes of beams on grating 1 are related as following:

$$\begin{aligned} A^{-}_{E,H\,1} &= i\,R_{E,H}\,A_{E,H\,i} + T_{E,H}\,A^{+}_{E,H\,1}, \\ A_{E,H\,t} &= T_{E,H}\,A_{E,H\,i} + i\,R_{E,H}\,A^{+}_{E,H\,1}. \end{aligned} \qquad (1)$$

Here $T_{E,H}$ is grating transmission coefficient to specular mount, $R_{E,H}$ is grating reflection coefficient to –1 Littrow mount. We consider transform coefficients $R_{E,H}$ and $T_{E,H}$ to have amplitudes and phases. Ohmic losses were not included in their values. Polarizations were not related on grating in approximation under consideration.

The transformation of beams on grating 3 occurs in accordance of:

$$A^{-}_{E,H\,r} = i\,R_{E,H}\,A^{+}_{E,H\,3}, \qquad A^{-}_{E,H\,3} = T_{E,H}\,A^{+}_{E,H\,3}. \qquad (2)$$

The propagation along resonator from mirror to mirror is described by operator $G_{L_{nm}/k}$, there L_{nm} is the distance between mirrors n and m. Mirror n diaphragms the beam and add a phase correction to it, which describes by operator $T_{k/F_{nxy}}$. The limiting of mirrors and ohmic losses are described by addition operator D_n. So we can put down the operator equation for the definition of the beam $\psi^{-}_{E,H1}$:

$$\begin{aligned} \psi^{-}_{E,H\,1} &= iR_{E,H}\,\mathrm{P}D_1\psi_{E,H\,i} + \\ &+ T^2_{E,H}D_1 G_{\frac{L_{41}}{k}} D_4 T_{\frac{k}{F_{4xy}}} G_{\frac{L_{34}}{k}} D_3 G_{\frac{L_{23}}{k}} D_2 T_{\frac{k}{F_{2w}}} G_{\frac{L_{12}}{k}} \psi^{-}_{E,H\,1}. \end{aligned} \qquad (3)$$

The operator of scale transform P is entered to this equation. It's entering is specify by the fact, that the incident to the gratings and reflection beams have different scales on transversal coordinates at the plane, perpendicular to the propagation direction. The action of the scale operator in simplest case – then incident and diffraction angles are equal 45° is:

$$\mathrm{P}\psi_i(x,y) = \psi_i(\bar{x}\sqrt{2}, \bar{y}/\sqrt{2}). \tag{4}$$

The similar computation need for equations, defined output beams:

$$\begin{aligned} \psi_{E,H\,t} &= D_1 T_{E,H}\,\psi_i + iD_1 R_{E,H}\,\mathrm{P}^{-1}\psi^{+}_{E,H\,1}, \\ \psi_{E,H\,r} &= iD_3 R_{E,H}\,\mathrm{P}^{-1}\psi^{+}_{E,H\,3}, \end{aligned} \tag{5}$$

where P^{-1} is operator inverse to P.

This method provides the accounting of diffraction and ohmic losses.

Omni-polarization grating

We suggest some improvements of the diplexer. The first of them is to make it available for work on waves with any polarization. Let's return to basic equation consideration (3) for *E*- and *H*-polarizations. These equations differs only by gratings factors $R_{E,H}$ and $T_{E,H}$. Modes for *E*- and H-polarization have different frequencies, so if we work of one of them, another been spent into radiation losses. If their frequencies are identical – the case of degeneration, it is possible to work on any polarization.

Diplexer operation on waves with any polarization is possible, if its gratings have identical factors of transformation on a power and on a phase into zero mount for both polarizations of electromagnetic field. It can be reached by a choice of a profile of gratings.

According to rough estimates, since the *E*-polarized wave reflects from tops of grooves inhomogeneities but *H*-polarized wave reflects from bottom of grooves, we have the possibility of independent control for reflection coefficients of *E*- and *H*-polarization by placing a tooth inside groove and changing its dept. For equalization of *E* and *H* phases we should choose the width of groove on a period.

For searching of a grating profile with the necessary diffraction properties we used the gratings computer program developed by us earlier. It is written on Visual Fortran and contained results visualization. The program is based on the rigorous solution of the integral equation of a problem of diffraction of a plane wave on the corrugated surface [3].

The example of grating with such groove profile theoretically designed for a 4-mirror diplexer is illustrated at Fig. 2.

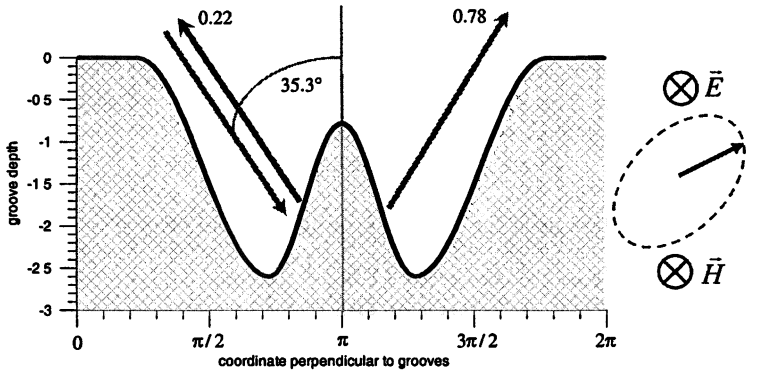

Fig. 2

The profile (see Fig. 2) represents sine on the part of period, constant on another part of period, and addition sine with its own amplitude. Horizontal and vertical scales are identical. The groove period $d = 0.866\lambda$ is taken equal to 2π.

This profile is described by formulas:

$$x \le a_1 \Leftrightarrow h(x) = 0, \qquad a_1 \le x \le a_2 \Leftrightarrow h(x) = A\left(\cos\frac{x-a_1}{q_d} - 1\right),$$

$$a_2 \le x \le a_3 \Leftrightarrow h(x) = A\left\{\tilde{A}\left[1 - \cos\frac{x-a_2}{1-\left[q_d + (1-q_d)(1-q_q)\right]}\right] - 2\right\}, \qquad (6)$$

$$a_3 \le x \le a_4 \Leftrightarrow h(x) = A\left(\cos\frac{x-a_4}{q_d} - 1\right), \qquad x \ge a_4 \Leftrightarrow h(x) = 0,$$

matching on the boundaries of 5 regions at the horizontal axis in 4 points.

The definition of conjunction points at the horizontal axis is:

$$a_1 = \pi(1-q_d)(1-q_q), \quad a_2 = \pi\left[q_d + (1-q_d)(1-q_q)\right],$$
$$a_3 = \pi\left\{2 - \left[q_d + (1-q_d)(1-q_q)\right]\right\}, \quad a_4 = \pi\left[2 - (1-q_d)(1-q_q)\right]. \qquad (7)$$

Here q_d, $q_q \in (0, 1)$ – parameters which belonging to the interval (0, 1). They define the width of groove at period and profile asymmetry.

The corrugation depth is defined by parameters A and $\tilde{A}$.

Optimized parameters are:

$$q_d = 0.5, \quad q_q = 0.55, \quad \tilde{A} = 0.7, \quad A = 1.3. \qquad (8)$$

The corresponding groove profile is shown in the Fig. 2 above.

A plane wave incident to the grating is partially reflected into the specular direction (78 %) and partially scattered into the –1st diffraction beam (22 %), which is counter-directional to the incident one (Littrow condition). The inci-

dence angle is 35.3°. Power distribution between the beams and the specular beam phase relative to the incident wave do not depend on the incident wave polarization: *E* or *H*.

Reduction of ohmic losses at plane configuration

The second suggestion of an improvement of the diplexer is the reduction of ohmic losses that may be reached in multi-mirror diplexer. For it achieving one must return to use a plane diplexer configuration [4] in which the incident on a diplexer grating beam and the beams reflected from it are in one plane which is passing through normals to the mirrors. So the *E*-polarization of electromagnetic field (then **E** is perpendicular to the incident plane on mirrors and parallel to the grating grooves) may be used in an offered configuration.

Let's consider the simplest case of reflection from the plane mirrors. Reflection coefficients from general formulas [5, 6] are the same than for two-layer medium, but the skin layer is taken in the capacity of second media. For the wave with **E** perpendicular to the incident plane reflection coefficient is equal $r_E = -\sqrt{1-2kd\cos\theta}$, there k is the wave number of free space, d – the depth of skin layer, θ – the incident angle on each mirror. For the wave with **E** laying in the incident plane reflection coefficient is equal $r_H = \sqrt{1-2kd/\cos\theta}$. Ohmic losses are: for *E*-polarization $2kd\cos\theta$ and for *H*-polarization $2kd/\cos\theta$. So the relation between losses for space diplexer with incident angle 45° and plane diplexer is 1.5.

The principle configuration of plane diplexer is shown on the Fig. 3.

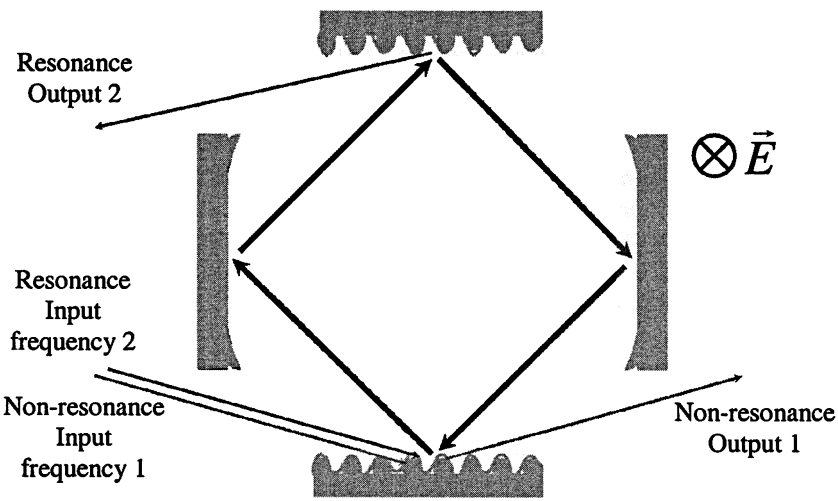

Fig. 3

The directions of corrugation on gratings are parallel each other. The polarization of incident beam is linear and electrical field is parallel to corrugation. Non-resonance frequency 1 reflects from corrugated mirror to the specular mount and leaves the diplexer. The resonance frequency 2 reflects from corrugated mirror to the –1 – here it is not Littrow mount – and cycles into resonator. Its output is on the opposite mirror to the –1 – (not Littrow mount) in direction opposite to non-resonance output. The equations describing wave interaction and scattering in this configuration of diplexer are the same that at space configuration (1–3).

Work is supported the RFBR (the Grant № 08-02-01233).

References

1. *Kasparek W., Petelin M., Erckmann V., Shchegolkov D., Bruschi A., Cirant S., Litvak A., Thumm M., Plaum B., Grünert M., Malthaner M.* Fusion Science and Technology, **52**, 281 (2007).
2. *Talanov V. I.* Izvestiya VUZ. Radiofizika, **8**, 260 (1965).
3. *Vlasov S. N., Koposova E. V. and Lapshina A. I.* Radiophysics and Quantum Electronics, **49**, 354 (2006).
4. *Turchin I. V.* Radiotechnics and electronics, **48**, 684 (2003).
5. *Katzenelenbaum B. Z.* Vysokochastotnaja elektrodinamika. Moscow: Nauka, 1966. 240 p.
6. *Vainstein L. A.* Electromagnetic waves. Moscow: Radio i svazj, 1988. § 15, p. 57.

PRESENT DESIGN AND PERSPECTIVES OF RESONANT COMBINERS BASED ON RECTANGULAR CORRUGATED WAVEGUIDES

A. Bruschi[1], *W. Bin*[1], *O. D'Arcangelo*[1], *F. Gandini*[1], *S. Garavaglia*[1], *W. Kasparek*[2], *A. Moro*[1], *V. Muzzini*[1], *B. Plaum*[2], *A. Simonetto*[1]

[1] Istituto di Fisica del Plasma-CNR, Milano, ITALY
[2] Institut für Plasmaforschung, Universität Stuttgart, Germany

The power from multiple sources can be combined or distributed to separate outputs using a new generation of devices recently developed. A family of these is based on the splitting properties of a rectangular corrugated waveguide characterised by a proper length and fed with a beam in a suitable geometry. A prototype based on a couple of resonating loops including these waveguide splitters has been measured at low power at 105 GHz. A report is given on the measurements, the alignment and the tuning procedures. A study on optics and on input configuration is required in order to guarantee a minimum degradation of performances in real applications. Configurations with side-input coupling to the waveguide and astigmatic beams in input are presented. They may drastically reduce the overall waveguide length, without performance degradation. The possibility to split beam power in unequal ratios using waveguides with fractional length allows a spectrum of new applications for devices using rectangular corrugated waveguides, from non-3dB couplers to resonators coupling more than two channels.

Introduction

A new generation of splitting/combining devices is in development for powerful millimeter-wave beams. These four-port devices are based on resonant circuits or interferometers with a long delay line using either quasi-optical or waveguide splitters. The two outputs and two inputs allow their use as diplexers and combiners controlled by small frequency shifts of the source or fine-tuning of the loop length [1, 2].

The goal of a high power capability in Electron Cyclotron (EC) transmission lines reduces the available beam splitting media. A promising one is the square or rectangular corrugated waveguide of proper length exploiting the imaging properties already used for the proposal of the remotely steerable (RS) antenna for EC on ITER [3]. Using three identical square corrugated (SC) waveguides with side b and length $2b^2/\lambda$ as splitters, a device based on a couple of resonating loops [4] has been made. In this paper the low power measurements of a 105 GHz prototype are reported and some alignment and tuning issues that arose during measurements are discussed. In perspective, a few problems of the angled input can be overcome with side-input coupling to the waveguide. This scheme can be achieved in two ways: using rectangular and longer waveguides for equal input beam size, or feeding the waveguides with astigmatic beams. Side input gives some additional features that can be exploited to widen the range of devices ap-

plicable to high power transmission lines. The last part of this paper will show some of them.

Low-power measurements and alignment issues

The 105 GHz prototype of a 2-loop version (see Fig. 1) has been assembled at IPF Stuttgart as shown in Fig. 2*a*, using the waveguide already used for the high-power test at 140 GHz of the RS antenna for ITER [5]. The three adjacent waveguides are fed with angled beams and coupled with spherical mirrors. Focal length of the mirrors equals their distance from the waveguide entrance. A gaussian beam generated with a horn-lens antenna is fed in input 1 (In1) and beams are measured at the outputs. Local measurements performed with a Vector Network Analyzer guided the system tuning.

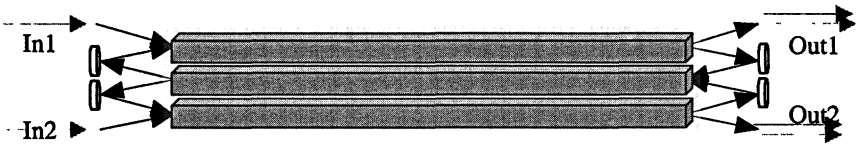

Fig. 1. Sketch of the 2-loop resonating combiner made using SC waveguide

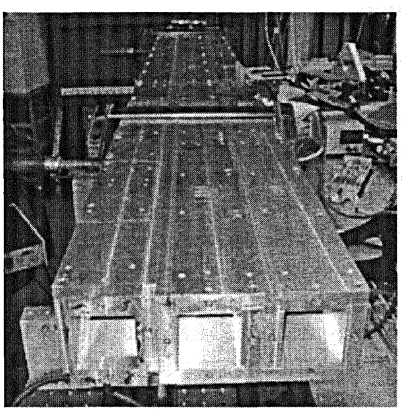

a

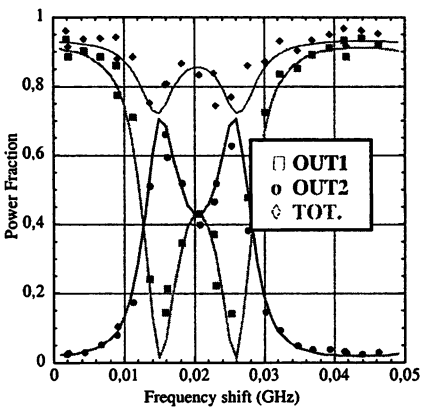

b

Fig. 2. Combiner assembly in IPF Stuttgart (*a*) and (*b*) measured power distribution in the two channels (markers) vs. frequency shift, compared to the expectations (solid lines)

Detailed description of the measurements is presented in [6]. In this paper the measurements outcome discussion is focused on the integrated power at the outputs, measured with quasi-optical bolometer vs. frequency shift (Fig. 2*b*). Evidences gained by measurements repeated after re-alignment show that an incom-

plete interference might occur. This is shown in Fig. 3*a*, where in particular an unexpected unequal distribution of the power occurs (see arrow in Fig. 3*a*), probably due to an imperfect alignment.

Analysis of the optical setup led to the conclusion that it is very sensitive to the alignment. In fact, considering the confocal optical arrangement and the waveguide imaging properties, a tilt or an offset in the beam input axis alignment causes a tilt or offset in two opposite directions for the two beam components that should interfere (destructively or constructively) at each output (see Fig. 3*b*). Thus either the alignment must be accurate, or a design of a new optical configuration (less sensitive to misalignment) is necessary.

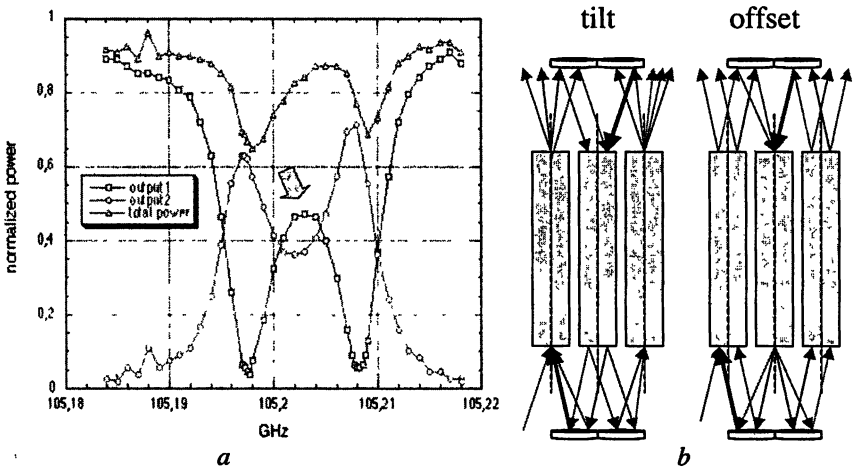

Fig. 3. Measurements of the power distribution in the two channels vs. frequency shift after re-alignment (*a*). Effect of tilt and offset in input: non-ideal superposition of beams at the outputs (*b*).

Side input alternatives

Resonators using side input [4] are found as possible alternatives. At a first sight they appear less interesting, due to the length needed, that for the same beam width is four times the one required with oblique input (beams have to be spatially separated at the entrance).

The imaging properties of the waveguide with length $2b^2/\lambda$ cause a splitting of an input beam in two beams at equal power at the exit (Fig. 4, top), making it a high-power 3dB coupler [7]. Looking at an example of calculated propagation of the field inside the waveguide (Fig. 4, bottom) it is possible to verify that for a length b^2/λ (half the previous length) a different splitting ratio can be obtained. For an input beam of gaussian profile, the output power density profile is shown in Fig. 5. The power is splitted according to the expression written in Fig. 5, as a

result of the imaging properties of the SC waveguide at reduced length, due to the superposition of images with different phase difference, described in [8].

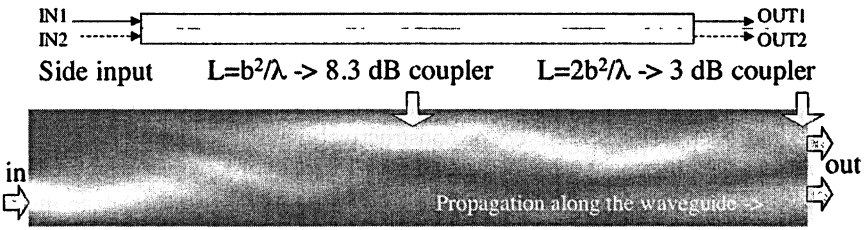

Fig. 4. Input-output configuration for a side-input waveguide coupler (top); power density (white is maximum) along the waveguide mid-plane (bottom): input is at the bottom left; arrows correspond to b^2/λ and $2b^2/\lambda$ distances from input aperture

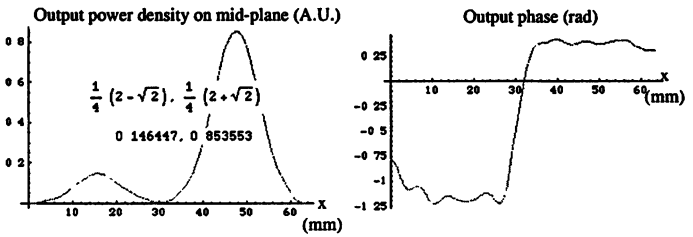

Fig. 5. Power density and phase at the exit mid-plane of a b^2/λ long waveguide

Using a waveguide b^2/λ long and exploiting the difference of power splitting between the two channels, a number of devices with different properties can be realized: the simple waveguide acts as a 8.3 dB coupler. Resonators with filtering capabilities and 4-port devices will have different characteristics depending on the input and output chosen. One of the most interesting is the diplexer/combiner shown at the top of Fig. 6. With only a single loop it achieves more than 99 % separation of the channels, due to the highest circulating power. As for all other side-input options, it can be made shorter by using in input an astigmatic beam (Fig. 6).

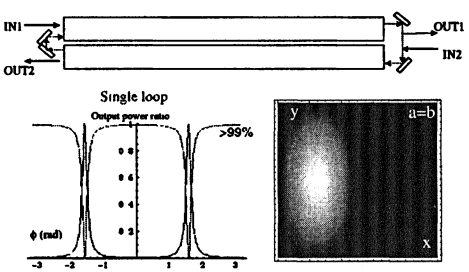

Fig. 6. Diplexer/Combiner with single loop, achieving > 99 % separation of the channels (*top*); output power ratio computed for this case (*left*). Astigmatic input (*right*).

For example with an input beam with 2:1 height-to-width ratio (Fig. 6, right) a square waveguide can be used with length halved with respect to the device shown in Fig. 1. Another advantage of the side input waveguide is that the optics can be made more easily less sensitive to misalignment, using for example a roof-top configuration, either in free space propagation or integrated in the waveguide.

Devices coupling multiple beam lines

Configurations coupling more than two lines can be realized with the same principle. Depending on the amount of radiation coupled and the frequency/phase-shift in the loop, the splitting ratios are different.

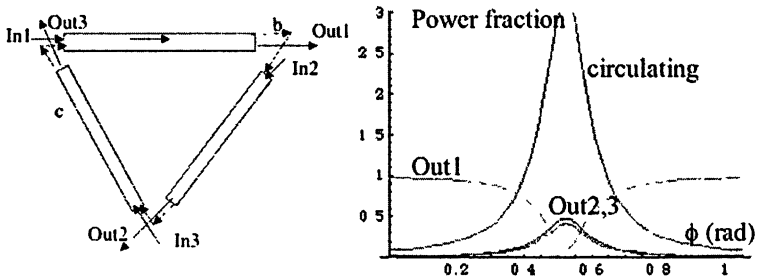

Fig. 7. Configuration coupling three lines (*left*); distribution of power found at the outputs and circulating when In1 is fed in, vs. phase delay in one turn (*right*)

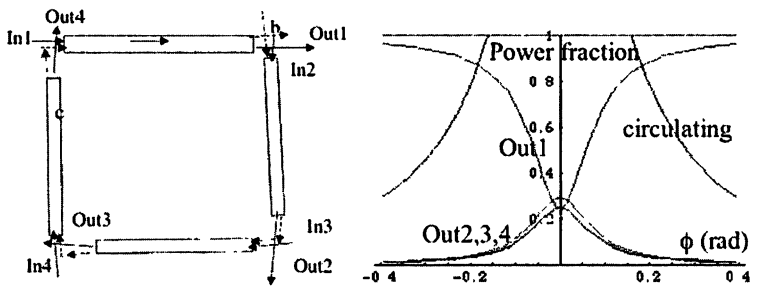

Fig. 8. Configuration coupling four lines (*left*); distribution of power found at the outputs and circulating when In1 is fed in, vs. phase delay in one turn (*right*)

Two examples are given in Fig. 7 and Fig. 8, where a b^2/λ long waveguide is considered and inputs and outputs are arranged so that most of the power is circulating in the loop. In resonant condition, a more balanced output is obtained, that can be used for example to send coherent power to multiple launchers, in order to exploit array-antenna effects to enhance focusing in multi-beam launchers.

Conclusions

The proposal of resonating combiners made with square or rectangular corrugated waveguide was validated by low-power measurements, which raised the issue of precise alignment. Prospects for integration in high-power transmission lines have to be confirmed by high-power tests. Alternative configurations may enhance the capability of EC systems.

This work is carried out in the frame of the virtual institute "Advanced ECRH for ITER" (collaboration between IPP Garching and Greifswald, FZK Karlsruhe, IHE Karlsruhe, IPF Stuttgart, IAP Nizhny Novgorod, and IFP Milano), supported by the Helmholtz-Gemeinschaft deutscher Forschungszentren.

References

1. *Kasparek W. et al.* Nucl. Fusion, 48, 054010 (2008)
2. *Kasparek W. et al.* High-power microwave diplexers for advanced ECRH systems // Strong Microwaves: Sources and Applications:Proc. 7th Int. Workshop. Nizhny Novgorod, 2009. P. 27–39.
3. *Denisov G. G. et al.* Int. J. Infrared Milli. Waves, Vol. 22, pp. 1735–1760 (2001).
4. *Bruschi A. et al.* Fusion Science and Technology, 53, p. 97 (2008).
5. *Plaum B. et al.* J. Phys. Conf. Series, 25, 120 (2005).
6. *D'Arcangelo O. et al.* Tests of a 105 GHz Prototype Diplexer-Combiner Based on Square Corrugated Waveguide // 25th Symposium on Fusion Technology, Rostock, Germany, Sept. 2008, submitted to Fusion Eng. Des.
7. *Kuzikov S. V.* Int. J. Infrared Millimeter Waves, 19, 11, 1523 (1998).
8. *Bachmann M. et al.* Appl. Opt., vol. 34, № 30, pp. 6898–6910 (1995).

SYNTHESIS OF MODE CONVERTERS FOR HIGH-POWER MICROWAVE SOURCES

S. V. Kuzikov, M. E. Plotkin

Institute of Applied Physics, Russian Academy of Sciences, Nizhny Novgorod, Russia

High-power microwave sources usually require efficient, compact, and electrically proof mode converters. In order to satisfy these (sometimes inconsistent) requirements a new method of synthesis, based on an iterative improvement of the converting waveguide wall, is suggested. A new synthesis algorithm develops the described in [1] iteration procedure which is based on a coupled mode formalism required a representation of whole fields in each cross-section as a sum of eigen modes. A new method is free of these requirements, because it operates with surface fields only which can be found using arbitrary computation codes. By means of the elaborated method many components for the IAP 30 GHz gyroklystron (TE_{53}–TE_{01} mode converter, TE_{53}–TEM_{00} converter, an electron beam collector with field repetition effect, a compact TE_{11}–TE_{01} mode converter) were synthesized and tested at low power level.

Definition of synthesis problem

Let us consider stationary solutions of Maxwell's equations at a given frequency ω. We start with a waveguide of length L with perfect conducting walls. The shape of this waveguide, which provides conversion of initial field distribution given in one cross-section into the required distribution given in another cross-section, has to be found. The Fig. 1 shows these fields at initial and final cross-sections correspondingly: $\vec{E}_{in}(0,r_\perp)$, $\vec{H}_{in}(0,r_\perp)$, at $z=0$; and $\vec{E}_{out}(L,r_\perp)$, $\vec{H}_{out}(L,r_\perp)$ at $z=L$. It is assumed that shape to be synthesized is smooth enough so that we neglect reflections everywhere.

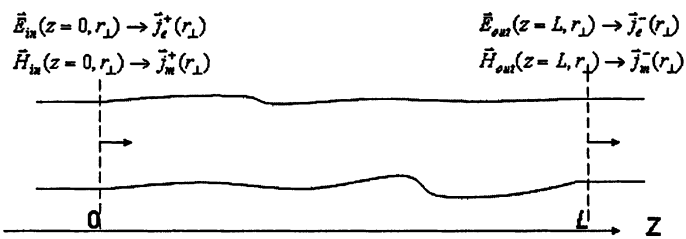

Fig. 1. Statement of the synthesis problem

For formulation of the iterative algorithm we will utilize two types of field solutions. The first one $\{\vec{E}^{+}(z,r_\perp), \vec{H}^{+}(z,r_\perp)\}$ can be interpreted as a solution

of the initial mathematical problem where Maxwell's equations are integrated in $t \to +\infty$ direction, within this formulation the fields $\vec{E}_{in}(0, r_\perp)$, $\vec{H}_{in}(0, r_\perp)$ play a role of radiating sources. The second solution $\{\vec{E}^-(z,r),\ \vec{H}^-(z,r)\}$ is obtained if to integrate Maxwell's equations in $t \to -\infty$ direction where $\vec{E}_{out}(L, r_\perp)$, $\vec{H}_{out}(L, r_\perp)$ are to be field sources.

Within each iteration a correction to the waveguide shape is calculated by means of the described fields of both types:

$$\Delta l = \alpha \cdot \mathrm{Im}\{\vec{H}_\tau^{+*} \cdot \vec{H}_\tau^- + \vec{E}_n^{+*} \cdot \vec{E}_n^-\}, \qquad (1)$$

where α is a positive constant. This constant should be chosen as a result of compromise: if α is too small, the iteration procedure obtains necessary solution too slowly; if α is too large, a convergence is not guaranteed. The practical algorithm of choice can be done in following way: 1) to estimate Δl using perturbation theory [5], 2) to choose α to be satisfied the inequality:

$$\alpha < \Delta l_{\max}. \qquad (2)$$

Iterative Algorithm

In order to start the iterative procedure, we need to have some initial approach of waveguide shape. For example, it could be a regular smooth waveguide surface. Then we calculate the complex fields $\vec{E}^+$, $\vec{H}^+$, $\vec{E}^-$, $\vec{H}^-$. Then we produce a new correction to the surface according to formula (1). Next new fields and the corresponding correction are derived within the already modified geometry. These iterations can be repeated as many times as necessary until the calculated conversion efficiency reaches a satisfactory high value. The efficiency at iteration number i should be calculated at final cross-section (η^+):

$$\eta_i^+ = \left| \int_S \left([\vec{E}_i^+ \times \vec{H}_{out}] + [\vec{E}_{out} \times \vec{H}_i^+] \right) d\vec{S} \right|^2. \qquad (3)$$

The whole block-scheme of the iterative procedure is shown in Fig. 2. Note that the suggested form of correction satisfies conditions: 1) when the derivable solution comes near to the required one the correction vanishes; 2) when the derivable solution differs from the required one the correction generates harmonics, that improve the conversion efficiency.

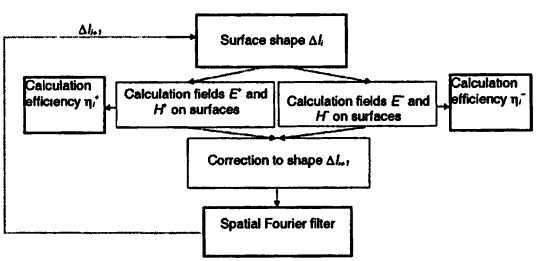

Fig. 2. Scheme of iterative procedure

Examples of synthesis

The output converter of a 30 GHz multi-MW gyroklystron has been synthesized [3–4]. The converter consists of three sections (Fig. 3).

In the first shortest section the operating TE_{53} mode is converted into TE_{04} mode, an efficient conversion in this case is achieved in a helical-corrugated waveguide due to a quasi-degeneration of the mentioned pair of modes.

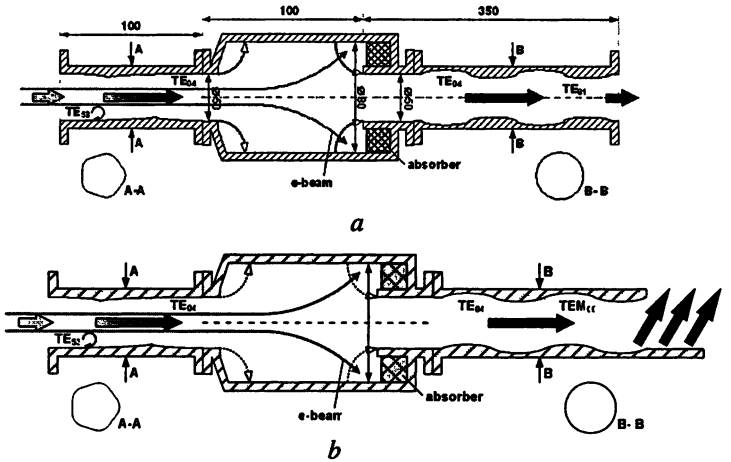

Fig. 3. Scheme of gyroklystron mode converter: *a* – with TE_{01} mode output, *b* – with TEM_{00} output

The problem of efficient output converter is connected with the problem of electron beam collector. Because electron beam power to be several tens of megawatts the electron beam must be sprayed on a sufficiently large surface. That is why, the beam collector appears as an axisymmetrical waveguide expansion which provides efficient repetition of the incident field structure at its output cross-section according to Talbot effect [6]. However, transmission efficiency in the smooth cylindrical expansion is not high, therefore the collector profile has been synthesized using FDTD technique [2] for field computation. Transmission efficiency at the final, 14th iteration reached 99 % (the same value was obtained by means of HFSS simulations), the *E*-filed distribution at this iteration is shown in Fig. 4.

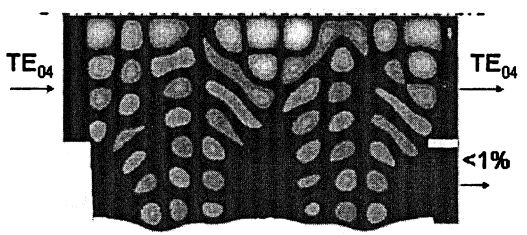

Fig. 4. Instantaneous field distribution in collector at the last (14th) iteration of synthesis

The third section of the converter has two modifications (Fig. 3*a* and 3*b* correspondingly). In the first version the TE_{04} mode is converted into the TE_{01} mode of the cylindrical waveguide with power output along the device axis (such version is attractive for accelerator's application of the gyroklystron). In the second version the TE_{04} mode is converted into the Gaussian beam (TEM_{00} mode) with output sideways (such version is aimed for radars and other applications).

The mentioned TE_{04} mode into the TE_{01} mode converter was synthesized at length 350 mm with average diameter about 50 mm. The efficiency of conversion at the level of about 99 % was obtained for 18 iterations (results of synthesis also were checked up with HFSS code). The Fig. 5 illustrates the synthesized converter shape and *E*-field distribution inside it (a half of the longitudinal cross-section of converter is shown).

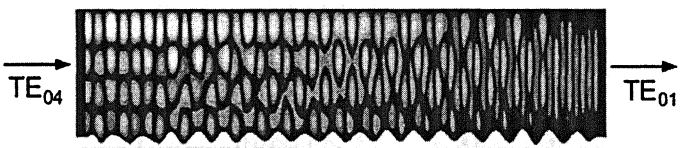

Fig. 5. Instantaneous field distribution in TE_{04}–TE_{01} mode converter at the last (18th) iteration

The TE_{04} mode into TEM_{00} mode converter (including a visor at the end) was synthesized by means of the integral equations technique in frames of the phase corrector approach [7]. Under the length 200 mm and diameter 50 mm it has 97 % efficiency with losses in side-lobes of radiation pattern taken into account. The synthesized shape and field distribution on wall surface are shown in Fig. 6 and Fig. 7 correspondingly.

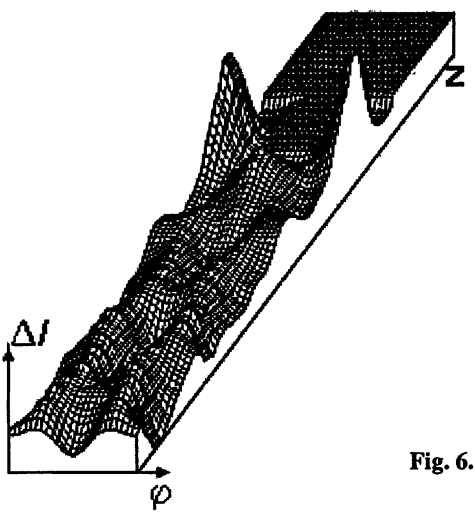

Fig. 6. Shape of TE_{04}–TEM_{00} mode converter

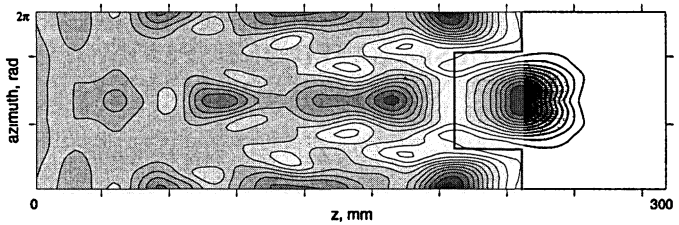

Fig. 7. Field distribution on surface of TE_{04}–TEM_{00} mode converter

The low power tests were carried out with the TE_{01} mode output version of the three-section gyroklystron mode converter. In accordance with the scheme of tests the TE_{01} mode was excited at the end of the tested converter so that we could measure a field distribution at the cross-section in the beginning. The measured radiation pattern was well coincided with the desired TE_{53} mode. The efficiency, calculated by means of the described field measurements, was $[96 \pm 2]$ %.

Conclusion

The iterative algorithm for synthesis of waveguide systems has been suggested. It can be used for computation of waveguide converters as well as mirror converters. Universality of the algorithm makes its application possible together with such powerful codes like HFSS, Microwave Studio, and others. The examples show high efficiency, the results of synthesis are well agreed with other numerical methods and results of low-power tests.

References

1. *Denisov G. G. et al.* Method for Synthesis of Waveguide Mode Converters // Radiophysics and Quantum Electronics. 2004. V. 47, № 8. P. 615.
2. *Yee K. S.* Numerical Solution of Initial Boundary Value Problems Involving Maxwell's Equations in Isotropic Media // IEEE Trans. on antennas and propagation. 1966. V. AP-14, № 8. P. 302.
3. *Kuzikov S. V., Plotkin M. E.* Synthesis of multi-mode waveguide systems // Conference Digest of the Joint 32nd IRMMW Conference and 15th International Conference on Terahertz Electronics, Cardiff, UK, 3–7 September, 2007. Vol. 1. P. 781–782.
4. *Zaitsev N. I. et al.* Microwave components for 30 GHz high-power gyroklystron // Conf. Digest of the Joint 32nd Int. Conf. on IRMMW, and 15th Int Conf. on Terahertz Electronics, Cardiff, UK, 3–7 September, 2007. Vol. 1. P. 369–370.
5. *Katsenelenbaum B. Z.* Theory of irregular waveguides with slowly varying parameters [in Russian] // Izd. AN SSSR. Moscow, 1961.
6. *Denisov G. G., Kuzikov S. V.* Microwave systems based on controllable interference of paraxial wavebeams in oversized waveguides // Strong Microwaves in Plasmas / ed. by A. G. Litvak. Nizhny Novgorod, 2000. Vol. 2. P. 960–966.
7. *Kuzikov S. V.* Paraxial Approach to Description of Wave Propagation in Irregular Oversized Waveguides // International Journal of Infrared and Millimeter Waves. 1997. Vol. 18, № 5. P. 1001–1014.

GENERATION OF POWERFUL ULTRASHORT MICROWAVE PULSES BASED ON SUPERRADIANCE FROM INTENCE ELECTRON BUNCHES

N. S. Ginzburg[1], A. S. Sergeev[1], I. V. Zotova[1], M. I. Yalandin[2], V. V. Rostov[3]

[1] Institute of Applied Physics RAS, N. Novgorod, Russia
[2] Institute of Electrophysics RAS, Ekaterinburg, Russia
[3] Institute of High Current Electronics, Tomsk, Russia

Superradiance (SR) of extended electron bunches can be considered as effective method of production of ultrashort electromagnetic pulse. Different types of SR associated with different mechanisms (cyclotron, Cherenkov, bremshstrahlung) of stimulated emission were recently observed experimentally at millimeter and centimeter wavelength bands. Progress in these researches has enabled a new type of generator to be created capable of generating unique short (under 200–300 ps) em pulses at super high peak (several GW) powers.

One of the effective methods of generation of ultrashort electromagnetic pulses is the stimulated emission of intense extended electron bunches [1–9]. Radiation of such bunches may be considered as a classical analogue of the well known in the quantum electronics Dike's superradiance (SR) effect. Superradiance of classical electrons may be associated with different mechanisms of stimulated emission (cyclotron, Cherenkov, bremshstrahlung etc). Different types of SR were recently observed experimentally at millimeter and centimeter wavelength bands. Progress in these researches have enabled a new type of millimeter band generator to be created capable of generating unique short (200–300 ps) em pulseы at super high peak powers exceeding 1 GW in millimeter and 3 GW in centimeter waveband. Supplementary development of high current accelerators allowed to realize repetitive rate regimes of generation with high frequency (several kHz) and high average power (up to 2.5 kW).

Basic models and the first experiments

1. Cyclotron SR in the group synchronism conditions

Cyclotron SR is realised in the bunch of electrons rotating in the homogeneous magnetic field. Cyclotron SR involves the process of azimuthal self-bunching and subsequent coherent emission of stored energy in the form of short single em pulse. As it was shown in [3] the most favourable condition for experimental observation of cyclotron SR in waveguide is the group synchronism condition, when the longitudinal velocity of electrons V_0 is close to wave group velocity V_{gr}. In commoving reference frame this regime corresponds to radiation near cut-off frequency $\bar{\omega}$ and in this sense has number of advantages in common with the interaction regimes in gyrotrons such as weak sensitivity to the spread in

the electrons velocities. One more factor is the rather low rate of em energy extraction from the electron bunch which results in the maximum gain of SR instability.

In comoving reference frame cyclotron SR can be described by the system of equations included parabolic equation for wave evolution and non-isochronous equations oscillators for electron motion:

$$i\frac{\partial^2 a}{\partial Z^2}+\frac{\partial a}{\partial \tau}=2if(Z)G\frac{1}{\pi}\int_0^{2\pi}\hat{\beta}_+ d\theta_0, \qquad \frac{\partial \hat{\beta}_+}{\partial \tau}+i\hat{\beta}_+\left(\left|\hat{\beta}_+\right|^2-\Delta-1\right)=ia, \tag{1}$$

$$\hat{\beta}_+(\tau=0)=\exp[i(\theta_0+r\cos\theta_0)], \quad r\ll 1, \quad \theta_0\in[0,2\pi], \quad a(\tau=0)=0.$$

Here $\hat{\beta}_+=\exp(i\bar{\omega}t)(\beta_x+i\beta_y)/\beta_{\perp 0}$ is the normalised transverse electron velocity, $\tau=t\beta_{\perp 0}^2\bar{\omega}/2$, $a=\left(2eA(z,t)/mc\bar{\omega}\beta_{\perp 0}^3\right)J_{m-1}(R_b\bar{\omega}/c)$, $Z=z\beta_{\perp 0}\bar{\omega}/c$, $A(z,t)$ is the slow varying field amplitude, R_b is injection radius of the hollow electron beam $\Delta=2(\omega_H'-\bar{\omega})/\bar{\omega}\beta_{\perp 0}^2$ is detuning of the cyclotron frequency in the comoving frame from the cut-off frequency and G is the parameter proportional to electron current. The function $f(Z)$ describes the axial distribution of the electron density. The initial conditions are written under the assumption that in the initial state the electrons are distributed uniformly in cyclotron rotation phases, aside from small fluctuations assigned by parameter r. Temporal evolution of the radiation power $P=\mathrm{Re}\left(a\partial a^*/\partial Z\right)$ for different values of Δ is presented in Fig. 1. It is seen that the maximum of growth rate and pulse peak power is achieved for $\Delta=0$ that corresponds to exact group synchronism regime. Detuning from this regime leads to decreasing of the gain and the SR pulse peak power.

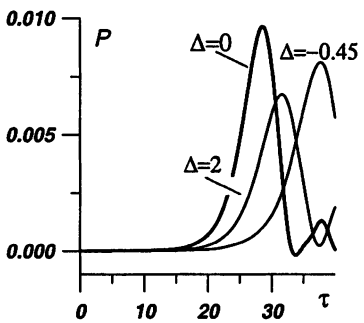

Fig. 1. Pulses of cyclotron SR for different parameter Δ that characterizes detuning from group synchronism regime.

The advantages of group synchronism regime were confirmed experimentally [4] based on the subnanosecond high-current accelerator RADAN which generated single 300 ps, 200 keV, 200 A electrons bunches. The transverse velocity with pitch factor ~1 was imparted to the electrons by the kicker (system with strongly inhomogeneous magnetic field). SR pulses (Fig. 2*a*) were observed in the regions corresponding to group synchronism with TE_{21} and TE_{01} modes. Maximal peak power of 40 GHz SR pulses was 400 kW for ultrashort pulse duration ~400 ps. According to theoretical consideration detuning from group synchronism regime by the varying of the guide magnetic field leads to the dramatic reduction of the SR pulse peak power (Fig. 2*b*).

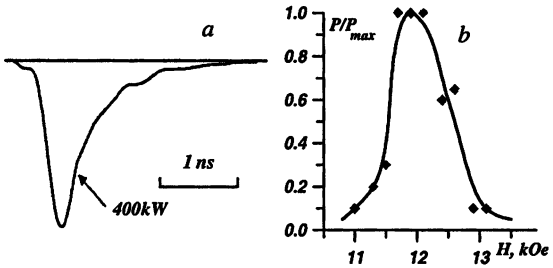

Fig. 2. Oscilloscope trace of cyclotron SR pulse (*a*). Experimental dependence of peak power on guide magnetic field (*b*)

2. Cherenkov superradiance

Cherenkov SR can be produced by a bunch of electrons moving along rectilinear trajectories in slow wave structures (SWS). Two varieties of Cherenkov SR have been studied. The first one is associated with the forward wave interaction in the dielectric loaded waveguide under synchronism condition $\omega = hV_0$, where ω and h are the frequency and longitudinal wave number respectively. The second type of Cherenkov SR occurs in the case of interaction with the slow spatial harmonic of the backward wave in periodically corrugated waveguide under synchronism condition: $\omega = \left(-h_0 + \bar{h}\right)V_0$, where h_0 is the longitudinal wave number of the fundamental harmonic, $\bar{h} = 2\pi/d$, d is the corrugation period. Under the assumption of a small variation of particles' velocity Cherenkov SR in the both cases can be described by the equations:

$$\frac{\partial a}{\partial \tau} \pm \frac{\partial a}{\partial Z} = \mp\chi(Z) f(\tau)\ \frac{1}{\pi}\int_0^{2\pi} e^{-i\theta} d\theta_0,\quad \frac{\partial^2 \theta}{\partial Z^2} = \left[1 + \nu\frac{\partial \theta}{\partial Z}\right]^{\frac{3}{2}} \chi(Z)\,\mathrm{Re}\left(a e^{i\theta}\right), \quad (2)$$

where the upper and lower signs correspond to the interaction with the forward and backward wave respectively. Here we use the following dimensionless variables:

$$\tau = \frac{\omega C(t - z/V_0)}{1 \pm V_0/|V_{gr}|},\quad Z = \frac{\omega C z}{V_0},\quad a = \frac{eA(z,t)E_\perp(R_0)}{C^2\gamma_0^3 V_0 m\omega},$$

$\theta = \omega t - hz$ is the phase of electrons with respect to the synchronous harmonic, $E_\perp(\mathbf{r}_\perp)$ is the transverse field profile, $\gamma_0 = \left(1 - \beta_0\right)^{-1/2}$, $\nu = 2\gamma_0^2 C$. $C = \left(eI_b \hat{Z}/2mc^2\gamma_0^3\right)^{1/3}$ is the Pierce parameter, $\hat{Z} \equiv 2c^2\left|E_\perp(R_0)\right|^2/\omega^2 N$ is the coupling impedance, N is the waveguide norm, I_b is the electron current. The function $\chi(Z)$ defines the longitudinal profile of the wave coupling impedance

(tapered, for example, by varying the corrugation depth). This function is normalised as $1/L\int_0^L \chi(Z)dZ = 1$, where $L = \omega Cl/V_0$ is the dimensionless length of the interaction space. The function $f(\tau)$ describes the current pulse profile. Below we assume that electron density is constant within bunch duration apart from small initial density perturbations:

$$\theta(Z=0) = \theta_0 + r\cos\theta_0, \quad r \ll 1, \quad \theta_0 \in [0, 2\pi], \quad \partial\theta/\partial Z(Z=0) = 0. \quad (3)$$

For em field amplitude initial and boundary conditions have the form: $a(\tau = 0)=0$, $a(Z = 0) = 0$ in the case of forward and $a(\tau = 0)=0$, $a(Z = L) = 0$ in the case of backward wave propagation.

For uniform SWS $(\chi(Z) = 1)$ formation of SR pulse is shown in Fig. 3*a* and Fig. 3*b* for forward and backward wave propagation respectively. This process is caused by electron bunching and slippage of the wave with respect to the electrons due to the difference between the wave group velocity and the electron longitudinal velocity. Slippage provides the coherence of radiation from entire volume of electron bunch.

Experiments with both forward and backward mechanisms of Cherenkov SR have been carried out based on RADAN accelerator. In the experiments with forward emission dielectric loaded waveguides were used. In these experiments SR pulses with power about 1 MW and duration ~300 ps were generated [5].

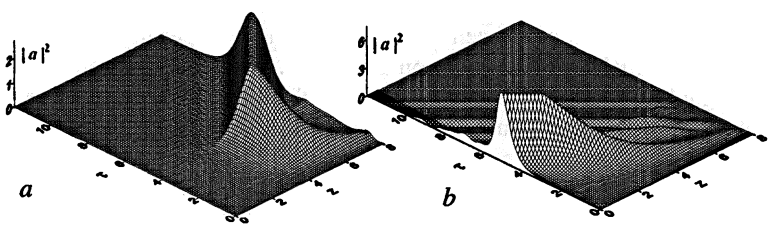

Fig. 3. Formation of SR pulse for forward (*a*) and backward (*b*) wave propagation

SR pulses with much higher peak power were achieved for the "backward" mechanism of SR in periodically corrugated waveguides. In the first experiments in Ka-band the uniform SWS was used with corrugation period 0.35 cm, depth 0.075 cm and mean diameter $D/\lambda = 0.8$ [6, 7]. For extraction of SR pulse from SWS reflection from cut-off narrowing on the cathode side was used. High current electron bunches were transported through the interaction space in a guide magnetic field created either by a pulsed solenoid (B ~ 1.5–5 T) or by a superconducting magnet (B ~ 8.5 T). The dependence of the SR pulse peak power on the value of the guide magnetic field is presented in Fig. 4*a*. Similar to the traditional BWO the fall in the power near the magnetic field value ~3 T is caused by

cyclotron absorption when the cyclotron resonance condition for the fundamental harmonic is matched. The maximal peak power of the SR pulse was obtained for a value of the magnetic field exceeding the cyclotron resonance value. A typical oscilloscope trace of the Ka-band microwave signal is presented in Fig. 4*b*. The observed microwave pulses had duration ~300 ps and a rise time of 200 ps. For the electron bunch with energy ~290 keV and current ~2 kA the peak power was ~150 MW in the single pulse regime [7]. Operation in the repetition rate mode at 25 Hz was realized with a peak power of the SR pulses ~60 MW [6].

To increase SR pulse peak power in the following experiments in Ka-band advanced SWS has been used [8]. To diminish the influence of dispersion spread a slightly oversized corrugated waveguide with $D/\lambda = 1.3$ and a resonant reflector

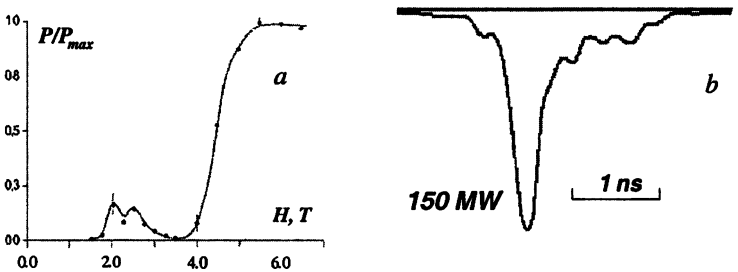

Fig. 4. Dependence of SR pulse peak power on value of guide magnetic field (*a*). Typical oscilloscope trace of the Ka-band microwave signal in uniform SWS (*b*)

for em pulse extraction have been implemented. In the experiments performed at the RADAN-303BP with an electron current 2.1 kA and electrons energy of 290 keV guiding in high magnetic field (5.5 T) 200–250 ps microwave pulses were obtained with a maximum peak power of 420 MW. In a low magnetic field (~2 T) the peak power decreased to 240–280 MW [8].

3. Superradiance in the process of stimulated backscattering

To generate SR pulses in high-frequency bands it is beneficial to use stimulated backscattering of powerful pump wave by intense electron bunch. In this situation, due to the Doppler up-conversion the radiation frequency can significantly exceed the frequency of the pump wave. With the relativistic microwave generator as a pump wave source such a mechanism is beneficial for generation of the powerful pulse radiation in the short millimeter and submillimeter wave bands.

Under assumption of the fixed pump wave amplitude A_i superradiance in this case can be described by the nonstationary equation for scattering wave amplitude A_s and the averaged equations for electrons' motion in the field of combination wave:

$$\frac{\partial a_s}{\partial Z}+\frac{\partial a_s}{\partial \tau}=if(\tau)a_i g\frac{I}{\pi}\int_0^{2\pi}e^{-i\theta}d\theta_0,\quad \frac{\partial^2\theta}{\partial Z^2}=\mu\,\mathrm{Im}\left(a_s a_i\, g e^{-i\theta}\right). \qquad (4)$$

Here $Z=\omega_c z/c$, $\tau=\omega_c c\left(t-z/V_0\right)\left(1/V_{gr}-1/V_0\right)^{-1}$, $a_{i,s}=eA_{i,s}/2m\gamma_0 c^2$ are the dimensionless amplitudes of pump and scattered waves, $\theta=\omega_n t-k_c z$ is the electrons phase with respect to the combination wave, $\omega_c=\omega_s-\omega_i$, $k_c=h_s+h_i$, $h_{i,s}$ are the longitudinal pump and scattered wave numbers, $\mu=\gamma_0^{-2}\beta_0^{-3}$, $I=\left(eI_b/mc^3\right)\cdot\left(2\gamma_0 h_s k_c R^2 N_s\right)^{-1}$, I_b is the electron current, N_s is the norm of the scattered wave. Factor $g=J_{n_i-1}\left(k_{\perp i}R_b\right)J_{n_s-1}\left(k_{\perp s}R_b\right)\Omega/\left(\Omega-\omega_H\right)$ describes the increase of oscillation velocity of electrons near the cyclotron resonance, $\omega_H=eH_0/mc\gamma_0$ is the gyrofrequency, $\Omega=\omega_i+h_i V_\parallel$ is the bounce frequency, $k_{\perp i,s}$ is the transverse wave number, $J_n(x)$ is the Bessel function, $n_{i,s}$ are the azimuth indices of the waveguide modes. The development of SR instabilities starts from small initial density perturbations in electron bunches (3). As it follows from simulations the scattered radiation has the form of a single short pulse (Fig. 5). The parameters of simulation were close to experimental ones. The 38 GHz 100 MW pump wave with 100 MW undergoes backscattering on 250 keV, 1 kA, 200 ps electron bunch guided in 24 kG magnetic field. According to simulations duration of scattered 150 GHz SR pulse is about 50 ps with peak power ~25 MW.

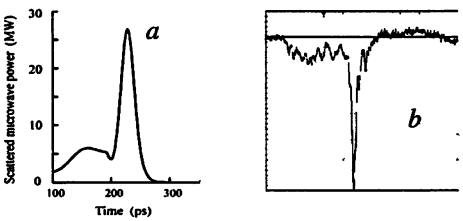

Fig. 5. SR pulse of backscattering radiation: *a* – simulations, *b* – experimental oscilloscope trace

Experiments on the observation of the stimulated backscattering in the SR regime [9] were carried out based on two synchronized nanosecond and subnanosecond high-current accelerators RADAN303. The 4 ns electron beam from the first accelerator was used to drive the pump wave generator (BWO). The pump wave undergoes backscattering with frequency up-conversion on the subnanosecond electron bunch produced by the second accelerator. Typical oscilloscope trace of SR pulse with peak power 2 MW and duration 200 ps is presented in Fig. 5. Spectrum measurements by a set of cut off waveguides showed that the scattered signal includes frequencies up to 150 GHz which was close to calculated.

Production of SR pulse with peak power exceeding the power of driving electron beam

It is important to note that in contrast with traditional microwave devices operating in steady-state regime the SR pulse peak power can exceed the power of the electron beam due to accumulation of energy from different electron fractions by moving SR pulse. In this case the power conversion coefficient $K = P_{SR}/P_{beam}$ can exceed 1. Obviously this fact does not contradict the energy conservation law because the full energy of the em pulse is still smaller than the total energy of the beam.

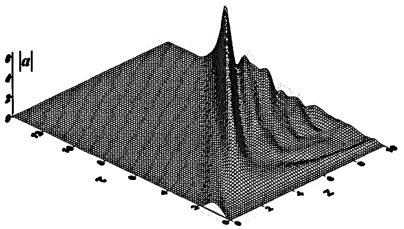

Fig. 6. Pulse amplification and shortening

In [10] cumulative effect was demonstrated for Cherenkov amplification of a short incident em pulse propagating through a quasi stationary electron beam. This process can be described by Eqs. (3), (4) (with upper sign). But in this case boundary condition has a form: $a(Z=0)=a_0(\tau)$, where function $a_0(\tau)$ describes the form of incident signal. Conversion coefficient in this case may be presented in the form: $K=(\gamma_0+1)\nu\,|a_{max}|^2/8\gamma_0$. Results of simulations are presented in Fig. 6. It is seen that due to the difference between wave group velocity and electron transversal velocity input pulse propagates through unmodulated electron fractions and effectively amplified. In this case the power conversion factor achieves 3.5. This process is limited by negative influence by natural fluctuations of beam density.

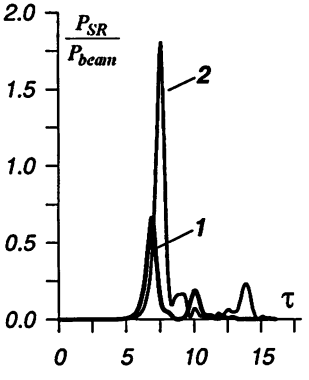

Fig. 7. Normalized SR pulse power vs time: *1* – uniform SWS, *2* – tapered SWS

The similar regime can be realised without incident signal. For the backward wave interaction to achieve a substantial excess of SR pulse peak power over power of driving beam it is necessary to use the non-uniform SWS with coupling impedance $\chi(Z)$ decreasing to the cathode end [11–13]. In this case the SR pulse forming in the initial stage propagates towards cathode through electron fractions with rather small modulation and extract energy from them. For example, it is possible to use a slow wave structure with a corrugation depth linearly decreasing to the cathode end along the first half of the SWS length. In this case the peak power of SR pulse exceeds the power of driving electron beam in 1.8 times (Fig. 7).

Generation of SR with peak power exceeding the power of driving electron beam was realized experimentally in Ka- and X-bands. In these experiments SR pulses with record power level have been generated.

In Ka-band the non-uniform SWS with increasing corrugation depth had a length of about 12 cm (~14λ) and a mean diameter ~1.3λ. Electron bunch with current 2.5 kA and energy 290 keV (power ~700 MW) is guided by strong magnetic field up to 6.5 T. The peak power of 300 ps SR pulse (Fig. 8) was over 1 GW. Correspondingly the power conversion coefficient achieved 1.4 [12].

The experiments with maximum conversion coefficient K was performed in X-band by using the SINUS-200 compact accelerator forming 5 kA 330 keV 9 ns electron beam (beam power ~1.7 GW). The corrugation amplitude increased from 0.1 to 0.25 cm along the system. The waveforms of the vacuum diode voltage and microwave detector signal are presented in Fig. 9. The peak power of the SR pulse with duration of 0.65 ns was ~3 GW which corresponds to a conversion factor of 1.8 [13].

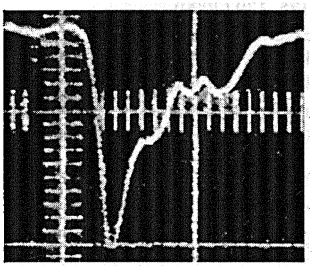

Fig. 8. Oscilloscope trace of 1 GW 300 ps Ka band SR pulse

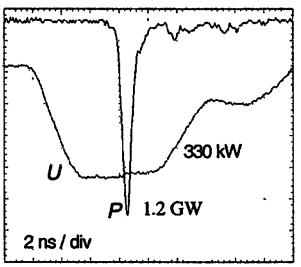

Fig. 9. The waveforms of vacuum diode voltage and microwave detector signal for X-band SR in tapered SWS

Repetitive generation of powerful SR pulses

To provide generation of powerful SR pulses in high repetitive rate mode specialy designed hybrid modulators with solid-state opening switches were exploited [14–16]. At the same time additional tapering of coupling impedance by using of special profile of guide magnetic field was used. This profiling allowed to obtain the rather high conversion coefficient in decreased magnetic field lower cyclotron resonance value.

Based on hybrid modulator SM-3NS in Ka-band the generator of 250 ps 300 MW (K ~ 0.5) SR pulses was realized with repetition frequency 1–3.5 kHz and pulse train width ~1 s [14]. Average microwave power achieved 200 W for repetition frequency 3.5 kHz.

In X-band for repetitive rate regime the high-voltage driver S-5N was used [15, 16]. SR pulse peak power achieved 3 GW for pulse duration ~0.8 ns

(K ~ 0.8). At a pulse repetition rate of 300 Hz average power was ~1 kW for train duration 10–100 s. For shorter train (~1 s) at repetition frequency 700–900 Hz average power achieved 2.5 kW [16]. Regimes with a (20–40)-picosecond stabilized phase of the high-frequency filling of SR pulses with respect to the accelerating voltage pulse front have been observed at a BWO peak output power of ~1 and 3 GW.

This work was supported in part by the Russian Foundation for Basic Research under Grants 08-02-01059, 08-02-00183, and 07-08-00083.

References

1. *Ginzburg N.* Pis'ma ZhTF, 14, 440 (1988).
2. *Bonifacio R., Piovella N., McNeil B.* Phys. Rev. A, 44, 3441 (1991).
3. *Ginzburg N., Sergeev A., Zotova I.* JETP Lett. 60, 513 (1994).
4. *Ginzburg N., Sergeev A., Zotova I., Phelps A., Cross A., Shpak V., Yalandin M., Shunailov S., Ulmaskulov M.* Phys. Rev. Lett. 78, 2365 (1997).
5. *Ginzburg N., Sergeev A , Zotova I., Novozhilova Yu., Rozental R., Phelps A., Cross A., Shpak V., Yalandin M., Shunailov S., Ulmaskulov M.* Opt. Comm. 175, 139 (2000).
6. *Ginzburg N., Zotova I., Novozhilova Yu., Sergeev A , Peskov N., Phelps A., Cross A., Shpak V., Yalandin M., Shunailov S., Ulmaskulov M., Tarakanov V.* Phys. Rev. E, 60, 3297 (1999).
7. *Ginzburg N., Zotova I., Sergeev A., Rozental R., Shpak V., Yalandin M., Sharypov K., Shunailov S., Phelps A., Cross A.* ZhTF 72, 83 (2002).
8. *Korovin S., Mesyats G., Rostov V., Ulmaskulov M., Sharypov K., Shpak V., Shunailov S., Yalandin V* Pis'ma v ZhTF, 28, 81 (2002).
9. *Reutova A., Ulmaskulov M., Sharypov A., Shpak V., Shunailov S., Yalandin M., Belousov V., Ginzburg N., Denisov G., Zotova I., Rozental R., Sergeev A.* JETP Lett. 82, 263 (2005).
10. *Ginzburg N., Zotova I., Sergeev A.* Tech. Phys. Lett. 25, 930 (1999).
11. *Elthaninov A., Korovin S., Rostov V., Pegel I., Mesyats G., Yalandin M., Ginzburg N.* JETP Lett. 77, 266 (2003).
12. *Korovin S., Mesyats G., Rostov V., Ulmaskulov M., Sharypov K., Shpak V., Shunailov S., Yalandin M.* Tech. Phys. Lett. 30, 117 (2004).
13. *Korovin S., Eltchaninov A., Rostov V., Shpak V., Yalandin M., Ginzburg N., Sergeev A., Zotova I.* Phys. Rev. E, 74, 016501 (2006).
14. *Grishin D., Gubanov V., Korovin S., Lubutin S., Mesyats G., Nikofirov A., Rostov V., Rukin S., Slovikovsky B., Sharypov K., Shpak V., Shunailov S., Yalandin M.* Tech. Phys. Lett. 28 (10), 806 (2002).
15. *Yalandin M., Lubutin S., Rukin S., Slovikovsky B., Ulmaskulov M., Shpak V., Shunailov S.* Tech. Phys. Lett 27 (1), 37 (2001).
16. *Korovin S., Lyubutin S , Mesyats G., Rostov V., Rukin S , Slovikovsky B., Ul'maskulov M., Sharypov K., Shpak V., Shunailov S., Yalandin M.* Tech. Phys. Lett. 30, 719 (2004).

DEVELOPMENT OF HIGH-POWER MICROWAVE SOURCES IN KANAZAWA UNIVERSITY

K. Kamada[1], K. Aizawa[1], M. Kawamura[1], S. Odawara[1], R. Ando[1], N. S. Ginzburg[2], I. V. Zotova[2], A. M. Malkin[2], N. Yu. Peskov[2], A. S. Sergeev[2], V. Yu. Zaslavsky[2]

[1] Graduate School of Natural Science and Technology, Kanazawa University, Japan
[2] Institute of Applied Physics, Russian Academy of Sciences, Nizhny Novgorod, Russia

S-band superradiance with frequency of 5 GHz, output power of 400 MW and duration of 4 ns was obtained using a 600 keV, 6 kA, 14 ns intense relativistic electron beam injected into a periodical slow wave structure. A new scheme of free electron maser with a hybrid resonator, in which advanced Bragg structure is utilized as up-stream mirror, was studied. Simulations demonstrated effective mode selection in this scheme.

Introduction

Microwave studies for high power and/or for high frequency have been carried out at the particle beam laboratory in Kanazawa University. Intense electromagnetic radiation sources are developed for applications in nuclear fusion, particle accelerators, radars, etc. Quasi steady-state radiation sources are successfully developed with output power of around 1 MW. However, radiation sources with output power over 1 GW are still in an experimental stage. The breakdown caused by the strong electric field of the radiation limits the output power and the duration of the radiation. Stimulated emission from extended electron bunches – superradiance (SR) is an attractive method of generation of ultrashort electromagnetic pulses. The duration of SR pulse is much shorter than the time that the breakdown occurs. One more advantages of SR it is high power which even can exceeds the power of driving electron beams. Theoretical and experimental studies of SR have been reported with different mechanisms of stimulated emission (bremsstrahlung, Cherenkov, cyclotron) through the frequencies 10–150 GHz [1–4]. We report here the experimental results of S-band SR pulse production with slow wave structure.

On the other hands, reliable electromagnetic radiation sources with frequency range of 0.1–10 THz, i.e. called THz gap, are eagerly expected. The THz Gap lies between the upper frequency of classical electronic (electron tubes) and the lower frequency of quantum electronics (laser).

One of the candidates of THz source among electron devices is a free electron maser (FEM). Many successful experiments with narrow band mm-wave FEM were performed by using the Bragg mirrors [5–7]. However, as the frequency increase, the traditional Bragg mirror loses the selective features over transverse indexes. The mode competition effects are a very severe problem for FEM. Selective properties can be improved using an advanced Bragg structure

(ABS) based on coupling of the propagating and quasi-cutoff modes [8]. Higher mode selectivity of this scheme was demonstrated in simulations as it compared with traditional Bragg mirror. In Kanazawa University, an intense relativistic electron beam was prepared for experimental study of FEM with hybrid resonator, in which advanced Bragg structure would be used as an upstream reflector.

Superradiance

The corrugated cylindrical waveguide was newly designed for 5 GHz SR. PIC simulation code KARAT was used to optimize the precise parameters. With the new corrugated waveguide the microwave pulse with frequency of 5 GHz, output power of 3.2 GW and duration of 3 ns was expected as shown in Fig. 1. The length of the new structure was designed for the beam with duration of 12 ns.

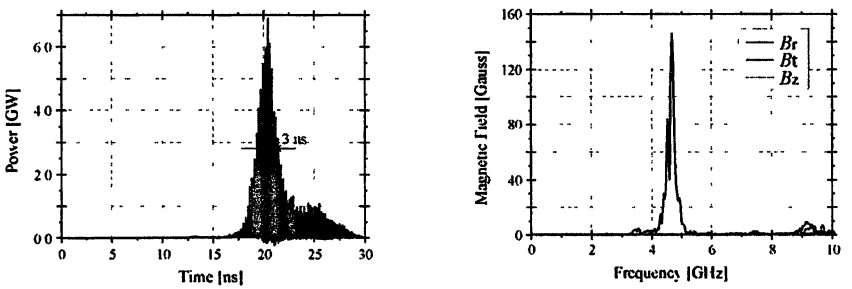

Fig. 1. Simulated microwave output (*left*) and frequency spectrum (*right*)

The experimental setup is shown in Fig. 2. An electron beam with energy of 600 keV, current of 6 kA, duration of 14 ns and radius of 56 mm was injected into the slow wave structure. The axial magnetic field of 1.3 T was applied by a solenoid coil. The radiated microwave was detected by a horn located more than 1 m far from output window. The microwave radiation received by the horn was attenuated by two variable attenuators. Five low pass filters with cut-off frequencies from 4 GHz to 8 GHz were utilized. Tunnel detectors detected microwaves passing through the low pass filters. The variable attenuators, low

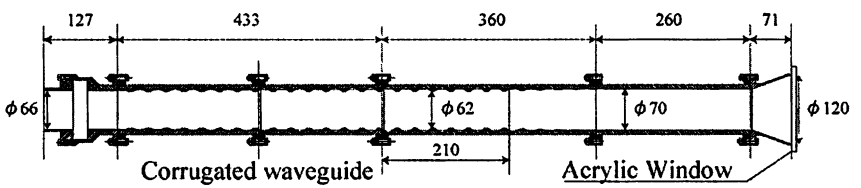

Fig. 2. Experimental setup

pass filters and tunnel detectors were calibrated by low power devices. The output power was estimated from the angular distribution of the microwave output. The output power was also estimated from the increase of the carbon plate temperature (calorimeter) located at the just behind the Lucite window.

The signals detected by tunnel detectors through low pass filters are shown in Fig. 3 (left). With corrugated waveguide, similar signals were detected with the low pass filters having the cut-off frequencies from 5 to 8 GHz or without the filter, though no signal was observed through the filter with the cut-off frequency of 4 GHz. It shows that the radiated frequency of around 5 GHz. The detected SR pulse duration was 4 ns that agreed with the simulated result. The angular distribution of the radiated microwave was measured by the horn moved along the circumference with radius of 1500 mm from the center of the Lucite window (Fig. 4, right). Total output power was estimated to be 600 MW from the angular distribution. Total output power estimated from the calorimeter was about 400 MW. Both output power showed a good agreement. By fluorescent tubes located 500 mm far from the Lucite window, a donut like pattern was observed and it corresponded to emission of TM_{01} mode (Fig. 4). This result agreed with the microwave output with one peak around 20 degrees from the beam axis as shown in Fig. 3 (right).

The frequency, the duration, the mode and the total power of the radiated microwave were in reasonable agreements with the simulated results of SR. Therefore, we concluded that the 5 GHz SR was observed.

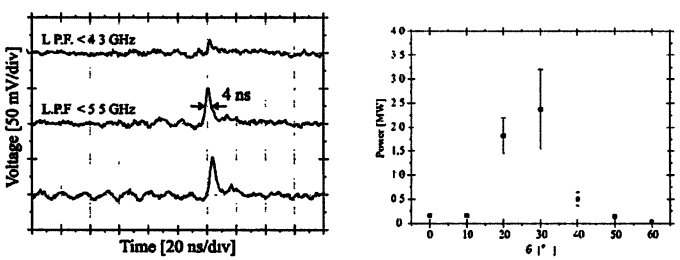

Fig. 3. Microwave output with 4.3 GHz low pass filter (upper), with 5.5 GHz and without low pass filter (*left*). Angular distribution of the microwave output (*right*).

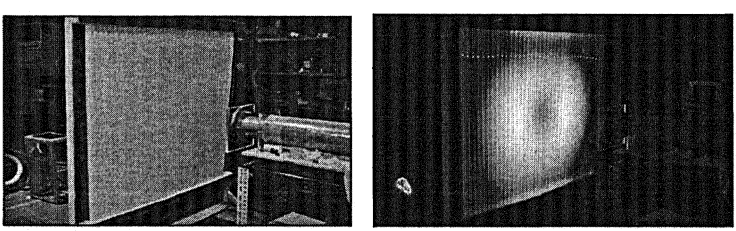

Fig. 4. Fluorescent tubes were located 500 mm far from the Lucite window (*left*). Donut like pattern was observed (*right*).

FEM with Hybrid Bragg Resonator

The advanced Bragg reflector based on coupling of the propagating and quasi-cutoff modes should be used in two mirrors resonator scheme as an up-stream reflector. To avoid large Ohmic losses associated with excitation of cut-off mode it is reasonable to use conventional Bragg reflector with rather small reflectivity as a down-stream reflector. Hybrid Bragg resonator (HBR) is composed of three parts as shown in Fig. 5. In free electron maser (FEM) with HBR, electron beam interacts with the propagating wave, which provides possibility of high Doppler frequency up-shift, while quasi cut-off mode provides transverse mode selection similar to a gyrotron. As a result, a higher mode selectivity is realized than in traditional Bragg FEM.

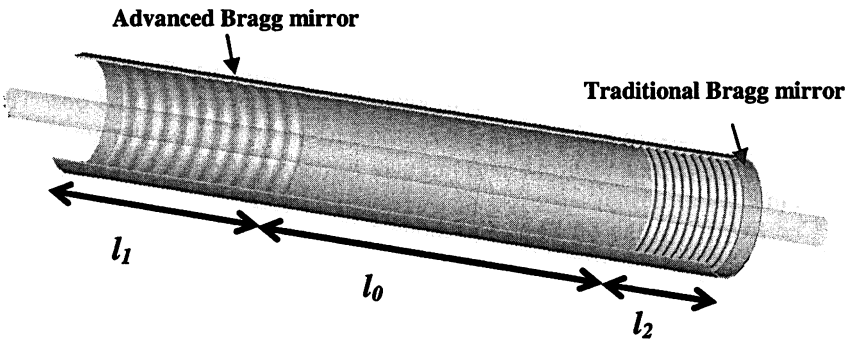

Fig. 5. Principal scheme of FEM with hybrid Bragg resonator

Simulation of nonlinear dynamics of the FEM

The input mirror represents a section of a cylindrical waveguide with its inner surface having shallow axially symmetric corrugation

$$r = (r_1/2)\cos \bar{h}_1 z, \tag{1}$$

where $\bar{h}_1 = 2\pi/d_1$, d_1 and r_1 is the period and the depth of corrugation, r_0 is the mean radius of the waveguide. Under the Bragg resonance condition $h \approx \bar{h}_1$ coupling and mutual scattering between the fields of cut-off mode

$$\vec{E} = \mathrm{Re}\left\{\vec{E}_B(r)B(t,z)e^{i\bar{\omega}t}\right\} \tag{2a}$$

and the two counter propagating waves

$$\vec{E} = \mathrm{Re}\left\{\vec{E}_A(r)\left(A_+(t,z)e^{-ihz} + A_-(t,z)e^{+ihz}\right)e^{i\bar{\omega}t}\right\} \tag{2b}$$

takes place, where $\bar{\omega}$ is the cutoff frequency, $\vec{E}_{A,B}(r)$ functions specify the transverse structure of the waves which is defined by the modes of regular

waveguide. Electron beam is synchronous to the propagating wave A_+. Mutual scattering of partial wave beams and excitation of the synchronous wave can be described in the quasi-optical approximation by the following system of equations

$$\frac{\partial A_+}{\partial Z}+\frac{1}{\beta_{gr}}\frac{\partial A_+}{\partial \tau}+\hat{\sigma}A_+ +2i\hat{\alpha}_1 B = J,\quad -\frac{\partial A_-}{\partial Z}+\frac{1}{\beta_{gr}}\frac{\partial A_-}{\partial \tau}+\hat{\sigma}A_- +2i\hat{\alpha}_1 B = 0,$$
$$\frac{iC}{2}\frac{\partial^2 B}{\partial Z^2}+\frac{\partial B}{\partial \tau}+\hat{\sigma}B+i\hat{\alpha}_1\left(A_+ + A_-\right)=0. \qquad (3)$$

Electron excitation factor $J = 1/\pi\int_0^{2\pi} e^{-i\theta}d\theta_0$ can be found from the electron motion equations

$$\left(\frac{\partial}{\partial Z}+\frac{1}{\beta_{\|}}\frac{\partial}{\partial \tau}\right)^2\theta = \mathrm{Re}\left\{A_+ e^{i\theta}\right\},$$
$$\theta\big|_{Z=0}=\theta_0\in[0,2\pi),\quad \left(\frac{\partial}{\partial Z}+\frac{1}{\beta_{\|}}\frac{\partial}{\partial \tau}\right)\theta\Big|_{Z=0}=\Delta. \qquad (4)$$

Output traditional Bragg reflector (Fig. 5) possesses corrugation $a=(a_2/2)\cos\bar{h}_2 z$ ($\bar{h}_2=2\pi/d_2$, d_2 is period of the structure) and provides mutual scattering of two counter propagating waves (2a) under resonance condition $2h\approx\bar{h}_2$, which can be described by the equations

$$\frac{\partial A_+}{\partial Z}+\frac{1}{\beta_{gr}}\frac{\partial A_+}{\partial \tau}-i\hat{\alpha}_2 A_- = J,\quad -\frac{\partial A_-}{\partial Z}+\frac{1}{\beta_{gr}}\frac{\partial A_-}{\partial \tau}-i\hat{\alpha}_2 A_+ = 0. \qquad (5)$$

Amplification of the synchronous wave A_+ in the regular section of the resonator is described by the equations (4), (5) where one should put $\hat{\alpha}_2=0$. In simulation we assumed that external energy fluxes are absent so the amplitudes of partial waves $A_\pm$ on the corresponding boundaries vanish. For the quasi cut-off mode we use the boundary conditions taking into account the diffraction of the field over the corrugation boundary

$$B\pm\sqrt{\frac{C}{\pi i}}\int_0^{\tau}\frac{e^{-\hat{\sigma}(\tau-\tau')}}{\sqrt{\tau-\tau'}}\frac{\partial B(\tau')}{\partial Z}d\tau'\Bigg|_{z=0,L_1}=0. \qquad (6)$$

The following normalized variables are used: $\tau = t\,C\bar{\omega}$, $Z = z\,C\bar{\omega}/c$, $C=\left(\frac{eI_0}{mc^3}\frac{\lambda^2\mu\kappa^2}{8\pi\gamma a_0}\right)^{1/3}$ is the gain parameter, I_0 is the beam current, $\hat{\sigma}=\sigma/\bar{h}C$ is the Ohmic losses parameter, $(A_\pm)=(A_\pm)\cdot e\kappa\mu/(\gamma mc\bar{\omega}C^2)$,

$B = e\kappa\mu B\sqrt{N_A}\,/\,mc\gamma_0 C^2\sqrt{\bar{\omega}N_B}$, N_A, N_B are the mode norms. For the scattering of the TE-type propagating modes into the TM-type quasicritical mode the coupling coefficients in the input and output Bragg structures are given by the relations

$$\alpha_1 = \left(\bar{h}r_1/4r_0\right)m\left(\nu_A^2 - m^2\right)^{-1/2},\ \alpha_2 = \left(r_2/4r_0\right)\nu_A^2/\bar{h}r_0^2\ ,\ \bar{\alpha}_{1,2} = \alpha_{1,2}/\bar{h}C\ ,$$

where ν_A is the Bessel function root, $k = \beta_\perp/\beta_{//}$ is the electron-wave coupling parameter, $\mu \approx \gamma^{-2}$ is the bunching parameter, $\Delta = \left(\bar{\omega} - h v_{//} - h_w v_{//}\right)/\bar{\omega}C$ is detuning from the undulator synchronism, $h_w = 2\pi/D_w$, D_w is the undulator period.

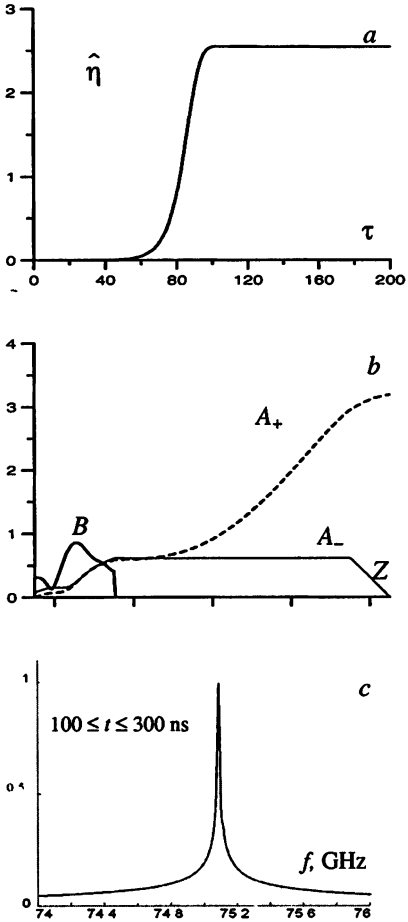

Fig. 6. Results of the simulations

Results of numerical simulations are presented in Fig. 6 in which the process of establishment of single mode single frequency oscillations is shown at the following parameters: lengths of the input, regular and output sections are correspondingly l_1 = 12.7 cm, l_2 = 6 cm, l_0 = 40 cm, particles energy 0.9 MeV, injection current 0.4 kA, amplification parameter $C \approx 0.005$. We choose TE_{11} modes as the propagating waves. In the input mirror at the corrugation period 4.1 mm and depth 0.5 mm the cutoff frequency of TM_{13} is close to the operating frequency. The output mirror has corrugation with period 2.1 mm and depth 0.4 mm. The wave coupling coefficients are α_1 = 0.8 cm^{-1} and α_2 = 0.03 cm^{-1}. In the signal spectrum at $t > 100$ ns there is only one component (Fig. 6*c*), i.e. the single mode single frequency oscillations are established. Distributions of the partial waves in the steady state regime are shown in the Fig. 6*b* demonstrating that the signal is amplified after the input mirror. As a result the amplitude of the cutoff mode B in the input Bragg structure is relatively small. Correspondingly, the Ohmic and diffraction losses associated with this mode are also small. In such conditions up to 90 % of energy extracted

from the electron beam is radiated with the propagating wave A_+. Thus the simulation shows the possibility of single frequency oscillation in the described 75 GHz FEM scheme with efficiency about 15 % and the output power 30 MW.

It is important to note that considered Bragg resonator scheme provides frequency stabilization when beam parameters vary in time. Simulations show that in the full generation band the radiation frequency is close to the frequency of the cutoff. As a result the frequency shift is less than 40 MHz over the particle energy variation $\Delta\gamma/\gamma \approx 20\,\%$.

Electron-optical experiments

Using intense electron beams generated by a conventional pulse line and a Marx generator, time evolution of diode impedance because of diode plasma expansion makes the beam electron energy decrease in time. To prevent from output impedance decrease for the pulse line, liquid resister was set in front of the diode as a shunt register as shown in Fig. 7.

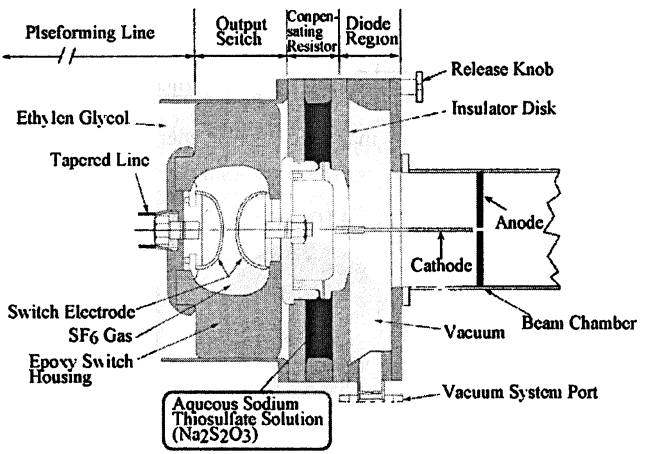

Fig. 7. Shunt resister was set at the upstream side of the diode.

The diode voltage showed nearly flat voltage over 100 ns as shown in Fig. 8 (left) by using the shunt register. Though the calculated diode impedance decreased from 150 to 70 Ω (Fig. 8, right), the diode voltage shows nearly flat part over 100 ns because of the shunt register.

The output signals from magnetic analyzer shows the variation of beam particle energy was less than 5 % (Fig. 9). The beam with energy of ~ 800 keV, current of 400 A and diameter of 3 mm was propagated through the drift tube with length of 2 m and diameter of 20 mm without radial expansion (Fig. 9). The axial magnetic field with strength over 7 kGs was applied. The helical wiggler coil has already tested successfully. The experiments of HBM will be started.

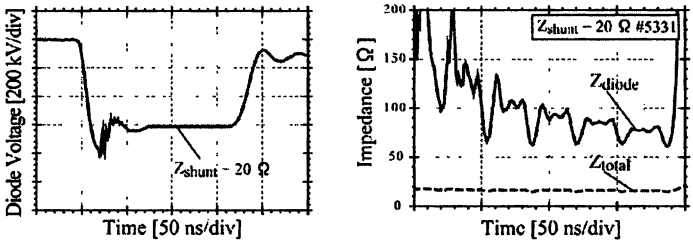

Fig. 8. Diode voltage and calculated diode (solid line) and total (dashed line) impedance

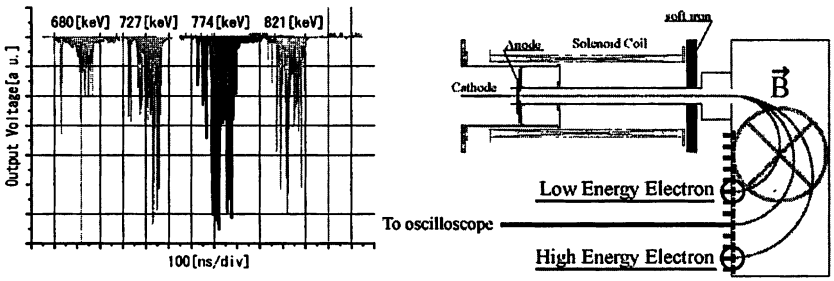

Fig. 9. Signals from magnetic electron energy analyzer

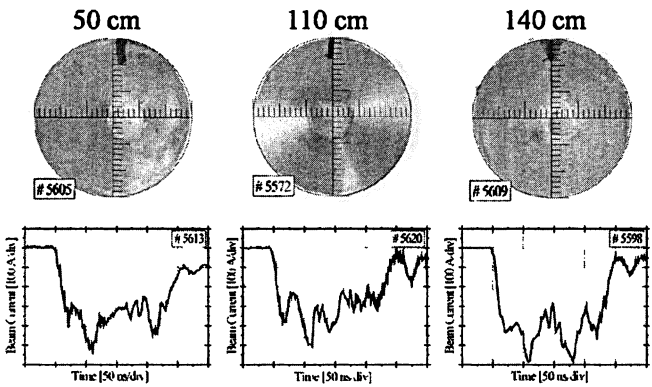

Fig. 10. Damage patterns of the beam along axis (up) and beam currents (down)

Conclusion

Superradiance is an effective method of generation of ultrashort intense electromagnetic pulses with high efficiency and without rf breakdown. The frequency range of superradiance was expanded to S-band. A 5 GHz, 400 MW,

4 ns superradiance microwave pulse was observed using the 600 keV, 5 kA, 12 ns electron beam injected into the slow wave structure.

A new scheme of FEM with hybrid Bragg resonator to improve mode selection was studied. Advanced Bragg structure for mode selection can be used as upstream mirror. Higher mode selection was demonstrated in the simulation in comparison with traditional Bragg cavities. In Kanazawa University an IREB with small radius and small energy spread was prepared for the proof of principle experiment of FEM with HBR.

A part of this work is supported by a Grant-in-Aid for Scientific Research from Ministry of Education, Science, Sports and Culture, Japan and Russian Foundation for Basic Research.

References

1. *Ginzburg N. S., Zotova I. V., Sergeev A. S.* Sov. Tech. Phys. Lett. **15**, 573 (1989).
2. *Ginzburg N. S., Zotova I. V., Sergeev A. S. et al.* Phys. Rev. Lett. **78**, 2365 (1997).
3. *Ginzburg N. S., Novozhilova N. Yu., Zotova I. V. et al.* Phys. Rev. E, **60**, 3297 (1999).
4. *Korovin S., Eltchaninov A. A., Rostov V. V. et al.* Phys. Rev. E, **74**, 016501 (2006).
5. *Bratman V. L., Denisov G. G., Ginzburg N. S., Petelin M. I.* IEEE J. Quantum Electron. **19**, 282 (1983).
6. *Chu T. S., Hartemann F. V., Danly B. G., Temkin R. T.* Phys. Rev. Lett. **72**, 2391 (1994).
7. *Ginzburg N. S , Kaminsky A. K., Peskov N. Yu. et al.* Phys. Rev. Lett. **84**, 3574 (2000).
8. *Ginzburg N. S., Malkin A. M., Peskov N. Yu. et al.* Phys. Rev. ST-AB, **8**, 040705 (2005).
9. *Kamada K., Kawamura M., Aizawa K. et al.* Proc. of 2008 Global Congress on Microwave Energy Applications, 577 (2008).

SPLITTING MODE EFFECT IN FEM WITH OVERSIZED BRAGG CAVITY

N. Yu. Peskov[1], *A. K. Kaminsky*[2], *S. V. Kuzikov*[1], *E. A. Perelshtein*[2], *S. N. Sedykh*[2], *A. S. Sergeev*[1]

[1] Institute of Applied Physics RAS, Nizhny Novgorod, Russia
[2] Joint Institute for Nuclear Research, Dubna, Russia

Splitting mode effect was observed in 30-GHz JINR-IAP FEM operated with Bragg resonator with step of phase of corrugation. Theoretical description of this effect was developed in the frame of the advanced (four-wave) coupled waves approach. Results of the theoretical analysis were corroborated by the 3D simulations, "cold" tests and data of the FEM experiment.

Introduction

Potential applications of FEM-oscillators, in particular, for testing of microwave components of high-energy accelerators, require increase of an output power strictly in regime of single-mode operation [1, 2]. In accordance with simulation of Bragg FEM an output power enhancement could be achieved when decreasing interaction length and simultaneous increasing corrugation depth. However, following this way in experiment with the 30-GHz JINR-IAP FEM based on Bragg resonator with step of phase of corrugation, which operates via feedback loop in the form of two waveguide waves of different transverse structures (TE_{11} – forward wave synchronous to the electrons, TM_{11} – feedback wave), we observed under the certain parameters a double-mode generation regime instead of generation of a single fundamental mode of the resonator.

In present paper the mentioned effect, called as a "splitting mode" effect, is described in the frame of advanced (four-wave) coupling waves approach. Results of the theoretical analysis are confirmed by 3D simulations as well as "cold" microwave tests. Data of the FEM experiment are discussed. Simulations of the FEM with the resonator having split modes demonstrate that the single-mode oscillation regime is established at the nonlinear stage via mode competition mechanism. Nevertheless, in the experiment the splitting mode effect leaded to widening the FEM radiation spectrum and made worse stability of the single-mode generation. This complicates the FEM application for feeding a high-Q component of supercollider [3]. The developed methods to suppress the splitting mode effect by profiling geometry of the Bragg resonator are discussed.

Theoretical model of the splitting mode effect

Cylindrical waveguide with axial-symmetrical corrugation [4, 5]

$$a = \frac{a_1}{2}\cos\bar{h}z \qquad (1)$$

($\bar{h} = 2\pi/d$, d is the period and a_1 is the depth of corrugation) provides coupling and mutual scattering of different pairs of counter-propagating waveguide modes with the wavenumbers $h_\pm$, which satisfy to the Bragg resonance condition

$$h_+ + h_- = \bar{h}. \tag{2}$$

Obviously, increase of the transverse size of the resonator leads to overlap of neighboring Bragg zones, which correspond to the scattering of modes with different transverse structure. However, even if the neighboring central lobes of Bragg resonances are frequency separated, an influence of side-lobes still can exist.

Let us assume that two waveguides modes with different transverse structures $\vec{E}_1$ and $\vec{E}_2$ are participated in the scattering process and present RF-field inside the Bragg structure (1) in the form of the four partial waves: two waves propagating in the forward (with respect to the electron beam) direction

$$A_1^+ \vec{E}_1^+ e^{i\omega t - ih_1^+ z} + A_2^+ \vec{E}_2^+ e^{i\omega t - ih_2^+ z} \tag{3a}$$

and two in the backward direction

$$A_1^- \vec{E}_1^- e^{i\omega t + ih_1^- z} + A_2^- \vec{E}_2^- e^{i\omega t + ih_2^- z}. \tag{3b}$$

In the coupling waves approach mutual scattering of these waves can be described by the system of equations for the slow amplitudes $A_{1,2}^{\pm}(z)$ [5]

$$\begin{aligned} &\frac{dA_1^+}{dz} + ih_1 A_1^+ = i\alpha_{1\leftrightarrow 2} A_2^- + i\alpha_{1\leftrightarrow 1} A_1^-, \quad \frac{dA_2^+}{dz} + ih_2 A_2^+ = i\alpha_{2\leftrightarrow 2} A_2^- + i\alpha_{1\leftrightarrow 2} A_1^-, \\ &\frac{dA_1^-}{dz} - ih_1 A_1^- = -i\alpha_{1\leftrightarrow 2} A_2^+ - i\alpha_{1\leftrightarrow 1} A_1^+, \quad \frac{dA_2^-}{dz} - ih_2 A_2^- = -i\alpha_{2\leftrightarrow 2} A_2^+ - i\alpha_{1\leftrightarrow 2} A_1^+, \end{aligned} \tag{4}$$

where $\alpha_{i\leftrightarrow j}(z)$ are coupling coefficients for the waves "i" and "j", which is proportional to the corrugation depth a_1. Note, that in (4) we neglect scattering of the co-propagating waves. We assume also that the operating feedback circle is completed at the waves $A_1^+ \leftrightarrow A_2^-$ and the nearest in frequency is scattering of the waves $A_2^+ \leftrightarrow A_2^-$. At the same time, zone of the scattering $A_1^+ \leftrightarrow A_1^-$ is frequency distant from the "operating zone", thus, we will neglect scattering of these waves. In such approximation Eqs. (4) can be reduced to the form

$$\begin{aligned} &\frac{da_1^+}{dz} + i\delta a_1^+ = i\alpha_{1\leftrightarrow 2} a_2^-, \quad \frac{da_1^-}{dz} - i\delta a_1^- = -i\alpha_{1\leftrightarrow 2} a_2^+, \\ &\frac{da_2^+}{dz} + i\delta a_2^+ = i\alpha_{1\leftrightarrow 2} a_1^- + i\alpha_{2\leftrightarrow 2} a_2^- e^{i(\Delta-\delta)z}, \\ &\frac{da_2^-}{dz} - i\delta a_2^- = -i\alpha_{1\leftrightarrow 2}(z) a_1^+ - i\alpha_{2\leftrightarrow 2}(z) a_2^+ e^{-i(\Delta-\delta)z}, \end{aligned} \tag{5}$$

where $a_1^{\pm} = A_1^{\pm} e^{\pm\frac{i}{2}(h_2 - h_1 - \bar{h})}$, $a_2^{\pm} = A_2^{\pm} e^{\pm\frac{i}{2}(h_1 - h_2 - \bar{h})}$, $\delta = h_1 + h_2 - \bar{h}$, $\Delta = 2h_2 - \bar{h}$. In the case of resonator with the moderate transverse oversize and small wave coupling coefficients parameter δ is small while $\Delta - \delta = h_2 - h_1$ is large. Averaging Eqs. (5) over the fast oscillating value $\Delta - \delta$ one get two independent sets of equations for scattering of two pairs of the waves: $a_1^+ \leftrightarrow a_2^-$ and $a_1^- \leftrightarrow a_2^+$. Obviously, in the resonator with step of phase of corrugation these two sets of equations describes two degenerated solutions at the Bragg frequency $\bar{\omega}$ (i.e. $\delta = 0$), which, in fact, correspond to the substitution $z \to -z$ (i.e. rotation of the system at 180°). The analysis of Eqs. (5) (see below) shows that the presence of the non-resonant scattering of the waves $A_2^+ \leftrightarrow A_2^-$ at the "fast" frequency $\Delta - \delta$ removes this degeneration and leads to the scattering of the fundamental eigenmode of the resonator.

Simulations of oversized Bragg resonators

In the simulations parameters of Bragg resonator were taken close to the conditions of JINR-IAP FEM experiment [1, 2]. The resonator was composed from two waveguide sections of the mean radius $r_0 = 0.95$ cm, which possessed corrugation in the form (1) with the period $d = 0.58$ cm. In accordance with (2) this corrugation provides effective zone of Bragg scattering for the pair of waves $TE_{1,1} \leftrightarrow TM_{1,1}$ in the vicinity of 30 GHz (operating frequency of JINR-IAP FEM). Waveguide sections were of the lengths of $l_1 = 20$ cm and $l_2 = 15$ cm and had step of phase π in the point of their connection.

Results of simulations of the resonator reflection coefficient based on Eqs. (5) are shown in Fig. 1. Simulations demonstrate that resonators with corruga-

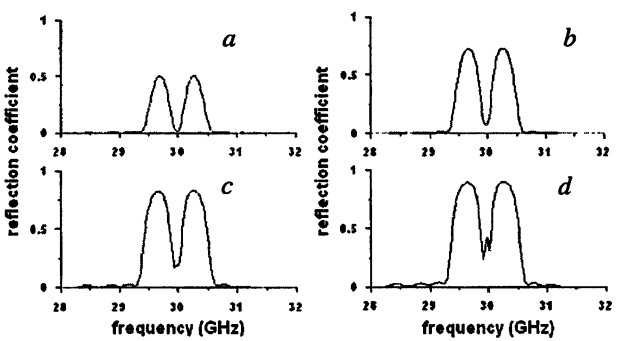

Fig. 1. Frequency dependence of the reflection coefficient from the Bragg resonator found in the frame of the four-wave coupling waves approach: (*a*) $a_1 = 0.2$ mm, (*b*) $a_1 = 0.3$ mm, (*c*) $a_1 = 0.4$ mm, (*d*) $a_1 = 0.5$ mm

tions of small depth possess fundamental mode at the Bragg resonance frequency $\bar{\omega}$ (Fig. 1*a*), which correspond to the drop of the reflection in the middle of the Bragg zone. With the increase of the corrugation depth a_1 (i.e. coupling coefficients) maximal reflection as well as Q-factor of the fundamental mode increase (Fig. 1*b*). However, after some depth the splitting of the fundamental mode occurs and two modes become distinguished in the middle of the Bragg zone (Fig. 1*c*). These modes are approximately of the same Q-factors and possess frequencies positioned symmetrically in opposite sides of the Bragg frequency. For more deep corrugation Q-factors of the splitting modes enhance with increase in frequency distance between them (Fig. 1*d*).

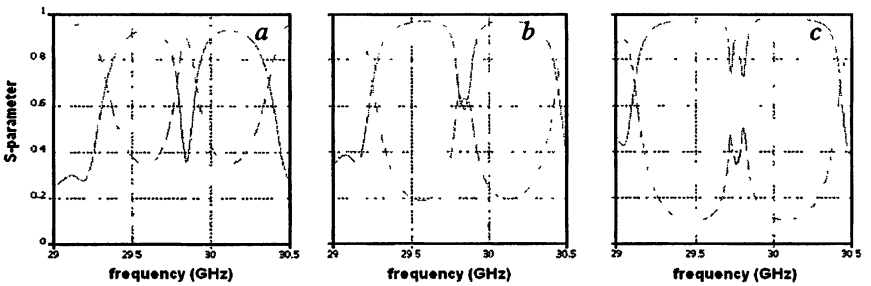

Fig. 2. Frequency dependence of the reflection and transmission coefficients into different waveguide modes found in 3D simulations (solid lines – reflection into $TM_{1,1}$ wave, dashed lines – transmission into $TE_{1,1}$ wave): $a_1 = 0.3$ mm (*a*), $a_1 = 0.4$ mm (*b*), $a_1 = 0.5$ mm (*c*)

To prove adequacy of the advanced ("four-wave") coupling waves model these Bragg resonators were also simulated using 3D electrodynamical code based on FDTD method. At the left edge the $TE_{1,1}$ wave entered the resonator. Simulations of frequency dependences of the reflection and transmission into different waveguide modes are shown in Fig. 2 and coincide well with the approach described above (see Fig. 1). Results of the theoretical analysis were confirmed by "cold" microwave tests, which are presented in Fig. 3. Obviously, splitting fundamental mode significantly reduces selective property of the Bragg resonator with step of phase of corrugation.

Experimental studies of 30 GHz JINR-IAP FEM

The JINR-IAP FEM-oscillator is driven by the induction linac LIU-3000 (0.8 MeV / 200 A / 250 ns). Transverse velocity in the magnetically guided beam is pumped in a helical wiggler of 6 cm period. The main features of JINR-IAP FEM is the use of a reversed guide field [6, 7], which provides high-quality beam formation in the tapered wiggler section with a low sensitivity to the initial beam

spread, alongside with Bragg resonator having a step of phase of corrugation [4, 5].

In experiments with FEM based on the resonator having split modes both single-mode and multi-mode regimes of oscillations were registered (Fig. 4). These regimes were tuned varying undulator and guide magnetic fields. Frequency difference between two split modes amount 20–50 MHz for parameters described above. The single-mode oscillation regime was established at the nonlinear stage via mode competition mechanism. Nevertheless, the splitting mode effect leaded to widening the FEM radiation spectrum and made worse stability of the single-mode generation in the presence of beam's jitter. This complicates the FEM application for feeding a high-Q component of supercollider [3].

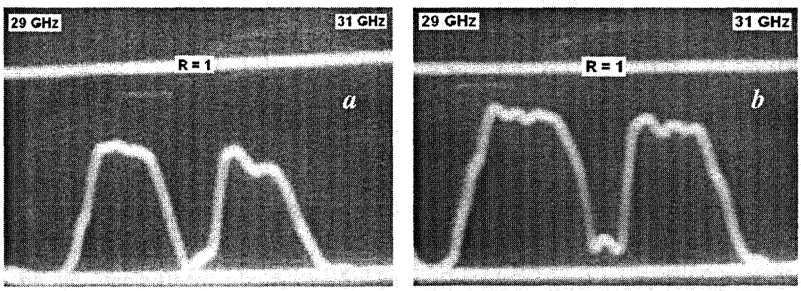

Fig. 3. Results of "cold" measurements of Bragg resonators having corrugations of different depth: (*a*) $a_1 = 0.3$ mm, (*b*) $a_1 = 0.4$ mm

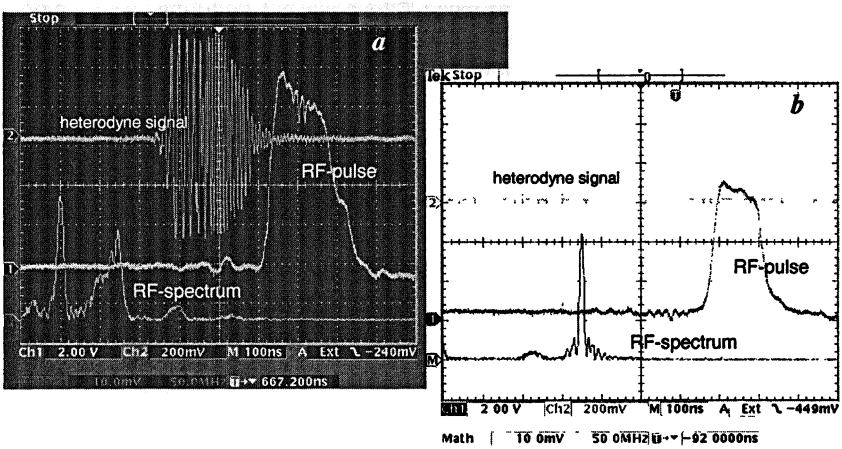

Fig. 4. Typical oscilloscope traces in different regimes of JINR-IAP FEM: double-frequency (*a*) and single-mode operation (*b*)

One of the ways to suppress splitting mode effect is a profiling of the resonator geometry, which allows reduction of the influence of the neighboring Bragg scattering zones each to other. The resonators with corrugation having profiling amplitude were studied and demonstrated best stability of the single-mode FEM operation when Bragg resonator with corrugation of high depth is used [2]. However, optimization of such resonators to obtain high efficiency of whole FEM source seems to be more complicated.

References

1. *Kaminsky A. K., Elzhov A. V., Ginzburg N. S. et al.* Proc. of the 5th Int. Workshop "Strong Microwaves in Plasmas", N. Novgorod, Russia, 2002, **1**, 184.
2. *Peskov N. Yu., Ginzburg N. S., Kaminsky A. K. et al.* The 16th Int. Conf. on High-Power Particle Beams, Oxford, UK, 2006, p. 56.
3. *Ginzburg N. S., Kaminsky A. K., Kuzikov S. V. et al.* J. Tech. Phys. **76**, 69 (2006).
4. *Kovalev N. F., Petelin M. I., Reznikov M. G.* USSR Authors Patent №. 720592 (Aug. 14, 1980).
5. *Bratman V. L., Denisov G. G., Ginzburg N. S., Petelin M. I.* IEEE J. Quant. Electron. **19**, 282 (1983).
6. *Kaminsky A. A., Kaminsky A. K., Rubin S. B.* Particle Accelerators **33**, 189 (1990).
7. *Conde M. E., Bekefi G.* Phys. Rev. Lett. **67**, 3082 (1991).

FIRST FULL-SCALE RESULT IN CLIC-JINR-IAP RAS EXPERIMENT ON 30 GHZ COPPER CAVITY HEATING

Yu. Yu. Danilov[1], N. S. Ginzburg[1], I. I. Golubev[2], A. K. Kaminsky[2], A. P. Kozlov[2], S. V. Kuzikov[1], E. A. Perelstein[2], N. Yu. Peskov[1], M. I. Petelin[1], S. N. Sedykh[2], A. P. Sergeev[2], A. S. Sergeev[1], A. A. Vikharev[1], N. I. Zaitsev[1]

[1] Institute of Applied Physics, Nizhny Novgorod, Russia
[2] Joint Institute for Nuclear Research, Dubna, Moscow region, Russia

The joint CLIC-JINR-IAP RAS experiment has completed its preparation to investigate the surface damage of 30 GHz imitator of the CLIC high gradient accelerating structure caused by repetitive high-power RF pulses. After preliminary experiments the design of the test cavity was substantially changed. The first full-scale experiment has shown that the copper surface damage is clearly seen after $3 \cdot 10^4$ pulses with each pulse heating from 200 °C to 220 °C.

Introduction

The project of high-energy (0.5–3 TeV center-of-mass), high-luminosity (10^{34}–10^{35}cm$^{-2} \cdot$ s^{-1}) electron-positron Compact Linear Collider (CLIC) has been in progress at CERN as a possible new accelerator facility for the post-LHC era [1]. The room-temperature accelerating structure has the design accelerating gradient equal to 100 MV/m at operating frequency of 12 GHz. One of the most severe limits on the accelerating gradient at such high frequency and accelerating field is damage of the structure wall due to very intensive cycling heating by short high-power RF pulses [2]. The reason is that the heating velocity is faster than the material expansion velocity, and the mechanical stress can exceed the limit of elasticity. The design lifetime of the structure should be of the order of 20 years (about $2 \cdot 10^{10}$ pulses) with pulse heating of approximately 70 °C, so direct experiments would have taken too much time. There are two possible ways to investigate these phenomena: 1) application of non-RF mechanical stresses with the repetition rate much higher than it is possible for powerful RF sources (ultrasound vibrators); 2) RF pulse heating till significantly higher temperature to observe the surface damage after a much smaller number of pulses.

Preparation for the joint experiment CLIC-JINR-IAP RAS to investigate lifetime of the 30 GHz high-gradient accelerating structure with RF pulse heating up to 200 °C, has now been completed. After preliminary experiments which have shown that pulse heating of the test cavity was only about 40 °C, the new design of the test cavity has been offered. Particularly, the shape of the central ring of the cavity has been changed and its Q-factor has been increased.

Experimental facility

The experimental facility is based on the 30 GHz Free-electron maser (FEM) oscillator. It was developed by collaboration of the Joint Institute for Nuclear

Research, Dubna, and the Institute of Applied Physics, RAS, Nizhny Novgorod [3]. The oscillator uses the electron beam from the induction linear accelerator and produces radiation with the output power up to 20 MW and pulse duration of 180 ns, while the spectrum width does not exceed 10 MHz. The repetition rate of the facility is 0.5–1 pulse per second.

One of the main features of the FEM oscillator is a Bragg resonator which produces the distributed selective feedback. It is transparent both for the electron beam and radiation of all the frequencies except the resonant one. For the electron beam pumping we have used a helical 4-wire electromagnetic wiggler with a big area of the uniform transverse field inside the waveguide and smooth field tapering on the both ends.

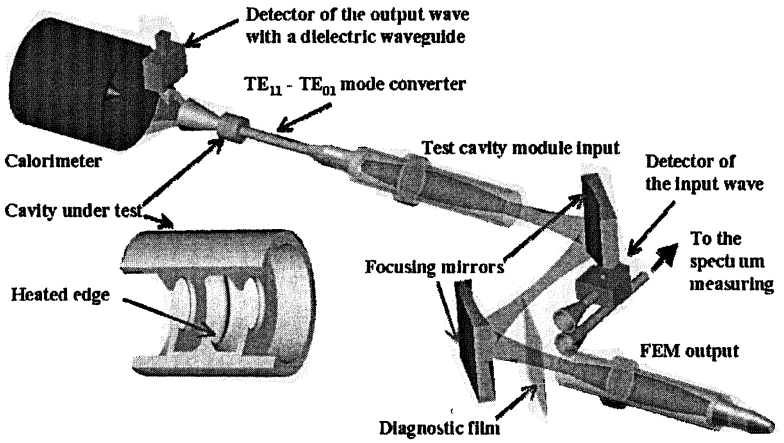

Fig. 1. Layout of the experimental facility

The radiation of the FEM is extracted out into the air. It is convenient for some applications, like biological experiments. That is why special attention has been paid to the output waveguide. The output horn forms almost Gaussian transverse distribution of the radiation most suitable for the quasi-optical transmission line. The difference of phase velocities of partial modes leads to the variation of the transverse distributions of the radiation along the oversized waveguide. At the end of the 90 cm waveguide again almost the Gaussian wave-beam has been obtained, but in the vicinity of 60 cm the distribution is almost uniform – more convenient for the output window.

To measure the radiation power, we have applied silicon detectors and a solid-state calorimeter with a big aperture. The spectral diagnostics is based on the heterodyne facility with the on-line Fourier analyzer.

Radiation from the FEM output waveguide is passing through the thin diagnostic film to the symmetrical two-mirror quasi-optical transmission line. After the oversized waveguide with an input vacuum window the radiation is trans-

formed by the input horn from the Gaussian distribution into the TE_{11} mode and then into TE_{01} mode by a specialized mode converter. After the output horn the radiation is monitored by a detector with a dielectric waveguide and then it is fully accepted by the calorimeter.

A specially designed test cavity operates at the mode TE_{01} with zero electric field near the wall to prevent the inner discharge. It consists of two diaphragms and the inner ring with a rather thin edge (Fig. 2). The most heated area is the inner edge of the ring. The quality factor of the cavity is 1500. The precise frequency matching of the cavity with the FEM oscillator can be achieved by changing the distance between the diaphragms. The test cavity module has its own vacuum system.

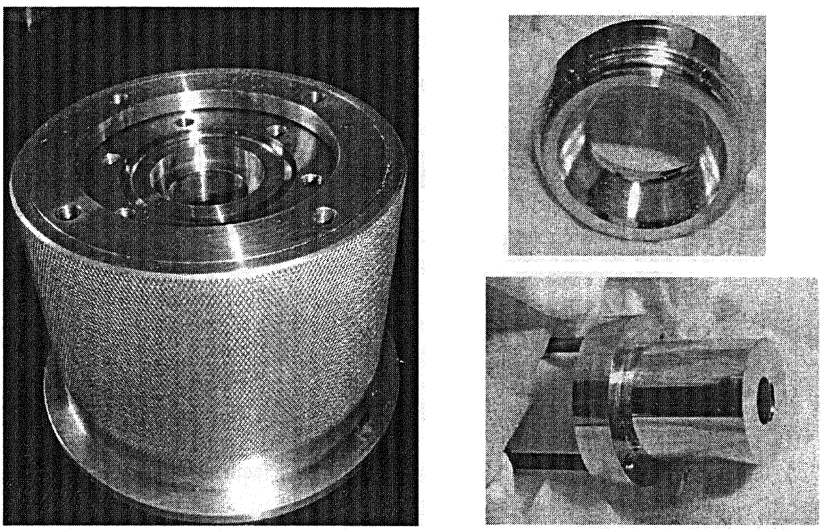

Fig. 2. Details of test cavity: vacuum box, central ring and input diaphragm

Experimental results

The radiation power pulse duration after the test cavity was 180 ns vs. 200 ns after the FEM output waveguide. We have calculated correlations between the pulse heating of the inner surface of the test cavity and RF pulse energy after it. The stable operation of the facility corresponds to the temperature rise from 200 °C to 220 °C.

The visual diagnostics is applied to control the purity of the wave mode inside the test cavity. It uses metal fillings on the plexiglass plate, which are the centers of air discharges in the high-intensity electromagnetic wave. The ring image at the plate installed after the output horn indicates that the wave mode

inside the test cavity is TE_{01}. The absence of the breakdown inside the test cavity has been controlled by the visual observations through the output diaphragm.

The first full-scale experiment has been performed using the inner ring manufactured from oxygen-free copper by turning with a diamond tool and without additional annealing. A preliminary analysis of the microphotographs of the ring before and after exposure (Fig. 3) has shown that the damage of the surface is clearly seen after the number of pulses $3 \cdot 10^4$ while the pulse heating was from 200 °C to 220 °C. The surface damage is the key argument that the experimental facility is now ready for regular investigations of the processes at the cavity wall caused by repetitive powerful pulses of RF radiation.

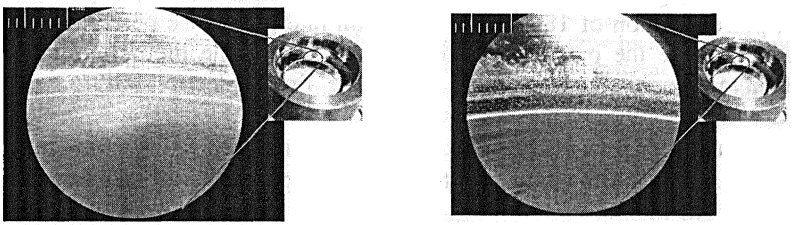

Fig. 3. Microphotographs of the inner surface of the test cavity before experiments (*left*) and after $3 \cdot 10^4$ pulses with pulse heating from 200 °C to 220 °C (*right*)

This result can be compared with the several-year activity of the CLIC collaboration investigating this limitation on the acceleration gradient. Figure 4 shows results of the CERN experiments using ultrasonic vibrators (number of cycles 10^7–10^{11} with equivalent pulse heating from 70 °C to 150 °C) [4], CERN experiments on the surface heating with ultraviolet laser (number of pulses

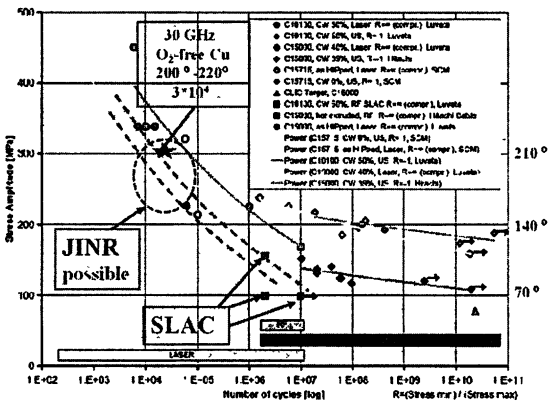

Fig. 4. Experimental results of different groups investigating the damage of the cavity surface by ultrasonic vibrators (CERN) (diamonds), heating by an ultraviolet laser (CERN) (rings), by RF radiation at frequency of 11.4 GHz (SLAC) (squares) and 30 GHz (JINR) (the star)

10^2–10^6 with pulse heating from 120 °C to 450 °C) [5] and recent SLAC experiments on RF heating at the frequency of 11.4 GHz with pulse heating from 70 °C to 110 °C and number of pulses 10^6–10^7 [6]. The correlation between our results and the results, obtained in the CERN experiments with surface heating by the ultraviolet laser, is rather good.

Conclusion

The facility for experiments on damage of the cavity wall due to RF pulse heating has been developed and put into operation by the JINR-IAP RAS collaboration using the 30 GHz free-electron maser with the output power of 20 MW, pulse duration of 180 ns and repetition rate of 1 pulse per second. These experiments are the part of the program to estimate the lifetime of the high-gradient accelerating structure of the future linear electron-positron collider CLIC.

The facility is now ready for experiments with pulse heating from 150 °C up to 220 °C and the pulse number up to 10^5, each experiment will take from several days up to one month.

The first full-scale experiment has shown that the oxygen-free copper was damaged after $3 \cdot 10^4$ pulses when the temperature rise was from 200 °C to 220 °C. This result corresponds rather well to the CERN experimental results with surface heating by ultraviolet, though the frequency of the electromagnetic field and skin-depth in these experiments differ significantly.

The comparison of the damage character with similar experiments on RF heating in SLAC would be very important and useful to investigate the parameter influence such as pulse duration and RF frequency.

References

1. *Wilson I.* The compact linear collider CLIC // CLIC Note-617. Geneva: CERN, 2004. 12 p.
2. *Pritzkau D. P., Siemann R. H.* Experimental study of RF pulsed heating on oxygen free electronic copper // Physical review special topics: Accelerators and beams. 2002. Vol. 5. P. 112002.
3. *Elzhov A. V., Ginzburg N. S., Kaminsky A. K. et al.* Test facility for investigation of heating of 30 GHz accelerating structure imitator for the CLIC project // Nuclear Instruments and Methods in Physics Research. 2004. Vol. A528. P. 225–230.
4. *Arnau-Izquierdo G., Calatroni S., Heikkinen S. et al.* High Power RF Induced Thermal Fatigue in the High Gradient CLIC Accelerating Structures // CLIC Note-708. Geneva: CERN, 2007. 13 p.
5. *Calatroni S., Neupert H., Taborelli M.* Fatique testing of materials by UV pulsed laser irradiation // CLIC Note-615. Geneva: CERN, 2004. 4 p.
6. *Laurent L.* Pulsed heating experiment // 2nd Collaboration meeting on X-band Accelerator structure Design and Test-program. – http://indico.cern.ch/contributionDisplay.py?contribId=35&sessionId=13&confId=30911.

HIGH-GRADIENT, QUASI-OPTICAL, ACCELERATING STRUCTURE

S. V. Kuzikov[1], S. Kazakov[2], M. E. Plotkin[1], J. L. Hirshfield[3], G. V. Sotnikov[4]

[1] Institute of Applied Physics, Russian Academy of Sciences, Nizhny Novgorod, Russia
[2] KEK, Tsukuba, Japan
[3] Yale University, Omega-P, Inc., New Haven, USA
[4] NSC "Kharkov Institute of Physics and Technology", Kharkov, Ukraine

A new accelerating structure which aims to provide high acceleration gradient (>150 MeV/m) for a next generation of multi-TeV linear collider is suggested. The structure is based on a periodic system of cavities operated with equidistantly-spaced on frequency eigenmodes. These modes are excited by the periodically bunched drive beam in such a way that all fields in structure oscillate in time with bunch period and represent narrow peaks separated by broad intervals of low fields. This principle promises an essential reduction of exposition time at structure surface and a higher gradient in comparison with a single-mode structure.

Introduction

We suggest a new accelerating structure which is based on chain of multi-mode cavities with nearly equidistant eigen frequencies [1–4]. A multi-mode superposition of fields localized in space is caused to bounce between the structure axis and wall at the bunch period and thereby to accelerate the particles. This principle is illustrated in Fig. 1, where particles are accelerated in a periodic system of cavities that are decoupled from one another. RF power that flows in the longitudinal direction is, for purposes of this discussion, neglected due to assumed small cutoff holes that are only large enough for beam transmission.

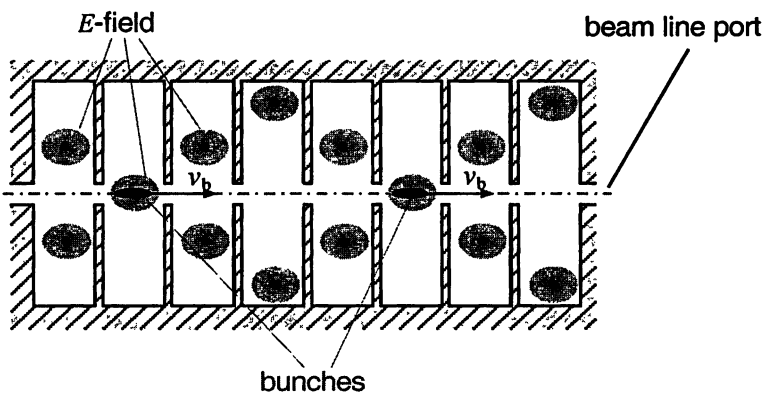

Fig. 1. Acceleration of moving periodic bunches by uncoupled cavities operated with synchronized eigen modes

The ideal electric field as seen by bunches along the structure is sketched in Fig. 2 (curve *1* – fat solid), in comparison with the field in a single-frequency structure (curve *2* – dashed). In the case of a limited number of modes used in the proposed accelerating structure the resulted field looks like that in curve *3* – thin solid. One notes that in the latter case the field is only strong during the short time intervals where bunches are localized.

The proposed solution means that fields in any point are periodic functions of time:

$$\mathbf{E}(\mathbf{r},t+T_b)=\mathbf{E}(\mathbf{r},t), \tag{1}$$

where T_b is the time interval between bunches. The same formula is valid for magnetic fields too.

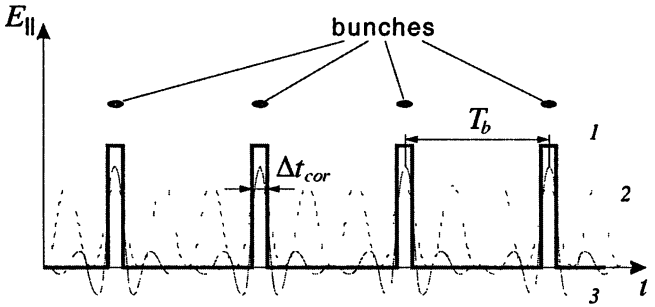

Fig. 2. Time dependence of field in accelerating structures: *1* – ideal (desirable) field dependence on time; *2* – field dependence in conventional single-frequency accelerating structure; *3* – field in multi-frequency accelerating structure operated with a limited number of modes

The condition (1) requires the RF field in each cavity to be represented as superposition of equidistantly spaced eigen modes:

$$\begin{aligned}\mathbf{E}(\mathbf{r},t)&=\sum_n a_n\cdot\mathbf{F}_n(\mathbf{r})\cdot\exp(i\omega_n t),\\ \omega_n&=\omega_0+n\cdot\Delta\omega,\ T_b=q2\pi/\Delta\omega,\end{aligned} \tag{2}$$

where $\Delta\omega$ is a distance between neighbour modes, $\omega_0/\Delta\omega=p/q$; n, p, and q are positive integers.

Duration of each power peak is determined by a condition that the phase difference between the lowest and highest modes is π:

$$\Delta t_{cor}\approx\pi/(\omega_N-\omega_0). \tag{3}$$

We assume below that the ratio of peak's width to time interval between peaks is a small parameter:

$$\frac{\Delta t_{cor}}{T_b}<<1. \tag{4}$$

Hence, the field at an arbitrary point is pulsed in time with significant near to zero field intervals between peaks.

Comparison of multi-frequency and single-frequency structures

There are three main phenomena which do not allow increasing an accelerating gradient in "warm" accelerators: a dark current, a pulse heating, and a surface breakdown. Let us consider all the mentioned phenomena comparing a single-frequency structure and a new multi-frequency structure.

The dark current limitation means that foreign particles (always existing due to not full vacuum as well as particle emission from surface by RF fields) might be captured by accelerating wave. In a single-frequency structure the accelerating gradient G is limited to that field magnitude which leads to acceleration of an initially motionless electron up to velocity close to phase velocity of slow accelerating wave [5]:

$$G_{\max} = \frac{\pi mc^2}{e\lambda}, \tag{5}$$

where e, m are charge and mass of electron, λ is a wavelength in vacuum, c is a light velocity.

For a multi-frequency structure the capture condition requires that such electron reaches the same velocity within a time interval Δt_{cor}. Therefore, the limiting gradient for a multi-frequency structure equals the threshold gradient of that a single-frequency structure which works at a frequency $\omega = \pi/\Delta t_{cor}$.

Surface degradation phenomena in high-gradient structures strongly depend on temperature rise due to pulsed surface heating by the RF magnetic field [6–7]. The temperature rise in a single frequency structure at frequency ω with heating diffusion inside a metal taken into account is proportional to square root of the pulse duration τ:

$$\Delta T = \alpha \cdot H^2 \cdot \sqrt{\tau}, \tag{6}$$

where α is a constant, and H is a surface magnetic field. For the same pulse duration and peak magnetic field in a multi-frequency structure with $\Delta t_{cor} = \pi/\omega$, the temperature rise during one pulse is smaller in proportion to the factor $(\Delta t_{cor}/T_b)^{1/2}$, because heating is absent between field peaks, although within one peak this heating is like in a comparing single-frequency structure within a half-period (Fig. 3).

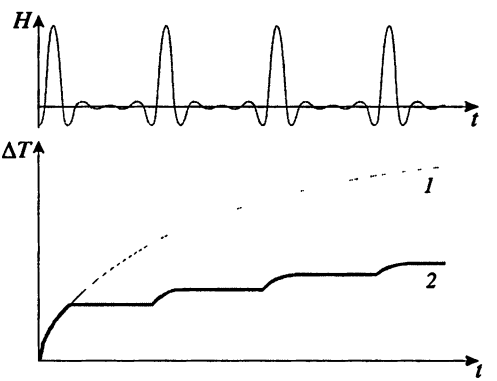

Fig. 3. Magnetic field and temperature as function of time: *1* – in single-frequency structure, *2* – in multi-frequency structure

A breakdown is complicated phenomena those theory is

still not well developed. Nevertheless, it is known that breakdown can be separated at several stages. At the primary stage RF electric field produces electrons to tunnel from microjuts, this effect is described by the Fowler-Nordheim law. At the second stage the microjuts are melted and evaporated. The freed molecules are ionized by oscillating electrons. The resulting plasma frequency grows up and approaches the field frequency.

In [8–9] it is suggested to consider the first stage only in order to find criteria of breakdown initiation. According to [8–9] the necessary condition to start the second stage of breakdown is a heating of surface by emission currents up to definite threshold temperature ΔT_{thr}.

Let us consider the temperature rise ΔT as a function of time t is given by formula (with heat diffusion into metal taken into account):

$$\Delta T(t) = A \cdot \int_0^t \frac{j(t') \cdot E(t')}{\sqrt{t - t'}} dt', \tag{7}$$

where j is a tunnel emission current, E is a normal to surface field component, A is a constant. If to substitute Fowler-Nordheim tunnel current in (8), we obtain formula:

$$\Delta T(t) = B \cdot \int_0^t \frac{E^3(t') \cdot \exp(-\gamma / E(t'))}{\sqrt{t - t'}} dt', \tag{8}$$

where the expression behind integral is assumed to be different from zero if only $E(t) > 0$, B and γ are constants. Exponential multiplier in (9) says that low field fractions do not bring a contribution to ΔT. That is why, in [10] it is suggested to calculate the integral (8) so that only contributions of E-fields which exceed 85 % on magnitude of maximum are not ignored. The contributions of lower fields than the mentioned value are neglected. Let us analyze formula (8). The simplest conclusion is that threshold value E_{thr} for RF pulses with rectangular shape is approximately scaled with pulse duration τ as:

$$E_{thr}^3 \cdot t^{1/2} = \text{const} \quad \text{or} \quad E_{thr}^6 \cdot t = \text{const} \equiv I. \tag{9}$$

Recent experimental data [9] are well agreed with this scaling law.

Another conclusion of analysis is that threshold value does not depend on frequency ω (it is assumed that $2\pi/\omega << \tau$), because $\Delta T(\tau)$ is a constant for arbitrary frequency.

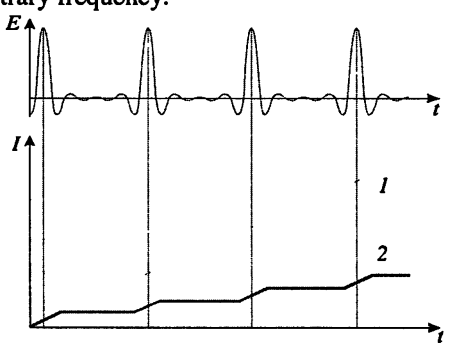

Fig. 4. Magnetic field and integral I as function of time: 1 – in single-frequency structure, 2 – in multi-frequency structure

Analysis of Fig. 4, where the integral I is plotted as function of time for a single- and a multi-frequency structures, shows that in accordance with the criterion (9) it is expected that the breakdown field threshold in a multi-frequency structure should be higher by a factor $(T_b/\Delta t_{cor})^{1/6}$ than in a comparing single-frequency structure at frequency $\omega = \pi/\Delta t_{cor}$.

Simulations of two-beam, two-section accelerating structure

We propose a two-beam accelerating structure where a high-current drive beam excites fields which accelerate a low-current beam, much as in the CLIC (CERN) scheme. The structure consists of rectangular cross-section cavities with approximate sizes $a \times 2a \times l_r$ which have an infinite number of equidistant $TM_{n,2n,0}$ ($n = 1, 3, 5, \ldots$) modes at frequencies:

$$f_{n,2n,0} = \frac{n \cdot c}{\sqrt{2} \cdot a}, \tag{10}$$

where c is the light velocity. Modes with $n = 2, 4, 6, \ldots$ have zero longitudinal E-fields near particle beams.

The bunches in either e^+e^- or e^-e^- combinations move in parallel direction as in Fig. 5 with different spacings L_b.

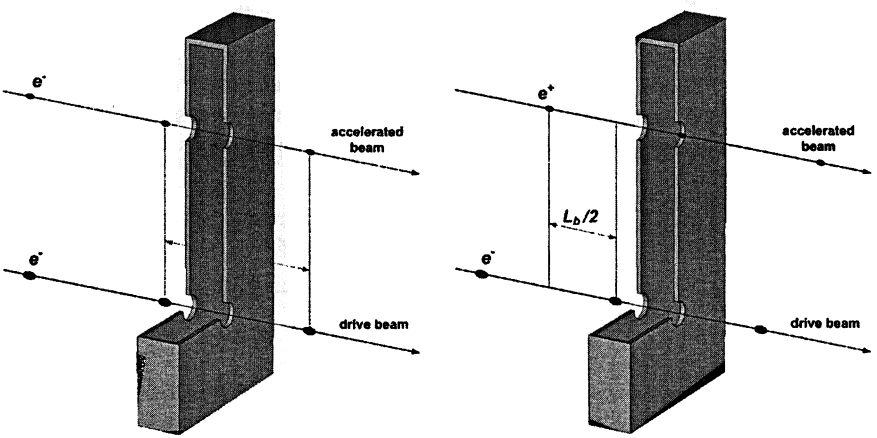

Fig. 5. Two-beam two-section accelerating structure with aspect ratio 1:2 (frequency detuning is not shown)

In order to not have an unreasonable number of drive beams along the accelerator, the structure should exhibit a high transformer ratio T (ratio of the magnitudes of fields felt by the accelerated particles to those felt by the drive particles). For the case of finite cavity Q one can show that the transformer ratio T for a single cavity mode is given by

$$T = \frac{\cos\varphi + \alpha - 2Q \cdot (\Delta\omega / \omega_d) \cdot \sin\varphi}{1 + \alpha\cos\varphi + 2\alpha \cdot Q \cdot (\Delta\omega / \omega_d) \cdot \sin\varphi}, \tag{11}$$

where $\alpha = I_{acc}/I_{drive}$ is a ratio of accelerated to drive currents, ω_d is a drive bunch frequency, $\Delta\omega$ is a detuning of the cavity resonance away from ω_d, and φ is a phase difference between I_{acc} and I_{drive}. The phase diagram for currents and gap voltages in the cavity is shown in Fig. 6; it is seen that the drive voltage does positive work on the accelerated current, while the accelerated voltage does negative work on the drive current.

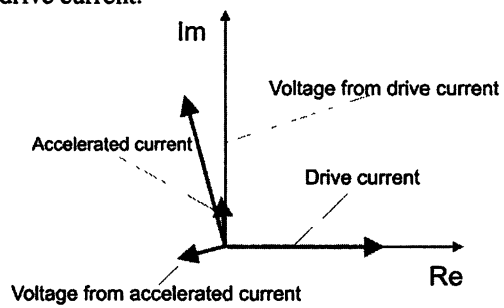

Fig. 6. Location of drive and accelerated bunches in the steady-state, relative to the wave field in the cavity

In accordance with (11) high-T values can be achieved only when the cavity eigen frequencies are detuned slightly away from the frequency of the drive bunches, in which case the electric field of the operating modes can be close to zero during the times when drive bunches pass through the cavity, as shown in Fig. 7.

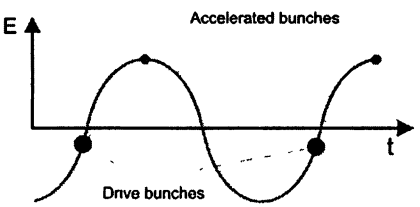

Fig. 7. Location of drive and accelerated bunches in the steady-state, relative to the wave field in the cavity

With multi-mode operation, different detuning is required for each mode. Moreover the steady-state situation as depicted in Fig. 7 evolves in time from the start of the drive bunch train, where the peak fields occur right at the bunches; the evolution time depends upon detuning, beam current, and cavity Q.

Simulation of the accelerating structure was carried out in a three-cell model (Figs. 8, 9) with parameters of the drive and accelerated beams as given in the CLIC project. Each cell with sizes 70 × 140 mm had 10 mm length and 3 mm iris thickness operated with first three modes at frequencies near 3 GHz, 9 GHz, and 15 GHz.

Results of simulations are depicted in Fig. 8 where cross-sections of drive and accelerated beams are shown at three subsequent times, and Fig. 9 where fields in the plane perpendicular to the beams in the central cell are shown. Times in Fig. 8 *a*, *b*, *c* are the same as those in Fig. 9 *a*, *b*, *c*, respectively.

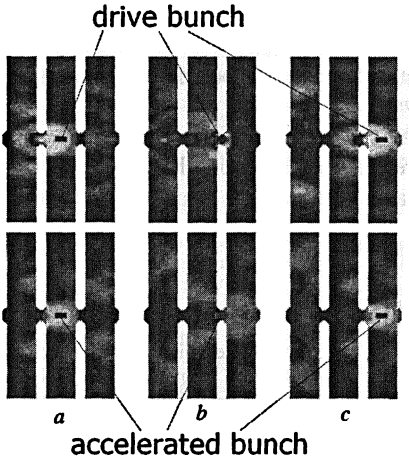

Fig. 8. Instantaneous $E_{||}$-field structures in drive beam plane (up) and accelerated beam plane (bottom): *a* – bunches in center of middle cell, *b* – bunches between cells, *c* – bunches in final cell

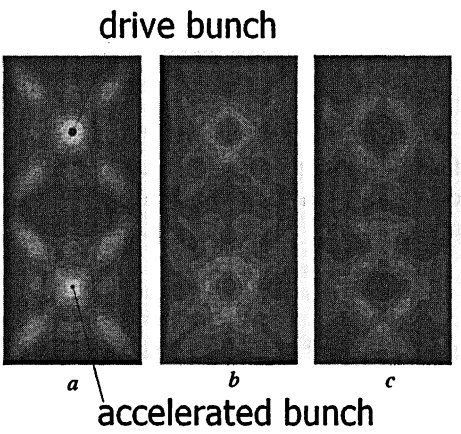

Fig. 9. Instantaneous field structures in transverse cross-section of the middle cell at three times corresponding to that in Fig. 8

The optimized parameters of the structure due to individual detuning of modes are summarized in Table for accelerating gradients 100 MeV/m and 150 MeV/m. Note that the ratio of maximum surface electric field E_s to accelerating gradient is ~1.5:1, i.e. less than the typical value of 2:1 in single-frequency structures.

Summary of optimization

Bunch charge, Q_0	33.6 nC	33.6 nC
Accelerating gradient, G	100 MV/m	150 MV/m
Drive current, I_{drive}	100.8 A	100.8 A
Accelerated current, I_{acc}	1.2 A	1.2 A
Transformer ratio, T	28.0	21.2
Efficiency	33.2 %	21.2 %
E_s max	146 MV/m	220 MV/m
$\Delta f_1/f_1$	$3.6 \cdot 10^{-3}$	$2.3 \cdot 10^{-3}$
$\Delta f_2/f_2$	$-1.2 \cdot 10^{-3}$	$-8.4 \cdot 10^{-4}$
$\Delta f_2/f_2$	$2.9 \cdot 10^{-3}$	$2.0 \cdot 10^{-3}$

Conclusion

The idea of a high-gradient multi-mode two-beam accelerating structure is described. Preliminary analysis shows that the structure exhibits a number of attractive properties:

1) High gradient due to decreased values of surface fields as well as decreased time of exposition by these fields.

2) High efficiency and transformer ratio from drive beam to accelerating beam.

In addition the proposed structure uses all metallic cavities, requires no transfer or coupling structures between the drive and acceleration channels, and has cavity fields that are symmetric around the axes of the drive beam and the accelerated beam.

References

1. *Kuzikov S. V., Plotkin M. E.* Quasi-optical accelerating structure operated with a superposition of synchronized modes // Conference Digest of the Joint 32nd IRMMW Conference and 15th International Conference on Terahertz Electronics, Cardiff, UK, September 3–7. 2007. Vol. 2. P. 797–798
2. *Kuzikov S. V.* High-Power RF Components for Accelerators, CLIC'07 Workshop, Geneva, October 16–18, 2007.
3. *Kazakov S., Kuzikov S. V., Hirshfield J. L.* Multi-mode, Multi-Frequency Two-Beam Accelerating Structure, High-Gradient Collaboration Workshop, Maryland, January 23–24, 2008.
4. *Kuzikov S. V., Kazakov S. Yu., Plotkin M. E., Hirshfield J. L.* High-Gradient Multi-Mode Two-Beam Accelerating Structure // Proc. of EPAC'08 Conf., Genoa, June 23–27. 2008. WEPP133.
5. *Wilson P. B.* Scaling Linear Colliders to 5 TeV and Above, LAC-PUB-7449, April, 1997.
6. *Nezhevenko O. A.* On the Limitation of Accelerating Gradient in Linear Colliders Due to the Pulse Heating, PAC97, Vancouver, 1997. P. 3013.
7. *Kuzikov S. V., Plotkin M E.* Theory of Thermal Fatigue Caused by RF Pulse Heating // International Journal of Infrared and Millimeter Waves. 2007. Vol. 29, № 3. P. 298–311.
8. *Petelin M. I.* A quasi-optical electron-positron collider? // Proc. of Strong Microwaves in Plasmas Workshop, Nizhny Novgorod, 1–9 August 2002 / edited by A. Litvak. 2003. V. 1. P. 82–89.
9. *Wuensch W.* Comprehensive Analysis of RF Test Results and New RF constraints, High-Gradient Collaboration Workshop, Maryland, January 23–24, 2008.
10. *Grudiev A.* Dependence of the breakdown rate on the pulse shape // CLIC Workshop, Switzerland, October 16, 2008.

A THREE-CHANNEL TERAHERTZ RECTANGULAR DIELECTRIC WAKEFIELD ACCELERATOR THAT DEVELOPS HIGH GRADIENTS

G. V. Sotnikov[1, 2], *T. C. Marshall*[3, 2], *S. V. Shchelkunov*[4], *J. L. Hirshfield*[4, 2]

[1] NSC Kharkov Institute of Physics and Technology, Kharkov, Ukraine
[2] Omega-P, Inc., New Haven Connecticut, USA
[3] Columbia University, New York City, USA
[4] Yale University, New Haven, Connecticut, USA

The wakefields set up in a seven-zone symmetric THZ structure are studied. It is found that for overall transverse dimensions 2.121 mm wide and 0.6 mm tall, two 5-GeV drive bunches (3 nC, and *x*/*y*/*z* dimensions 0.3/0.3/0.12 mm^3 as available at SLAC) will set up an axial wakefield ~350 MV/m in the witness channel. The symmetry of the structure assures that not only small transverse forces are set up on the witness bunch, but also that the two components of transverse force are equal and opposite at the bunch location that could enable dynamical stabilization in an accelerator comprising many modules. Transverse forces on the drive bunch tails are small enough to allow bunches to move ~0.35 m without suffering erosion. The use of multiple channels allows a transformer ratio ~20.

Recently a novel dielectric structure was proposed for a two-beam wake field accelerator which is configured as a rectangular metallic pipe with five zones formed by three parallel dielectric slabs creating two vacuum channels. One channel is for a drive bunch and the other for an accelerated witness bunch [1, 2]. A 30 GHz 5-zone dielectric structure (DS) has been designed at present and is under construction. A proof-of-principle test of this high transformer ratio accelerator is to be carried out at Argonne National Laboratory [3]. A 5-zone two-channel DWA structure has many advantages: separate paths for drive bunch and accelerated bunch; continuous coupling of energy between channels; good transformer ratio set by channel width ratio; a rectangular structure easy to construct. However, the drive bunch excites unwanted modes which can destabilize the accelerated ("witness") bunch motion.

The cure is to use a 7-zone rectangular structure which eliminates non-symmetrical modes, permits dynamical stabilization of the accelerated bunches using many modules, and retains the good features of the 5-zone model. In this paper we present the results of the design and simulation of a 7-zone accelerator structure in the THz range. Computations based on the analytic theory and a 3D EM code are described.

Design and Simulation of a Seven-Zone DWA

In Fig. 1 the geometry of the structure under studies is shown.

When using the analytical description of wakefield excitation in a multizone waveguide structure we shall proceed from the nonhomogeneous equations for components of electric and magnetic fields [4, 5] transverse to the dielectric

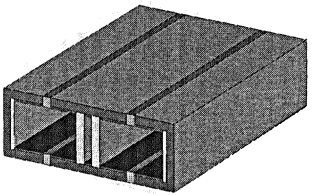

Fig. 1. Schematic of the seven-zone structure studied here. The vertical dielectric slabs (gray color) line the witness bunch channel (center) and the two adjacent drive bunch channels. Wall slots are for pumping. At the top and the bottom of channels are deposited thin diamond films (dark gray shade).

slabs. The first equation describes the excitation of LSM modes and the second equation describes the excitation of LSE modes. These components are generating; other components are expressed through these eigen-functions. The designed accelerating structure should provide a symmetric distribution of longitudinal electric field in each of the vacuum channels and a high transformer ratio. For implementation of these requirements we note the following. It is possible to present the 7-zone dielectric structure as a particular case of a 9-zone DS where the dielectric permeability of all slabs is the same. The 9-zone DS consists of three 3-zone symmetric structures. It is known that eigen-waves of any symmetric 3-zone dielectric structure can be presented as a superposition of LSM and LSE modes having a symmetric and nonsymmetric transverse distribution of axial electric field. For the acceleration purpose we are interested only in the symmetric waves. Therefore if we introduce the metal walls at the boundary of two dielectric slabs, the distribution of the axial electric field is not changed. Now we can split the 9-zone structure into three 3-zone dielectric structures surrounded by a metal waveguide, compute the dimensions of slabs and vacuum channel for a fixed operating frequency and, finally, combine the 7-zone structure from three 3-zone structures. After choosing the dimensions of the DS we can compute the wakefield excited by electron bunches using the analytical theory [4, 5]. There is an important provision: if we want to obtain a high transformer ratio, the dimension of the accelerating channel must be significantly less than the transverse dimension of the accelerating channel.

Analytical computations have shown that the required condition of symmetrical distribution of axial electric field is satisfied by the LSM_{41} wave. For LSM_{41} mode operation frequency of 1 THz the design parameters of a DS excited by two co-moving drive bunches (each is located in the center of corresponding channel) are presented in Table.

Along with the operating mode LSM_{41}, the pair of synchronously moving drive bunches excite other modes. The main part of the radiated power is concentrated in the LSM_{21}, LSM_{41} and LSE_{11} modes. The frequencies of the LSM_{41} and LSE_{21} modes are very close.

The composite axial forces in the center of the drive and the center of the accelerating channels are presented in Fig. 2. At the second maximum the value of accelerating force is ~350 MeV/m. The decelerating force is significantly less. The average decelerating force acting on the drive bunch is 19.7 MeV/m. Thus the designed structure provides a transformer ratio ~20.

Parameters for a three-channel symmetric dielectric wakefield accelerator module

LSM_{41} design mode	1003.4276 GHz
drive channels dimensions $2a_1 = 2a_3$	958μm
accl. channel dimensions $2a_2$	100 μm
structure height $2d$	600 μm
transformer ratio	~20
slab-1 and slab-4 thickness	13 μm
slab-2 and slab-3 thickness	39.5 μm
slab relative dielectric constant	5.7
bunch size	0.3 × 0.3 × 0.12 mm
bunch energy	5 GeV
bunch charge	3 nC

For the numerical simulation of a wakefield build-up in the designed DWA we used a wakefield solver of the Microwave Studio code. In this study, the two drive bunches enter (from the left) of the three-channel structure and exit to the right. The component of electric field $E_z(x, z)$ is shown in Fig. 3. The wakefields excited in the central witness bunch channel are strong and periodic immediately following the drive bunches, but these fields are attenuated and disorganized by the "quenching wave" which follows behind at approximately the group velocity of the modes in the structure [6]. The quenching wave arises from the need to satisfy the boundary and initial conditions at the input to the structure. As the bunches move further, their wakefields "outrun" the slower-moving quenching disturbance so that a more periodic wakefield pattern dominates eventually. Peak accelerating fields on a favorably-positioned witness bunch are ~350–400 MeV/m.

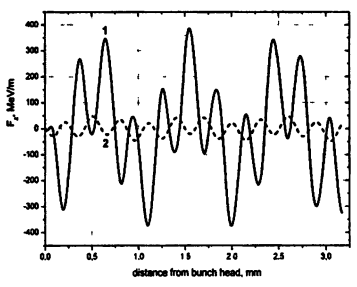

Fig. 2. Axial profiles of composite axial forces along center of accelerating (*1*) line and drive (*2*) channels

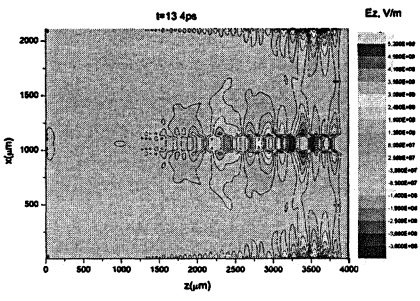

Fig. 3. Accelerating field: the drive bunches are located on the right in the centers of the drive bunch channels. Apparent peaks at $z = 3.25$ mm and $z = 3.55$ mm correspond to the accelerating phase of field.

At this point the analytic theory has an important role to play. If the expressions for the transverse force $\mathbf{F}_\perp$ (all components, all fields) are expanded in the vicinity of the axis of the drive bunch channel, it is found that $F_x = -F_y$, that is,

there is a "quadrupole" like focusing/defocusing effect. The equality $F_x = -F_y$ is held if $d << n\gamma_0\lambda_{mn}/4$ (d is a height of the DS, λ_{mn} is operational wavelength, γ_0 is the relativistic factor). For the parameters of the designed structure (see Table) the specified inequality is well satisfied.

In Fig. 4 the example of witness electrons traveling in a cross section of the rectangular DS is shown. At the initial time, the accelerated electrons are located at the second maximum of the accelerating field (Fig. 2, $z = 0.646$ mm). It is seen from Fig. 4 that the witness electrons are being focused in the x-direction and defocused in the y-direction.

In Fig. 5 the drive beam electrons travel across the DS as shown. For calculations we take the particles located at the initial time at the tail of the bunch. In comparison with the accelerated particles, the drive electrons are defocusing in x-direction but are focusing in x-direction. The tail drive bunch electrons can travel ~0.4 m before they hit the dielectric.

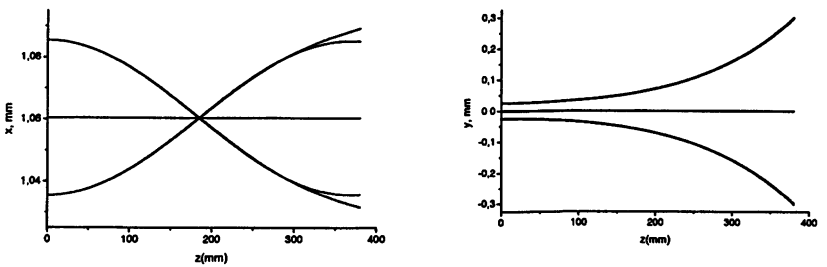

Fig. 4. The trajectories of "witness" particles along the center of the accelerating channel. The initial energy of the test particles is 5 GeV. The calculation uses 9 particles with initial positions (x_i, y_j) $x_i = x_{ac} + x_a(i/2-1)$, $y_j = y_a(j/2-1)$.

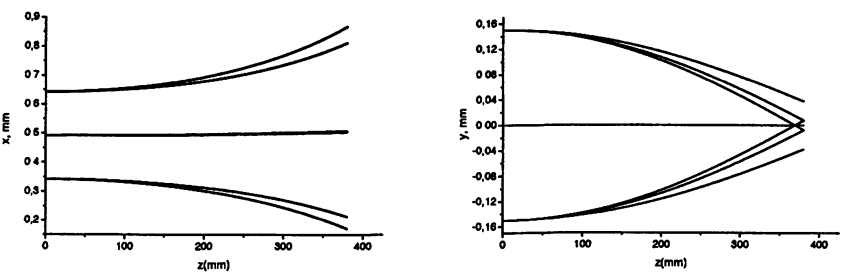

Fig. 5. The trajectories of electrons located at the tail of the first drive bunch. The initial energy of the test particles is 5 GeV. For the calculation we take 9 particles with initial positions (x_i, y_j) $x_i = x_1 + x_a(i/2-1)$, $y_j = y_a(j/2-1)$.

This excellent property of the 7-zone symmetric dielectric structure allows modular sections to be used in a future accelerator. Let (see Fig. 4), in the first

section, the witness bunch be defocusing across the dielectric slabs (x-direction), and focusing along the dielectric slabs (y-direction). If we rotate the second section through 90 degrees about the axis defined by the witness electrons, then the second section will focus the electron bunch in x-direction and will defocus it in the y-direction. Thus we can realize the alternating dynamical focusing of the witness bunch.

It should be noted that the top and bottom walls of the structure are metallic. Indeed this situation is not desirable, as there is a strong component of electric field E_y at these walls. We have studied the effect of lining these walls with a dielectric layer (indicated as the thin dark gray shaded layer shown in Fig. 1). The dielectric will reduce the intensity of the electric field near the metal surface by a factor ~5. Computations show that introducing this layer does not spoil the representation of fields in terms of the LSM/LSE modes. The numerical results showed, for all practical purposes (the dielectric film was 10 % of the thickness of the dielectric slabs), the same field distribution as the case without the insulating slabs.

Thus we can conclude:

1. The seven-zone structure enjoys symmetry advantages which reduce transverse forces on the accelerated bunch and favor long travel distances. The designed structure allows realizing "quadrupole"-like alternating focusing of the accelerated bunch along the transverse *x/y* directions in pairs of structures.

2. The use of two symmetrically-located drive bunches increases the drive energy available for acceleration.

3. Wall coatings can shield the metal surfaces from high fields and do not disturb the LSM/LSE modes appreciably.

4. A small (~1 mm), but not microscopic, structure will permit THz accelerating fields to build up to "interesting" levels in connection with future colliders.

Acknowledgements

This research was supported by the Department of Energy, High Energy Physics Division, Advanced Accelerator R & D.

References

1. *Wang C., Marshall T. C., Yakovlev V. P., and Hirshfield J. L.* PAC Proc, May 2005, TPAE-013.
2. *Wang C., Yakovlev V. P., Marshall T. C., LaPointe M. A., and Hirshfield J. L.* // 12th AAC Workshop, AIP Conf. Proc, 2006, **877**, 910.
3. *Sotnikov G. V., Marshall T. C., Shchelkunov S. V., Didenko A., and Hirshfield J. L.* Two Channel Rectangular Dielectric Wakefield Accelerator Structure Experiment, and references therein (Proc. 13th AAC Workshop, to be published).
4. *Wang C. and Hirshfield J. L.* Phys. Rev. ST-AB, 2006, **9**, 031301.
5. *Sotnikov G. V., Onishchenko I. N., Hirshfield J. L., Marshall T. C.* Problems of Atomic Science and Technology, No. 3. Series: Nuclear Physics Investigations, 2008, **49**, p. 148–152.
6. *Onishchenko I. N., Sidorenko D. Yu., Sotnikov G. V.* Phys. Rev E. 2002, **65**, 066501; see also 12th AAC Workshop, AIP Conf. Proc. 2006, **877**, 888.

LIMITING SATURATION LEVELS OF WAKE FIELDS EXCITED BY LENGTHY ELECTRON BUNCHES IN THE DIELECTRIC RESONATOR

K. V. Galaydych[1], S. V. Kuzikov[2], P. I. Markov[1], G. V. Sotnikov[1]

[1] NSC "Kharkov Institute of Physics and Technology", Kharkov, Ukraine
[2] Institute of Applied Physics, Nizhny Novgorod, Russia

Theoretical research and numerical modeling of excitation of a wake field in the dielectric resonator by regular sequence of lengthy relativistic magnetized electron bunches are carried out. The nonlinear system of the equations, describing multimode excitation of a wake field in the completely filled dielectric resonator is obtained. Numerical modeling is carried out and dependences of the maximal amplitude of a longitudinal electric field on length of bunch are investigated. Physical explanations to the obtain dependences are given.

Charge particles acceleration in the wake field excited by relativistic electron bunches (REB), injected in the dielectric resonator, is one of perspective methods of acceleration, which is investigated and developed recently.

Formation of a wake field wave occurs due to spontaneous Cherenkov radiation by REB. As the amplitude of a wake field wave is proportional to bunch charge, and use of bunches with a greater charge is interfaced to a difficulties, for the obtaining of high gradients of an accelerating field it is possible to use sequence of relatively low-current REB.

For accumulation of energy of fields from the great number of a regular sequence of bunches and achievement high gradients accelerations at rather low charge of a single bunch the most effective is use of dielectric resonators [1].

The purpose of the given work was research of dependence of the maximal values of a longitudinal electric field and the stored electromagnetic energy in the resonator from length of bunch. According to results of the linear theory of interaction of electron bunches with the electromagnetic field excited by it in the resonator [2], the amplitude of a wake field is the maximal for point-size bunches and falls with increasing of the bunch length.

Consideration of the self-consistent interaction shows, that the intrinsic bunch particles dynamics leads to new results.

Wake field structure in the cylindrical dielectric resonator

Let's consider the cylindrical resonator completely filled by dielectric with dielectric permeability ε along which axis with frequency f electron bunches with a charge Q_b are injected. Bunches are hollow cylinders with radius r_b, and length L_b. We shall model a bunch with method of macroparticles and to describe in terms of the Lagrange variables. Effect of the drift channel on a dispersion we will neglect, assuming its cross-section size small in comparison with those of resonator. The distribution of charge and current density has the form of:

$$\rho_b(t,z,r) = I_b \frac{\delta(r-r_b)}{2\pi r_b} \int_0^t dt_0 \Psi(t_0)\delta(z - Z_L(t,t_0))\ddot{I}\ (t,t_0),$$
$$j_{bz}(t,z,r) = I_b \frac{\delta(r-r_b)}{2\pi r_b} \int_0^t dt_0 \Psi(t_0)\frac{dZ_L}{dt}\delta(z - Z_L(t,t_0))\ddot{I}\ (t,t_0), \quad (1)$$

where I_b is the amplitude of a bunch current, which equal $I_b = Q_b v_0 / L_b$ (v_0 is a start bunch velocity, and L_b is the bunch length), t_0 is the time of the macroparticle injection into the resonator, $Z_L(t,t_0)$ is longitudinal coordinate of a macroparticle, $\delta(t)$ is the Dirac function. The function $\Psi(t_0)$ describes current form at the input in the resonator, in case of a regular train of identical bunches with homogeneous distribution of a charge it has the form of sequence of rectangular impulses:

$$\Psi(t_0) = \sum_{i=0}^{N_b-1} \theta(t_0 - iT_{rep}) - \theta(t_0 - T_b - iT_{rep}), \quad (2)$$

T_{rep} is the bunch repetition time, $T_b = L_b / v_0$ is time duration of a bunch, summation in definition of function $\Psi(t_0)$ is made on number N_b of the injected bunches. Integration in the expression (1) is made on the particles which are in the resonator. This condition is described by function $\ddot{I}\ (t,t_0)$, which is equal to 1 if the particle is inside of the resonator and 0 if the particle has not entered yet or has already left the resonator.

The self-consistent system of the equations describing interaction of sequence of charged bunches with fields in the resonator, excited same bunches, consists of Maxwell equations for a field (3), and the moving equations of particles of bunch (4).

$$\text{rot}\,\mathbf{H} = \frac{\varepsilon}{c}\frac{\partial \mathbf{E}}{\partial t} + \frac{4\pi}{c}\mathbf{j}_b,\ \text{div}\,\mathbf{H} = 0,\ \text{rot}\,\mathbf{E} = -\frac{1}{c}\frac{\partial \mathbf{H}}{\partial t},\ \text{div}\,\mathbf{E} = \frac{4\pi}{\varepsilon}\rho_b, \quad (3)$$

$$\frac{dP_L(t,t_0)}{dt} = q_L E_z(t, z=Z_L, r=r_b),\ \frac{dZ_L(t,t_0)}{dt} = \frac{P_L}{m_L\sqrt{1+(P_L/m_L c)^2}}, \quad (4)$$

where $V_L(t,t_0)$, $P_L(t,t_0)$, q_L, and m_L are velocity, momentum, charge and mass of a macroparticle accordingly. It is supposed, that the system is placed in strong enough magnetic field so transverse moving of bunch particles is not considered.

Subject to boundary conditions for fields on ideally conducting walls of the resonator, having solved the wave equation for axial-symmetric oscillations we obtain the expression for the longitudinal electric field:

$$E_z = -\frac{8I_b}{\varepsilon R^2 L}\sum_{m,n}\frac{\alpha_m}{J_1^2(\lambda_n)} J_0\left(\frac{\lambda_n r_b}{R}\right) J_0\left(\frac{\lambda_n r}{R}\right)\left(A_{m,n}^{\cos}\cos\omega_{m,n}t + A_{m,n}^{\sin}\sin\omega_{m,n}t\right)\cos k_m z, \quad (5)$$

where R is radius of resonator, $k_m = \pi m / L$ is longitudinal wave number, $J_i(x)$

is Bessel function of the i-th order, λ_n is the Bessel function root $J_0(\lambda_n)=0$; $\alpha_m=1$, if $m\neq 1$ and $\alpha_m=1/2$ if $m=0$; $\omega_{m,n}^2=c^2(k_m^2+(\lambda_n/R)^2)/\varepsilon$ are eigen frequencies of resonator. Using conditions of orthogonality of trigonometrical and cylindrical functions, we'll obtain equations for $A_{m,n}^{\cos}(t)$ and $A_{m,n}^{\sin}(t)$:

$$\frac{dA_{m,n}^{\cos}(t)}{dt}=\left(\cos\omega_{m,n}t\cdot\int_0^t dt_0\Psi(t_0)\frac{dZ_L(t,t_0)}{dt}\cos k_m Z_L(t,t_0)\Pi(t,t_0)-\right.$$
$$\left.-\frac{c^2k_m}{\varepsilon\omega_{m,n}}\sin\omega_{m,n}t\cdot\int_0^t dt_0\Psi(t_0)\sin k_m Z_L(t,t_0)\Pi(t,t_0)\right), \quad (6)$$

$$\frac{dA_{m,n}^{\sin}(t)}{dt}=\left(\sin\omega_{m,n}t\cdot\int_0^t dt_0\Psi(t_0)\frac{dZ_L(t,t_0)}{dt}\cos k_m Z_L(t,t_0)\Pi(t,t_0)+\right.$$
$$\left.+\frac{c^2k_m}{\varepsilon\omega_{m,n}}\cos\omega_{m,n}t\cdot\int_0^t dt_0\Psi(t_0)\sin k_m Z_L(t,t_0)\Pi(t,t_0)\right). \quad (7)$$

Using the equations (4)–(7) we have numerically investigated the dependence of the maximal energy stored in the resonator, and the maximal amplitude of a longitudinal electric field from bunch length.

Before bringing the results of the nonlinear analysis of excitation of the dielectric resonator we want to pay attention, that amplitude of a longitudinal electric field at a linear stage of excitation of the dielectric resonator is proportional to quantity of the bunches which have been pass through the resonator, and besides it is proportional to the interference multiplier $\sin(\omega_{m,n}L_b/2V_0)/(\omega_{m,n}L_b/2V_0)$. This multiplier is similar to multiplier, describing Cherenkov radiation in a waveguide of lengthy electron bunches (see, for example, [3]). Thus, at a linear stage the maximum of amplitude of an excited field is achieved for short bunches, when $\omega_{m,n}L_b/2V_0\to 0$. We will compare now this result to results of a nonlinear stage of excitation of the dielectric resonator.

Numerical simulation results

For numerical calculations the next parameters have been chosen: frequency of bunches repetition f = 2.722 GHz, its energy 2 MeV, charge of bunch was equal to –6.4 nC, radius of bunch r_b = 0.5 cm, dielectric permeability ε = 2.1. Length and radius of resonator have been chosen in compliance with conditions, present at [4], and for cylindrical geometry they are desctibed the expressions: $L=V_0N_{res}/2f$, $R=\lambda_1 L/\pi N_{res}\sqrt{\varepsilon\beta_0^2-1}$, $\beta_0=V_0/c$, N_{res} is a number of resonance harmonic (in our case it is equal to 12). For given energy, frequency f, and εL = 64.7 cm, R = 4.099 cm.

Results of numerical calculations of system of the equations (4)–(8) for various length of bunch at fixed other parameters of bunch sequence and structure are

presented on Fig. 1 and Fig. 2. On Fig. 1 dependences of energy of the electromagnetic field stored in the resonator versus time are resulted, at continuous injection in it bunch sequences, for different values of length of bunch. Vertical dashed lines on the Fig. 1*a* correspond to time of 71 ns (the time when values of energy for lengths of bunches $L_b = 0.25$ cm and $L_b = 4.89$ cm are equal among themselves), and the time of 216 ns (at length of bunch $L_b = 0.25$ cm energy has already reach on saturation, and for the length of $L_b = 4.89$ cm saturation has not come yet, and energy continues to increase).

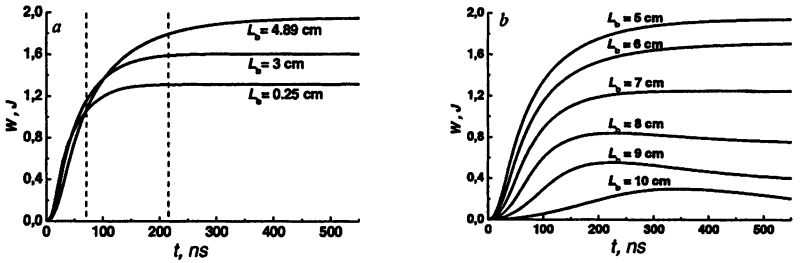

Fig. 1. Energy of the electromagnetic field stored in the resonator versus time for different values of bunch length.

As follows from the resulted in Fig. 2 dependences, the amplitude of axial electric field and saturation energy, stored in the resonator, depends on bunch length, and has a maximum. Numerical calculations have shown, that bunch length at which the maximum is achieved, is close to half of length of a wave of a resonant harmonic.

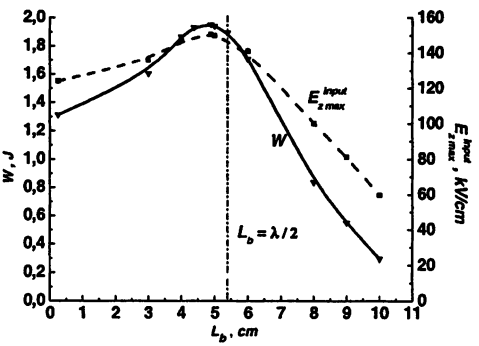

Fig. 2. Saturation energy and amplitude of an axial electric field ($r = 0$, $z = 0$) versus bunch length. Vertical dotted corresponds to the bunch length is equal to half of length of a wave of a resonance harmonic.

To explain increase in amplitude of a field for lengthy bunches in comparison with point-size bunches it is possible, having assumed, that particles of lengthy bunches are on the average in weaker decelerating field. This proves to be true by view of phase portraits of bunches in the resonator for the different moments of time.

In Fig. 3 phase planes for the time of 71 ns (*a*) and the time of 216 ns (*b*) (it correspond vertical dashed lines on the Fig. 1*a*) for values of length of bunch 0.25 cm and 4.89 cm are presented.

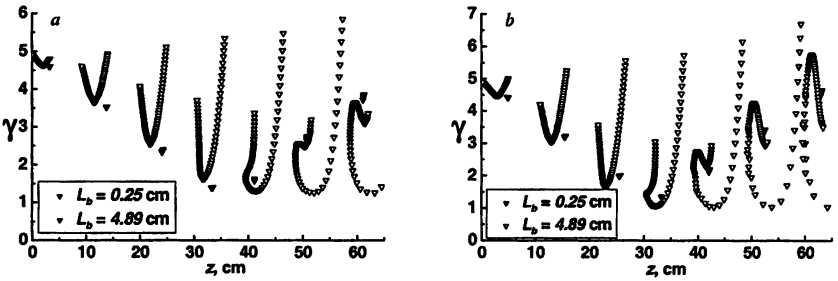

Fig. 3. Phase planes for time 71 (*a*) and 216 ns (*b*) for bunches length 0.25 and 4.89 cm

As shown in [5], saturation of the stored electromagnetic field energy in the resonator is due to return influence of a field on bunches exciting it. Thus bunches at the first half of resonator are in a decelerating phase of a field and lose energy. Then bunches pass to accelerating phase and at second half of resonator start to gain energy. Such dynamics is characteristic for bunches having the length $L_b \le \lambda_{res}/4$, where λ_{res} is the resonant length of the wave equal for given parameters 10.78 cm. It show phase planes on Fig. 3 for bunches in length L_b = 0.25 cm for the time of 71 ns (Fig. 3*a*, before achievement of saturation) and the time of 216 ns (Fig. 3*b*, after achievement of saturation). Phase space dynamics of bunches in length $L_b \le \lambda_{res}/2$ as the whole remains same, but inside of each separate bunch it begins to vary. The velocity of particle transition from accelerating in a decelerate phase is determined by force acting on it. The particles which are being a maximum of the decelerating field stop to give the energy to the field in the first place, and on a phase plane their dynamics is similar to dynamics of point bunch. In long bunch, in difference from point one, there is a great number of particles which will continue to give energy, as shown on Fig. 3 for bunch in length L_b = 4.89 cm. And due to presence of such particles energy of saturation increases. At the further increasing of the bunch length the energy of saturation starts to decrease. It is possible to explain it to that the part of bunch of the train starts to be accelerated that leads to decrease in the energy transfered by bunch train to a field.

Conclusions. Theoretical researches and numerical modeling of a nonlinear regime of excitation of the cylindrical resonator completely filled a dielectric, by sequence of relatively low-current relativistic electron bunches of finite length are carried out. Results of the given researches have shown that dependence of a longitudinal electric field and the stored electromagnetic energy in the resonator from length of bunch has a maximum being near to half of length of resonant wave length.

References

1. *Balakirev V. A., Onishchenko I. N., Sidorenko D. Yu., Sotnikov G. V.* Tech. Phys. Letters, **29**, 589 (2003) (in Russian).
2. *Kurilko V. I.* JETF, **57**, 885 (1969) (in Russian).
3. *Burshtein E. L., Voskresenskiy G. V.* Linear electron accelerators with intensive electron beams. Moscow: Atomizdat, 1979.
4. *Onishchenko N. I., Sotnikov G. V.* Problems of Atomic Science and Technology. Series: Plasma electronics and advanced acceleration methods, **2**, 174 (2000).
5. *Tolstoluzhsky A. P.* Ukr. Phys. J. **24**, 326 (1979) (in Russian).

CONTENTS OF VOLUME 1

HIGH POWER MILLIMETER AND TERAHERTZ WAVE SOURCES

Scientific edition

STRONG MICROWAVES: SOURCES AND APPLICATIONS

PROCEEDINGS
OF THE VII INTERNATIONAL WORKSHOP

In two volumes

Volume 1

Publication approved by the Institute of Applied Physics
of the Russian Academy of Sciences

46 Ul'yanov Street, 603950 Nizhny Novgorod, Russia

Printed by Printing House № 2, "Nauka" Publishers,
6 Shubinsky Pereulok, 121099 Moscow